energies

Alternative Sources of Energy Modeling, Automation, Optimal Planning and Operation

Edited by
George S. Stavrakakis

Printed Edition of the Special Issue Published in *Energies*

www.mdpi.com/journal/energies

Alternative Sources of Energy Modeling, Automation, Optimal Planning and Operation

Alternative Sources of Energy Modeling, Automation, Optimal Planning and Operation

Editor

George S. Stavrakakis

MDPI • Basel • Beijing • Wuhan • Barcelona • Belgrade • Manchester • Tokyo • Cluj • Tianjin

Editor
George S. Stavrakakis
Technical University of Crete
Greece

Editorial Office
MDPI
St. Alban-Anlage 66
4052 Basel, Switzerland

This is a reprint of articles from the Special Issue published online in the open access journal *Energies* (ISSN 1996-1073) (available at: https://www.mdpi.com/journal/energies/special_issues/alternative_sources_energy_modeling_automation_optimal_planning_operation).

For citation purposes, cite each article independently as indicated on the article page online and as indicated below:

LastName, A.A.; LastName, B.B.; LastName, C.C. Article Title. *Journal Name* **Year**, *Volume Number*, Page Range.

ISBN 978-3-0365-5711-3 (Hbk)
ISBN 978-3-0365-5712-0 (PDF)

© 2022 by the authors. Articles in this book are Open Access and distributed under the Creative Commons Attribution (CC BY) license, which allows users to download, copy and build upon published articles, as long as the author and publisher are properly credited, which ensures maximum dissemination and a wider impact of our publications.
The book as a whole is distributed by MDPI under the terms and conditions of the Creative Commons license CC BY-NC-ND.

Contents

About the Editor

George S. Stavrakakis

Prof. George S. Stavrakakis received his first degree in Electrical Engineering from N.T.U.A. (National Technical University of Athens), Athens, in 1980. His postgraduate "D.E.A. in Automatic Control and Systems Engineering" was obtained from I.N.S.A., Toulouse, France in July 1981 and his PhD in the same area was obtained from "Paul Sabatier" University-Toulouse-III, Toulouse, France in January 1984. He has worked as a Research Fellow in the Robotics Laboratory of N.T.U.A., Athens (1985–1988), and as a Visiting Scientist at the Institute for System Engineering and Informatics/Components Diagnostics and Reliability Sector of the EC - Joint Research Centre (JRC) at Ispra, Italy (Sept.1989–Sept.1990). He was Vice President of the Hellenic Center of Renewable Energy Sources (CRES), in the period of November 2000–Apr.2002. In September 1990, he joined the former Electronic and Computer Engineering Dpt., and currently works at the School of Electrical and Computer Engineering, Technical University of Crete, Chania, Crete, Greece as an Associate Professor. He is currently a Full Professor (from November 1995) in the same Department, Laboratory of Circuits, Sensors and Renewable Energy Sources (www.elci.tuc.gr). He performed and performs prototype and advanced engineering research and applications in process re-engineering, systems safety and reliability analysis, robotics and automation, real-time industrial processes fault monitoring and diagnosis, modeling and diagnosis in bioengineering systems, informatics and electronics and microcomputer applications in power systems, renewable energy sources (RES) modeling and automation and autonomous power systems, smart and micro grids, energy storage and autonomous RES integration and optimal operation, increased RES penetration in non-interconnected power grids, energy efficiency and Building Energy Management Systems (BEMS), solid waste management, and waste-to-energy technologies. He is the author and co-author of about a hundred fifty full papers in international refereed journals, chapters in international edition refereed books and refereed conferences, about seventy five research reports, six international edition and dissemination scientific books and approximately seventy papers in international no-refereed conferences on the above topics. He has participated in 41 European Commission and nationally funded research projects and served as the coordinator of nine of these. He is the author of the chapter "Electrical parts of wind turbines" in the award winning handbook "Comprehensive Renewable Energy" of Elsevier May 2012, 1st edition, and June 2022, 2nd edition. He is a permanent invited reviewer in the following high impact factor international scientific journals: IEEE Transactions on Energy Conversion, Electric Power Systems Research, International Journal of Distributed Sensor Networks, Renewable Energy journal, IEEE Transactions on Automation Science and Engineering, Energies (member of the Editorial Board), Applied Sciences, Journal of Intelligent and Robotic Systems.

Preface to "Alternative Sources of Energy Modeling, Automation, Optimal Planning and Operation"

This Special Issue entitled "Alternative Sources of Energy Modeling, Automation, Optimal Planning and Operation" was proposed in order to cover alternative/renewable sources of energy (ASE/RES) modeling and computer simulation, RES automation and more precisely solar thermal plants, photovoltaic (PV) plants, autonomous PV installations, wind energy plants, small hydro plants, modeling, automation, optimal planning and operation. Fuel cells, hydrogen, batteries, and energy storage technologies, modeling, automation, optimal planning and operation were also considered within the SI's main purposes. Biomass, biofuels, biogas, gasification, bioenergy in general, tidal systems, geothermal systems, waste to energy modeling, automation, optimal planning and operation were also of interest. Moreover, hybrid ASE/RES models, automation, optimization, smart micro grids integration as well as ASE/RES forecasting and optimal planning based on artificial neural networks, fuzzy logic, neuro-fuzzy methods, machine learning and artificial intelligence (AI) methods were welcomed. Finally, optimization methods as well as decision support systems (DSS) applied in ASE/RES optimal planning and/or optimal operation as well as to the RES plants reliable grid integration were considered.

George S. Stavrakakis
Editor

energies

MDPI

Article

Information and Public Knowledge of the Potential of Alternative Energies

Galvão Meirinhos [1], Mariano Malebo [2], António Cardoso [2], Rui Silva [3,4,*] and Reiville Rêgo [5]

[1] LABCOM-IFP, University of Trás-os-Montes e Alto Douro—UTAD, 5001-801 Vila Real, Portugal; galvaomeirinhos@gmail.com
[2] Department of Business and Communication Sciences (DBCS), University of Fernando Pessoa—UFP, Praça 9 de Abril 349, 4249-004 Porto, Portugal; 37418@ufp.edu.pt (M.M.); ajcaro@ufp.edu.pt (A.C.)
[3] CETRAD Research Center, University of Trás-os-Montes e Alto Douro—UTAD, 5000-801 Vila Real, Portugal
[4] NECE-Research Center in Business Sciences, University of Beira Interior, 6201-001 Covilha, Portugal
[5] Campus Tomé-Açu, Universidade Federal Rural da Amazônia/UFRA, Rod. PA 140, 2428-4822, Tomé-Açu 68680-000, PA, Brazil; reiville.rego@ufra.edu.br
* Correspondence: ruisilva@utad.pt

Abstract: The objective of this research project is to study the economic development model of the Angolan economy in order to analyze the adoption of an alternative strategy capable of leveraging the economy, based essentially on alternative energies, and therefore, to demonstrate and prove the need to diversify Angola's economic model, highlighting the benefits of a diversified versus a non-diversified economy with respect to sustainability. The first stage of the design of this empirical study involved establishing a focus group in order to construct and adjust a data collection instrument in the form of a questionnaire to be applied to a broader set of managers and informed professionals with a critical view of the country's future and the models and alternatives to economic development and diversification of the economy on a sustainable basis. Energy plays a fundamental role in Angola's economic and social development. Excessive dependency on the oil sector and inefficient production due to high costs, combined with changes in global environmental and energy policies, make it essential to reflect on the evolution of the country's energy sector, equating a different economic development model, the diversification of the economy, and the exploration of other sources of energy, such as biofuels. Renewable energies emerge as a safe, healthy, environmentally friendly and economically viable energy alternative that could bring the Angolan economy closer to that of developed countries. Biofuels have become popular and have begun to be seen as a valid alternative to fossil fuels because they have lower production costs and they cause less impact on nature. Furthermore, since they are biodegradable, they can be commercialized at a lower cost from renewable sources. According to the respondents, the research results show that the best energy alternatives to reduce oil dependency are solar energy, biodiesel, hydraulic energy, and bioethanol. An assessment of the attractiveness and potential of biofuels show that the best alternative is bioethanol, followed by biodiesel.

Keywords: Angolan economy; diversification; strategic alternative; biofuels

Citation: Meirinhos, G.; Malebo, M.; Cardoso, A.; Silva, R.; Rêgo, R. Information and Public Knowledge of the Potential of Alternative Energies. *Energies* **2022**, *15*, 4928. https://doi.org/10.3390/en15134928

Academic Editor: George S. Stavrakakis

Received: 8 June 2022
Accepted: 4 July 2022
Published: 5 July 2022

Publisher's Note: MDPI stays neutral with regard to jurisdictional claims in published maps and institutional affiliations.

Copyright: © 2022 by the authors. Licensee MDPI, Basel, Switzerland. This article is an open access article distributed under the terms and conditions of the Creative Commons Attribution (CC BY) license (https://creativecommons.org/licenses/by/4.0/).

1. Introduction

The primary source of revenue for Angola's GDP is oil, thus, defining Angola's economic model as practically monolithic. Since oil is a commodity, a change in market value is predictable and can be positive or negative for Angolan interests. If the change in market value is negative, the Angolan government would be forced, as it has been in the past, to adjust its general budget to reflect updated oil prices. Oil is the country's largest generator of revenue, which could mean that many of the actions planned for a given year would not be carried out. This situation could force expenditure restraint or restriction situations and could even generate serious social and political pressures.

The World Bank's Report No. AUS6794, clearly stated that "an effective economic diversification strategy could increase Angola's long-term GDP growth trajectory". In the report, there is an obvious association between economic growth and the need to diversify domestic production, and therefore, create a more balanced fiscal balance. Based on the above, we justify the need to address this topic, since it is clear that strategic alternatives for Angola are necessary and mandatory to concretely change their economic model, generating greater sustainability and economic growth in the long term.

According to the Central Intelligence Agency, the Angolan economy is driven by the oil sector, representing around 50% of the GDP, accounting for more than 70% of the government's revenues, and corresponding to more than 90% of the country's exports, which confirm Angola's flagrant dependency on the oil sector. Oil prices are defined on the international markets with daily price oscillations, which become an economic instability factor and a problem for managing an economy that depends essentially on the oil industry. On the one hand, the problem of the Angolan economy lies precisely in the fact that oil is a non-renewable natural resource that could compromise the country's economic position in the long term. On the other hand, as we have seen, oil is a commodity and the Angolan government has no control over its price since it depends on the international markets. This reality already occurred in 2008, 2009, 2015, 2016, and 2017, when the Angolan government's general budget had to be revised due to a drop in the price of oil on the international markets. Between July and December of 2008, oil prices fell by about 70%, and since then, have fluctuated constantly. According to the International Monetary Fund Report No. 18/157, Angola, although it is the second largest oil producer in Africa, suffers severely when the price of oil is between USD 50 and 55, which involves reducing oil production because it is unprofitable, thus, creating severe budgetary problems because of the gigantic investment needs in infrastructure and social spending. The ideas presented in the abovementioned report justify the need for this research on energy alternatives. Therefore, we aim to analyze strategic alternatives for diversification of the Angolan economy and to evaluate the attractiveness of biofuels.

To better frame the knowledge problem and objective, this research was conducted in three phases:

1. In the exploratory phase, we conducted a bibliographical review to obtain greater familiarity with the theme's problem, to clarify the understanding and focus of the research on alternative energies and, to facilitate the construction of the research hypotheses [1].
2. In a second phase, we collected the opinions of Angolan economic experts on the sustainability of strategic alternative energies for diversification of the Angolan economy. To support the analysis, the Delphi technique was adopted to obtain a specialized understanding regarding the sustainability of ethanol or other energy possibilities, as possible strategic alternatives for diversification of the Angolan economy.
3. In the third phase, we applied a debugged and validated survey to understand, from the point of view of managers and specialists from various activity sectors, the possible energy alternatives as a means of diversifying the Angolan economy.

This is an exploratory study with a descriptive design in which, in the first phase, we established a "focus group" to construct and adjust a data collection instrument in the form of a questionnaire to be subsequently applied to a broader set of managers and specialists [2,3].

Despite the vast literature that addresses the phenomenon of economic development, and the related areas of knowledge, the approaches have been focused on territorial scales. Thus, it is important to address the exogenous and endogenous economic development models that are relevant to the configuration of an intended analysis. According to [4] endogenous economic growth is long-term growth determined by internal forces in the economic system. Development is based, though not exclusively, on locally available resources, local knowledge, culture, and leadership. It has mechanisms for local learning and experimentation, building local economies, and retaining benefits in the local area [5,6].

2. Literature Review

2.1. Models of Endogenous Development of an Economy

Endogenous development is a paradigm based on the basic idea that the productive system of a country grows and is transformed using the development potential existing in the territories, that is, regions and cities, through investments made by companies and public entities, under the control of local communities, with the ultimate goal of improving the standard of living of the populations in these territories [7,8]. In this sense, it is clear that the concept of endogenous development integrates the social and economic dimensions. The protagonism claimed for the territorial dimension, in turn, is suggested not only as an expression of the spatial anchorage of organizational and technological processes but, equally, of the circumstance that any locality or region offers itself as the result of a history that has been shaping its economic, cultural, and institutional environment.

Endogenous development is linked to the dynamics of a country, its cities and regions and the network of agents and interests that give them substance. This is to underline, in line with what [9–11] have stated, among others, that the processes of growth and structural transformation that take place arise as a consequence of the transfer of resources from traditional to modern activities, the exploitation of external economies, and the introduction of innovations, which are aimed at increasing the well-being of the population of the city, locality, or region that generated a change. In other words, growth is organized around the expansion and transformation of pre-existing activities, using the resources and innovation potential available in a territory, conditioned by the social and cultural structure and codes of conduct of human communities based in particular spaces, which favour or limit it and, in any case, give it its unique shape.

From a policy point of view, starting from the framework described above, the actions to be developed should take into consideration the availability of the country's resources and promote their economic enhancement, whether natural resources or others. The solidity of the economic affirmation processes and the capacity to internalize the wealth generated is due to political initiatives that should take advantage of the network of local solidarities and the existing or developed concertation capacity, involving all the economic operators' social agents and political decision-makers. The emphasis on a country's potential, which is the starting point for this approach to development, takes the form of a policy to enhance the resources and capacities of a region or country, which, as we shall see below, must be at the root of regional or even national policymaking.

2.2. Models of Exogenous Development of an Economy

An exogenous model studies the growth of a country's economy over a long period of time. The model presents the source of economic growth: capital accumulation, labor force growth, and technological change [12]. was concerned with demonstrating that product per capita was an increasing function of the relationship between capital and labor. Labor force grows at a natural rate (exogenous to a model). In this sense, an amount of savings per capita is necessary, which must be used to equip new workers with capital per capita equal to that of other workers. The other part of the savings should be used to guarantee non-depreciation of the capital. The first part of the savings quoted above to equip new workers is called "capital enlargement" (expansion of the labor force), and the savings used to increase the capital/labor ratio is called "capital deepening". To reach a steady-state situation, the savings per capita must equal capital enlargement. The capital per worker has a decreasing income, therefore, when this equilibrium point is reached, there is no point in investing more in a worker who has per capita savings equal to the capital expansion because this worker's productivity will not be maximized. Thus, the conditioning factor of economic growth is the growth rate of the labor force.

For [7], exogenous economic growth is long-term growth determined by forces that are external to the economic system. Exogenous development restricts the use of endogenous resources. It seeks opportunities for economic development abroad, considering the supply of raw materials, as well as knowledge, financing, skilled labor, and markets [5,13]. In the

case of the Angolan economy, it is necessary to analyze the conditions and potentialities that the country possesses and to evaluate which economic development model best adapts to its reality. However, determining the optimal size of the public sector is difficult. The state's concern with maximizing long-term growth must weigh the effects of public intervention policy and the growth-retarding effects of higher taxes and regulations.

Regarding higher taxes and regulations, economic growth theory that takes consideraiton public sector functions such as correcting market failures, investments in infrastructure, and taxes, may neglect the state's role in redistributing income and how policy behavior is determined by sometimes conflicting interests. This is a situation that occurs in many countries, and we believe that sometimes political decision-makers are not in a position to make strategic decisions for the development of their countries.

2.3. Oil

Brazil's National Electrical Energy Agency [14] defines oil as a flammable oil formed, over millions of years, from the decomposition of organic matter such as plants, marine animals, and vegetation typical of flooded regions and found only in sedimentary terrain. Oil is composed of hydrocarbons, made up of carbon and hydrogen, to which atoms of oxygen, nitrogen, and sulphur can be added, as well as metallic ions, mainly nickel and vanadium. According to BP, world oil production in 2014 was around 4226.60 million tons per day, while daily consumption was around 4211.10 million tons. From the figures presented at the time, one can see that oil is a resource in high demand on the international markets [15]. Oil is a primary source resource on the stock exchange and its price is determined by supply and demand. Therefore, this explains the importance of oil when analyzing some of its derivatives, such as petrol, paraffin, diesel, asphalt, synthetic rubber, lubricants, and plastics, among others. The BP report published in June 2015 illustrated the importance of oil in the Angolan economy, as the second largest oil producer on the African continent, with the ranking led by Nigeria [16].

The Economic Report of Angola 2016, prepared by the Catholic University of Angola, outlined the importance and impact of oil, evidencing the clear dependency on oil in relation to the economy. Oil is undoubtedly of paramount importance to the Angolan economy because it leverages a good part of other sectors of national activity such as agriculture, fisheries, manufacturing, and transport. Thus, economic sustainability involves a greater balance in the sources that generate the gross domestic product to generate new opportunities and reduce costs by reducing the need to import and leverage new possibilities and opportunities for internal capacity building and investments in new forms of energy production. When nearly 30% of the state budget is dependent on oil and gas revenues, the country is in a weak position to make reforms and strategic investments for the integral and ongoing development of the Angolan economy and society [17].

2.4. Biofuels

According to [18], biofuels are obtained from renewable organic matter, also called biomass, which can be products of animal or vegetable origin, as is the case of sugar cane, corn, soya, sunflower seeds, wood, and cellulose. Therefore, it is possible to produce fuels such as alcohol, ethanol, or biodiesel from these products. Biofuels are popular because they are a valid alternative to fossil fuels such as oil in specific sectors. In addition, they have lower production costs because they cause less impact on nature since they are biodegradable, they are marketed at a lower cost, and they are the result of renewable sources.

Brazil is an example of one country that have been looking at biofuels since very early on. According to the Ministry of Mines and Energy (MME), the pioneer tests were carried out between 1905 and 1925. In 1931, the Brazilian government established a decree that made mixing 5% alcohol in imported gasoline compulsory. However, with the discovery of extensive oil reserves in the Middle East, interest in biofuels declined globally. However, with the first world oil crisis in 1973, the search for new energy sources re-emerged.

In 2015, Paris, France hosted the 21st United Nations Conference on Climate Change (COP 21), whose objective was to bring countries to an agreement on global warming by reducing the emission of greenhouse gases [19]. Unfortunately, that same year, there was a drastic fall in oil prices, generating considerable constraints in the economies of the producing countries, which had to review their budgets and were forced to reflect on alternatives. However, even before the great discussions on climate, greenhouse effect, and oil crisis, several countries were already producing biofuels in considerable quantities, such as the United States of America, Brazil, Germany, and Indonesia.

2.5. Ethanol

Ethanol is obtained from sugar cane as a biofuel, since the term biofuel is generic and may encompass several types and several origins. Nevertheless, we identified different energy alternatives in the questionnaire, such as biodiesel, algae biodiesel, H-BIO, geothermal, hydraulic, solar, wind, and tidal energy alternatives. According to Petrobras, ethanol is alcohol with an oxygenated organic compound, also called ethyl alcohol, and its chemical formula is C_2H_5OH. Ethanol is obtained from various raw materials such as sugarcane, corn, manioc, and sugar beet [18].

According to the Ethanol Industry Association (IEA), and in terms of applications and uses of ethanol, it can be used as a raw material in three areas, i.e., beverages, fuels, and industry, the latter being the final use in: the manufacture of pharmaceuticals, cosmetics, toiletries, detergents and cleaning products, printer ink cartridges, paints, and coatings. The ethanol industry will always depend, in a first analysis, on the existence of the minimum conditions for the generation of raw material, and the potential that this raw material has in terms of quantities and respective renewal conditions [20]. According to [21], implementing biofuel projects in Angola require about two years of research related to product tests and choices of best species. In addition to expenses and direct costs required to implement an ethanol industry, there are other important areas to take into consideration, such as legislation, equipment, and human capital that always vary, and therefore, require a feasibility study involving experts in the most distinct areas, who can determine with proven evidence the probability of success or otherwise in implementing an ethanol industry.

Concerning the ethanol industry, the approach taken in this study is not focused on the details of the feasibility or otherwise of implementing an industry. Rather, the focus is on an analysis that seeks to understand the capacity these industries can offer to Angola's GDP in terms of economic and social impact, based on existing successful experiences with already implemented industries. An economic development model of the Angolan economy is highly dependent on its endogenous characteristics, namely its oil production capacity, but it is also totally dependent on exogenous characteristics, namely the international fixing of oil barrel prices. This circumstance leaves the country's real economic growth dependent on finite natural resources and the impossibility of intervening in the fixation of the price of a barrel of oil. In this sense, there is a possibility that alternative energies may be a solution to the abovementioned dependency on oil, namely through ethanol production.

3. Methodology

The definition of the research problem, the research questions, and the objectives were crucial to the definition of the methodological and operational framework since the aim was to analyze the perception of specialists on alternatives for diversifying the economy and the viability of biofuels as a way of breaking the dependency on the Angolan oil industry. This empirical study was developed, in the first stage, by setting up a focus group in order to construct and adjust a data collection instrument in the form of a questionnaire to be applied to a broader set of managers and specialists. The methodology used in this study is described in detail below.

Given that the nature of the research problem focuses on understanding the social and economic phenomena relative to Angola's development strategies and economic diversification, as well as the evaluation of energy alternatives that seek to reduce dependency on the

oil industry, equating the potential of biofuels, in this study, we began by considering the spatial, cultural, and organizational context in which the phenomena occurred within the framework of the naturalistic, exploratory, and descriptive nature of the study [2,3]. Thus, the previous literature review provided information that allowed us to know the "state of the art" and to support the empirical research model, contributing to the development of the methodological path. Furthermore, the process of constructin the data collection models and instruments took place in close inter-relation and cooperation with the perspectives of expert actors since they knew the terrain and the socio-cultural, economic, technological, and political realities where the phenomena occurred [22,23]. Thus, first, it was deemed appropriate to conduct an exploratory approach through a focus group (qualitative analysis) with some experts of different nationalities (Angolan, Portuguese, and Brazilian) in order to identify practices, models, strategies, interests, and problems that could serve as a basis for the development of a questionnaire (quantitative analysis) to be applied to a broader and more robust sample of experts.

The research problem was translated into the following initial questions: (1) What are the strategic alternatives for diversification of the Angolan economy? (2) What is the potential/attractiveness of biofuels to reduce dependency on the oil sector? Based on these starting questions, many other questions arose, namely:

- What are the experts' perceptions of the strategic goals for sustainable development and competitiveness?
- What are Angola's main economic, social, and environmental vulnerabilities?
- What is the impact of clusters on the development of the economy and business competitiveness?
- What are the priority goals for Angola's economic development?
- What is the time frame for the development of an alternative diversification model?
- What are the priority sectors to develop in Angola?
- What are the best government measures to diversify the Angolan economy?
- What are the strategic alternatives for diversification of the economy?
- What are the reasons for the lack of competitiveness in the oil sector in Angola?
- What are the energy alternatives to oil to be explored in Angola?
- What is the potential/attractiveness of biofuels?

The methodology adopted in this research required the identification of specialists to be involved in the study in order to generate qualified information and to participate interactively in the various phases, and then to explore the information obtained, generating consensus or guidelines, either by validating the information produced or by the experience developed in the form of benchmarking. Thus, the principles inherent to Delphi techniques were followed, following [24–28].

As previously mentioned, the first phase of the questionnaire required the interpretation of the models and theoretical concepts for the identification and classification of the dimensions and explanatory variables; 11 dimensions and 56 variables were identified (Table 1):

Table 1. Identification of dimensions and variables.

Dimension	Most Important Variables
Strategic goals for sustainable development and competitiveness	Diversification of Angola's economy Reducing external dependency Decrease in dependency on the oil sector Development and empowerment of human resources (science, education and training) Development of infrastructures (communications and transportation) Creation of a local environment that promotes private investment and the attraction of foreign investment

Table 1. *Cont.*

Dimension	Most Important Variables
Angola's economic, social, and environmental vulnerabilities	Bureaucracy Corruption The informality of the economy Excessive weight of the state in the economy Transport and communication infrastructure costs External dependency Dependency on the oil sector
Clusters in economic development and business competitiveness	Promotion and development of different sectors (agriculture, industry, and new services) can make the country more competitive
Priority targets for Angola's economic development	Valorization of human capital (education, capacity building, and training) Valorization of "endogenous" resources Reduction in external dependency Increase in internal productivity Promotion of exports
Time horizon	From 5 to 10 years From 10 to 20 years From 20 to 30 years From 30 to 40 years
Priority sectors to be developed in Angola	Primary sector (agriculture, fisheries, and forestry) Secondary sector (development of industry) Tourism Energy Commerce Construction Services Education
Government measures to diversify the Angolan economy	Economic policies Fiscal policies Education policies Support for innovation, science, and technology.
Strategic alternatives for diversification of the economy	Valorization of human resources Valorization and exploitation of endogenous resources Science, innovation, and technology Reduction in imports Increase in exports
Lack of competitiveness in the oil sector	The complexity of the sector Price dependency on international markets Lack of seriousness and delays in accountability
Energy alternatives to oil	Clean energies to consider: solar, biodiesel, bioethanol, geothermal, hydro, wind, marine, algae biodiesel, H-bio
Potential and attractiveness of biofuels	Evaluation criteria: technology costs, gas emissions, productivity, natural resources, contribution to competitiveness, energy potential, and systemic innovation

After identifying the concepts associated (dimensions and variables) with the diversification of the economy and the evaluation of strategic alternatives for growth, these were assessed by a group of specialists connected to the economic and energy sector and with knowledge of the Angolan reality. Each participant was given a summary of the concepts and a pre-questionnaire for evaluation during the focus group. The session and group discussion took place in a conference room equipped with multimedia support and recorded on video and audio support [29]. The focus group discussions included the

following: (1) participants expressed their ideas in a free "open-minded" way; (2) participants expressed their opinions about certain keywords associated with the concepts under study; (3) participants evaluated the research questionnaire proposal. The focus group was composed of eight members with complementary skills: two economists (both were university professors), two petroleum engineers, two public managers, and two consultants in economic development with experience and work carried out at the UN.

The focus group participants generally considered it urgent that Angola diversify its economy and invest in a new model of economic development based on the potential of its endogenous resources, therefore, leading to reduced imports (reduce dependency on foreigners) and increased exports. They considered the importance of a new dynamic of private business activity (to reduce the weight of the state) based on entrepreneurship, knowledge (education and training of human resources), and innovation and technology (infrastructure, transportation, and communications). This activity would industrialize the country, and the state should create the conditions and policies (economic, financial/fiscal, social, and technological) necessary for its development.

The specialists and professionals involved in this phase also contributed by selecting or adding variables corresponding to the dimensions defined in the initial questionnaire. For each dimension, the experts expressed their opinions, suggesting the elimination or addition of concepts and/or variables. The focus group participants were unanimous in affirming that the "strategic goals for sustainable economic development", conceived for the medium and long term, should include diversification of Angola's economy and a reduction in foreign dependency and the oil sector. They also indicated the need for the development and training of human resources (science, education, and training), the development of infrastructure (communications and transportation), and the creation of a local environment that promotes private investment and attracts foreign investment.

Concerning the vulnerability dimension, the professionals recognized the bureaucracy, corruption, and informality in the Angolan economy. They also noted the excessive weight of the state in the economy, the costs of transport and communications infrastructures, Angola's foreign dependency, and the oil sector. The creation of several clusters could promote and develop different sectors in Angola related to agriculture, industry, and new services, making the country more competitive. The following priority goals were noted: the "valorization of human capital" (education, capacity building, and training) and of "endogenous resources"; reduction in external dependency; and increased internal productivity to promote exports. The speakers were not unanimous as to the period needed to implement policies and programs to diversify the Angolan economy, with time indications ranging from 5 to 40 years, above all, because they considered that there were medium-term initiatives (economic and fiscal programs) and other long-term innitiatives (science and technology).

Regarding the priority sectors, the specialists considered it relevant to focus on the primary sectors (agriculture, fishing, and forestry) and the secondary sector (development of industry) to valorize the country's immense exogenous resources, and thus, reduce economic dependency on the exterior. However, they also indicated tourism, energy, commerce, civil construction, services, and education. In terms of government policies, they pointed to fiscal and educational economic policies as priorities and support for innovation, science, and technology. In terms of strategic alternatives, the participants referred to "valorization of human resources", "valorization and use of endogenous resources", "science, innovation, and technology", and "reduction in imports and an increase in exports". The specialists stated that they believed the lack of competitiveness in Angola's oil sector was due to the complexity of the sector, the dependency on oil prices in the international market, and a lack of seriousness and delays in accountability. In terms of alternatives, the professionals indicated the feasibility of several alternatives considered to be sustainable and environmentally friendly, such as solar, biodiesel, bioethanol, geothermal, hydro, wind, tides, biodiesel from algae, and H-bio. Their choice should result from evaluating some

criteria, such as technology costs, gas emission, productivity, natural resources, contribution to competitiveness, energy potential, and systemic innovation.

The third phase of the process consisted of creating the questionnaire, which formulated statements or prepositions based on the research objectives, taking into consideration the dimensions and variables identified in the literature and the contributions identified through the focus group. A 5-point Likert-type ordinal scale was associated with each statement in the questionnaire, selected at random, ranging from "1 (I strongly disagree)" to "5 (I strongly agree)". In addition, some sociodemographic questions were also included to characterize the respondents, such as gender, age, education, marital status, activity sector, and nationality. This phase included validation of the questionnaire, which functioned as a pretest of the research instrument [3].

3.1. Sample

Given the theme to be explored in this dissertation, it was essential to obtain information from specialists and informed professionals with a critical view of the country's future and the models and alternatives to economic development and diversification of the economy on a sustainable basis. Furthermore, given the impossibility of investigating the entire population, using a sample was the most effective way to study and understand the phenomenon, generating empirical material for analysis [3]. Thus, a set of national and international experts was identified, and, after obtaining their e-mail addresses, the questionnaire was sent to each of the respondents in the set. Therefore, this was a non-probability convenience sample [30]. A total of 160 questionnaires were sent out, and 120 questionnaires were returned and validated by the deadline of 30 September 2020. In addition to the essential inclusion criterion that the respondent must be a specialist or professional in the areas of economics, management, politics, education, or engineering, the opportunity and availability criteria were also taken into consideration in order to participate in the production of information for a period of time, limited to two months, by completing and returning a questionnaire distributed via email.

3.2. Data Collection Tools

After the data collection instrument administration, the next stage of the research process was data analysis and interpretation to find answers to the research problem and objectives [31]. Given the exploratory nature and design, a univariate data analysis was performed using descriptive statistics (frequency, means, and standard deviation) [31,32]. The Statistical Package for Social Science (SPSS) version 25 [33] was used for data analysis.

The first part of the questionnaire contained questions for characterizing the respondents (gender, age, education, marital status, activity sector, and nationality), thus, constituting independent variables (pre-existing characteristics). In the second part of the questionnaire, explanatory variables were included referring to the dimensions subject to measurement in the form of variables, alternatives, and criteria (see Table 2).

Table 2. Dimensions and items used in the questionnaire.

Dimension	Number of Items
Strategic goals for sustainable development and competitiveness	14 variables
Economic, social, and environmental vulnerabilities of Angola	20 variables
Clusters in the development of the economy and business competitiveness	7 variables
Priority goals for Angola's economic development	6 variables
Time horizon	4 alternatives
Priority sectors to be developed	8 variables
Government measures to diversify the economy	9 variables

Table 2. *Cont.*

Dimension	Number of Items
Strategic alternatives for diversifying the economy	10 variables
Lack of competitiveness in the oil sector	5 variables
Energy alternatives to oil	9 alternatives
Potential and attractiveness of biofuels	8 criteria

Source: Authors.

Considering the research problem and objectives, the construction of the questionnaire was based on the studies and works identified in the literature, as well as on the contributions obtained in the focus group.

To assess the "strategic goals for sustainable development", the work of [34] was taken into consideration, as well as endogenous development models [35–37] and the philosophy of sustainable development [38] that seek to integrate in a balanced way the economy, society, and natural environment [5,38]. Thus, taking into consideration the priority goals for sustainable development, the respondents expressed their degree of agreement with the statements presented (14 statements) on a 5-point Likert-type scale [30], ranging from "totally disagree" to "totally agree". The variables included were:

V1 Improve the local business investment environment;
V2 Invest in tangible strategic infrastructure;
V3 Invest in business parks and facilities;
V4 Invest in intangible strategic infrastructure;
V5 Promote local business growth;
V6 Promote the creation of new enterprises;
V7 Attract foreign investment;
V8 Develop business sectors and clusters;
V9 Integrate unproductive or hard-to-employ workers;
V10 Establish an adequate system of environmental protection, natural disaster prevention, and air and maritime safety;
V11 Develop, train, and empower human resources;
V12 Develop transportation and communications;
V13 Promote science, technology, innovation, and entrepreneurship;
V14 Diversify the economy.

Regarding the "economic, social and environmental vulnerabilities of Angola", the indications of the [38] were used as a reference, subsequently adapted by [5,39]. Respondents expressed their degree of agreement with the statements presented (20 prepositions) on a 5-point Likert-type scale [30], ranging from "totally disagree" to "totally agree". The selected statements were as follows:

V1 A narrow resource base and little or no opportunity to create economies of scale;
V2 Small domestic markets, heavy dependency on some external markets, and long distances from export and import markets for resources;
V3 High energy, infrastructure, transport, communication, and maintenance costs;
V4 Low and irregular international traffic volumes;
V5 Fragile natural environments and vulnerability to natural disasters;
V6 Small but growing population;
V7 High volatility of economic growth;
V8 Limited opportunities for the private sector;
V9 A proportionately large dependency of the economy on its public sector;
V10 A disproportionately costly public administration;
V11 Corruption and informality of the economy;
V12 Restricted access to credit;
V13 Deficient energy distribution systems;

V14 High inflation;
V15 Excessive bureaucracy;
V16 Inefficient judicial system;
V17 Unskilled labor force;
V18 Dependency on oil;
V19 Weak currency;
V20 Literacy/education of the population.

In order to assess the impact of "clusters on the development of the economy and business competitiveness" [40,41], works were used as a reference, which contemplates 7 statements on which respondents expressed their degree of agreement on a 5-point Likert-type scale [30] ranging from "strongly disagree" to "strongly agree":

V1 Promote competitiveness of enterprises and locations;
V2 Promote increased productivity of enterprises;
V3 Facilitate complementarities between the activities of the different actors;
V4 Facilitate access to institutions and benefits;
V5 Help measure the performance of domestic activities and limit;
V6 Opportunistic behavior;
V7 Facilitate the implementation of innovations;
V8 Facilitate the formation of new companies.

To assess the "priority goals for the economic development of Angola", the works of [5,39] were taken into consideration. After the specialists' contributions to the "focus group", six variables were selected on which the respondents expressed their degree of agreement. Namely:

V1 Give sufficient focus to technological, innovation, and creativity systems as part of a sustainable development strategy;
V2 Emphasize building of human capital through investments in education and training;
V3 Give sufficient attention to the development or adoption of climate change resilience systems;
V4 Address Angola's most critical issues, such as high debt levels, inadequate access to technology, difficulties with business transactions, and inadequate access to sources of finance;
V5 Present energy alternatives to break the dependency on oil, namely in terms of biofuels;
V6 Increase the rate of independency and reduce the imbalances of all factors.

In as much as the time horizon (period of time) that respondents deemed acceptable/realistic to develop an alternative model for the diversification strategy of Angola's economic development is concerned, the alternatives suggested by the professionals who participated in the focus group were taken into consideration:

- From 5 to 10 years;
- From 10 to 20 years;
- From 20 to 30 years;
- From 30 to 40 years.

To identify the priority sectors for Angola's development, the recommendations of the professionals involved in the focus group and the works of [42,43] were considered. The respondents put the recommendations in order of priority/importance according to "1" represents the highest priority" and "8" represents the least priority/importance. The sectors considered were: agriculture, livestock and forestry; tourism; oil and gas; manufacturing; diamonds and precious stones; construction; trade and distribution and the services, with the chance for respondents to include and indicate "other sectors".

In order to assess the "government measures to diversify the economy", the work of [39] was taken into consideration. After the "focus group", 9 statements/positions were contemplated by the respondents who indicated their degree of agreement:

V1 Tax reduction;
V2 Subsidized interest rates;
V3 Economic policies;
V4 Actions to enhance human capital;
V5 Export subsidies;
V6 Creation of agendas for diversification and national agencies with responsibility for stimulating and coordinating the process of structural change;
V7 Organize meetings, lectures, seminars, workshops, etc., to inculcate a new spirit of greater openness to international competition;
V8 Technological innovation;
V9 Tax systems and financial incentives that encourage diversification and stimulate private investment.

Regarding the evaluation of strategic alternatives for diversification of the economy, the works of [39,44] were considered, as well as the suggestions of the professionals who participated in the focus group:

V1 Import substitution (through efficiency and not through administrative protection mechanisms, which only generate bureaucracy and corruption);
V2 Production of intermediate products;
V3 Valorization of national human resources (reducing dependency on expatriates);
V4 Technological innovation;
V5 Use of national raw materials;
V6 Diversify export destinations;
V7 Definition of long-term industrial and investment policies to promote the sustained growth of the Angolan economy;
V8 Strengthening the role of the national investment system and development of the financial and banking sector;
V9 Enhancing human potential and innovation;
V10 The emergence of specializations around the strengthening of supply based on new producers and new services.

In order to assess the lack of competitiveness in the oil sector, the works of [45,46], and the report of the [47] were taken into consideration:

V1 The revenues Sonangol receives from taxes and joint ventures and other sources of income do not appear in government accounts;
V2 The price of oil is undervalued in the state budget, and any revenue above this estimate is never declared;
V3 Government expenditure declarations are inaccurate;
V4 The share of taxes and royalties that Sonangol pays to the government is transferred with significant delay and in local currency;
V5 The network of financial arrangements created by oil-backed loans is complicated.

In terms of identifying and assessing energy alternatives to explore in Angola in order to reduce dependency on the oil industry [46], the suggestions raised by [48,49], and inputs from practitioners were followed. Thus, the following alternatives were included: biodiesel, bioethanol, biodiesel from algae, H-BIO, geothermal, hydraulic, solar, wind, and tidal.

Finally, and in order to evaluate the attractiveness of biofuels, we considered the works of [48,49] that, as considered by several experts [50,51], consider it pertinent to weight several criteria, through the use of the MACBETH method (decision support method that allows evaluating options taking into account multiple criteria) namely:

Criterion 1 Cost of technology developed for production;
Criterion 2 Emission of pollutant gases due to burning in engine combustion;
Criterion 3 Job creation;
Criterion 4 Productivity of raw materials;
Criterion 5 Existence of natural resources;
Criterion 6 Contribution to country's competitiveness;
Criterion 7 Energy potential;
Criterion 8 Innovation and systemic change.

Four biofuels were selected, and respondents were asked to rate each criterion based on the following scale: (1) extreme, (2) very strong, (3) strong, (4) moderate, (5) weak, (6) very weak, (7) null. The questionnaire was sent by e-mail to the specialists/professionals identified in the network of contacts which, after being completed, was returned for subsequent data analysis. This process took place in August and September 2020.

4. Analysis of Results

The sample was then characterized, followed by data analysis using descriptive statistics (absolute and relative frequencies, mean, and standard deviation), the assessment of the scale's reliability (Cronbach's alpha), and bivariate analysis of the data.

As can be seen in the following table, there is a gender imbalance among the respondents, with a higher percentage of females (86) than males (34).

The sample ranged in age from 30 to 65 years (Table 3). For operational reasons, three age groups were created. It is noted that the age group "up to 35 years old" consisted of 56 respondents (46.7%), followed by the age group "36–50 years old" (42 respondents), and then the age group "over 50 years old" with 22 respondents (9.4%).

Table 3. Sample.

Title	Title	F	%
Gender	Male	34	28.3
	Female	86	71.7
Age groups	Up to 35 years old	56	46.7
	From 36 to 50 years old	42	35.0
	Over 50 years old	22	18.3
Marital status	Single	30	25.0
	Married/living with a partner	86	71.7
	Divorced	2	1.7
	Widowed	2	1.7
Qualifications	Bachelor	4	3.3
	Graduate	74	61.7
	Master's degree	26	21.7
	Doctorate	16	13.3
Sector of activity	Public sector (central government, local government, public administration)	54	45.0
	Private sector	62	51.7
	Social and non-profit sector (local NGO, youth group, religious organization, voluntary movement)	2	1.7
	International organization	2	1.7
Nationality	Angolan	94	78.3
	Portuguese	22	18.3
	Brazilian	4	3.4

The vast majority of respondents are married/cohabiting (71.7%), with 30 single respondents (25%) and only two divorced and widowed respondents (1.7%), as can be seen in Table 3.

Concerning academic qualifications, as shown in the following table, the majority of the respondents have a Bachelor's degree (61.7%), 26 respondents have a Master's degree (21.7%), 16 respondents have a PhD (13.3%), and 4 respondents have a Bachelor's degree (3.3%).

Most of the respondents (see Table 3) work in the private sector (51.7%), followed very closely by those who work in the public sector (45%).

In terms of nationality (see Table 3), the majority of respondents are Angolan (78.3%), Portuguese (18.3%), and Brazilian (3.4%).

4.1. Analysis of the Results Obtained

A univariate data analysis was first performed using descriptive statistics (absolute and relative frequencies, mean, and standard deviation) for data analysis. Then, the internal consistency of the research instrument was assessed through Cronbach's alpha values. In the analysis of the reliability for all items making up the scale used, a Cronbach's alpha value of 0.882 (good internal consistency) was obtained, which could be considered to be a good result [30].

4.1.1. Evaluation of Strategic Goals for Sustainable Development and Competitiveness

To assess the strategic goals considered to be a priority for development and competitiveness, 14 items were used [38], with scores above the arithmetic mean in all the alternatives presented (see Table 4). As can be seen in this table, respondents considered diversification of the economy to be the most important, with 83 total concordances (M = 4.59, SD = 0.670), followed by the training of human resources, with 72 total concordances (M = 4.58, SD = 0.561); the development of transport and communications with 70 total concordances (M = 4.58, SD = 0.496); and the promotion of science, technology, innovation, and entrepreneurship with 66 total concordances (M = 4.46, SD = 0.675). The lowest values were obtained on the items "integrate unproductive or difficult to employ workers (M = 3.03, SD = 1.132), "invest in business parks and facilities" (M = 3.63, SD = 0.959), and "establish an adequate system of environmental protection, natural disaster prevention, and air and maritime safety" (M = 3.69, SD = 1.034).

Table 4. Priority strategic goals for sustainable development and competitiveness.

Cronbach's Alpha 0.745	**Totally Disagree**		**Disagree**		**Neither Agree Nor Disagree**		**Agree**		**Totally Agree**		**M**	**SD**
	F	**%**	**F**	**%**	**F**	**%**	**F**	**%**	**F**	**%**		
Improving the local business investment environment					8	6.7	54	45.0	56	46.7	4.41	0.617
Investing in tangible strategic infrastructure					6	5.0	68	56.7	46	38.3	4.32	0.568
Investing in business parks and facilities	2	1.7	14	11.7	30	25.0	52	43.3	20	16.7	3.63	0.959
Investing in intangible strategic infrastructure	12	10.0	34	28.3	48	40.0	24	20.0			3.71	0.907
Promoting local business growth			6	5.0	6	5.0	50	41.7	58	48.3	4.32	0.794
Promoting the creation of new companies	2	1.7	8	6.7	22	18.3	52	43.3	36	30.0	3.92	0.948

Table 4. *Cont.*

Cronbach's Alpha 0.745	Totally Disagree		Disagree		Neither Agree Nor Disagree		Agree		Totally Agree		M	SD
	F	%	F	%	F	%	F	%	F	%		
Attracting foreign investment			2	1.7	10	8.3	60	50.0	46	38.3	4.27	0.688
Developing business sectors and clusters			10	8.3	20	16.7	74	61.7	14	11.7	3.78	0.764
Integrating unproductive or hard-to-employ workers	16	13.3	18	15.0	40	33.3	36	30.0	8	6.7	3.02	1.132
Establishing an adequate system of environmental protection, natural disaster prevention, and air and maritime safety	4	3.3	12	10.0	26	21.7	50	41.7	28	23.3	3.69	1.034
Develop, train, and empower human resources					4	3.3	42	35.0	72	60.0	4.58	0.561
Develop transportation and communications							50	41.7	70	58.3	4.58	0.496
Promote science, technology, innovation, and entrepreneurship			2	1.7	6	5.0	46	38.3	66	55.0	4.46	0.675
Diversify the economy			2	1.7	6	5.0	30	25.0	82	68.3	4.59	0.670
KMO test and Bartlett's test	Kaiser–Meyer–Olkin (KMO) of sampling adequacy										0.527	
	Bartlett's test of sphericity								Chi-square gl Sig.		508.056 91 0.000	

The reliability analysis for all items that make up the "priority goals" scale obtained a Cronbach's alpha of 0.745, which is considered to be a scale with good internal consistency [30]. In addition, the Kaiser–Meyer–Olkin (KMO) measure of sampling adequacy was positive and significant (KMO = 0.527, Bartlett's with sig = 0.000), causing no problems with data analysis, revealing positive correlations among the variables.

4.1.2. Analysis of Angola's Key Economic, Social, and Environmental Vulnerabilities

The assessment of Angola's main economic, social, and environmental vulnerabilities was based on previous works by the [38,39]. As shown in the Table 5, the majority of respondents (55%) consider that the main vulnerabilities are "corruption and informality of the economy" (M = 4.37, SD = 0.865), followed by bureaucracy (M = 4.27, SD = 0.940); oil dependency M = 4.27, SD = 0.993); and high costs of energy, infrastructure, transportation, and maintenance (M = 4.24, SD = 0.967). The results also show that the least valued economic, social, and environmental vulnerabilities were "fragile environments and vulnerabilities to natural disasters" (M = 3.02, SD = 1.132) and "a narrow resource base and little or no opportunity to create economies of scale" (M = 3.27, SD = 0.993). The internal reliability obtained on this dimension was good (Cronbach's Alpha = 0.899), and positive and significant results were obtained on the Kaiser–Meyer–Olkin (KMO) measure and Bartlett's test of sphericity (KMO = 0.527, Bartlett's sig = 0.000).

Table 5. Major economic, social, and environmental vulnerabilities in Angola.

Cronbach's Alpha 0.899	Totally Disagree		Disagree		Neither Agree Nor Disagree		Agree		Totally Agree		M	SD
	F	%	F	%	F	%	F	%	F	%		
Narrow resource base and little or no opportunity to create economies of scale	10	8.3	18	15.0	30	25.0	58	48.3	4	3.3	3.27	0.993
Small domestic markets, strong dependency on some foreign markets, distances to export, and resource import markets	8	6.7	6	5.0	2	1.7	54	45.0	50	41.7	4.15	1.043
High energy, infrastructure, transport, communication, and maintenance costs	4	3.3	4	3.3	8	6.7	46	38.3	56	46.7	4.24	0.967
Low and irregular international traffic volumes	2	1.7	10	8.3	40	33.3	42	35.0	26	21.7	3.68	0.969
Fragile natural environments and vulnerability to natural disasters	12	10,	34	28.3	22	18.3	46	38.3	6	5.0	3.02	1.132
Small but growing population	8	6.7	20	16.7	28	23.3	60	50.0	4	3.3	3.31	0.965
High economic growth volatility	2	1.7	22	18.3	36	30.0	52	43.3	8	6.7	3.37	0.904
Limited opportunities for the private sector	6	5.0	18	15.0	10	8.3	58	48.3	28	23.3	3.75	1.088
A proportionately large dependency of the economy on its public sector	4	3.3	6	5.0	12	10.0	60	50.0	38	31.7	4.07	0.884
A disproportionately costly public administration	2	1.7	10	8.3	14	11.7	52	43.3	42	35.0	4.07	0.903
Corruption and informality of the economy	4	3.3	2	1.7	12	10.0	36	30.0	66	55.0	4.37	0.865
Restricted access to credit	2	1.7	10	8.3	10	8.3	46	38.3	52	43.3	4.19	0.915
Weak energy distribution systems	4	3.3	8	6.7	10	8.3	58	48.3	40	33.3	4.07	0.922
High inflation	4	3.3	10	8.3	6	5.0	42	35.0	58	48.3	4.22	0.997
Excessive bureaucracy	6	5.0	4	3.3	4	3.3	50	41.7	56	46.7	4.27	0.940
Inefficient judicial system	2	1.7	12	10.0	14	11.7	48	40.0	44	36.7	4.05	0.950
Unskilled labor force	4	3.3	16	13.3	22	18.3	44	36.7	34	28.3	3.78	1.063
Dependency on oil	2	1.7	12	10.0	4	3.3	40	33.3	62	51.7	4.27	0.993
Weak currency	4	3.3	8	6.7	8	6.7	48	40.0	52	43.3	4.19	0.951
Literacy/education of the pop.	4	3.3	12	10.0	10	8.3	54	45.0	40	33.3	3.98	1.038
KMO test and Bartlett's test	Kaiser–Meyer–Olkin (KMO) of sampling adequacy										0.527	
	Bartlett's test of sphericity							Chi-square			1651.767	
								gl			190	
								Sig.			0.000	

4.1.3. Impact of Clusters on the Development of the Economy and Business Competitiveness

The specialists questioned generally consider that the creation and development of clusters (for example, energy, agriculture, and livestock, etc.) influence the development of the Angolan economy [40] and promote the competitiveness of businesses and locations (see Table 6). Thus, the main impacts recognized are related to the promotion of business productivity (M = 4.07, SD = 0.560), the implementation of innovations (M = 4.04, SD = 0.797), and the formation of new businesses (M = 4.02, SD = 0.809).

Table 6. Influence of clusters on the development of the economy and business competitiveness.

Cronbach's Alpha 0.816	**Totally Disagree**		**Disagree**		**Neither Agree Nor Disagree**		**Agree**		**Totally Agree**		**M**	**SD**
	F	**%**	**F**	**%**	**F**	**%**	**F**	**%**	**F**	**%**		
Promote business and local competitiveness	2	1.7	6	5.0	8	6.7	76	63.3	24	20.0	3.96	0.797
Promote an increase in company productivity			4	3.3	2	1.7	90	75.0	20	16.7	4.07	0.560
Facilitate complementarities between the activities of the different actors			4	3.3	28	23.3	64	53.3	20	16.7	3.84	0.724
Facilitate access to institutions and benefits			4	3.3	30	25.0	70	58.3	12	10.0	3.75	0.659
Help measure the performance of domestic activities and limit opportunistic behavior			14	11.7	46	38.3	44	36.7	10	8.3	3.44	0.820
Facilitate the implementation of innovations			8	6.7	10	8.3	66	55.0	30	25.0	4.04	0.797
Facilitate the formation of new enterprises			8	6.7	12	10.0	64	53.3	30	25.0	4.02	0.809
KMO test and Bartlett's test	Kaiser–Meyer–Olkin (KMO) of sampling adequacy.										0.745	
	Bartlett's test of sphericity								Chi-square gl Sig.		277.846 21 0.000	

The items making up the scale obtained good reliability (alpha = 0.816), as did the Kaiser–Meyer–Olkin measure of sampling adequacy (KMO = 0.745) with a significant Bartlett's sphericity (p = 0.000).

4.1.4. Assessment of Priority Goals for Angola's Economic Development

Concerning the priority goals for Angola's economic development (see Table 7), respondents consider that they emphasize the building of human capital through investments in education and training (M = 3.92, SD = 0.958) and address solutions to Angola's most critical issues, such as high levels of indebtedness, inadequate access to technology, difficulties with commercial transactions, and inadequate access to sources of financing (M = 3.55, SD = 0.887).

Table 7. Assessment of priority targets for Angola's economic development.

Cronbach's Alpha 0.782	Totally Disagree		Disagree		Neither Agree Nor Disagree		Agree		Totally Agree		M	SD
	F	%	F	%	F	%	F	%	F	%		
Give sufficient focus on innovation, creativity, and technological systems as part of a sustainable development strategy			30	25.0	32	26.7	50	41.7	8	6.7	3.30	0.922
Emphasis the building of human capital through investments in education and training			16	13.3	12	10.0	58	48.3	34	28.3	3.92	0.958
Give sufficient attention to the development or adoption of climate change resilience systems	6	5.0	50	41.7	42	35.0	22	18.3			2.67	0.833
Address Angola's most critical issues such as high debt levels, inadequate access to technology, difficulties with commercial transactions, and inadequate access to sources of finance	2	1.7	16	13.3	26	21.7	66	55.0	10	8.3	3.55	0.887
Present energy alternatives to break the dependency on oil, namely at the level of biofuels	8	6.7	24	20.0	30	25.0	48	40.0	10	8.3	3.23	1.075
Increase the rate of dependency and imbalances in all factors			22	18.3	60	50.0	30	25.0	8	6.7	3.20	0.816
KMO test and Bartlett's test	Kaiser–Meyer–Olkin (KMO) of sampling adequacy										0.812	
	Bartlett's test of sphericity								Chi-square gl Sig.		170.754 15 0.000	

The least valued item was "pay sufficient attention to the development or adoption of climate resilience systems" (M = 2.67, SD = 0.833), which may mean that policymakers (and even Angolan citizens) are more concerned with short-term measures to mitigate current problems, to reduce the economic and social vulnerability of populations, and to protect their livelihoods. The reliability analysis for all items that make up the scale used obtain a Cronbach's alpha value of 0.782, which can be considered to be a good result (Pestana & Gageiro, 2005). Similarly, the KMO and Bartlett's test show high and significant values (KMO = 0.812, Bartlett's with sig = 0.000), showing that the variables are related.

4.1.5. Time Horizon for the Development of an Alternative Diversification Model

The period of time that respondents consider acceptable/realistic to develop an alternative model for a diversification strategy for Angola's economic development (see Table 8) is 10–20 years (48.3%). However, 36 respondents (30%) consider that developing an alternative model will take between 5 and 10 years, 16 specialists (13.3%) consider that between 20 and 30 years will be necessary, and 10 specialists (8.3%) consider that between 30 and 40 years will be necessary.

Table 8. Time frame for the development of an alternative diversification model.

Time Period	F	%
5–10 years	36	30.0
10–20 years	58	48.3
20–30 years	16	13.3
30–40 years	10	8.3

4.1.6. Priority Sectors to Be Developed in Angola

The priority sectors (Francisco Miguel Paulo—CEIC) that the respondents consider a priority to develop in Angola (see Table 9) are agriculture, livestock, and forestry (74); manufacturing (16); and tourism (10). Oil and gas (2), trade and distribution, and construction appear in an intermediate position. Diamonds and precious stones and services are in the last positions.

Table 9. Priority activity sectors to be developed in Angola.

	Sorting Priority		Mean
	F	%	
Agriculture, livestock, and forestry	74	61.7	1.52
Manufacturing industry	16	13.3	3.04
Tourism	10	8.3	4.39
Oil and gas	2	1.7	5.00
Trade and distribution			5.34
Building and construction	2	1.7	5.70
Diamonds and precious stones			6.11
Services	2	1.7	6.23

4.1.7. Government Measures to Diversify the Angolan Economy

To assess government measures for diversifying the Angolan economy, the work of [39] was considered. In the reliability analysis for all items, a Cronbach's alpha value of 0.728 was obtained, thus, revealing good internal consistency. Bartlett's test of sphericity evidences that the variables are correlated in the population (KMO = 0.670, Bartlett's sig = 0.000). As shown in the Table 10, respondents consider that the main measures are technological innovation (M = 4.47, SD = 0.593), actions to enhance human capital (M = 4.38, SD = 0.780), tax regimes and financial incentive systems friendly to diversification and stimulating private investment (M = 4.38, SD = 0.663), and economic policies (M = 4.37, SD = 0.634). The least valued, although positive, measures were export subsidies (M = 3.60, SD = 0.956) and tax cuts (M = 3.67, SD = 0.892).

Table 10. Measures that the government should take to diversify the Angolan economy.

Cronbach's Alpha 0.728	Totally Disagree		Disagree		Neither Agree Nor Disagree		Agree		Totally Agree		M	DP
	F	%	F	%	F	%	F	%	F	%		
Tax reduction			14	11.7	32	26.7	54	45.0	20	16.7	3.67	0.892
Subsidised interest rates			12	10.0	26	21.7	56	46.7	26	21.7	3.80	0.894
Economic policies					10	8.3	56	46.7	54	45.0	4.37	0.634
Human capital development measures			4	3.3	10	8.3	42	35.0	64	53.3	4.38	0.780
Export subsidies			18	15.0	34	28.3	46	38.3	22	18.3	3.60	0.956

Table 10. *Cont.*

Cronbach's Alpha 0.728	Totally Disagree		Disagree		Neither Agree Nor Disagree		Agree		Totally Agree		M	DP
	F	%	F	%	F	%	F	%	F	%		
Creation of agendas for diversification and national agencies with the responsibility of stimulating and coordinating the process of structural changes	2	1.7	4	3.3	20	16.7	72	60.0	22	18.3	3.90	0.793
Organizing meetings, lectures, seminars, workshops, etc., to inculcate a new spirit of greater openness to international competition			6	5.0	18	15.0	80	66.7	16	13.3	3.88	0.688
Technological innovation					6	5.0	52	43.3	62	51.7	4.47	0.593
Tax regimes and systems of financial incentives that are friendly to diversification and stimulate private investment					12	10.0	50	41.7	58	48.3	4.38	0.663
KMO test and Bartlett's test	Kaiser–Meyer–Olkin (KMO) of sampling adequacy										0.670	
	Bartlett's test of sphericity								Chi-square		271.550	
									gl		36	
									Sig.		0.000	

4.1.8. Strategic Alternatives for Diversifying the Economy

In order to evaluate the strategic alternatives for diversification of the Angolan economy, based on the works identified in the literature [39,44], and as presented in the Table 11, the specialists surveyed considered the most relevant strategies to be "harnessing of national raw materials", with 58.3% of total concordances (M = 4.55, SD = 0.563), "valorization of national human resources", with 60% of total concordances (M = 4.45, SD = 0.787), and "valorization of human potential and innovation", with 51.7% of concordances (M = 4.42, SD = 0.693).

Table 11. Strategic alternatives for diversifying the economy.

Cronbach's Alpha 0.801	Totally Disagree		Disagree		Neither Agree Nor Disagree		Agree		Totally Agree		M	SD
	F	%	F	%	F	%	F	%	F	%		
Import substitution (through efficiency and not through administrative protection mechanisms, which only generate bureaucracy and corruption),	2	1.7	6	5.0	12	10.0	62	51.7	38	31.7	4.07	0.877
Production of intermediate products			2	1.7	12	10.0	78	65.0	28	23.3	4.10	0.627

Table 11. *Cont.*

Cronbach's Alpha 0.801	Totally Disagree		Disagree		Neither Agree Nor Disagree		Agree		Totally Agree		M	SD
	F	%	F	%	F	%	F	%	F	%		
Valorization of national human resources (reducing dependence on expatriates),			4	3.3	10	8.3	34	28.3	72	60.0	4.45	0.787
Technological innovation			6	5.0	2	1.7	58	48.3	54	45.0	4.33	0.748
Use of national raw materials					4	3.3	46	38.3	70	58.3	4.55	0.563
Diversify the destination of exports.	2	1.7	2	1.7	18	15.0	56	46.7	42	35.0	4.12	0.842
Definition of long-term industrial and investment policies			2	1.7	20	16.7	68	56.7	30	25.0	4.05	0.696
Accentuation of the role of financing the national investment system and the development of the financial and banking sector			2	1.7	26	21.7	62	51.7	30	25.0	4.00	0.733
The valorization of human potential and innovation			2	1.7	8	6.7	48	40.0	62	51.7	4.42	0.693
The emergence of specializations around the reinforcement of supply based on new producers and new products			2	1.7	18	15.0	74	61.7	26	21.7	4.03	0.660
KMO test and Bartlett's test	Kaiser-Meyer-Olkin (KMO) of sampling adequacy										0.764	
	Bartlett's test of sphericity								Chi-square		465.523	
									gl		55	
									Sig.		0.000	

Reliability analysis on the totality of the items revealed a good internal consistency ($\alpha = 0.801$), and the Kaiser–Meyer–Olkin measure and sampling adequacy (KMO = 0.764) revealed positive and significant correlations among the variables (Bartlett with sig = 0.000).

4.1.9. Reasons for a Lack of Competitiveness in Angola's Oil Sector

Respondents point to the lack of competitiveness in Angola's oil sector, based on the Economist Intelligence Unit (EIU), as being mainly due to "the complicated web of financial arrangements created by oil-backed loans" (M = 3.97, SD = 0.777) and "the inaccuracy of government expenditure declarations" (M = 3.92, SD = 0.922) (Table 12).

Table 12. Reasons for the lack of competitiveness of Angola's oil sector.

Cronbach's Alpha 0.825	Totally Disagree		Disagree		Neither Agree Nor Disagree		Agree		Totally Agree		M	SD
	F	%	F	%	F	%	F	%	F	%		
Revenues Sonangol receives from taxes, joint ventures, and other sources of income do not appear in government accounts	4	3.3	18	15.0	46	38.3	38	31.7	14	11.7	3.33	0.982
Oil prices are undervalued in the government budget, and any revenue above this estimate is never declared	6	5.0	10	8.3	20	16.7	54	45.0	30	25.0	3.77	1.075
Government expenditure declarations are not accurate	4	3.3	4	3.3	20	16.7	62	51.7	30	25.0	3.92	0.922
The share of taxes and royalties that Sonangol actually pays to the government is transferred with significant delay and in local currency			10	8.3	48	40.0	36	30.0	26	21.7	3.65	0.913
The web of financial arrangements created by oil-backed loans is complicated			4	3.3	26	21.7	60	50	30	25.0	3.97	0.777
KMO test and Bartlett's test	Kaiser–Meyer–Olkin (KMO) of sampling adequacy										0.732	
	Bartlett's test of sphericity								Chi-square gl Sig.		237.865 10 0.000	

The reliability analysis through Cronbach's alpha revealed good internal consistency ($\alpha = 0.825$), also verifying that there are correlations among the different items (KMO = 0.732, Bartlett's with sig = 0.000).

4.1.10. Energy Alternatives

When asked to evaluate the best energy alternatives to reduce dependency on oil, most of the respondents (see Table 13) put solar energy as the priority (48), followed by biodiesel (22), hydraulic energy (14), and bioethanol (8).

Table 13. The best alternatives to oil to be explored in Angola.

Energy Alternatives	Ranking of Alternatives
Solar	1st priority (48)
Biodiesel	2nd priority (22)
Hydro	3rd priority (14)
Bioethanol	4th priority (8)
Wind	5th priority (2)
Geothermal	Priority 6th (2)
Offshore	Priority 7th (2)
Biodiesel from algae	8th priority (2)
H-BIO	9th priority (0)

The least valued alternatives were H-bio, biodiesel from algae, and geothermal and wind energy.

4.1.11. Assessing the Attractiveness of Biofuels

In order to assess the attractiveness of biofuels, we considered works developed by [50,51] and, in particular, four alternatives: bioethanol, biodiesel, H-bio, and algae. The analysis of Cronbach's alpha allows us to conclude that there is good reliability of the scale ($\alpha = 0.711$), and the Kaiser–Meyer–Olkin measure of sampling adequacy attests to the correlations among the variables (KMO = 0.615, Bartlett with sig = 0.000). Thus, regarding bioethanol, in general, respondents rated this biofuel as attractive (M = 3.274), having obtained a value below 3.5 (arithmetic mean) in most criteria (Table 14).

Table 14. Assessing the attractiveness of biofuels.

Cronbach Alpha 0.711	Extreme		Very Strong		Strong		Moderate		Weak		Very Weak		Nil		M	SD
	F	%	F	%	F	%	F	%	F	%	F	%	F	%		
Criterion 1: Cost of technology	8	6.7	4	3.3	26	21.7	28	23.3	6	5.0	4	3.3	76	63.3	3.65	1.033
Criterion 2: Emission of pollutant gases	4	3.3	22	18.3	16	13.3	8	6.7	12	10.0	4	3.3	4	3.3	3.35	1.581
Criterion 3: Employment generation	14	11.7	18	15.0	26	21.7	14	11.7	2	1.7	4	3.3			2.82	1.281
Criterion 4: Productivity	10	8.3	14	11.7	32	26.7	6	5.0	4	3.3	6	5.0	2	1.7	3.18	1.455
Criterion 5: Natural resources	10	8.3	20	16.7	22	18.3	10	8.3	10	8.3	2	1.7			2.88	1.264
Criterion 6: Contribution to competitiveness	14	11.7	8	6.7	14	11.7	30	25.0			4	3.3	2	1.7	3.26	1.512
Criterion 7: Energy potential	16	13.3	10	8.3	10	8.3	22	18.3	8	6.7	2	1.7	4	3.3	3.35	1.691
Criterion 8: Innovation and change	10	8.3	12	10.0	10	8.3	20	16.7	12	10.0	2	1.7	4	3.3	3.53	1.643
KMO test and Bartlett's test	Kaiser-Meyer-Olkin (KMO) of sampling adequacy														0.615	
	Bartlett's test of sphericity										Chi-square				161.223	
											gl				28	
											Sig.				0.000	

As can be seen in the Table 14, the most valued criteria were Criterion 3 (generation of jobs) (11.7% of respondents rated it as "strong", 15% as "very strong", and 21.7% as "strong" (M = 2.82, SD = 1.281)), and Criterion 5 (existence of natural resources) (rated as "strong" by 18.3% of respondents, as "very strong" by 16.7% of respondents, and as "extreme" by 8.3% of respondents (M = 2.88, SD = 1.264)). However, two criteria were rated slightly higher than the arithmetic mean (3.5): Criterion 1 (cost of technology developed for production (M = 3.65, SD = 1.033)) and Criterion 8 (innovation and systemic change (M = 3.53, SD = 1.643)), and therefore, were considered to be the least attractive factors for this biofuel by the experts surveyed.

Regarding biodiesel, the respondents evaluate this biofuel as attractive (M = 3.356) (Table 15).

The reliability analysis on the totality of the items revealed good internal consistency ($\alpha = 0.747$). Similarly, significant correlations were found among the items that make up the scale (KMO = 0.550, Bartlett's with sig = 0.000). As presented in the Table 15, the best-ranked criteria were Criterion 3 (generation of jobs), which was rated as "very strong" by 20% of the respondents, as "strong" by 15% of the respondents, and as "extreme"

by 10% of the respondents (M = 3.00, SD = 1.509) and Criterion 7, (energy potential), which was rated as "very strong" by 20% of the respondents and as "extreme" by 10% of the respondents (M = 3.18, SD = 1.578). Criteria 2 (gas emissions) and 5 (existence of natural resources) were similar in terms of average (M = 3.24), Criterion 1 (cost of technology developed for production (M = 3.70; SD = 1.176)), Criterion 6 (contribution to the country's competitiveness (M = 3.70, SD = 1.617)), and Criterion 8 (innovation and systemic change (M = 3.52; SD = 1.491)) were rated as less attractive with a result higher than the arithmetic mean.

Table 15. Biodiesel attractiveness assessment.

Cronbach's Alpha 0.747	Extreme		Very Strong		Strong		Moderate		Weak		Very Weak		Nil		M	SD
	F	%	F	%	F	%	F	%	F	%	F	%	F	%		
Criterion 1: Cost of technology	4	3.3	8	6.7	14	11.7	28	23.3	14	11.7	2	1.7			3.70	1.176
Criterion 2: Emission of pollutant gases	8	6.7	28	23.3	6	5.0	10	8.3	14	11.7	4	3.3	4	3.3	3.24	1.665
Criterion 3: Employment generation	12	10.0	24	20.0	18	15.0	14	11.7	2	1.7	4	3.3	2	1.7	3.00	1.509
Criterion 4: Productivity	6	5.0	14	11.7	26	21.7	10	8.3	8	6.7	6	5.0			3.27	1.387
Criterion 5: Natural resources	12	10.0	16	13.3	8	6.7	22	18.3	4	3.3	8	6.7			3.24	1.570
Criterion 6: Contribution to competitiveness	10	8.3	10	8.3	8	6.7	24	20.0	14	11.7	6	5.0	2	1.7	3.70	1.617
Criterion 7: Energy potential	12	10.0	24	20.0	8	6.7	16	13.3	14	11.7	2	1.7			3.18	1.578
Criterion 8: Innovation and change	8	6.7	12	10.0	10	8.3	32	26.7	6	5.0	4	3.3	2	1.7	3.52	1.491
KMO test and Bartlett's test	Kaiser–Meyer–Olkin (KMO) of sampling adequacy														0.550	
	Bartlett's test of sphericity										Chi-square				236.730	
											gl				28	
											Sig.				0.000	

The evaluation of attractiveness of H-bio was assessed as uninteresting with a result higher than the arithmetic mean (M = 3.782) (Table 16).

The scale showed good internal consistency, with a Cronbach's alpha value of 0.835. There were also correlations among items (KMO = 0.760, Bartlett test sig = 0.000), and only two criteria were considered to be attractive, i.e., Criterion 7 (energy potential), rated as "strong" by 16.7% of respondents, as "very strong" by 11.7% of respondents, and as "extreme" by 5% of respondents (M = 3.35, SD = 1.631) and Criterion 8 (innovation and systemic change), rated as "strong" by 18.3% of respondents, as "extreme" by 10% of respondents, and as "very strong" by 6.7% of respondents (M = 3.39, SD = 1.653). Among the remaining criteria with less attractive evaluations, Criterion 2 (emission of pollutant gases (M = 4.81, SD = 1.502)) and Criterion 6 (contribution to the country's competitiveness (M = 3.81, SD = 1.458)) stand out.

Finally, the assessment of the attractiveness of the biofuel from algae was considered to be unattractive or not attractive (M = 4.133), with all criteria scoring higher than the arithmetic mean. The worst score was obtained on Criterion 2 (emission of pollutant gases) (M = 4.78, SD = 1.777) and on Criterion 6 (contribution to the country's competitiveness (M = 4.28, SD = 1.804)). The best scores were obtained in Criterion 4 (productivity (M = 3.81, SD = 1.859)) and Criterion 5 (existence of natural resources (M = 3.91, SD = 1.892)). The

scale revealed good internal consistency, obtaining a Cronbach's alpha value of 0.798. The Kaiser–Meyer–Olkin (KMO) measure of sampling adequacy and Bartlett's test of sphericity showed that the variables were correlated in the population (KMO = 0.683, Bartlett's test sig. 0.000) (Table 17).

Table 16. Evaluation of the attractiveness of H-Bio.

Cronbach's Alpha 0.835	**Extreme**		**Very Strong**		**Strong**		**Moderate**		**Weak**		**Very Weak**		**Nil**		**M**	**SD**
	F	**%**	**F**	**%**	**F**	**%**	**F**	**%**	**F**	**%**	**F**	**%**	**F**	**%**		
Criterion 1: Cost of technology	4	3.3	10	8.3	14	11.7	14	11.7	6	5.0	10	8.3	6	5.0	3.94	1.754
Criterion 2: Emission of pollutant gases	4	3.3	4	3.3	6	5.0	14	11.7	14	11.7	18	15.0	6	5.0	4.81	1.502
Criterion 3: Employment generation	4	3.3	2	1.7	22	18.3	24	20.0	4	3.3	6	5.0	2	1.7	3.74	1.330
Criterion 4: Productivity	8	6.7	8	6.7	20	16.7	16	13.3	4	3.3	6	5.0	6	5.0	3.58	1.713
Criterion 5: Natural resources	10	8.3	4	3.3	18	15.0	18	15.0	4	3.3	8	6.7	4	3.3	3.65	1.631
Criterion 6: Contribution to competitiveness	6	5.0	6	5.0	18	15.0	24	20.0	2	1.7	6	5.0	4	3.3	3.81	1.458
Criterion 7: Energy potential	6	5.0	14	11.7	20	16.7	8	6.7	8	6.7	4	3.3	4	3.3	3.35	1.631
Criterion 8: Innovation and change	12	10.0	8	6.7	22	18.3	10	8.3	10	8.3	2	1.7	6	5.0	3.39	1.653
KMO test and Bartlett's test	Kaiser–Meyer–Olkin (KMO) of sampling adequacy														0.760	
	Bartlett's test of sphericity										Chi-square gl Sig.				279.155 28 0.000	

Table 17. Algae attractiveness assessment.

Cronbach's Alpha 0.798	**Extreme**		**Very Strong**		**Strong**		**Moderate**		**Weak**		**Very Weak**		**Nil**		**M**	**SD**
	F	**%**	**F**	**%**	**F**	**%**	**F**	**%**	**F**	**%**	**F**	**%**	**F**	**%**		
Criterion 1: Cost of technology	6	5.0	16	13.3	16	13.3	14	11.7	2	1.7	12	10.0	8	6.7	4.00	1.764
Criterion 2: Emission of pollutant gases	4	3.3	10	8.3	4	3.3	4	3.3	22	18.3	14	11.7	12	10.0	4.78	1.777
Criterion 3: Employment generation	6	5.0	8	6.7	20	16.7	14	11.7	6	5.0	8	6.7	8	6.7	3.97	1.699
Criterion 4: Productivity	10	8.3	10	8.3	14	11.7	10	8.3	10	8.3	10	8.3	6	5.0	3.81	1.859
Criterion 5: Natural resources	14	11.7	6	5.0	12	10.0	22	18.3	4	3.3	6	5.0	12	10.0	3.91	1.892
Criterion 6: Contribution to competitiveness	8	6.7	4	3.3	4	3.3	20	16.7	14	11.7	10	8.3	8	6.7	4.28	1.804

Table 17. *Cont.*

Cronbach's Alpha 0.798	Extreme		Very Strong		Strong		Moderate		Weak		Very Weak		Nil		M	SD
	F	%	F	%	F	%	F	%	F	%	F	%	F	%		
Criterion 7: Energy potential	12	10.0	4	3.3	8	6.7	10	8.3	22	18.3	4	3.3	8	6.7	4.06	1.851
Criterion 8: Innovation and change	6	5.0	4	3.3	10	8.3	22	18.3	12	10.0	10	8.3	4	3.3	4.09	1.498
KMO test and Bartlett's test	Kaiser–Meyer–Olkin (KMO) of sampling adequacy														0.683	
	Bartlett's test of sphericity												Chi-square gl Sig.		204.586 28 0.000	

In comparative terms, and as presented in the Table 18, the best alternatives are bioethanol (M = 3.254), followed by biodiesel (M = 3.356).

Table 18. Comparison between alternatives (average values).

Criteria	Bioethanol M	Biodiesel M	H-BIO M	Algae M
Criterion 1: Cost of technology developed for production	3.65	3.70	3.94	4.00
Criterion 2: Emission of pollutant gases due to combustion in engine	3.35	3.24	4.81	4.78
Criterion 3: Job creation	2.82	3.00	3.74	3.97
Criterion 4: Productivity of raw material	3.18	3.27	3.58	3.81
Criterion 5: Existence of natural resources	2.88	3.24	3.65	3.91
Criterion 6: Contribution to country's competitiveness	3.26	3.70	3.81	4.28
Criterion 7: Energy potential	3.35	3.18	3.35	4.06
Criterion 8: Innovation and systemic change	3.53	3.52	3.39	4.09
TOTAL	26.02	26.85	30.27	32.9
Item mean	3.254	3.356	3.782	4.113
Correlation between items	0.235	0.269	0.388	0.331

H-bio (M = 3.782) and biofuel from algae (M = 4.113) are considered to be unattractive (values higher than the average), the latter having the worst classification among all criteria (all higher than the arithmetic average).

5. Discussion of Results and Conclusions

The results obtained in the empirical research, in general, coincide with the observations, evaluations, suggestions, and recommendations presented by the professionals who participated in the focus group. Thus, the strategies considered to be priorities for development and competitiveness include diversification of the economy; training and education of human resources; development of transportation and communications; and promotion of science, technology, innovation, and entrepreneurship, as pointed out by the specialists and by the [38]. Angola's main economic, social, and environmental vulnerabilities are related to corruption and the informality of the economy; bureaucracy; dependency on oil; and the high costs of energy, infrastructure, transportation and maintenance, which are factors that have been already highlighted in the work of [39]. As suggested by [40], the specialists consider that the creation and development of regional clusters influence the development of Angola's economy and promote the competitiveness of companies and locals since they contribute to the productivity of companies and the implementation of

innovations and the formation of new companies. Regarding the priority goals for Angola's economic development, the professionals surveyed consider that they value the building of human capital through investments in education and training and contemplate solutions for Angola's most critical issues such as high levels of indebtedness, inadequate access to technology, difficulties with commercial transactions, and inadequate access to sources of financing. Most respondents consider it acceptable/realistic that between "10 and 20 years" will be required to develop an alternative model for Angola's diversification strategy for economic development. This time frame is aligned with the recommendations made by the professionals who participated in the focus group. However, this time horizon is shorter than the scenarios projected by international organizations [38] and studies identified in the literature [52]. The priority sectors that the respondents consider a priority to develop in Angola are agriculture, livestock and forestry, manufacturing, and tourism, corroborated by the specialists who participated in the focus group. The main government measures to diversify the Angolan economy target technological innovation, actions to enhance human capital, tax regimes, and financial incentive systems that are friendly to diversification and stimulate private investment and economic policies, similar to what was already pointed out in the work of [39]. The professionals consider that the strategic alternatives for diversification of the Angolan economy include the use of national raw materials (development of endogenous resources), the valorization of national human resources, and the valorization of human potential and innovation, as already considered in studies by [39,44]. As noted by the Economist Intelligence Unit (2018), respondents point out that the lack of competitiveness of Angola's oil sector is related to the "complicated web of financial arrangements created by oil-backed loans and the inaccuracy of government expenditure declarations. The best energy alternatives [48] to reduce oil dependence are, according to respondents, solar energy, biodiesel, hydropower, and bioethanol. In assessing the attractiveness and potential of biofuels [48,49], the best alternatives have been bioethanol, followed by biodiesel. In summary, the specialists and professionals who participated in this research consider it a priority, and an urgent priority, to diversify the Angolan economy based on a sustainable development model, supported by the valorization of endogenous resources (primary sector and industrialization of the country) through the promotion of education, a reduction in external dependency (potentialize the immense existing resources, i.e., internal production), the leveraging of exports, as well as a reduction in dependency on oil, through the exploitation of biofuels.

The results show that the strategies considered to be priorities for development and competitiveness include diversification of the economy; training and education of human resources; the development of transportation and communications; and the promotion of science, technology, innovation, and entrepreneurship. On the one hand, the professionals consulted consider that Angola's main economic, social, and environmental vulnerabilities are related to corruption and the informality of the economy; bureaucracy; dependency on oil and high energy; and infrastructure, transport, and maintenance costs. On the other hand, the research participants positively evaluate the creation and development of regional clusters, considering their influence on the development of Angola's economy and the promotion of business and territorial competitiveness. In line with the studies and works identified in the literature, the specialists consider that the priority goals for Angola's economic development must prioritize the valorization of human capital (investments in education, training, and capacity building) and that policies should be developed to solve the high levels of indebtedness, inadequate access to technology, difficulties with commercial transactions, and inadequate access to sources of financing. The sectors that respondents consider to be a priority to develop in Angola are agriculture, livestock and forestry, manufacturing, and tourism. The main government measures to diversify the Angolan economy should focus on technological innovation, actions to enhance human capital, tax regimes, and systems of financial incentives that are friendly to diversification and stimulate private investment and economic policies.

The professionals consider that the strategic alternatives for diversification of the Angolan economy include taking advantage of national raw materials (development of endogenous resources), valuing national human resources, and valuing human potential and innovation. The lack of competitiveness of the oil sector in Angola is related to the complicated network of financial arrangements created by loans guaranteed with oil and the inaccuracy of government spending declarations. According to the respondents, the best energy alternatives for reducing dependency on oil are solar energy, biodiesel, hydroelectric power, and bioethanol. When assessing the attractiveness and potential of biofuels, the best alternative is bioethanol, followed by biodiesel.

In summary, the specialists and professionals who participated in this research consider it a priority, and an urgent priority, to diversify the Angolan economy based on a sustainable development model, supported by the valorization of endogenous resources (primary sector and industrialization of the country) through the promotion of education, a reduction in external dependency (potentialize the immense existing resources, i.e., internal production), leveraging of exports, as well as a reduction in oil dependency through the exploitation of biofuels.

6. Limitations and Future Research

It is important to draw attention to two limitations associated with this research. One limitation is the methodological nature, more precisely the depth and scope of the research technique used. The other limitation is associated with the detailed analysis of the strategic alternative proposed by the theme for diversification of the Angolan economy.

Concerning the methodological limitation, the "Delphi" technique used for the research has advantages. It brings together specialists in the field of knowledge who can present precise and coherent points with scientific support, experience, and research on the subject matter. However, at the same time, their opinions, despite being valid and well supported, always carry some subjectivity and/or personal bias that must be compared, analyzed, and proven.

Author Contributions: Conceptualization, A.C., G.M., M.M. and R.S.; methodology, R.S.; software, M.M.; validation, R.S., G.M., A.C., M.M. and R.R.; formal analysis, R.S. and R.R.; investigation, G.M.; resources, R.R. and A.C.; data curation, R.S.; writing—original draft preparation, G.M.; writing—review and editing, M.M.; visualization, R.R., A.C., G.M., M.M. and R.S.; supervision, G.M.; project administration, G.M., M.M. and R.S.; funding acquisition, G.M., A.C., M.M., R.R. and R.S. All authors have read and agreed to the published version of the manuscript.

Funding: The work of author Rui Silva is supported by national funds, through the Portuguese Foundation for Science and Technology (FCT) under project UIDB/04011/2022 and by NECE-UBI, Research Centre for Business Sciences, Research Centre under project UIDB/04630/2022. The work of author Carmem Leal is supported by national funds, through the Portuguese Foundation for Science and Technology (FCT) under project UIDB/04011/2022.

Institutional Review Board Statement: The study was conducted in accordance with the Declaration of Helsinki and approved by the Institutional Review Board.

Informed Consent Statement: Informed consent was obtained from all subjects involved in the study.

Data Availability Statement: Not applicable.

Acknowledgments: The authors gratefully acknowledge the University of Trás-os-Montes and Alto Douro, CETRAD (Centre for Transdisciplinary Development Studies) and NECE-Research Center in Business Sciences, University of Beira Interior, (NECE–UBI).

Conflicts of Interest: The authors declare no conflict of interest.

References

1. Gil, A. Métodos e Técnicas de Pesquisa Social. 2008. Available online: https://ayanrafael.files.wordpress.com/2011/08/gil-a-c-mc3a9todos-e-tc3a9cnicas-de-pesquisa-social.pdf (accessed on 20 January 2020).
2. Lambin, J. *Marketing Estratégico*; McGraw-Hill: Lisboa, Portugal, 2000.

3. Malhotra, N. *Pesquisa de Marketing*; Atlas: São Paulo, Brazil, 2005.
4. Cavalcanti, J. Comunicando Modelos de Crescimento Económico. 2007. Available online: http://www.creativante.com.br/download/Crescimento.pdf (accessed on 8 March 2020).
5. Francisco, A. Desenvolvimento Económico Endógeno: Construção de um Modelo Conceptual para os Pequenos Estados Insulares em Desenvolvimento. Ph.D. Thesis, Universidade Fernando Pessoa, Porto, Protugal, 2015.
6. ETC Foundation-Compas. *Learning Endogenous Development. Building on Bio-Cultural Diversity*; Practical Action Publishing: Warwickshire, UK, 2007.
7. Stöhr, W. *Development from Below: The Bottom-Up and Periphery-Inward Development Paradigm, Development from Above or from Below?* Stöhr, W., Tailor, D., Eds.; John Wiley: Chichester, UK, 1981.
8. Vázquez Barquero, A. Desarrollo local y dinámica regional. In *Economía y Política Regional en España ante la Europa del s*, XXI ed.; Mella, J. (Coord.), Ed.; Akal: Madrid, Spain, 1998.
9. Garofoli, G. Le aree sistema in Italia. *Política E Econ.* **1983**, *11*, 17–34.
10. Maillat, D. Territorial dynamic, innovative milieus and regional policy. *Entrep. Reg. Dev.* **1995**, *7*, 157–165. [CrossRef]
11. D'arcy, E.; Giussani, B. Local economic development: Changing the parameters? *Entrep. Reg. Dev.* **1996**, *8*, 159–178. [CrossRef]
12. Solow, R.M. A contribution to the theory of economic growth. *Q. J. Econ.* **1956**, *70*, 65–94. [CrossRef]
13. Ahmed, S. An Examination of the Development Path Taken by Small Island Developing States: Jamaica a Case Study. Master's Thesis, Faculty of Arts, The University of Prince Edward Island, Charlottetown, PE, Canada, 2008.
14. ANEEL. Derivados de Petróleo. Atlas de Energia Elétrica. 2008. Available online: http://www.aneel.gov.br/arquivos/pdf/atlas_par3_cap7.pdf (accessed on 14 March 2020).
15. Abdelrehim, N.; Maltby, J.; Toms, S. Narrative reporting and crises: British Petroleum and Shell, 1950–1958. *Account. Hist.* **2015**, *20*, 138–157. [CrossRef]
16. BP. Statistical Reviews of World Energy. 2015. Available online: http://www.bp.com/content/dam/bp/pdf/energy-economics/statistical-review-2015/bp-statistical-review-of-world-energy-2015-full-report.pdf (accessed on 14 September 2020).
17. CEIC. Relatório Económico de Angola 2016-Universidade Católica de Angola. 2016. Available online: http://www.ceic-ucan.org/wp-content/uploads/2017/06/Apresenta%C3%A7%C3%A3o-do-Relat%C3%B3rio-Econ%C3%B3mico-de-Angola-2016.pdf (accessed on 15 March 2020).
18. Petrobras, B. 50 Perguntas e Respostas Sobre Este Novo Mercado 2007. 2007. Available online: https://www.agencia.cnptia.embrapa.br/Repositorio/matprima1_000g7pcetcc02wx5ok0wtedt32e6jis7.pdf (accessed on 14 October 2020).
19. United Nations Climate Changes. What Is the Paris Agreement? 2015. Available online: https://unfccc.int/process-and-meetings/the-paris-agreement/the-paris-agreement/ (accessed on 15 July 2020).
20. IEA (Industrial Ethanol Association). Market and Applications. 2015. Available online: http://www.industrial-ethanol.org/index.php?page=industrial-ethanol (accessed on 28 January 2020).
21. Copercana. Odebrecht Acelera Plano de Produzir Álcool em Angola. 2015. Available online: http://www.copercana.com.br/index.php?xvar=ver-ultimas&id=3218 (accessed on 16 December 2020).
22. Foucault, M. *La Liberté de Savoir*; Presses Universitaires de France: Paris, France, 1987.
23. Brown, A.; Dowling, P. *Doing Research/Reading Research: A Mode of Interrogation for Education*; The Falmer Press: London, UK, 1998.
24. Kaynak, E. Using the Delphi technique to predict future tourism potential. *Mark. Intell. Plan.* **1994**, *12*, 18–29. [CrossRef]
25. Adler, M.; Ziglio, E. *Gazing into the Oracle: The Delphi Method and Its Application to Social Policy and Public Health*; Kingsley: London, UK, 1996; pp. 3–33.
26. Landeta, J. *El método Delphi. Una Técnica de Previsión Para la Incertidumbre*; Ariel: Barcelona, Sapin, 1999.
27. Cuhls, K. Delphi surveys. In *Teaching material for UNIDO Foresight Seminars*; United Nations Industrial Development Organization: Vienna, Austria, 2005.
28. Fernandes, G. Aplicação da metodologia Delphi na definição de estratégias de gestão territorial. In Proceedings of the Atas do 16° Congresso da APDR, Funchal, Portugal, 8–10 July 2010.
29. Greenbaum, T. *The Handbook of Focus Group Research*; Sage Publications: London, UK, 1998.
30. Pestana, M.; Gageiro, J. *Análise de Dados Para Ciências Sociais: A Complementaridade do SPSS*; Edições Sílabo: Lisboa, Portugal, 2005.
31. Gil, A. *Como Elaborar Projectos de Pesquisa*; Atlas: São Paulo, Brazil, 1999.
32. Hill, M.; Hill, A. *Investigação por Questionário*; Edições Sílabo: Lisbo, Protugal, 2002.
33. IBM. *SPSS Statistics for Window*; Version 25; IBM Corp.: New York, NY, USA, 2021.
34. Coffey, W.; Polèse, M. The concept of local development: A stages model of endogenous regional growth. *Pap. Reg. Sci.* **1984**, *55*, 1–12. [CrossRef]
35. Swinburn, G.; Goga, S.; Murphy, F. *Local Economic Development: A Primer Developing and Implementing Local Economic Development Strategies and Action Plans*; Bertelsmann Stiftung & The World Bank: Washington, DC, USA, 2006.
36. World Bank. People's: Republic of Angola, Angola Economic Update. Report No. AUS6794, 2014. Available online: https://openknowledge.worldbank.org/bitstream/handle/10986/19314/AUS67940WP0P140385283B00PUBLIC00ACS.pdf?sequence=1 (accessed on 29 October 2020).
37. UNIDO. Cluster Development-Improving Prosperity by Building up Networks. 2012. Available online: http://www.clustersfordevelopment.org (accessed on 19 September 2020).

38. UN. *Programme of Action for the Sustainable Development of Small Island Developing States*; The United Nations (UN): Bridgetown, Barbados, 1994; pp. 6–56.
39. Rocha, A.; Paulo, F.; Bonfim, L.; Santos, R. *Estudos sobre a Diversificação da Economia Angolana. Centro de Estudos e Investigação Científica*; Universidade Católica de Angola: Luanda, Angola, 2016.
40. Porter, M. *Competitive Advantage of Nations*; The Free Press: New York, NY, USA, 1998.
41. Porter, M. Location, competition, and economic development: Local clusters in a global economy. *Econ. Dev. Q.* **2000**, *14*, 15–35. [CrossRef]
42. Jensen, S.; Paulo, F. Reforms of the Angolan budget process and public financial management: Was the Crisis a Wakeup Call? CEIC-CMI Report. 2011. Available online: https://www.cmi.no/publications/4259-reforms-of-the-angolan-budget-process-and-public (accessed on 19 September 2020).
43. Paulo, F. Que Diversificação Económica Angola Precisa? 2017. Available online: http://www.ceic-ucan.org/wp-content/uploads/2017/09/Que-Diversifica%C3%A7%C3%A3o-Econ%C3%B3mica-Angola-Precisa.pdf (accessed on 11 August 2020).
44. Rodrik, D. *Políticas de Diversificação Económica*; Revista CEPAL: Santiago, Chile, 2004; pp. 1–17.
45. Fragoso, M. Angola–o Papel do Sector Energético na Comunidade de Desenvolvimento da África Austral–Estudo de Caso do Petróleo. Master's Thesis, Faculty of Humanities and Social Sciences, Universidade Nova de Lisboa, Lisboa, Portugal, 2010.
46. Dombaxe, M. Os Problemas Energéticos em Angola: Energias Renováveis, a Opção Inadiável. Master's Thesis, Faculty of Humanities and Social Sciences, Universidade Nova de Lisboa, Lisboa, Portugal, 2011.
47. Economist Intelligence Unit. State of the Nation Address Reiterates Ongoing Reforms. 2018. Available online: http://country.eiu.com/Angola/ArticleList/Analysis/Economy (accessed on 11 July 2020).
48. Chaves, M.; Gomes, C. Avaliação de biocombustíveis utilizando o apoio multicritério à decisão. *Production* **2014**, *24*, 495–507. [CrossRef]
49. Carvalho, A.; Ferreira, R. The use of biofuel as a sustainable alternernative within the brazilian energy matrix. *Cad. Meio Ambiente e Sustentabilidade* **2014**, *5*, 139–157.
50. Bana e Costa, C.A.; De Corte, J.M.; Vansnick, J.C. On the mathematical foundations of macbeth. In *Multiple Criteria Decision Analysis: State of the Art Surveys*; Springer: New York, NY, USA, 2005; Volume 78, pp. 409–437.
51. Bana, C.A.; Meza, L.A.; Oliveira, M.D. O método MACBETH e aplicação no Brasil. *Engevista* **2013**, *15*, 3–27. [CrossRef]
52. Carvalho EA, S.; Rodriguez RJ, S.; de Freitas Boa Morte, E.; de Freitas e Castro, M.; Marum, D.S.; Candido, V.S.; Monteiro, S.N. Magnetic Modified Natural Polymers for Biotechnological Application. In *Materials Science Forum*; Trans Tech Publications Ltd.: Freienbach, Switzerland, 2014; Volume 775, pp. 738–742.

energies

MDPI

Article

Supporting the Clean Electrification for Remote Islands: The Case of the Greek Tilos Island

John K. Kaldellis

Lab of Soft Energy Applications & Environmental Protection, University of West Attica, 12241 Athens, Greece; jkald@uniwa.gr

Abstract: Many islands around the world present considerable energy supply problems, while their energy mixture is controlled by oil products. Meanwhile, several of these isolated islands enjoy excellent RES potential that support actions to maximize RES integration. In order to ameliorate energy supply security and energy autonomy of the Aegean Archipelagos Greek islands, an integrated solution is deployed based on the exploitation of the existing RES potential in conjunction with the application of an appropriate energy storage scheme, as well as complementary smart-grid elements. The proposed solution has been applied for the Greek Tilos island in the framework of the Tilos-Horizon 2020 program. In this context, the implementation of the integrated Tilos energy solution under the current local legislative frame is a great success story introducing several important innovative characteristics in the European market, like the combined operation of a wind turbine and a PV installation, the application of new technology battery energy storage, the installation of a DSM network/platform and the development of a large number of reliable forecasting algorithms. The innovative integrated solution is a real-world working operating example offering knowledge and proving that the solution deployed could be equally well applied in various other remote islands throughout the European territory with very promising results.

Keywords: hybrid power station; green island; energy storage; remote community

Citation: Kaldellis, J.K. Supporting the Clean Electrification for Remote Islands: The Case of the Greek Tilos Island. *Energies* **2021**, *14*, 1336. https://doi.org/10.3390/en14051336

Academic Editor: George S. Stavrakakis

Received: 2 November 2020
Accepted: 18 February 2021
Published: 1 March 2021

Publisher's Note: MDPI stays neutral with regard to jurisdictional claims in published maps and institutional affiliations.

Copyright: © 2021 by the author. Licensee MDPI, Basel, Switzerland. This article is an open access article distributed under the terms and conditions of the Creative Commons Attribution (CC BY) license (https://creativecommons.org/licenses/by/4.0/).

1. Introduction

1.1. The Current Situation of Greek Remote Islands Electricity System

Many islands around the world present considerable energy supply problems, while their energy mixture is controlled by oil products [1,2]. Actually, energy supply security is related to both the dependence on oil imports as well as to the fact that the majority of these islands are subject to even greater challenges in the occasion of critical damage to local thermal power generation stations or a power network failure [3]. In this context, improving energy security would dictate to not only reduce the energy dependence on imported fuels [4], but also to establish a diversified energy mix [5], considering the increasing contribution of high percentages of Renewable Energy Sources (RES) power generation. Unfortunately, introducing high RES percentages normally entails a price, since the risk that has to be addressed by the local operator of isolated weak electrical grids, either through the employment of adequate reserve capacity [6] or the implementation of RES curtailments [7,8], is proportional to the relevant RES contribution in such grids. To face this challenge, local grid operators impose certain constraints that are related to the strongly variable penetration of RES and the compliance with the technical limitations (technical minima) that characterize the currently operating oil-based power generation units [9,10]. The result of all these restrictions normally limits the maximum contribution of RES concerning the local load fulfillment, in the range of 15–20% on an annual basis (Figure 1). More specifically, according to the data of Figure 1, the RES production during the last years is presented on a monthly basis (taking values from 60 GWh_e up to 150 GWh_e per month), while the RES percentage (penetration) on monthly electricity demand varies between 12% and 22%.

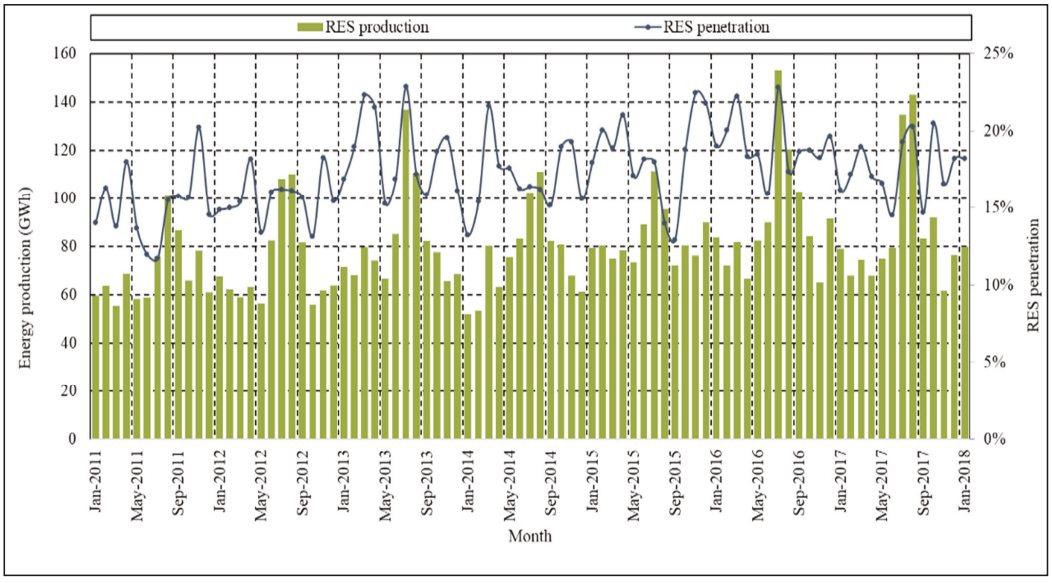

Figure 1. The Renewable Energy Sources (RES) contribution on the Non-Interconnected Islands' (NIIs) electricity consumption.

Actually, during the last fifty years, the Non-Interconnected Islands' (NIIs) electricity requirements have been almost exclusively covered by autonomous power generation stations (APS) comprised of internal combustion engines and gas turbines. More specifically, the electricity demand of the aforementioned islands is mainly covered by almost thirty (30) APSs [4,11], based on permanent as well as portable units of a broad nominal capacity range. The total capacity of all these APSs is approximately 700 MW (excluding the electrical systems of Crete and Rhodes islands, including, however, the ones of the Cyclades' complex just recently interconnected to the Greek mainland electricity grid). Moreover, the significant increase encountered in the local electricity demand of NIIs during the tourism season results in a limited utilization of thermal power units during the rest of the year, particularly if the latter are oversized with regards to the average autonomous network electricity requirements. This is exactly the case for the very small to medium scale Aegean Archipelagos islands.

The direct result of this situation is the low capacity factors for all these APS, combined also with excessive specific fuel consumption (SFC) values, in the range of 200–300 gr/kWh$_e$, which, in turn, results in quite elevated electricity generation cost for most of the local electrical systems. In this context, the combined effect of high SFC values in conjunction with extensive maintenance requirements and APS assets' amortization results in a continuous increase of the total electricity generation cost. More specifically, during the last years, the annual electricity generation cost of all the NIIs has exceeded 300 M€ (electrical systems of Crete and Rhodes not included) and is strongly affected by the imported oil quantities and their price volatility.

1.2. RES Power Generation in NIIs of the Aegean Archipelagos

According to long-term measurements, most of these isolated islands possess excellent RES potential that supports actions to maximize RES integration. Albeit the very high-quality wind potential that characterizes most of the NIIs as well as the excellent solar potential of the entire Aegean Archipelagos (Figure 2), the progress noted in RES power applications has not met the expectations. Based on available official data [12,13], wind power has presented a stagnation at ~75 MW, distributed on approximately 100 wind parks, dispersed mainly across the biggest and medium-scale Aegean Archipelagos islands,

while PV capacity slightly exceeds 40 MW_P, also gathered in the biggest islands of the aforementioned area (see also Figure 3).

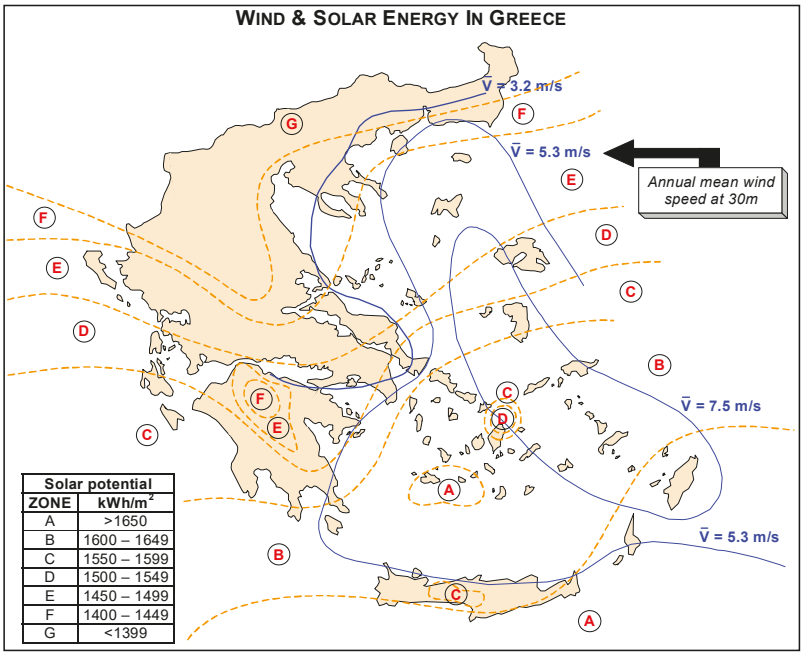

Figure 2. Wind & Solar Potential in Aegean Sea.

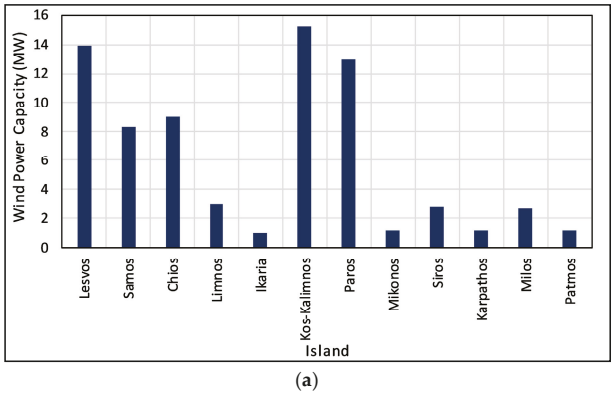

(**a**)

Figure 3. *Cont.*

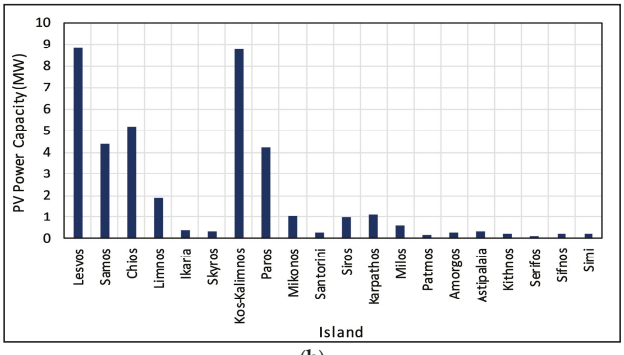

(**b**)

Figure 3. (**a**) Installed wind power capacity; (**b**) PV power capacity in NIIs of the Aegean Archipelagos.

Besides, stagnation encountered in new RES power plants implementation is further reflected in Figure 1, where one may find the RES contribution in the local load demand coverage for all NIIs, on a monthly basis. From the data presented, it can be concluded that RES share presents an almost constant pattern, despite the small increase starting from 15% in 2011 to attain 18% in 2017. As already mentioned, this specific penetration upper limit is the outcome of local electricity grids' restrictions (thermal power units' technical minima and local grid dynamic penetration margins) that discourage new RES power stations' implementation, due to the expected high values of curtailments. Such curtailments for already operating wind parks are already apparent in saturated insular electrical networks, such as the relatively big one configured by Kos and Kalymnos islands, to where Tilos island's electricity grid is connected. In the abovementioned electrical network, the curtailments that local wind parks (with an installed capacity approximately equal to 15 MW) face could even approach the value of 30% of the pertinent annual wind energy yield [13]. Consequently, the imposed grid and thermal power units' constraints challenge the effective capacity factor of the existing wind parks, strongly hindering the maximum exploitation of the available wind potential [7–10].

To improve the limited share of RES power generation in all these remote islands, pilot projects being characterized by state-of-the-art, integrated solutions which combine intelligent and sophisticated management features (forecasting and DSM) as also energy storage, could pave the way. To this end, the pioneering TILOS Horizon 2020 project [14], deployed on the Greek Tilos island that belongs as already mentioned to the saturated—with regards to RES applications—Kos and Kalymnos electrical network, indicates the way community-scale battery storage can optimally cooperate with locally developed RES power generation and advanced techniques such as DSM.

2. Proposed Integrated Electricity Solution for Remote Islands

To improve energy autonomy and energy supply security of the several existing islands, an integrated solution has been developed (Figure 4) based on the available wind and solar potential exploitation along with an appropriate energy storage infrastructure, introducing also some extra smart-grid elements. This solution is quite promising for various Greek islands belonging to the Aegean Archipelagos area, and particularly the most distant and small-scale ones.

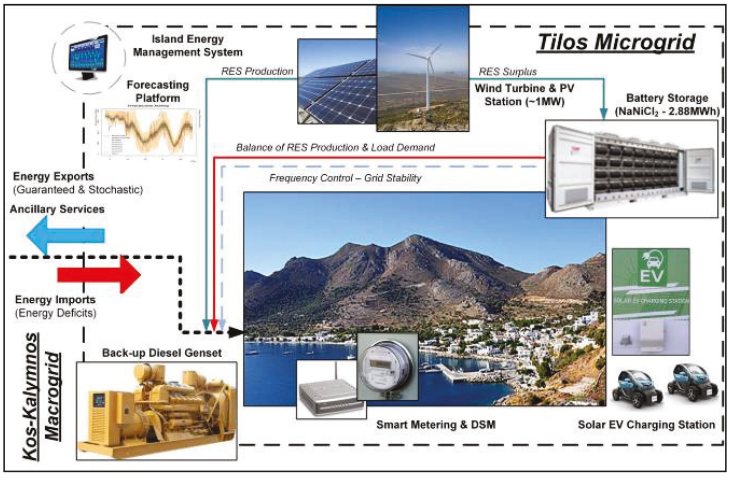

Figure 4. The RES-based energy solution for NIIs. The case of Tilos island.

More specifically, for every island, one should estimate the available RES (i.e., wind/solar/biomass and geothermal) potential. In this context, real-world operational data are necessary (see, for example, Figures 5 and 6), originated—if possible—from long-term in situ measurements. Actually, for a period of three years (2015–2017), detailed measurements were carried out concerning the wind speed and the solar irradiance data as well as the main meteorological parameters by our research team (Soft Energy Applications and Environmental Protection Lab of UNIWA) [14]. To this end, the expected RES-based annual electricity generation "E_{tot}" can be estimated by defining the maximum rated power "P_{RES}" for several configurations consisted of wind "P_w" and photovoltaic parks "P_{PV}", i.e.,:

$$E_{tot} = 8760.(CF_w.P_w + CF_{PV}.P_{PV}) \quad (1)$$

where "CF_w" and "CF_{PV}" are the capacity factor values of the selected wind turbines and PV panels according to the available wind and solar potential, correspondingly.

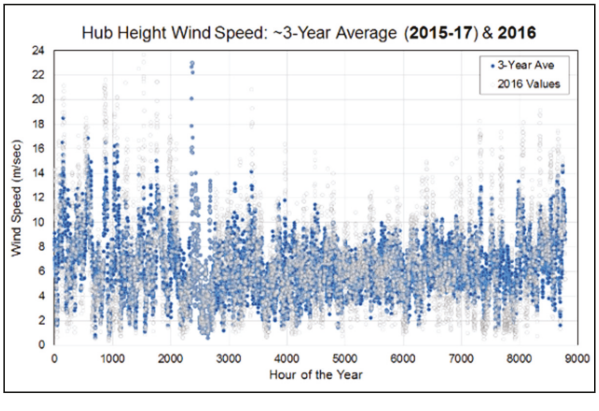

Figure 5. Wind speed time series for Tilos island.

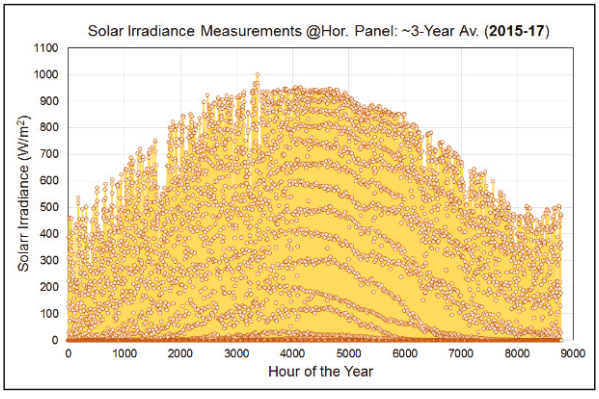

Figure 6. Solar irradiance time series at horizontal plane for Tilos island.

On the basis of existing licensing procedure in Greece, the maximum RES power to be installed on an autonomous island grid cannot exceed the local consumption peak load demand (e.g., 960 kW), hence:

$$P_{res} = P_w + P_{PV} \leq \text{Max Load Demand} \quad (2)$$

Considering that the rated power of the smallest contemporary commercial wind turbine in the market is 900 kW, a similar machine has been selected and has been down-rated at 800 kW, in order to install also a small PV power station of 160 kW_p. In the near future, additional PV panels may be added if the peak power of the island increases also, since the PV installations have the option of modularity.

Subsequently, using accurate measurements (Figure 7), even on a sec-time-interval basis, stemming from official recordings, the pertinent load demand time-evolution is investigated to ensure the local electricity grid stability as well as the uninterruptible power supply of high priority loads. Furthermore, both deferrable loads as well as loads of secondary priority have been pinpointed (Figure 8). Actually, in Figure 8, one may find the electricity consumption needs for water pumping (including also water transferring between water tanks), which is maximum during the summer due to the increased tourist activities. In the same Figure 8, one may find the monthly public lighting electricity consumption for the four villages of the island (Megalo Chorio, Livadia, Agios Antonios, Eristos). As can be revealed from the existing data, the relevant electricity consumption is also increased during the summer period since all the local tourist facilities are in operation. Finally, the technical specifications of the "in-operation" thermal power units and the actual interconnections deployed until now to satisfy the local load demand have been scrutinized as well.

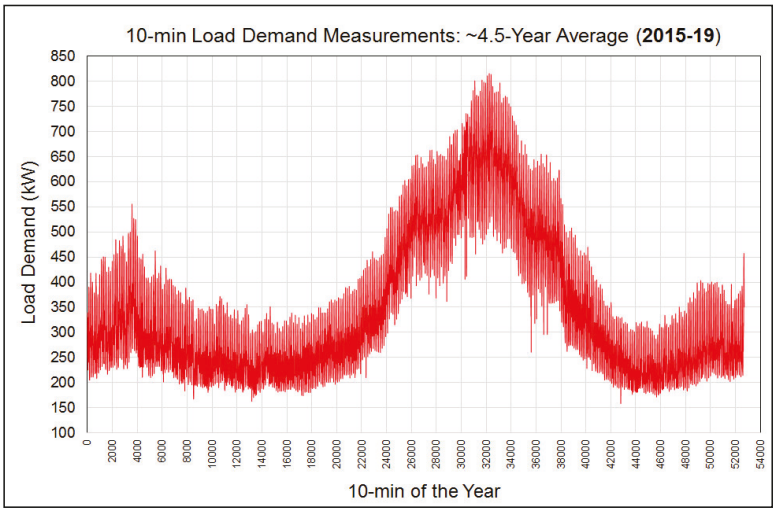

Figure 7. Load demand data for Tilos island. The 4.5 year average 10 min load.

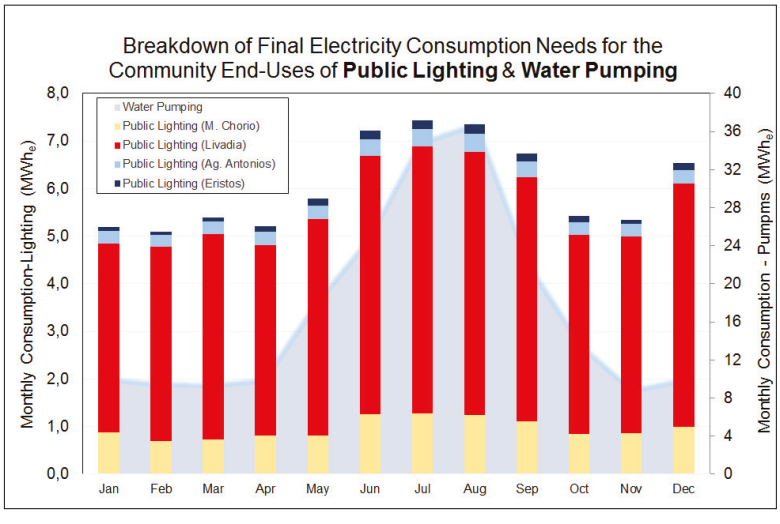

Figure 8. Public lighting-water pumping electricity consumption breakdown.

Consequently, a thoroughly designed and sized energy storage system has been installed [15–18], to improve the electricity system power (active and reactive) balance and reduce the dependence on fossil fuels. The corresponding energy storage technology and its main operational parameters (i.e., input–output power, charging/discharging rate, round-trip efficiency, depth of discharge, energy capacity, etc.) are determined by the island's peak load demand, its inherent characteristics (e.g., land availability, topography, etc.) as well as the degree of energy autonomy to be attained (or the intended maximum oil contribution in the island energy mix).

The introduction of DSM techniques in conjunction with smart meters for the major deferrable loads stands out as another crucial parameter for obtaining enhanced electrical grid power balance [13,19]. Moreover, load management may also be applied in the residential and hotel sectors as well as for other principal consumers of the island (Figure 9).

One of the most promising cases is the application of load management strategies at the existing eight (8) water pumping installations with maximum power of 70 kW, representing a considerable part (e.g., 15%) of the island's average load. In this context, the local load demand can be adjusted to better match the available RES production without jeopardizing the local population living standards. Additionally, penetration of electric vehicles in the transportation sector of the island (Figure 10) could also assist in this direction, with the local, relatively restricted (maximum distance 15 km), road networks suggesting the ideal ground for electro-mobility applications.

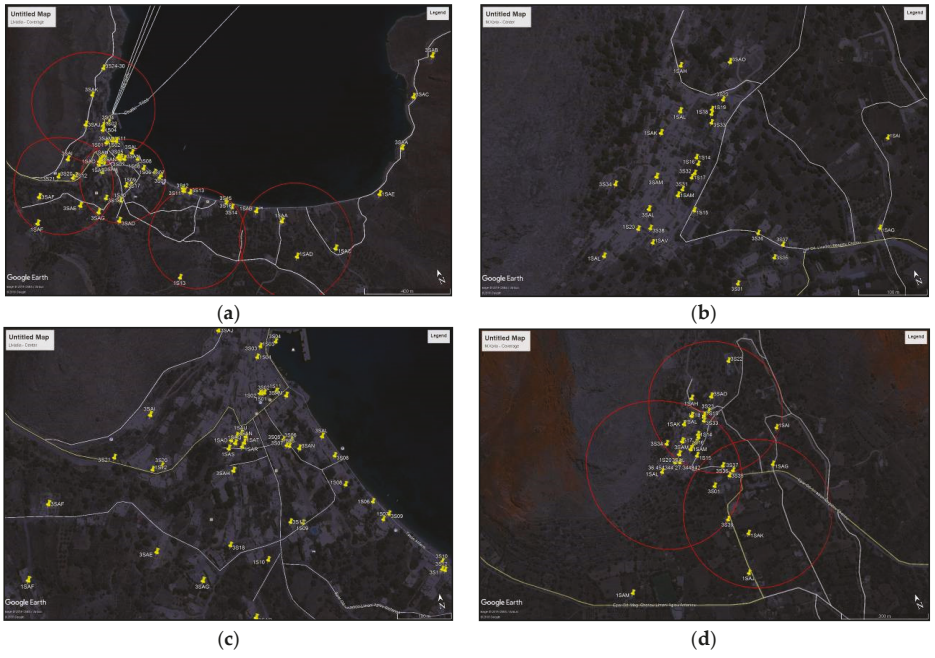

Figure 9. DSM panels—overall and at village centre @ Livadia (**a**,**b**) and @ M. Chorio (**c**,**d**).

Figure 10. Photos of the charging area and EV charger at TILOS info-kiosk in Livadia.

Furthermore, forecasting methods and associated systems can also be taken into account under the scope of upgrading the operation and ameliorating the flexibility of the complete electricity production system (EPS), while in parallel maximizing RES contribu-

tion. Such an example is the deployment of an innovative Forecasting Platform (FP) that is capable of providing reliable predictions of load demand, solar power and wind power generation several hours ahead [20,21]. The aforementioned features comprise the core of a High-Level Energy Management System (EMS) and Centre, in charge of coordinating the programming and optimum operation of the various subsystems of such an integrated solution. In this context, based on forecasting signals, the operation and dispatch strategy of energy storage can be improved, while also keeping end users informed on the potential for demand response, hence favoring RES contribution maximization and cost-effectiveness.

As a final point, it is important also to mention that all the aforementioned steps impose continuous education and interaction with the local community [22]. To that end, close collaboration with the local authorities should be established, respecting their priorities, while at the same time the potential project developer should disseminate to the local people the information for the new infrastructure introduction and the benefits anticipated.

3. The Application Paradigm of Tilos Island

Tilos is a unique, small-scale "S"-shaped island found at the SE side of the Aegean Sea in Greece, a region of great symbolism and major geopolitical interest for Europe as a whole. Part of the Dodecanese group of islands, Tilos lies mid-sea between Kos and Rhodes (Figure 11). Northwest to south-east, the island is ~14.5 km long, with a maximum stretch of 8 km and an overall area of approximately 64 km^2. Standing at a distance of 240 n. miles from the Greek mainland (Piraeus, Attica), Tilos belongs to the very special group of remote and small-scale European islands.

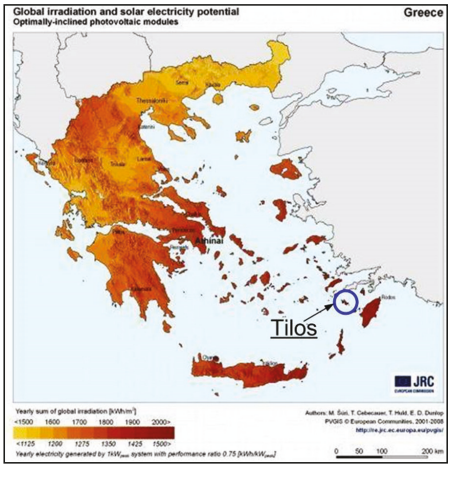

Figure 11. Tilos island location.

The island counts four main (populated) settlements/villages, namely, Megalo Chorio, which is the capital; Livadia, which is the biggest village and where the island's port and main center of economic activities are found; Agios Antonios and Eristos.

The climate of Tilos is typical of the Mediterranean region, with mild winters and hot, sunny summers. Concerning the local RES potential, Tilos appreciates an excellent-quality solar potential, determined by ~1800 kWh/(m^2.a) at the horizontal plane (Figure 6). On the other hand, the local wind potential is of medium quality, with the average wind speed ranging between 6 and 8 m/sec in the largest part of the island (see also Figure 5).

According to the most recent census, Tilos has a total of 829 registered inhabitants. The actual population of the island during the winter months, however, is estimated to narrow down to ~400–500, as most of the residents move to the more populated, vicinal islands

of Rhodes and Crete. The rest of the permanent residents gradually return to the island (between April and May each year), on time for the tourist season, with tourism suggesting the main economic activity on Tilos. In this context, and as already implied, the local population increases dramatically during the tourist season of the year, which normally lasts for a full 6 months (mid-April to mid-October). The island can host ~1200 visitors, with the number of tourists normally exceeding the hosting capacity of hotels and apartments by far, especially during the peak summer period of August.

3.1. Tilos Electricity Grid

Tilos belongs to the electrical complex of the Kos and Kalymnos islands, forming an electricity system of nine (9) islands in total, with Tilos located at the very southern tip of the complex. In more detail, Tilos is connected to the island of Kos via the R-44 feeder line (see relevant configuration in Figure 12). The R-44 feeder (in light blue) departs from the central bus bar at the Kos thermal power station, has three underwater sections between four islands and serves—via overhead lines—a few MV consumers on the Kos and Gyali island, as well as the entire electricity demand of the Nisyros and Tilos islands. Moreover, and for redundancy reasons, there are two undersea cables, each corresponding to a different cable link on Kos, with only one being typically operated, which means that the switch from one side of the second link remains open.

Figure 12. The R-44 Interconnector from Kos.

The feed-in point from Kos stands also as a point of common coupling between the broader electricity system of Kos and Kalymnos and the electrical grid of Tilos. This means that Tilos can be isolated from the R-44 line and thus be operated as a completely independent, geographical island microgrid, relying exclusively on its own power generation sources.

The Kos and Kalymnos island complex, to which Tilos belongs, comprises, as already mentioned, an electrical system of nine (9) islands, with an installed capacity of ~145 MW (mainly thermal, oil-fired units), an annual peak load demand of more than 90 MW and an annual electricity demand in the order of 365 GWh_e. The system relies mainly on the thermal power station of Kos island (capacity of ~102 MW), employing heavy-oil fired engines of 87.3 MW and diesel-fired units of 14.6 MW, and secondarily on the thermal power station of Kalymnos (capacity of 18.15 MW), employing heavy-oil units alone. At the same time, RES units across the complex (excluding Tilos) include four wind parks of total installed capacity equal to 15.2 MW and 92 PV parks of ~8.8 MW_p in total. The annual energy yield of the latter is estimated in the order of 16.6 GWh (capacity factor of ~19%), while for the existing wind parks, the estimated annual energy yield reaches almost 46 GWh (capacity factor of 34.5%) (see also Figure 6), with 1/3 of this

number, however, being curtailed. This reflects the saturation levels of the Kos and Kalymnos electricity system in terms of RES capacity. More specifically, due to the dynamic penetration limit for RES on the one hand (e.g., RES contribution should be no more than 30% of instantaneous load demand) and the technical minima of the in-operation thermal units on the other, the residual load available for the absorption of considerable RES power generation is significantly reduced. The specific shortcoming is critical for the further increase of renewables in the system, which, if not supported by energy storage and/or new interconnections, does not seem to suggest an economically viable option.

The average load demand profile of Tilos currently adopted (Figure 7) is configured on the basis of a long-term measurement campaign carried out within the context of TILOS project, covering a period of almost 4.5 full years, i.e., from mid-2015 to autumn 2019 on the basis of 10 min measurements. To this end, the total electricity consumption of the island is found (Figure 13) to marginally exceed 3 GWh_e (3.035 GWh_e), while the average peak demand of the year exceeds 800 kW, although, if looking at individual years, summer peak demand is actually in the order of 900 kW.

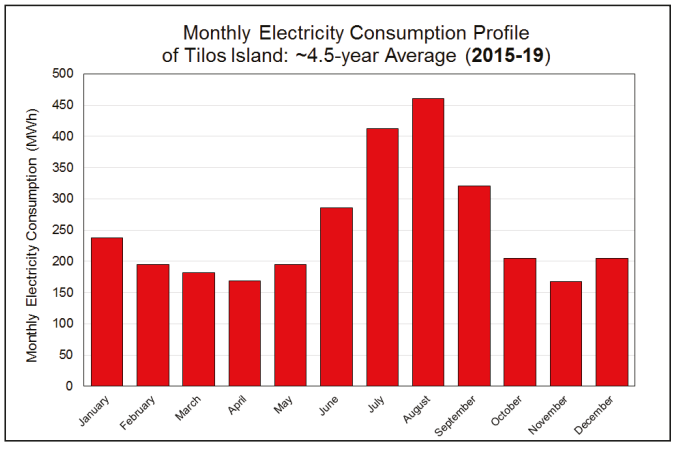

Figure 13. The 4.5 year average monthly consumption profiles of Tilos island.

3.2. Tilos Hybrid Power Station

In view of the successful implementation of the TILOS project, the first-ever battery-based, wind and PV Hybrid Power Station (HPS) in Greece has been developed. At the same time, an integrated microgrid has also been developed on the island and several innovative elements have been introduced, altogether transforming Tilos into an exemplary island case in terms of local-scale clean energy production and management.

This comprised a major breakthrough, not only for Tilos, but also for the Greek energy market as a whole, disrupting the norms of the past and presenting a new energy paradigm and solution for the electrification of island regions. Acknowledging the above, the main assets and elements of the power generation side are first presented.

Concerning the electricity generation sector, the main power generation assets that are currently in operation on Tilos include:

- the Tilos HPS, comprising:
  - an 800 kW, medium scale wind turbine
  - an 160 kW_p PV station
  - an 800 kW/2.88 MWh integrated Battery Energy Storage System (BESS)
- the back-up diesel genset of 1.45 MW, located in the village of M. Chorio
- distributed, small-scale PV installations supporting early prosumer schemes and including:

- two monitored PV installations in M. Chorio & Livadia (capacity of 3.36 kW_p at local residence and 4.93 kW_p at the TILOS info-kiosk/EV charging station respectively)
- four non-monitored PV installations (operational capacity of ~10 kW_p in total).

The above assets, together with the rest of the innovative elements that will also be analysed in the following paragraphs, comprise the integrated Tilos energy solution. As also reflected in Figure 14, the integrated Tilos energy solution suggests an energy microgrid that is normally found to interact with the host electricity system of Kos and Kalymnos (mainly the HPS), or, in rare cases, operated in isolation (such as in cases of emergency or microgrid testing).

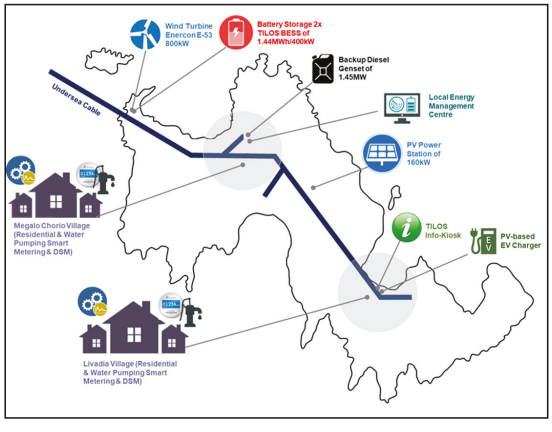

Figure 14. Description of Tilos island microgrid and geographical location of main assets.

3.2.1. HPS-Wind Turbine

The Tilos HPS wind turbine was installed in June 2017 by the Greek energy company, Eunice, which acted both as a private investor and a major partner of the TILOS project. As can also be seen from Figure 14, the wind turbine is co-located with the HPS battery storage system, at the northwestern tip of Tilos (area of Pachy), next to the undersea cable junction (Figure 15). To this end, the main technical features of the Enercon E-53 wind turbine are provided in Table 1.

Figure 15. Photo of the Tilos HPS wind turbine, installed in the northwestern part of the island.

Table 1. Main characteristics of installed wind turbine.

Wind Turbine Type:	ENERCON E-53
Nominal capacity:	800 kW
Rotor diameter:	52.9 m
Hub height:	60 m
Tower type:	Tubular steel tower
Wind Class/IEC 61400-1:	S
Electrical configuration:	Grid Performance FT
Location:	Pachy

3.2.2. HPS-PV Plant

The Tilos HPS PV plant was also installed in June 2017 by Eunice, and is located at the central part of the island (Figures 14 and 16), sharing the distance between the villages of M. Chorio and Livadia. The PV plant is comprised of 592 polycrystalline PV panels of 270 W_p maximum capacity each, manufactured by JA Solar. Every 74 panels form an array with a maximum capacity of 19.98 kW_p and are connected to the respective array inverter of 20 kW nominal capacity, manufactured by FRONIUS. The produced energy is collected from each string inverter and directed to the MV transformer and consequently to the local grid overhead lines. To this end, the main technical features of the PV panels employed are provided in Table 2 on the upper right, together with additional information, such as the exact location of the installation.

Figure 16. Photo of the Tilos HPS PV plant, installed at the central part of the island.

Table 2. Main characteristics of installed PV park.

Type:	JAP6(K)-60-270/4BB
Maximum Power:	270 Wp
Max Power Current (lmp):	8.67 A
Max Power Voltage (Vmp):	31.13 V
Short Circuit Current (lsc):	9.18 A
Open Circuit Voltage (Voc):	38.17 V
Temperature Coefficient of Voc:	−0.330%/°C
Operating Temperature:	−40 °C ~ +85 °C
Maximum System Voltage:	1000 V DC
Dimensions:	1650 × 991 × 35 mm
Total surface/tilt angle:	1635.2 m^2/30°
Location/orientation	Agios Konstantinos/South

3.2.3. HPS-BESS

The integrated battery system of Tilos was fully installed on the island in January 2018, following the earlier installation of two battery containers and the introduction

of individual battery modules right after. It comprises a fully containerized solution based on the high-temperature $NaNiCl_2$ technology, standing as a fully recyclable storage configuration. The battery modules, which are manufactured by the Italian FZSonick, i.e., one of the lead partners of TILOS, under the type FZSonick ST523, are containerized into two 20 ft containers (Figure 17). Each of the containers comprises an energy storage system of 64 FZSonick ST523 modules that are connected in parallel. The technical specifications of the battery module and of the standard energy storage application are provided in Table 3. Concerning the AC side, each of the battery containers is connected to a dedicated battery inverter (PCS) manufactured by the Swiss Indrivetec (IDT). The two employed inverters are of 500 kVA each under the type SOLO S and are combined with two 630 kVA, 20/0.3 kV MV transformers, altogether forming the battery AC side. The inverters' main specifications are given in Table 4.

Figure 17. Photo of the Tilos HPS BESS, installed at the northwestern part of the island.

Table 3. Main characteristics of installed BESS.

Nominal Energy Capacity	**1.4 MWh-100% DOD @C/10**
Nominal energy (nom. voltage-capacity)	1.44 MWh
Nominal current capacity	2432 Ah (100% DOD)
Constant power discharge	400 kW for 3 h
Standard charge/discharge	8 h/3 h
Max heating power	64 kW
Heater av. consumption@ floating	10 kW
Max charge current	960 A
Max discharge current	1920 A
Max charge power for controlled charge	216 kW
No. of FIAMM gateway	1

Table 4. Main technical characteristics of the Indrivetec SOLO S inverter.

Nominal AC Power (PAC)	**450 kW**	**At Power Factor cosφ = 1**
Maximum apparent power	500 kVA	
Power factor cosφ	±0.9	
AC Nominal operating voltage (UAC)	300 V	UACmax = 330 V
AC Nominal current (IAC)	875 A	970 APEAK RMS
Grid Frequency	50 Hz	±10%
Harmonic Distortion (% THD IAC)	<3%	
Efficiency	98.2%	Charging and discharging
Control Modes	P/Q—U/f	

In contract with the two RES units, the integrated BESS was commissioned in April–May 2018. This enabled the energization and warm-up of the battery modules and allowed for the execution of a series of Site Acceptance Tests (SAT). The SAT lasted for a total of 2 weeks and included communication tests, software integration, emergency tests, battery

warm-up, power exchange between containers, cycling, grid perturbation and internal black start, as well as a set of set-point profile tests.

3.3. Tilos Island Demand Side Management

Following the detailed presentation of the generation side and energy management aspects, the demand side of the island is next presented, with the focus given on the Smart Metering and DSM platform of Tilos, bringing together a pool of almost 100 end consumers and community loads. Note that the remote electricity grid of Tilos comprises a vulnerable system often faced with power cuts, which affects living conditions on the island in an adverse manner, hindering also economic activities, especially during the summer period.

Concerning consumers, there are no MV customers on the island, neither large-scale consumers, which is attributed to the lack of local industrial activities. Essentially, it is the local residential and tertiary sector that carry the biggest share of electricity consumption, with local hotels and summer apartments increasing the local demand during the summer period, altogether belonging to the broader category of the building sector analysed accordingly.

Apart from the local building sector, other important sources of electricity consumption correspond to community-scale loads, such as water pumping (a total of 8 water pumping systems of ~62 kW and several smaller scale borehole pumps for irrigation) and public lighting (see also the respective monthly consumption profile in Figure 8), while grid-connected is also the telecommunication infrastructure of the island.

As already seen, the Smart Metering and DSM platform, developed by Eurosol (also partner of TILOS) and currently owned by local end users and the Municipality of Tilos, comprises one of the main components of the integrated energy solution of Tilos, bringing together a pool of ~100 Smart Meter and DSM panels (Figure 9). The prototype DSM panels can be used both directly by local end users (mainly for electricity consumption monitoring) and offer a pool of controllable loads. In this context, the DSM platform can in aggregate serve different purposes in order to improve the operation of the Tilos microgrid (e.g., load shifting in favour of increased RES shares or control of loads during recovery from black-out events / stand-alone island operation of Tilos in support of the local HPS operation, etc.), comprising at the same time the end-nodes of the integrated Smart Metering and DSM platform. The latter is also responsible for the monitoring, data collection, classification and remote, centralized control of all active DSM loads, acting at the same time as an integrated element of the developed High-Level Energy Management Centre (HL-EMC). DSM panels were gradually installed during the implementation of TILOS, distributed across local residences, hotels, commercial stores and the public sector, as well as in eight (8) water pumping stations of the island standing as community-level loads. Their distribution over the two main villages of Livadia and M. Chorio is given in Figure 9, followed by the distribution of controlled community loads across the entire island.

Apart from the monitoring and control of loads at the end-user level, the entire pool of loads can also be centrally monitored at the DSM server, co-located with the HL-EMS server at the old power station of the island. Following the commissioning of the HL-EMC/EMS, the Smart Metering and DSM solution acquired a twofold role, acting as an independent system branch (aggregate pool of DSM loads that can support different types of grid services) on the one hand, and supporting interoperability with the rest of the system components as part of the HL-EMC on the other. In this context, load demand monitoring is also active in aggregate fashion, supported by an advanced UI and relevant dashboards that group together DSM loads per type of end user.

In the meantime, further classification, based on the type and elasticity/flexibility of loads has been carried out. What should be stressed at this point is that the total DSM loads' installed capacity rises to more than 700 kW, which is expected to ensure a minimum DSM pool of 15–20% in comparison to the appearing load demand of the island at all times.

4. Evaluation of Tilos Island Solution

After the completion of the commissioning phase for the RES units, the HPS of Tilos became fully functional and, as such, it entered the "prosumer" stage of operation. To this end, consecutive, 20 day duration time windows of trial operation were exploited in order to test the HPS performance, first under a certain daily profile/schedule of max-permitted power output per hour of the day. The specific profile (provided by the local network manager-Kos APS) is depicted in Figure 18 (with the max-permitted power output of the entire HPS set to vary between the fixed values of 0 kW, 400 kW and 800 kW) and it is the one governing the operation of the HPS from mid-September until early in January, i.e., when a second round of trial operation started for the testing of different set-point profiles for the HPS.

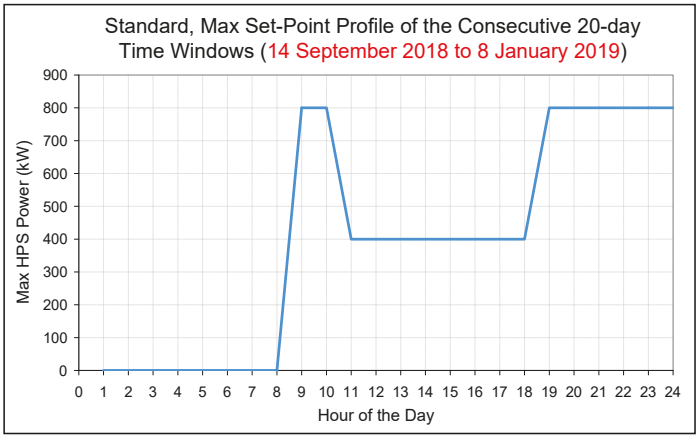

Figure 18. The standard profile of max set-point for the Tilos island HPS.

More specifically, following the issuance of all the necessary permits in 2018, the wind turbine was commissioned in mid-September and was fully activated on September 19, 2018, i.e., when it started generating power as part of the integrated HPS of Tilos. With regards to its anticipated energy performance, the medium quality wind potential of the area (long-term average wind speed of ~6.5 m/sec at 30 m height, based on on-site measurements from a dedicated wind mast) produces an annual capacity factor of 27.5–30% concerning the theoretical output of the machine, which is equivalent to an annual power generation between 1.9 GWh_e and 2.1 GWh_e. However, during the examined period, the actual wind energy production falls below these numbers, owing primarily to the saturation levels of the overall Kos and Kalymnos system noted earlier, with the ex-post capacity factor estimated in the area of 20%. In addition, and during the demonstration stage of the TILOS project, that coincided also with the very early period of HPS operation, trial tests for the HPS dictated the application of certain set-point profiles, which further compromised the exploitation of local wind energy production. The combined impact of the two is better reflected in the figures (Figure 19a,b), comparing the actual and theoretical production of the wind turbine till the end of January 2019 (end-month of TILOS project).

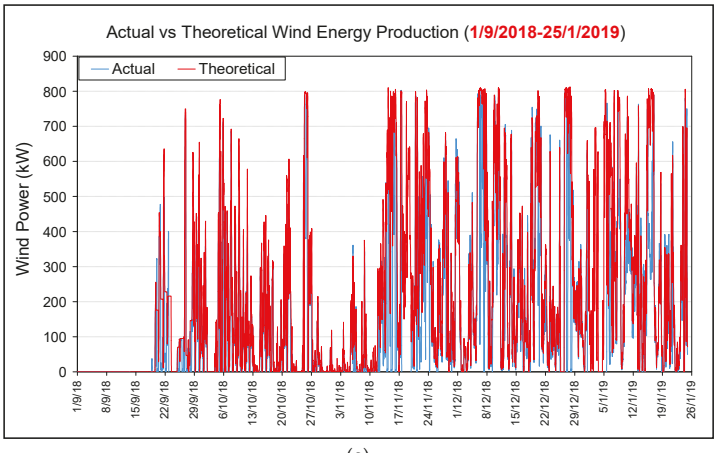

(**a**)

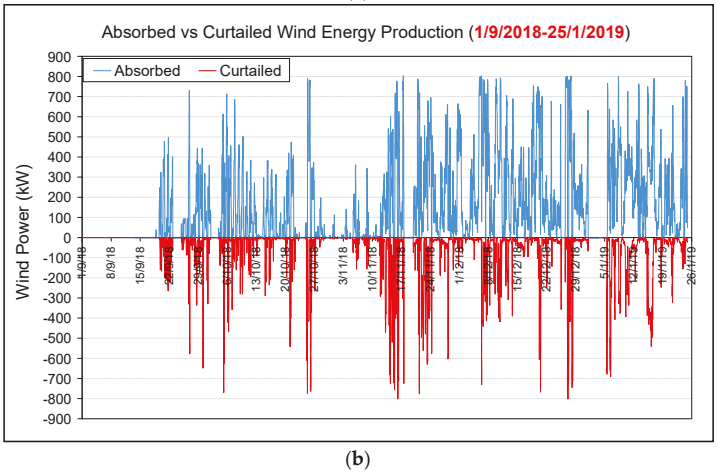

(**b**)

Figure 19. (**a**) Actual vs theoretical; (**b**) absorbed vs curtailed wind energy over the period of TILOS demonstration.

To this end, the levels of wind energy curtailments encountered are better illustrated in Figure 19b, while another way to express and quantify the difference between the potential and the actual wind power generation is given in the results of Figure 20a,b, where the actual and theoretical capacity factors are compared. In this context, the resulting average difference is in the order of 10%, i.e., the expected capacity factor on the basis of the available wind potential and operational curve of the wind turbine used is almost 30%, while the finally absorbed wind power by the local grid corresponds to capacity factor value equal to 20%. This real-world situation means that 1/3 of the energy yield of the wind turbine during the given period was curtailed by the local network operator due to limited electricity demand and the restrictions imposed by the local grid stability and the existing thermal units technical minima.

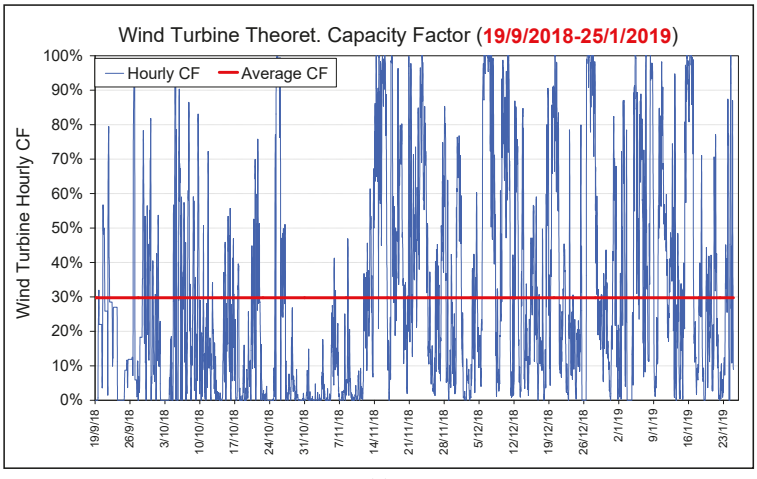

(**a**)

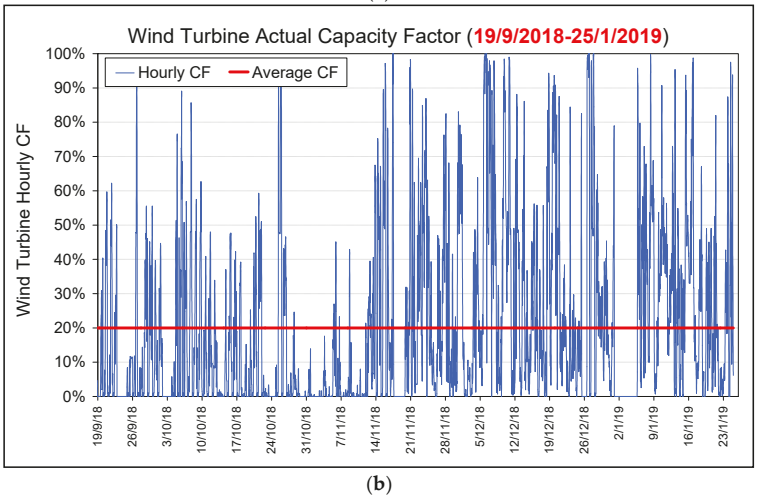

(**b**)

Figure 20. (**a**) Theoretical; (**b**) actual wind capacity factor over TILOS demonstration stage.

Similar to the case of the wind turbine installation, commissioning of the PV station was also successfully completed in September 2018, enabling power generation on the 14th of September 2018. To this end, and as far as the expected energy performance of the PV station is concerned, the excellent solar potential of the area (~1800 kWh/(m^2.a) at the horizontal plane) produces an annual capacity factor of ~18–19% concerning the theoretical output of the station, which is equivalent to an annual power generation between 250 and 270 MWh_e. Although subject to considerable curtailments as well, the PV station is considered to be less vulnerable in comparison to the wind turbine, mainly owing to its more dispatchable character as a renewable energy source. In this context, energy generation results from the operation of the PV station during the period examined are shown in the following Figure 21. As one may see in this figure, the maximum power output is limited in the order of 130 kW, owing to the winter season encountered during the reference period. On the other hand, it is for almost 80% of the time (including night-time periods) that the PV generation output falls below 40 kW, which compares unfavorably with the local load demand and also challenges the predictability of the RES resource, especially with regards to the obligation of the HPS to provide day-ahead guaranteed

energy offers. Concerning the capacity factor of the PV station over the demonstration period of TILOS, it was estimated at 12%, which for the specific (September to January) season of the year is considered satisfactory.

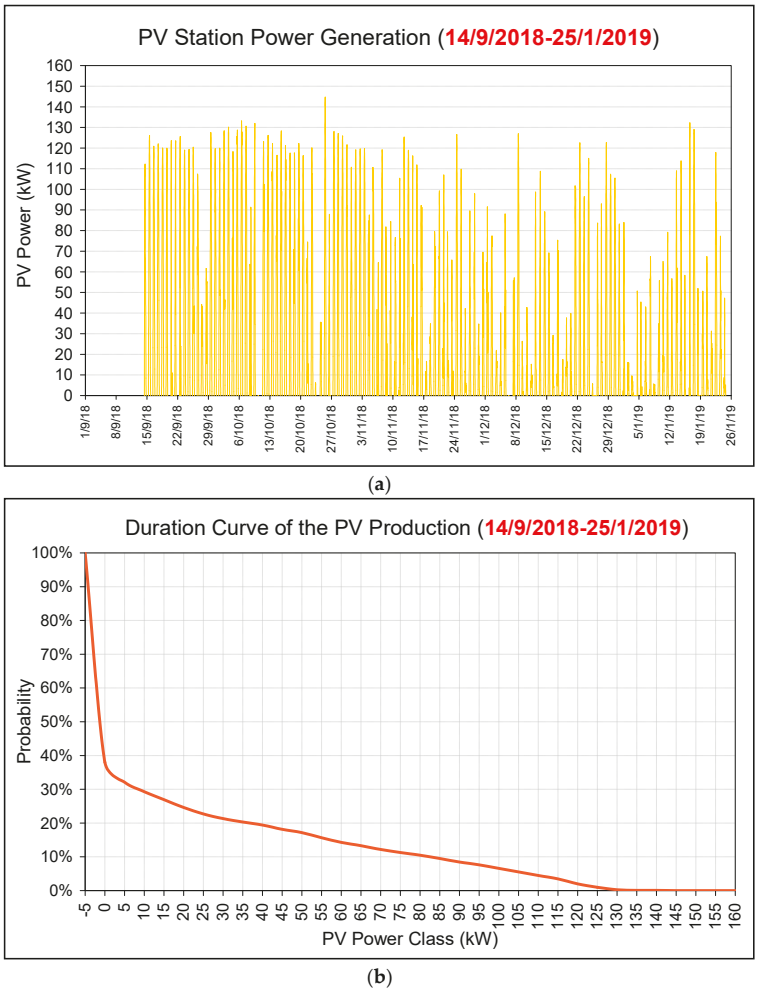

Figure 21. (**a**) PV station power generation; (**b**) relevant duration curve.

Recapitulating, in Figure 22, we demonstrate the daily energy balance between the HPS production and the local island electricity consumption, together with a breakdown of the HPS production to its main components (i.e., wind turbine, PV station and battery operation). Note that during the first two weeks of September the HPS had not received the energy production licence, thus electrical energy was consumed (imported by the local grid) in order to keep in operation (at desired temperature) and test the two battery banks. As one may see, for the first two months of operation, the HPS contribution was moderate, directly dependent on both the performance of the wind turbine and the hourly cap on the basis of the adopted schedule (Figure 18). Following the end of that initial period, which coincides also with a considerable reduction of the load demand and an improvement of the wind turbine performance, contribution of the HPS to the local consumption was found

to increase remarkably, especially during December 2018, even under these sub-optimal conditions of operation imposed by the local network management.

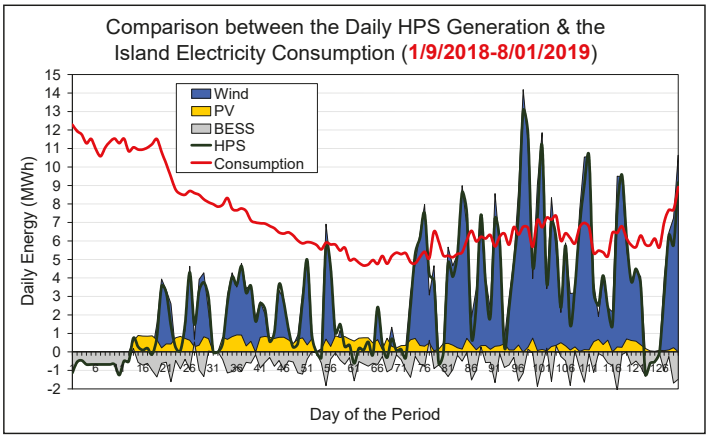

Figure 22. The daily energy balance analysis for Tilos island.

What is worth noticing is that for December, local-only RES shares exceeded 70%, which, impressively enough, even reach 90% of the local consumption if RES imports and exports are also taken into account. On the other hand, RES shares during the summer period drop in the order of 25–30%, which is due to both the lower wind energy yield and the higher electricity demand appearing during that period (see also Figure 23). Note that even these extremely low RES participation values are quite higher than the ones appearing in Figure 1, not exceeding 22% in any occasion. As one may see from Figure 22, the inclusion of RES exports makes little difference, which reflects on the increased curtailments faced over the period of study. On an annual basis, the energy provided of the Tilos island HPS is slightly less than 1500 MWh_e, mainly due to the local network curtailments and the poor exploitation profile dictated by the local network manager, completely neglecting the values provided by the existing forecasting algorithms.

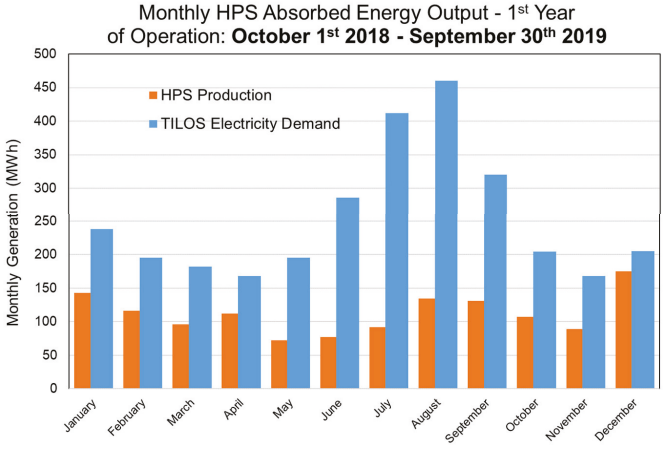

Figure 23. Actual, monthly energy output (absorbed) of Tilos HPS vs. Tilos island electricity consumption, as recorded from HEDNO.

5. Conclusions and Proposals

The implementation of the integrated TILOS energy solution under the current local legislative frame is a great success story introducing several important innovative characteristics in the European market. More specifically, the combined operation of a wind turbine and a PV installation (hybrid power station), the application of new technology battery energy storage, the installation of DSM network/platform and the development of a large number of reliable forecasting algorithms are among the main results of the proposed strategy.

Undoubtedly, the core component of the integrated TILOS solution, i.e., the local HPS, carries a bundle of innovative features synopsized below:

- The HPS of Tilos comprises the first-ever, fully licensed, MW-scale, battery-based HPS in Greece. As such, it disrupted the local energy market and introduced new aspects in the Greek energy agenda, especially with regards to non-interconnected island electricity systems.
- Although rather sophisticated, the Greek regulation for HPSs was tailored to the operation of pumped hydro, concerning the storage technologies employed. A series of advancements were introduced to this end to the local regulations within the context of TILOS in order to accommodate the operation of battery-based HPSs, positively affecting the early-stage storage market of Greece as well.
- The HPS of Tilos has been the first to comply with the requirements of a day-ahead dispatch operation that is based on the declaration of guaranteed energy (power) offers and which entails the need for the exploitation of forecasting means as well.
- The integrated BESS is able to offer a bundle of services including RES balancing and ancillary services to the local grid, like frequency and voltage regulation, while, under a set of conditions, it can also support black-starting of Tilos; thus standing as a novel, multiple-service storage system.

To our knowledge, the microgrid of Tilos is one of the most advanced island microgrids in Europe with smart aspects and many novel technologies and components. All these novel elements, following the TILOS project demonstration stage, are gradually evolving in order to support the operation of a mature energy ecosystem, fostering in the course of time the addition of new agents and actors such as the envisaged pool of prosumers, towards the full-scale decarbonisation of the island of Tilos.

As far as the energy performance is concerned, evidence of operations that are drawn from the core period of TILOS project demonstration stage (i.e., May 2018 to January 2019) is provided. The specific period is exploited in order to give a preliminary performance assessment of individual assets comprising the overall Tilos energy solution, which, although determined by sub-optimal operational conditions during the examined span, does provide a first set of indications on the potential of the system to provide increased shares of RES for the island of Tilos.

According to the results obtained, the innovative integrated Tilos island solution can be definitely improved by adopting already existing forecasting techniques in order to improve the energy balance between the local HPS and the main grid of Kos-Kalimnos, ameliorating also the battery bank energy management. Moreover, remarkable RES-based energy production curtailments should be minimized, introducing the opportunities of clean electromobility. In any case, the real-world operating example of Tilos island may be equally well applied in several other remote islands all over Europe with very promising results.

Funding: This research received no external funding.

Institutional Review Board Statement: Not applicable.

Informed Consent Statement: Not applicable.

Data Availability Statement: All data are based on our Lab research efforts.

Conflicts of Interest: The author declares no conflict of interest.

References

1. Kuang, Y.; Zhang, Y.; Zhou, B.; Li, C.; Zeng, L. A review of renewable energy utilization in islands. *Renew. Sustain. Energy Rev.* **2016**, *59*, 504–513. [CrossRef]
2. Cross, S.; Padfield, D.; Ant-Wuorinen, R.; King, P.; Syri, S. Benchmarking island power systems: Results, challenges, and solutions for long term sustainability. *Renew. Sustain. Energy Rev.* **2017**, *80*, 1269–1291. [CrossRef]
3. Anagnostatos, S.D.; Halevidis, C.D.; Polykrati, A.D.; Bourkas, P.D.; Karagiannopoulos, C.G. Examination of the 2006 blackout in Kefallonia Island, Greece. *Int. J. Electr. Power Energy Syst.* **2013**, *49*, 122–127. [CrossRef]
4. Kaldellis, J.K.; Zafirakis, D. Present situation and future prospects of electricity generation in Aegean Archipelago islands. *Energy Policy* **2007**, *35*, 4623–4639. [CrossRef]
5. Chalvatzis, K.J.; Ioannidis, A. Energy supply security in the EU: Benchmarking diversity and dependence of primary energy. *Appl. Energy* **2017**, *207*, 465–476. [CrossRef]
6. De Vos, K.; Petoussis, A.G.; Driesen, J.; Belmans, R. Revision of reserve requirements following wind power integration in island power systems. *Renew. Energy* **2013**, *50*, 268–279. [CrossRef]
7. Kaldellis, J.K.; Kapsali, M.; Tiligadas, D. Presentation of a stochastic model estimating the wind energy contribution in remote island electrical networks. *Appl. Energy* **2012**, *97*, 68–76. [CrossRef]
8. Kaldellis, J.K.; Kavadias, K.A.; Papantonis, D.E.; Stavrakakis, G.S. Maximizing the Contribution of Wind Energy in the Electricity Demand Problem of Crete Island. *Wind Eng. J.* **2006**, *30*, 73–92. [CrossRef]
9. Kaldellis, J.K. The Wind Potential Impact on the Maximum Wind Energy Penetration in Autonomous Electrical Grids. *Renew. Energy J.* **2008**, *33*, 1665–1677. [CrossRef]
10. Papathanassiou, A.S.; Boulaxis, N.G. Power limitations and energy yield evaluation for wind farms operating in island systems. *Renew. Energy J.* **2005**, *31*, 457–479. [CrossRef]
11. Tzanes, G.; Zafeiraki, E.; Papapostolou, C.; Zafirakis, D.; Moustris, K.; Kavadias, K.; Chalvatzis, K.; Kaldellis, J.K. Assessing the Status of Electricity Generation in the Non-Interconnected Islands of the Aegean Sea Region. In Proceedings of the Applied Energy Symposium and Forum, Renewable Energy Integration with Mini/Microgrids—REM 2018, Rhodes, Greece, 29–30 September 2018.
12. Kaldellis, J.K.; Tzanes, G.T.; Papapostolou, C.; Kavadias, K.; Zafirakis, D. Analyzing the Limitations of Vast Wind Energy Contribution in Remote Island Networks of the Aegean Sea Archipelagos. *Energy Procedia* **2017**, *142*, 787–792. [CrossRef]
13. Hellenic Electricity Distribution Network Operator, Issues of the Operator for the non-Interconnected Islands, Athens, Greece. 2018. Available online: https://www.deddie.gr (accessed on 17 September 2020).
14. Technology Innovation for the Local Scale Optimum Integration of Battery Energy Storage (TILOS), Horizon 2020 Program. Available online: http://tiloshorizon.eu (accessed on 17 September 2020).
15. Cabrera, P.; Lund, H.; Carta, J.A. Smart renewable energy penetration strategies on islands: The case of Gran Canaria. *Energy* **2018**, *162*, 421–443. [CrossRef]
16. Kaldellis, J.K.; Zafirakis, D.; Kavadias, K. Techno-economic comparison of energy storage systems for island autonomous electrical networks. *Renew. Sustain. Energy Rev.* **2009**, *13*, 378–392. [CrossRef]
17. Greek Public Power Corporation. *Annual Report on the Operation of Autonomous Power Stations*; Greek Public Power Corporation: Athens, Greece, 2016.
18. Kaldellis, J.K.; Zafirakis, D. Optimum Energy Storage Techniques for the Improvement of Renewable Energy Sources-Based Electricity Generation Economic Efficiency. *Energy J.* **2007**, *32*, 2295–2305. [CrossRef]
19. Kaldellis, J.K.; Zafirakis, D. Prospects and challenges for clean energy in European Islands. *The TILOS Parad. Renew. Energy* **2020**, *145*, 2489–2502. [CrossRef]
20. Moustris, K.; Kavadias, K.A.; Zafirakis, D.; Kaldellis, J.K. Medium, Short and Very Short-Term Prognosis of Load Demand for the Greek Island of Tilos Using Artificial Neural Networks and Human Thermal Comfort-Discomfort Biometeorological Data. *Renew. Energy* **2020**, *147*, 100–109. [CrossRef]
21. Zafirakis, D.; Tzanes, G.T.; Kaldellis, J.K. Forecasting of wind power generation with the use of Artificial Neural Networks and Support Vector Regression models. *Energy Procedia* **2019**, *159*, 509–514. [CrossRef]
22. Stephanides, P.; Chalvatzis, K.; Li, X.; Mantzaris, N.; Zafirakis, D. Sustainable energy solutions for the Aegean Archipelago Islands: What is the public attitude? *Energy Procedia* **2019**, *159*, 243–248. [CrossRef]

energies

MDPI

Article

An Overview of Probabilistic Dimensioning of Frequency Restoration Reserves with a Focus on the Greek Electricity Market

Anthony Papavasiliou

Center for Operations Research and Econometrics, Université Catholique de Louvain, 1348 Louvain-la-Neuve, Belgium; anthony.papavasiliou@uclouvain.be

Abstract: The dynamic dimensioning of frequency restoration reserves based on probabilistic criteria is becoming increasingly relevant in European power grid operations, following the guidelines of European legislation. This article compares dynamic dimensioning based on *k*-means clustering to static dimensioning on a case study of the Greek electricity market. It presents a model of system imbalances which aims to capture various realistic features of the stochastic behavior of imbalances, including skewed distributions, the dependencies of the imbalance distribution on various imbalance drivers, and the contributions of idiosyncratic noise to system imbalances. The imbalance model was calibrated in order to be consistent with historical reserve requirements in the Greek electricity market. The imbalance model was then employed in order to compare dynamic dimensioning based on probabilistic criteria to static dimensioning. The analysis revealed potential benefits of dynamic dimensioning for the Greek electricity market, which include a reduction in average reserve requirements and the preservation of a constant risk profile due to the adaptive nature of probabilistic dimensioning.

Keywords: reserves; *k*-means; probabilistic dimensioning; dynamic dimensioning; balancing

Citation: Papavasiliou, A. An Overview of Probabilistic Dimensioning of Frequency Restoration Reserves with a Focus on the Greek Electricity Market. *Energies* **2021**, *14*, 5719. https://doi.org/10.3390/en14185719

Academic Editor: George S. Stavrakakis

Received: 21 April 2021
Accepted: 3 September 2021
Published: 10 September 2021

Publisher's Note: MDPI stays neutral with regard to jurisdictional claims in published maps and institutional affiliations.

Copyright: © 2021 by the author. Licensee MDPI, Basel, Switzerland. This article is an open access article distributed under the terms and conditions of the Creative Commons Attribution (CC BY) license (https://creativecommons.org/licenses/by/4.0/).

1. Introduction

1.1. Context

The increasing integration of renewable energy sources and other industry drivers is increasing the uncertainty that system operators face in the daily operation of power grids [1]. Reserves are a key resource for responding to the uncertainty of system operations. Two types of uncertainty are typically faced in system operations: component failures, also referred to as contingencies, and "normal" disturbances related to forecast errors (of wind production, solar production, load, and so on), rapid variations (dispatch ramps related to market interval changes), or other "smooth" disturbances to system operations that are not related to contingencies.

Reserves can be classified into three main categories in European system operations, as a function of how fast these reserves can respond to system conditions. Frequency containment reserves (FCR) provide instantaneous responses based on variations in system frequency, and correspond to the highest-quality reserves in the system. Frequency restoration reserves correspond to resources with a full activation time of a few seconds to a few minutes. Automatic frequency restoration reserves (aFRR) respond to automatic control signals, whereas manual frequency restoration reserves (mFRR) are activated manually and are typically slower than aFRR resources. Replacement reserves (RR) have the longest full activation time in the system, and are therefore the lowest-grade reserve in European system operation. All of these reserve types respond to both contingencies and normal imbalances. The present paper is concerned with frequency restoration reserves.

The sizing of reserves is an increasingly challenging and relevant problem in system operations. This is due to the fact that system conditions vary significantly from day to day,

and these system conditions can be important indicators of the risk that the system may face for the following day of system operation. Reserves are costly, but they secure and determine the reliability of system operations; therefore, adapting the sizes of such reserves in accordance with anticipated risk is desirable. One can expect to cope during days with lower risk with fewer reserves, and during days with higher risk with more reserves. The goal of this dynamic adaptation of reserve requirements is meant to ensure a target reliability level with fewer reserves *on average*, compared to a non-adaptive reserve dimensioning method. Moreover, such dynamic adaptation of reserve requirements is expected to achieve a more constant exposure of the system to risk. Thus, the adaptive dimensioning of reserve requirements to observable system conditions is becoming increasingly relevant, both in the scientific literature and among practitioners [2].

1.2. Reserve Dimensioning Methods

Having made the case for adaptive dimensioning of reserves in power system operations, the question becomes how one can quantify these requirements in a disciplined fashion. The methods proposed in the literature can be classified into the following three levels of complexity: heuristic methods, probabilistic methods, and bottom-up unit commitment and economic dispatch models.

1.2.1. Heuristic Reserve Sizing

Heuristic sizing methods refer to sizing methods that determine the amount of reserves that a system should carry on the basis of simple system statistics. These methods have been widely employed in practice, due to their attractive simplicity. Indeed, it is the current method of choice in the Greek system. However, these methods are currently under scrutiny on account of not being able to adapt *accurately* to system conditions that can vary significantly as a function of renewable energy supply and other system indicators on which one can perform advanced analytics.

An example of a heuristic sizing method is in [3]. Section B-D5.1 on page 14 of [3] prescribes secondary reserves (formerly the term used for aFRR) as a function of the maximum consumer load for the control area. Similarly, section B-D5.3 of [3] recommends a reserve sizing criterion that can cover a large number of failure incidents.

In [4], the authors presented a number of heuristic approaches for computing additional reserve requirements due to wind integration. One such sizing approach depends on the standard deviation of hourly load and net load, and prescribe reserves that are four times the difference between the standard deviation of load and net load.

In [5], the authors predicted balancing power requirements from a set of features that included wind, photovoltaic (PV) production, load, and the day of the week. The k-nearest neighbors algorithm was then used to detect observations whose features were closest to those characterizing the real-time operation. The authors then computed a weighted sum of these k observations in order to determine reserve requirements for the following interval. In [6], the authors extended the method of [5] by considering alternative weighting methods for the k-nearest neighbors.

Another example of a heuristic sizing method based on statistical parameters is the so-called "3 + 5 rule" of the US National Renewable Energy Laboratory [7,8], which dictates that the system should carry reserves equal to 3% of the forecast load plus 5% of forecast renewable supply. The rationale of such a rule is that higher demand forecasts or higher load forecasts expose the system to greater uncertainty, and should therefore be accompanied by more reserves in the system.

1.2.2. Probabilistic Methods

Probabilistic dimensioning is intrinsically linked to loss of load probability, and is thus aligned with EU legislation—in particular, the Electricity Balancing Guideline [9] and the System Operation Guideline [10]. Since probabilistic dimensioning responds to the requirements of recent EU legislation, it is currently being implemented or considered in a

number of European markets. Belgium is an interesting case in point, where the measure is advancing towards implementation [2]. The paper therefore focuses on probabilistic dimensioning, and specifically on frequency restoration reserves.

Probabilistic methods depend largely on the assumed imbalance drivers, i.e., the factors that are assumed to influence the distribution of imbalances in the system. A wide variety of drivers can be considered [11], including load forecast errors, load noise errors, scheduling step errors (i.e., imbalances caused by transitions from one market clearing dispatch interval to the next), outages, wind forecasts, and PV forecast errors.

Another dimension in which these methods are differentiated is whether or not they can be used for the joint sizing of aFRR and mFRR (also referred to as secondary and tertiary reserves in the literature). In order to arrive at such a split, it is common to assume that specific types of imbalances should be handled by specific types of reserves. For example, secondary reserves can be sized in order to handle load noise [12]. Alternatively, tertiary reserves can be sized so as to balance 15-min-average deviations, whereas secondary reserves can be used for balancing fluctuations within a 15-min interval [13]. In [14], the authors classified sources of uncertainty as relating to 15-min intervals (and therefore resulting in the need for secondary reserves), as opposed to hourly intervals (and therefore resulting in the need for tertiary reserves).

Note that probabilistic methods can be used for sizing both upward and downward reserve capacities. In [15], tertiary reserves were sized based on the distribution of load forecast errors, wind forecast errors, PV forecast errors, and power plant outages. Upward secondary reserves were sized for plant outages and load noise, and downward secondary reserves were sized for load noise.

1.2.3. Bottom-Up Unit Commitment/Economic Dispatch Models

An alternative to heuristic and probabilistic methods is sizing based on unit commitment—economic dispatch models that endogenously represent uncertainty. Such models attempt to develop a bottom-up description of the system and trade off explicitly the increased costs of running the system more securely (e.g., due to startup and minimum load costs, or the higher fuel costs of reserve) with the increased security that the system enjoys when it carries more reserves [16]. Such models are typically not employed in practice, due to the complexity of the underlying stochastic formulation and the ensuing difficulty of solving the resulting model. They are nevertheless widely studied in the academic literature.

There are various paradigms for representing uncertainty in such bottom-up formulations. Stochastic programming formulations [8,17] represent reserve commitment decisions as first-stages decision, followed by the revelation of system uncertainty in the second stage, and an adaptive dispatch in response to the realization of uncertainty, *given* the revealed uncertainty. For certain stochastic programming formulations, reserves are represented explicitly [17]. Other formulations [18] do not model reserves explicitly; nevertheless, since these models are determining commitment decisions, they are implicitly endogenizing reserve commitment decisions.

In adaptive robust optimization formulations [19], the realization of uncertainty is chosen in an adversarial fashion from an uncertainty set, and the goal of the decision maker is to arrive to first-stage commitment decisions that are adapted to this worst-case pattern of uncertainty.

Certain bottom-up models are restricted to normal imbalances, and neglect component outages [20,21]. More advanced bottom-up models typically represent composite uncertainty (contingencies and normal imbalances) either explicitly or implicitly. Explicit modeling of uncertainty involves sampling the Cartesian products of component failures and forecast errors, often supplemented by an appropriate scenario selection methodology [22]. The implicit modeling of uncertainty involves a convolution of the outage probability of committed units with a discretization of load forecast errors [23].

1.3. The Taxonomy of Reserve Dimensioning

Based on the aforementioned discussion, one can derive a taxonomy of reserve dimensioning methods on the basis of three principal axes:

- **Sizing methodology:** The sizing methodology refers to how the decision-making problem of sizing reserves is quantified. The three predominant approaches in this respect that were listed in Section 1.2 are heuristic methods, probabilistic methods, and bottom-up unit commitment and economic dispatch models.
- **Adaptiveness**: Adaptiveness refers to whether the sizing methodology is adaptive to the forecast conditions of the system or not. Two options in this respect are static sizing and dynamic sizing.
- **Stochastic models**: This dimension refers to the way in which uncertainty is modeled. Two options are possible among stochastic models: parametric or non-parametric.

This classification is summarized in Table 1 with respect to the literature that was covered in the introduction of the present publication. The goal of the table is to provide a convenient lookup that can be useful for practitioners navigating among the range of options that can be considered for implementation in system operations. For instance, a probabilistic dynamic dimensioning methodology based on parametric uncertainty models has been considered for implementation in the Belgian electricity market [2]. The performance of this reserve dimensioning method is assessed in the context of the Greek electricity market in the present paper.

1.4. Contributions and Outline of the Paper

The taxonomy that is presented in Table 1 presents a wide range of options for dimensioning reserves, with a delicate tradeoff between simplicity of implementation and benefits derived from adaptive dimensioning. This tradeoff is discussed abstractly in Section 1.2 and it is investigated in the context of the Greek electricity market in the remainder of the present publication.

An important consideration in the quantitative investigation of this tradeoff is the absence of imbalance data. Concretely, system imbalances exhibits a number of features that drive the relevance of dynamic dimensioning. These features include (i) the simultaneous influences of normal imbalances and contingencies on total system imbalance, (ii) the important contribution of idiosyncratic noise to total system imbalance, (iii) the dependence of system imbalance on observable system conditions such as load and renewable energy forecasts with specific empirical patterns (e.g., high load forecasts often imply large imbalances), and (iv) the skewed distribution of forecast errors when forecasts are near the nominal rating of a certain resource. In lieu of system imbalance data, the present paper proposes a stochastic model that meets the aforementioned set of requirements.

To summarize, therefore, the contributions of the paper are as follows: (i) A stochastic model of system imbalances is proposed which can be employed in the absence of available historical data for system imbalances. The model can be calibrated against historical data of reserve requirements. (ii) The added value of dynamic probabilistic reserve dimensioning relative to static dimensioning was established for the Greek electricity market based on an out-of-sample simulation. This added value was exhibited both in terms of lower average reserve requirements and a more constant risk profile for the system throughout the year.

The paper is structured as follows. Section 2 summarizes certain relevant features of the reserve dimensioning methodology employed in the Greek electricity market before and after the implementation of the November 2020 reforms pertaining to the implementation of the target model. Section 3 proposes an imbalance model that captures salient features of system imbalances that can be used in lieu of available system imbalance data. Section 4 summarizes the application of k-means clustering to the dynamic probabilistic dimensioning of reserves, which was employed in the case study of Section 5.

Table 1. A classification of reserve sizing literature.

	Heuristic	Probabilistic	UC/ED	Static	Dynamic	Parametric pdfs	Non-Parametric pdfs
[24]							X
[25]							X
[19]			X		X		
[26]					X	X	
[12]		X			X		
[18]			X	X			
[16]			X		X		
[7]	X		X		X		
[3]	X			X			
[27]		X		X			
[23]		X	X	X			X
[4]	X				X		
[28]					X		X
[11]		X			X		X
[29]		X			X		X
[30]							X
[15]		X			X		
[14]		X		X		X	
[31]	X				X	X	
[32]		X			X	X	
[13]		X			X	X	
[17]			X		X		
[33]							X
[20]	X		X		X	X	
[5]	X				X		
[6]	X				X		
[1]			X		X		
[22]			X		X		
[34]		X		X			
[2]		X			X		X
[35]			X		X		
[36]						X	X
[21]			X		X		X
[37]							X

2. Sizing Methodology in the Greek Electricity Market

The present publication is focused on a case study of the Greek electricity market. In November 2020, the target model methodology was implemented in the Greek electricity

market. The present section provides an overview of the evolution of reserve requirements in the Greek electricity market before and after November 2020.

2.1. Sizing before the Target Model

Figure 1 describes representative reserve requirements of the Greek electricity market for January 2018–October 2020. The data were sourced from the following website of the Hellenic Energy Exchange, which was accessed on 20 August 2021: https://www.enexgroup.gr/el/day-ahead-scheduling-archive of the Hellenic Energy Exchange. In addition to reserve requirement data, the website includes the day-ahead schedules of individual units; hourly energy production schedules; and commitments of FCR, aFRR, and mFRR for individual units in the Greek system. The figure concentrates on FRR, i.e., the sum of mFRR and aFRR, since the sizing of FCR follows a separate procedure and is out of scope for the present analysis. Note that the mFRR requirements on the aforementioned website are assumed to correspond to both upward and downward reserves.

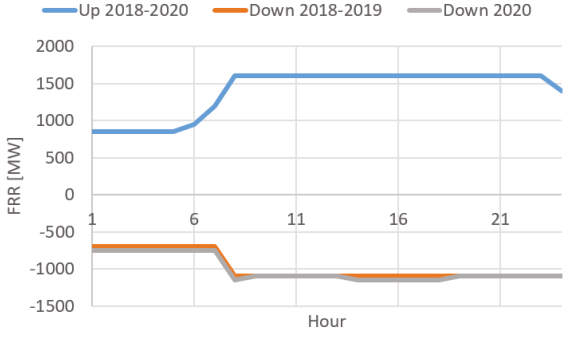

Figure 1. Representative reserve sizing values for upward/downward capacity in the Greek electricity market in 2018–2020.

The splitting of FRR between mFRR and aFRR was considered as being out of scope for the present analysis, although a number of publications [11–13,15,29,34,38] have considered this important design question. On the other hand, downward sizing was considered in the analysis, and representative values are presented in Figure 1.

It is worth noting that the FCR, upward aFRR, and mFRR requirements have remained fairly constant in Greece throughout January 2018–October 2020. In the figure, there is a slight change in the requirement of 2020 for downward aFRR, which increases slightly (by 50 MW) in hours 1–8 and 14–18. Furthermore, note that the downward aFRR requirements are notably lower than the upward aFRR requirements, which is typically due to the asymmetric exposure of the system to contingencies.

2.2. Target Model Methodology

The existing reserve sizing procedure that is employed by the Greek Transmission System Operator (TSO), ADMIE, was approved by decision 1092/2020 of the Regulatory Authority for Energy and corresponds to the Target Model of the Greek electricity market. The procedure is laid out by ADMIE in [39], which can be accessed in the following link, which was accessed on 20 August 2021: https://perso.uclouvain.be/anthony.papavasiliou/public_html/ADMIE2020V2.pdf. As discussed previously, the methodology became effective in November 2020.

ADMIE, like other European TSOs, distinguishes between "normal imbalances" (e.g., forecast errors) which need to be dealt with by aFRR and mFRR, and contingencies, which need to be dealt with by FCR and FRR. Thus, ADMIE follows a dynamic sizing procedure based on heuristics related to the statistical parameters of system characteristics.

The existing sizing procedure adopted in the Greek electricity market for upward/downward aFRR is driven by

- The minimum FRR requirement (which in itself is a function of maximum load in the system);
- A constant corresponding to the technical minimum of a typical thermal unit (meant to capture the possibility that a unit is asked to turn on but fails to do so);
- The scheduled interchange;
- The scheduled demand.

The way in which one distinguishes the sizing for upward and downward aFRR in these cases is driven by the differences between the coefficients that are used for how each of these factors is assumed to contribute to the total aFRR requirement [39].

Similarly (but not identically) to aFRR, the existing sizing procedure for upward/downward mFRR is driven by:

- Upward/downward aFRR;
- Renewable forecasts;
- Demand ramps;
- Scheduled interchanges;
- An indicator for extreme conditions (indicatively, unfavorable weather, large renewable forecast deviations, reduced adequacy, contingencies, strikes, reduced fuel reserves for thermal units, low hydro energy levels, or a combination of the above).

3. Model of Imbalances in the Greek System

Due to the absence of publicly accessible real-time imbalance data for the Greek market, in this section a simplified model is proposed, which aims to serve as the basis for the case study of the probabilistic dimensioning methodology. Note that this imbalance model is not meant to be realistic, but rather to convey certain first principles. On the other hand, the probabilistic dimensioning methodology does not depend on this imbalance model, and can be applied directly to historical data.

3.1. Modeling Imbalances

The following data have been provided by the Regulatory Authority for Energy:

- Load data with hourly resolution from 1 January 2018 until 31 October 2020, thereby spanning 2 years and 10 months (namely, 1035 days).
- Renewable energy supply data with the same characteristics.
- Import/export data with the same characteristics.

Additionally, the day-ahead commitments of individual units is accessible at the following link of the Hellenic Energy Exchange, which was accessed on 20 August 2021: https://www.enexgroup.gr/el/day-ahead-scheduling-archive. Notably, however, historical *real-time* imbalance data for the Greek system is not publicly available. As an alternative, an imbalance model is proposed here.

When developing the imbalance model, a number of features that affect reserve dimensioning were targeted:

- Imbalances are driven by both contingencies and "normal" imbalance drivers, such as forecast errors.
- Imbalances can be explained by a number of factors in the system, such as renewable energy forecasts, load forecasts, and scheduled imports. These factors are referred to as *imbalance drivers*. Other imbalance drivers may include the change of the hour (due to market ramps), temperature, and so on. Higher forecasts tend to result in higher imbalances.
- On the other hand, a significant portion of the system imbalance signal may not be possible to explain based on imbalance drivers. Past analyses of the Belgian system [2] have shown that approximately half of the imbalance signal may not be attributable to

imbalance drivers. It is assumed that this portion of the imbalances can be represented by white noise.
- Imbalance drivers do not have symmetric distributions in the upward and downward directions. For example, high renewable supply forecasts are more likely to lead to significant negative imbalances (under-supply) and low positive imbalances (over-supply) since the renewable supply will mostly decrease during periods of high output.

The imbalance model is thus based on the following methodology. The proposed methodology attempts to strike a balance between data availability and a desire to capture empirically relevant effects that drive reserve dimensioning decisions [2]:

- Use representative "day types" to model contingency risk in the system. The idea is presented in Section 3.2.
- Use imbalance drivers (load, RES and imports) to model factors that contribute to the system imbalance based on skewed distributions, the variance of which depends on the imbalance drivers. The idea is presented in Section 3.3.
- Use "white noise" to model the part of the imbalance signal that cannot be explained by imbalance drivers. The idea is presented in Section 3.4.
- Tune the parameters of the model so that the resulting imbalance is consistent with the reliability achieved by the reserve dimensioning that is employed in the Greek market. The idea is presented in Section 3.5.
- The baseline dimensioning methodology is then compared to the probabilistic dimensioning methods that are described in Section 4.

In the sequel, "normal imbalances" refer to the sum of imbalances related to imbalance drivers and idiosyncratic imbalances. These should be contrasted to imbalances resulting from contingencies.

3.2. Contingencies

In order to represent the risks of generator failure, eight representative day types (one for each season, and weekdays versus weekends) were considered. For each of these day types, generator schedules were fixed to historically observed data. The following day types were considered for 2018:

- Winter weekday: 15 January 2018
- Winter weekend: 7 January 2018
- Spring weekday: 8 March 2018
- Spring weekend: 11 March 2018
- Summer weekday: 7 June 2018
- Summer weekend: 10 June 2018
- Fall weekday: 6 September 2018
- Fall weekend: 9 September 2018

Alternatively, one could have considered a clustering method for determining different day types, or one could have worked directly with each day of the dataset. The latter option was not possible for us, due to IT difficulties, given the format in which the data became available by RAE, and could be investigated further in future work.

A failure probability of one incident per year was considered. It was further assumed that each failure corresponded to four imbalance intervals (i.e., the time to clear the fault by repairing the unit or bringing online another unit was assumed to be one hour). This assumption is an intermediate choice between the values that were assumed in previous analyses of the Belgian and Swedish systems.

Contingencies are assumed to occur independently of normal imbalances and idiosyncratic imbalances. This allows sampling contingencies independently from one period to the next. Concretely, since there are no inter-temporal constraints in the model, one can assume that the contingencies are sampled for each balanced market time unit, without worrying that a failure will last for four consecutive 15-min imbalance intervals.

There are 28 thermal units and 18 hydro units in the system, and 4 pumping units. Failures between these components were assumed to be independent of each other.

3.3. Imbalance Drivers

Regarding the modeling of normal imbalances, the goal is to specifically capture two effects: higher forecasts are correlated with higher forecast errors, and the support of the probability density function depends on the imbalance driver. The latter effect introduces skewness to the probability density functions of imbalances for reasons that are explained below.

Regarding modeling the first effect, a simple assumption is adopted. Imbalances are specifically assumed to follow a normal distribution with a mean of 0 MW and a standard deviation of $C \cdot |L|$ (for load forecast errors), $C \cdot |R|$ (for renewable supply forecast errors), and $C \cdot |I|$ (for import forecast errors), where L is the system load, R is the renewable energy supply, and I represents the imports. The idea is to adapt the constant C such that the average sizing value of Figure 1 achieves the target unreliability of 3 h per year. Note that this simple modeling assumption captures the effect whereby higher load forecasts/renewable supply forecasts/import forecasts imply larger imbalances.

Regarding skewness, the chosen modeling assumption is driven by the fact that load, renewable supply, and imports are lower and upper bounded. Concretely, based on the data provided by RAE, it is possible to estimate the following values:

- The minimum load in the dataset is 2840 MW; the maximum load is 9529 MW.
- The minimum renewable supply within the dataset is 103 MW; the maximum renewable supply is 4245 MW.
- The minimum amount imported was −1428 MW (i.e., the maximum amount that has been *exported* historically is 1428 MW); the maximum amount imported was 2041 MW (i.e., the maximum amount that has been *imported* historically is 2041 MW).

These bounds imply a skewness in the distribution of the imbalances caused by these drivers. This idea is explained concretely in Figure 2. The left panel of this figure presents the probability distribution function of an imbalance driven by renewable supply, which is symmetrical. The vertical line in the left panel corresponds to the installed capacity of renewable generation. Since the total renewable supply, which is the sum of the day-ahead forecast supply and the renewable supply imbalance, cannot exceed the installed renewable capacity, a model that captures this physical feature is proposed. When simulating imbalances driven by renewable supply forecast errors, it was assumed that the supply "bounced back"/was reflected on the wall of the vertical line of the left panel of Figure 2. As a result, we arrived at the probability density function of the right panel of Figure 2. Note that, whereas we commenced with a probability density function with zero skewness in the left panel, a skewed probability density function was derived in the right panel.

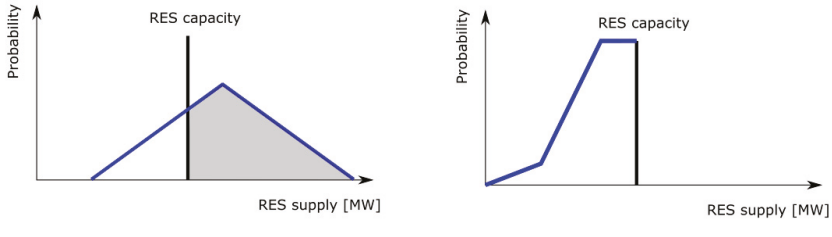

Figure 2. Left panel: Hypothetical probability distribution function of renewable supply (RES-driven imbalance plus the underlying imbalance driver) which exceeds installed RES capacity. **Right** panel: Probability distribution function of renewable supply which reflects on the installed capacity boundary.

The effect of Figure 2 was modeled by drawing the original imbalance from a normal distribution, as indicated in the beginning of this section. This process was then "reflected" against the lower and upper bounds of the load/renewable supply/imports to derive the final simulated imbalance value.

This modeling feature attempts to capture an effect that has been observed to be empirically relevant in the sizing of reserves, e.g., in Belgium [2]: upward and downward imbalances are skewed, and depend on imbalance drivers. As a concrete example, large renewable forecasts pose a significant threat for negative imbalances, and a minor threat for positive imbalances.

To summarize, imbalances that are driven by imbalance drivers are generated as follows:

$$Imb = \begin{cases} 2 \cdot X^- - X - C \cdot |X| \cdot N, & C \cdot |X| \cdot N + X < X^- \\ C \cdot |X| \cdot N, & X^- \leq C \cdot |X| \cdot N + X \leq X^+ \\ 2 \cdot X^+ - X - C \cdot |X| \cdot N, & C \cdot |X| \cdot N + X > X^+ \end{cases}$$

where X denotes the value of the imbalance driver, X^- and X^+ correspond to its minimum and maximum possible values, respectively; C is a tunable parameter that is used in Section 3.5 in order to tune the level of uncertainty in the system; and N is a standard normal random variable. Note that $C \cdot |X| \cdot N + X$ corresponds to the signal before reflection on the barrier. The three cases above correspond to this signal landing below the lower barrier, within the lower and upper barrier, and above the upper barrier, respectively. The above formulas for the first and third case can then be derived by exploiting the fact that the reflected signal is equidistant to the barrier as the signal before reflection, but on the opposite side of the barrier.

Note that the imbalances that can be attributed to imbalance drivers are assumed to be independent of each other and of the imbalances related to contingencies. Thus, random variables N are drawn independently for each of the imbalance drivers.

3.4. Idiosyncratic Noise

Our motivation for introducing an idiosyncratic component to the total imbalance signal was based on the implementation of dynamic dimensioning in Belgium [2]. In that work, it was observed that a significant portion of the imbalance signal could not be explained by imbalance drivers, such as renewable supply, load, import, and market ramps. This can be interpreted as a "white noise" component to the imbalance signal which cannot be specifically attributed to observable information in the system.

Concretely, idiosyncratic noise is modeled as normal random variables that are drawn independently of the imbalances related to imbalance drivers:

$$Imb = C \cdot D \cdot N \tag{1}$$

where C is the tunable parameter introduced in Section 3.3 and D is a parameter that must be estimated so as to ensure that the idiosyncratic imbalances represent a realistic fraction of the normal imbalance signal.

In order to decide on the variance of the idiosyncratic noise, i.e., on the parameter D, note that the goal was for the idiosyncratic noise to represent 40% of the normal imbalance signal. The choice of 40% was based on empirical observations of the contribution of idiosyncratic noise on total system imbalance in the Belgian system [2]. Concretely, the variance of idiosyncratic imbalances should correspond to approximately 40% of the variance of normal imbalances. This can be expressed mathematically as follows,

where T is the number of periods that are considered in the data set of available import/load/renewable forecasts:

$$T \cdot C^2 \cdot D^2 = 0.4 \cdot (\sum_{t=1}^{T} C^2 \cdot (|I|_t^2 + |L|_t^2 + |R|_t^2) + T \cdot C^2 \cdot D^2) \quad (2)$$

$$\Rightarrow D = \sqrt{\frac{0.4 \cdot \sum_{t=1}^{T} (|I|_t^2 + |L|_t^2 + |R|_t^2)}{0.6 \cdot T}} \quad (3)$$

Equation (2) is a consequence of the fact that the variance of the sum of independent random variables is equal to the sum of the variance of the variables. Equation (3) then provides the appropriate value of parameter D that results in idiosyncratic imbalances contributing to 40% of the normal imbalances in the system.

3.5. Matching the Model to a Static Sizing Methodology

The next step in the proposed methodology is to tune the parameter C which was introduced in Section 3 such that the sizing indicated in Figure 1 matches the reliability target of 3 h per year. The idea is to scale the normal imbalances according to the parameter C, and to perform a bisection until one finds a level of imbalance for which 3 h of failures occur per year. Note that these 3 h include failures from imbalances in both upward *and* downward directions.

The appropriate value of C given the available data was found to be 0.0384. Note that Figure 1 presents a best-case scenario, since the observed reliability is exactly matched with that of the target level of 3 h per year. Hence, there is no redundant capacity (the observed reliability is not below 3 h per year), and the reliability target is also respected (the observed reliability is not above 3 h per year).

Further, note that this "training" data have been generated with a fixed seed. It is then possible to generate test data from the same imbalance drivers but different realizations of the imbalances themselves, which was the methodology that adopted for Section 5.

It is interesting to note that among the 34 incidents that are recorded in the training dataset, 4 are related to shortages in upward balancing capacity, and 30 to shortages in downward balancing capacity. Moreover, note that none of the incidents were caused by a contingency. Among these, 11 incidents correspond to 2018 (2 upward and 9 downward), 18 incidents correspond to 2019 (2 upward and 16 downward), and 5 incidents correspond to 2020. Thus, the reliability target was upheld over the 2 years and 10 months of the simulation, even if reliability in certain years may have been higher than the target and in other years lower than the target. By contrast, a probabilistic dimensioning methodology can achieve a relatively constant risk profile, as described in Section 5.

4. Probabilistic Dimensioning Methodology

This section presents a methodology that has been considered for the implementation of probabilistic dimensioning in the Belgian system [2]. This method is then compared to the dimensioning of Figure 1 in Section 5.

4.1. Overview of k-Means Clustering Applied to Probabilistic Dimensioning

The k-means approach for probabilistic dimensioning is based on [38] and is also one of the methods that was proposed for implementation in the Belgian system [2]. The k-means problem is a clustering problem which aims to cluster a dataset into k groups, such that the sums of the distances of the original data from the means of the nearest clusters are minimized. The problem is computationally hard, since one in principle needs to consider all possible ways in which the original dataset can be clustered, and select the configuration that minimizes the sum of distances of cluster elements from the cluster means. The intuition of the clustering method is that the distance of a cluster element from the mean is a measure of similarity of the data points. Thus, minimizing the sum of distances implies grouping the data such that each group contains maximally similar data.

In the context of the application considered in the present paper, the data points that were clustered were the imbalance drivers, namely, day-ahead load forecasts, day-ahead scheduled imports, and day-ahead renewable supply forecasts. The idea is that each cluster corresponds to the same day type which, when observed one day in advance of operations, can provide refined information about the distribution of normal imbalances. Thus, if the imbalance drivers indicate a risky day of operations (e.g., due to high load forecasts which imply high load forecast errors), then the reserve sizing can adapt to this information by committing fewer reserves for the following day. Conversely, if a low-risk day is anticipated, then the system can resort to fewer reserves without compromising system reliability, which implies economic savings for the TSO.

4.2. Implementation of Probabilistic Dimensioning Based on k-Means

In order to implement the *k*-means probabilistic dimensioning method with contingencies, the following steps are required:

- Step 1: Cluster imbalance drivers in order to determine the day types.
- Step 2: Approximate imbalances, e.g., using kernel density estimation or the empirical distribution of the data.
- Step 3: Determine the reserve requirement of each day type from the appropriate quantile of the distribution computed in step 2.

Step 1: determination of day types.

In the analysis, clustering was performed in three dimensions, namely, forecast load, forecast renewable supply, and forecast imports. Each of these data inputs was clustered into two values. This gave eight types of days: (high load, high wind, high solar), . . ., (low load, low wind, low solar). Regarding the interactions of the method with contingencies, note that the preliminary analysis of Section 3.5 indicates that observed incidents are ones in which the system experiences a large normal imbalance, even if there is no contingency. We therefore chose to work with 8 day types, as determined by imbalance drivers, instead of further differentiating day types as a function of how generators are committed in the system on the day ahead.

It is interesting to note that the most commonly used *k*-means algorithms are inherently non-deterministic. For example, Loyd's algorithm [40] is initialized with a random selection of points which act as centroids. Initializing with *k*means++ [41] also involves a random selection of points at the first step of the initialization procedure. The clustering was therefore replicated ten times, and the solution with the best performance was kept. The consistency of the result was validated in the present analysis by repeating the sizing three times. The reserve dimensioning decisions in each run were identical, and are presented in Table 2.

Step 2: estimation of imbalance distribution.

Once clusters of imbalance drivers have been defined, it is possible to observe the imbalance that materializes in the corresponding imbalance period. Kernel density estimation (KDE) can be used for the estimation of the distribution within each cluster, or simply the empirical probability density function obtained from the observations within each cluster, assuming that a sufficient number of points within the cluster are observed. For each cluster, a different reserve target was estimated, based on the target reliability level. This produced the results of Table 2.

Step 3: probabilistic reserve requirement.

In this step, the appropriate quantiles of the distributions obtained in step 2 were used in order to determine upward and downward reserve requirements. The same procedure was followed, in order to make the results consistent with the sizing of Figure 1:

- The upward capacity requirement of Figure 1 served all but 4/99,360 incidents, as noted in Section 3.5.

- The downward capacity requirement of Figure 1 served all but 30/99,360 incidents, as noted in Section 3.5.

The results are presented in Table 2. A number of effects that are consistent with intuition can be observed: (i) Downward reserve requirements are lower than upward reserve requirements for a given day type, due to the asymmetric risk of contingencies in upward requirements. (ii) Higher load implies higher reserve requirements. (iii) Higher renewable supply implies higher reserve requirements. (iv) Higher imports imply higher reserve requirements. (v) The effect of load on reserve requirements is the strongest; the effect of imports on reserve requirements is the least strong.

Table 2. Reserve requirement for each type of day. All quantities are in MW.

Load	Renewables	Imports	Reserve Up	Reserve Down
6810 (H)	2091 (H)	1331 (H)	1383	1085
6810 (H)	2091 (H)	471 (L)	1282	1043
6810 (H)	782 (L)	1331 (H)	1119	1028
6810 (H)	782 (L)	471 (L)	1187	919
4886 (L)	2091 (H)	1331 (H)	981	855
4886 (L)	2091 (H)	471 (L)	912	845
4886 (L)	782 (L)	1331 (H)	991	802
4886 (L)	782 (L)	471 (L)	970	737

5. Case Study of Probabilistic Dimensioning

This section compares the dimensioning of Figure 1 to the probabilistic dimensioning method based on *k*-means.

5.1. Case Study Description

As indicated previously in the article, system imbalance data have not been made available for this study. Instead, we employed other data that are publicly available at the websites of the Greek market operator and the Greek transmission system operator, and data provided by the Greek regulatory authority for energy, in order to calibrate a *model* of system imbalances which captures salient system characteristics, as indicated in Section 3. The specific input data used for the analysis are briefly recalled below.

Reserve requirement data for the Greek system for 2018–2020 were sourced from the following link of the Hellenic Energy Exchange, which was accessed on 20 August 2021: https://www.enexgroup.gr/el/day-ahead-scheduling-archive. In addition to reserve requirement data, the website includes the day-ahead schedules of individual units, and a number of other scheduling results related to dispatch and reserve provision.

Additionally, the following data have been provided by the Regulatory Authority for Energy:

- Load data with hourly resolution from 1 January 2018 until 31 October 2020, thus spanning 2 years and 10 months (namely, 1035 days).
- Renewable energy supply data with the same characteristics.
- Import/export data with the same characteristics.

The results are presented in Tables 3 and 4. For each sizing policy, the following metrics are reported for both the upward and downward direction in Table 3:

- Average reserves committed, measured in MW.
- Unreliability: a measure of how many incidents of oversupply or undersupply occur per year, measured in hours per year. This corresponds to the loss of load expectation (LOLE) measure in reliability studies, but is here measured in both the case of upward and downward imbalances.

- Shortage or oversupply, measured in MWh/year. This corresponds to expected energy not served in adequacy studies, but is also measured in the downward direction (in the sense of quantity of energy oversupplied).

Moreover, Table 4 reports the relative contribution of each day type to the overall failure profile of each reserve sizing policy. This is explained further in Section 5.3.

Table 3. Comparative results of the probabilistic dimensioning against the sizing of Figure 1.

	Figure 1	**Probabilistic**
Res-Up (MW)	1392	1111
Unrel.-Up (hours/y)	0.3	0.4
Shortage (MWh/y)	40.2	21.5
Res-Down (MW)	993	950
Unrel.-Down (hours/y)	2.8	1.9
Oversupply (MWh/y)	208.4	159.1

Table 4. Number of intervals belonging to each cluster of the probabilistic dimensioning method and corresponding number of incidents within each cluster.

Interval Type	**No. Occurrences**	**Fails Prob. (h/yr)**	**Fails Figure 1 (h/yr)**
LoH-ReH-ImH	13,292 (13.4%)	0.44 (18.5%)	0.44 (14.3%)
LoH-ReH-ImL	9644 (9.7%)	0.09 (3.7%)	0.09 (2.9%)
LoH-ReL-ImH	12,144 (12.2%)	0.09 (3.7%)	0.26 (8.6%)
LoH-ReL-ImL	10,812 (10.9%)	0.53 (22.2%)	0.09 (2.9%)
LoL-ReH-ImH	7960 (8.0%)	0.26 (11.1%)	0.18 (5.7%)
LoL-ReH-ImL	6952 (7.0%)	0.09 (3.7%)	0.09 (2.9%)
LoL-ReL-ImH	26,296 (26.5%)	0.53 (22.2%)	1.59 (51.4%)
LoL-ReL-ImL	12,260 (12.3%)	0.35 (14.8%)	0.35 (11.4%)

5.2. Reserve Requirements

With respect to the reserves committed by the compared sizing methods, one can observe that the probabilistic dimensioning approach achieved a significant improvement in the upward dimensioning requirement, with average upward reserves being reduced by 281 MW, or 20.2% of the average upward requirement of Figure 1. Similarly, the downward dimensioning decreased by 43 MW, or 4.3%, which is less than the savings of the upward dimensioning, but still notable.

In terms of reliability performance, it can be observed that the sizing of Figure 1 remained close to the failure target of 3 h/year. The probabilistic dimensioning resulted in total failures of 2.3 h/year, thereby staying below the reliability target of 3 h/year. The MWh of shortage and oversupply were correspondingly lower values in the case of the probabilistic dimensioning method. Thus, the probabilistic dimensioning method was more reliable, while also relying on less reserves.

The results presented in Table 3 are based on an out-of-sample simulation, in the sense that an entirely new sample of 99,360 imbalance intervals (2 years and 10 months) was generated, based on the imbalance driver data that were provided by the regulatory authority, and based on the imbalance model that was developed in Section 3.

5.3. Risk Profile

Table 4 presents the numbers of intervals that belong to the clusters of the probabilistic dimensioning method. These are equal in both the training and the testing phase, since the same day-ahead data were used for both training and testing. The table additionally presents the number of failures that occurred in each day type in the testing phase, for both the sizing of Figure 1 and the probabilistic dimensioning. This serves as a measure of the risk assumed by each of the methods.

An indication of the extent to which a sizing method is able to maintain a constant level of risk is how well the observed out-of-sample risk of the method is able to track the frequency of each interval type. This assessment is shown in Figure 3. The horizontal axis of the figure represents the eight day types/clusters that were considered in the analysis. The blue curve corresponds to the empirical frequencies of occurrence of the eight day types in the out-of-sample simulation. For instance, for day type "HHH" (the first day type), the blue curve demonstrates that it occurred 13.4% of the time. The orange curve then depicts the relative contributions of failures in these day types to the total failures for the probabilistic sizing method. For day type "HHH", reading off of the orange curve implies that failures in this day type contributed to 18.5% of the total failures of the probabilistic sizing method. Similarly, the gray curve provides the corresponding figure for the sizing method of Figure 1. Reading again off of the figure for day type "HHH", it can be observed that failures in this day type correspond to 14.3% of the total failures of this reserve sizing method.

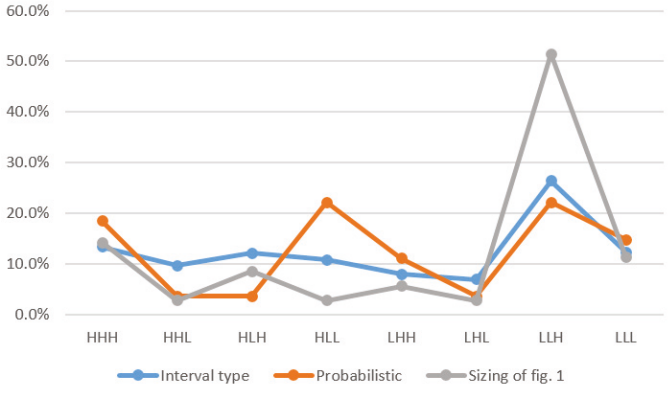

Figure 3. Frequency of each interval type, and frequency of failures for the probabilistic dimensioning method and the sizing of Figure 1.

One can observe in Table 4 that, although interval type 7 (low load, low renewable supply, large amount imported) corresponds to 26.5% of the intervals in the data sample, the sizing method of Figure 1 exhibits a frequency of failures in the seventh interval type, which is twice as high as the frequency of this interval type. This indicates that a fixed reserve requirement corresponding to Figure 1 tends to be undersized for this specific interval type (which corresponds to a quarter of the time).

Figure 3 represents the percentages of Table 3 visually. The closer the curves remain to the blue curve, the more consistent they are in terms of maintaining a constant risk. Deviating too far above the blue curve indicates an exposure to a disproportionately high risk (i.e., undersizing), and deviating too far below the blue curve indicates an exposure to a disproportionately low risk (i.e., oversizing). It is clear that the probabilistic dimensioning method was able to remain closer to the blue curve, thereby indicating an improved risk profile relative to the sizing of Figure 1. Similar results emerged with the probabilistic dimensioning method that was employed in Belgium [2].

5.4. Integration with System Operations

An alternative way to approach the simulation could be to implement it in a rolling fashion, in the sense of training a sizing model once a year, based on the data of the past year. One would then use the trained clustering algorithm one day in advance of operations in order to determine the cluster in which the following day belongs, so as to then decide on the reserve capacity that should be procured for the day ahead. This is the approach that has been proposed and considered for implementation in the Belgian

system [2]. The timeline of this rolling procedure is depicted in Figure 4, which is similar in spirit to [2].

The figure outlines a rolling procedure, where training takes place once a year, six months in advance of the beginning of the relevant year of operation. The clustering of days into day types takes place in the "*k*-means clustering" box. These clusters are then used for deriving reserve requirements for different day types according to probabilistic criteria in the "Probabilistic reserve sizing" box. This allows the system operator to have at hand a mapping of day types to upward and downward reserve requirements. On the day ahead of operation (indicated in the figure as the gray "Day ahead" box), the system operator can identify the day type that is anticipated for the following day based on the observable day-ahead explanatory factors (renewable supply forecasts, load forecasts, and import forecasts in the case of the present publication). Once the day type of the coming day is identified, the pre-computed mapping of the day type to the corresponding probability distribution and thus the appropriate quantile which implies the reserve requirement for the following day can be determined. The sizing result can then be used as input for the day-ahead procurement of reserve capacity, which may take place before, simultaneously with, or after the day-ahead procurement of energy. The Greek market specifically operates an integrated scheduling process (ISP), where reserves are committed on a daily basis (with three runs of ISP, on the day ahead and two intraday adjustment runs). The proposed probabilistic dimensioning procedure would then generate input for this ISP procedure.

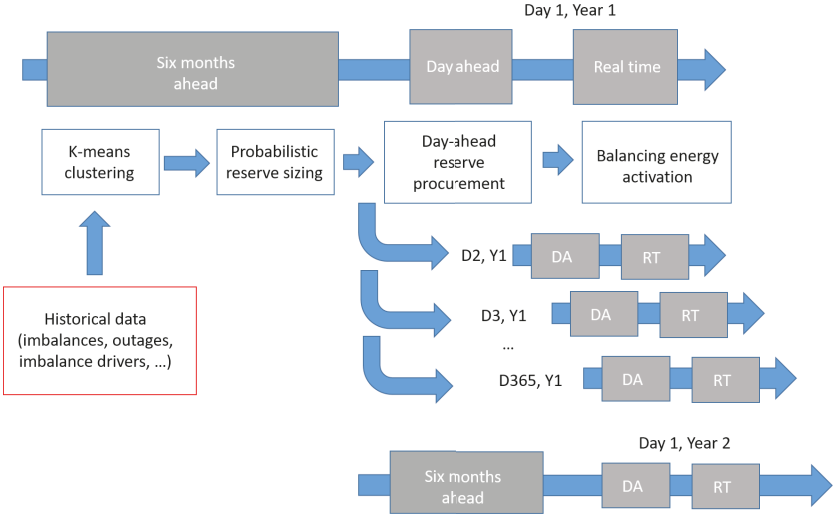

Figure 4. Timeline of a probabilistic dimensioning procedure, where the training of the probabilistic dimensioning algorithm takes place once a year based on the data of the previous year.

An important attribute of this process relates to regulatory approval. Reserve requirements proposed by the TSO are typically approved by the competent national regulatory authority on an annual basis. Since reserve requirements vary on a daily basis according to the above procedure, what would be required in the proposed implementation would be the regulatory approval of the proposed *methodology*, instead of the MW requirement itself [2].

Note that the procedure described above and investigated in this paper can be improved in a number of ways. The analysis would clearly benefit from the presence of real system imbalance data. The levels of detail of the analysis could have been improved by considering the generator availability of each day of the year, instead of the eight days indicated in Section 3.2. Alternative probabilistic methods are also worth considering in

future work, with common alternatives considered in the literature including *k*-nearest neighbors clustering [2] and quantile regression based on artificial neural networks [28], although the latter has been found to perform poorly in small systems where contingencies dominate sizing decisions. An crucial extension from a practical standpoint is the careful analysis of various alternatives for joint dimensioning of aFRR and mFRR capacity, and the consideration of transmission constraints which pertain to reserve deliverability [42]. The author is currently working on those two extensions, and preliminary results have been presented in [43].

6. Conclusions

Probabilistic dimensioning is becoming increasingly relevant in European systems, due to the spirit of EU law—in particular, the System Operation Guideline [10] and the Electricity Balancing Guideline [44]—which places loss of load probability as the cornerstone criterion of reserve sizing. This paper specifically considered the reserve dimensioning method that is advancing towards implementation in the Belgian electricity market, and examined its possible application in the Greek electricity system.

The initial investigation presented in this paper suggests that probabilistic dimensioning may merit further investigation for the Greek electricity system. Significant potential savings were uncovered in the sizing of upward frequency restoration capacity, and notable savings in the sizing of downward balancing capacity. These savings resulted from the fact that the system can adapt its sizing to the anticipated day type: days with higher risk can be planned with more reserves at hand, but days with lower risk can be planned with less reserves, with the end result being that the *average* reserves are reduced throughout the year. The adaptive nature of the sizing of the reserve requirement also allows the system to operate at a more constant level of risk. This should be contrasted with a static sizing method, where days with less favorable conditions expose the system to greater risk, and during days with more favorable conditions the system is over-protected and carries unnecessarily high reserves.

In order to conduct the analysis, and in the absence of system imbalance data, the paper proposed a stochastic model of imbalances which captures a number of salient features which render dynamic dimensioning relevant. These features include skewed distributions, the dependencies of the imbalance distribution on the levels of various imbalance drivers, and the contribution of idiosyncratic noise to system imbalances.

Additionally, the literature review provides a lookup table that can be useful for practitioners navigating among the range of options that can be considered for implementation in system operations. The classification of the literature was performed using three axes, including the analytical method that can be used for dimensioning (heuristics, probabilistic dimensioning, or bottom-up models), static versus dynamic dimensioning, and whether the proposed method relies on a parametric or non-parametric model of uncertainty.

The procedure described in the paper can be improved in a number of way. An extension that is crucial from a practical standpoint is the application of probabilistic dimensioning to the joint dimensioning of aFRR and mFRR capacity, which goes beyond the current state of the art [11–13,15,29,34,38]. Transmission constraints which pertain to reserve deliverability will also need to be considered [42].

Funding: This research has been supported by the Hellenic Regulatory Authority for Energy.

Institutional Review Board Statement: Not applicable.

Informed Consent Statement: Not applicable.

Conflicts of Interest: The author declare no conflict of interest.

References

1. Papavasiliou, A.; Oren, S.S.; O'Neill, R.P. Reserve requirements for wind power integration: A scenario-based stochastic programming framework. *IEEE Trans. Power Syst.* **2011**, *26*, 2197–2206. [CrossRef]
2. De-Vos, K.; Stevens, N.; Devolder, O.; Papavasiliou, A.; Hebb, B.; Matthys-Donnadieu, J. Dynamic Dimensioning Approach for Operating Reserves: Proof of Concept in Belgium. *Energy Policy* **2019**, *124*, 272–285. [CrossRef]
3. ENTSO-E. Load-Frequency Control and Performance. In *Continental Europe Operation Handbook*; Technical Report; ENTSO-E: Brussels, Belgium, 2009.
4. Holttinen, H.; Milligan, M.; Kirby, B.; Acker, T.; Neimane, V.; Molinski, T. Using standard deviation as a measure of increased operational reserve requirement for wind power. *Wind Eng.* **2008**, *32*, 355–377. [CrossRef]
5. Ohsenbruegge, A.; Klingenberg, T.; Lehnhoff, S. Dynamic Data Driven Dimensioning of Balancing Power with k-Nearest Neighbors. In Proceedings of the Power and Energy Student Summit (PESS) 2015, Dortmund, Germany, 13–14 January 2015.
6. Ohsenbrugge, A.; Lehnhoff, S. Dynamic Dimensioning of Balancing Power with Flexible Feature Selection. In Proceedings of the 23rd International Conference on Electricity Distribution, Lyon, France, 15–18 June 2015.
7. Dvorkin, Y.; Ortega-Vazuqez, M.A.; Kirschen, D.S. Wind generation as a reserve provider. *IET Gener. Transm. Distrib.* **2015**, *9*, 779–787. [CrossRef]
8. Papavasiliou, A.; Oren, S.S. Multi-Area Stochastic Unit Commitment for High Wind Penetration in a Transmission Constrained Network. *Oper. Res.* **2013**, *61*, 578–592. [CrossRef]
9. European Commission. *Commission Regulation (EU) 2017/2195 of 23 November 2017 Establishing a Guideline on Electricity Balancing*; Technical Report; European Commission: Brussels, Belgium, 2017.
10. European Commission. *Commission Regulation (EU) 2017/1485 of 2 August 2017 Establishing a Guideline on Electricity Transmission System Operation*; Technical Report; European Commission: Brussels, Belgium, 2017.
11. Jost, D.; Speckmann, M.; Sandau, F.; Schwinn, R. A new method for day-ahead sizing of control reserve in Germany under a 100% renewable energy sources scenario. *Electr. Power Syst. Res.* **2015**, *119*, 485–491. [CrossRef]
12. Breuer, C.; Engelhardt, C.; Moser, A. Expectation-based reserve capacity dimensioning in power systems with an increasing intermittent feed-in. In Proceedings of the 2013 10th International Conference on the European Energy Market (EEM), Stockholm, Sweden, 27–31 May 2013.
13. Maurer, C.; Krahl, S.; Weber, H. Dimensioning of secondary and tertiary control reserve by probabilistic methods. *Eur. Trans. Electr. Power* **2009**, *19*, 544–552. [CrossRef]
14. Kays, J.; Schwippe, J.; Rehtanz, C. Dimensioning of reserve capacity by means of a multidimensional method considering uncertainties. In Proceedings of the IEEE PSCC Stockholm Conference, Stockholm, Sweden, 22–26 August 2011.
15. Kippelt, S.; Schlüter, T.; Rehtanz, C. Flexible dimensioning of control reserve for future energy scenarios. In Proceedings of the 2013 IEEE Grenoble Conference, Grenoble, France, 16–20 June 2013.
16. Dvorkin, Y.; Pandžić, H.; Ortega-Vazquez, M.A.; Kirschen, D.S. A hybrid stochastic/interval approach to transmission-constrained unit commitment. *IEEE Trans. Power Syst.* **2014**, *30*, 621–631. [CrossRef]
17. Meibom, P.; Barth, R.; Hasche, B.; Brand, H.; Weber, C.; O'Malley, M. Stochastic optimization model to study the operational impacts of high wind penetrations in Ireland. *IEEE Trans. Power Syst.* **2010**, *26*, 1367–1379. [CrossRef]
18. Dietrich, K.; Latorre, J.; Olmos, L.; Ramos, A.; Perez-Arriaga, I. Stochastic unit commitment considering uncertain wind production in an isolated system. In Proceedings of the 4th Conference on Energy Economics and Technology, Dresden, Germany, 3–6 April 2009.
19. Bertsimas, D.; Litvinov, E.; Sun, X.A.; Zhao, J.; Zheng, T. Adaptive Robust Optimization for the Security Constrained Unit Commitment Problem. *IEEE Trans. Power Syst.* **2013**, *28*, 52–63. [CrossRef]
20. Ortega-Vazquez, M.A.; Kirschen, D.S. Estimating the spinning reserve requirements in systems with significant wind power generation penetration. *IEEE Trans. Power Syst.* **2008**, *24*, 114–124. [CrossRef]
21. Zhou, Z.; Botterud, A.; Wang, J.; Bessa, R.J.; Keko, H.; Sumaili, J.; Miranda, V. Application of probabilistic wind power forecasting in electricity markets. *Wind Energy* **2013**, *16*, 321–338. [CrossRef]
22. Tuohy, A.; Meibom, P.; Denny, E.; O'Malley, M. Unit Commitment for Systems with High Wind Penetration. *IEEE Trans. Power Syst.* **2009**, *24*, 592–601. [CrossRef]
23. Gooi, H.; Mendes, D.; Bell, K.; Kirschen, D. Optimal scheduling of spinning reserve. *IEEE Trans. Power Syst.* **1999**, *14*, 1485–1492. [CrossRef]
24. Bessa, R.J.; Mendes, J.; Miranda, V.; Botterud, A.; Wang, J.; Zhou, Z. Quantile-copula density forecast for wind power uncertainty modeling. In Proceedings of the 2011 IEEE Trondheim PowerTech, Trondheim, Norway, 19–23 June 2011.
25. Bessa, R.J.; Miranda, V.; Botterud, A.; Zhou, Z.; Wang, J. Time-adaptive quantile-copula for wind power probabilistic forecasting. *Renew. Energy* **2012**, *40*, 29–39. [CrossRef]
26. Bruninx, K.; Delarue, E. A statistical description of the error on wind power forecasts for probabilistic reserve sizing. *IEEE Trans. Sustain. Energy* **2014**, *5*, 995–1002. [CrossRef]
27. Elia. *Evolution of Ancillary Services Needs to Balance the Belgian Control Area towards 2018*; Technical Report; Elia: Brussels, Belgium, 2013.
28. Jost, D.; Braun, A.; Fritz, R. Dynamic Dimensioning of Frequency Restoration Reserve Capacity based on Quantile Regression. In Proceedings of the 12th International Conference on the European Energy Market (EEM), Lisbon, Portugal, 19–22 May 2015.

29. Jost, D.; Braun, A.; Fritz, R.; Otterson, S. Dynamic sizing of automatic and manual frequency restoration reserves for different product lengths. In Proceedings of the 2016 13th International Conference on the European Energy Market (EEM), Porto, Portugal, 6–9 June 2016.
30. Juban, J.; Siebert, N.; Kariniotakis, G.N. Probabilistic short-term wind power forecasting for the optimal management of wind generation. In Proceedings of the 2007 IEEE Lausanne Power Tech, Lausanne, Switzerland, 1–5 July 2007; pp. 683–688.
31. Kim, S.K.; Park, J.H.; Yoon, Y.T. Determination of Secondary Reserve Requirement Through Interaction-dependent Clearance Between Ex-ante and Ex-post. *J. Electr. Eng. Technol.* **2014**, *9*, 71–79. [CrossRef]
32. Menemenlis, N.; Huneault, M.; Robitaille, A. Computation of dynamic operating balancing reserve for wind power integration for the time-horizon 1–48 h. *IEEE Trans. Sustain. Energy* **2012**, *3*, 692–702. [CrossRef]
33. Nielsen, H.A.; Madsen, H.; Nielsen, T.S. Using quantile regression to extend an existing wind power forecasting system with probabilistic forecasts. *Wind Energy* **2006**, *9*, 95–108. [CrossRef]
34. De Vos, K.; Morbee, J.; Driesen, J.; Belmans, R. Impact of wind power on sizing and allocation of reserve requirements. *IET Renew. Power Gener.* **2013**, *7*, 1–9. [CrossRef]
35. Zhou, Z.; Botterud, A. Dynamic Scheduling of Operating Reserves in Co-Optimized Electricity Markets with Wind Power. *IEEE Trans. Power Syst.* **2014**, *29*, 160–171. [CrossRef]
36. Zhang, Y.; Wang, J.; Wang, X. Review on probabilistic forecasting of wind power generation. *Renew. Sustain. Energy Rev.* **2014**, *32*, 255–270. [CrossRef]
37. Ren, Z.; Yan, W.; Zhao, X.; Li, W.; Yu, J. Chronological Probability Model of Photovoltaic Generation. *IEEE Trans. Power Syst.* **2014**, *29*, 1077–1088. [CrossRef]
38. Bucksteeg, M.; Niesen, L.; Weber, C. Impacts of Dynamic Probabilistic Reserve Sizing Techniques on Reserve Requirements and System Costs. *IEEE Trans. Sustain. Energy* **2016**, *7*, 1408–1420. [CrossRef]
39. ADMIE. *Methodology for the Determination of Zonal/System Needs for Balancing Power*; Technical Report; ADMIE: Athina, Greece, 2020.
40. Lloyd, S. Least squares quantization in PCM. *IEEE Trans. Inf. Theory* **1982**, *28*, 129–137. [CrossRef]
41. Arthur, D.; Vassilvitskii, S. *k-Means++: The Advantages of Careful Seeding*; Technical Report; Stanford InfoLab Publication Server: Stanford, UK, 2006.
42. Zheng, T.; Litvinov, E. Contingency-based zonal reserve modeling and pricing in a co-optimized energy and reserve market. *IEEE Trans. Power Syst.* **2008**, *23*, 277–286. [CrossRef]
43. Papavasiliou, A.; Bouso, A.; Apelfröjd, S.; Wik, E.; Gueuning, T.; Langer, Y. *Multi-Area Reserve Dimensioning Using Chance-Constrained Optimization*; Technical Report; IEEE: Piscataway, NJ, USA, 2021.
44. European Commission. *EU Reference Scenario 2016*; Technical Report; European Commission: Brussels, Belgium, 2016.

energies

MDPI

Article

One-Day-Ahead Solar Irradiation and Windspeed Forecasting with Advanced Deep Learning Techniques

Konstantinos Blazakis [1,*], Yiannis Katsigiannis [2] and Georgios Stavrakakis [1]

[1] School of Electrical and Computer Engineering, Technical University of Crete, GR-73100 Chania, Greece; gstavr@electronics.tuc.gr
[2] Department of Electrical and Computer Engineering, Hellenic Mediterranean University, GR-71004 Heraklion, Greece; katsigiannis@hmu.gr
* Correspondence: konst.blazakis@gmail.com

Abstract: In recent years, demand for electric energy has steadily increased; therefore, the integration of renewable energy sources (RES) at a large scale into power systems is a major concern. Wind and solar energy are among the most widely used alternative sources of energy. However, there is intense variability both in solar irradiation and even more in windspeed, which causes solar and wind power generation to fluctuate highly. As a result, the penetration of RES technologies into electricity networks is a difficult task. Therefore, more accurate solar irradiation and windspeed one-day-ahead forecasting is crucial for safe and reliable operation of electrical systems, the management of RES power plants, and the supply of high-quality electric power at the lowest possible cost. Clouds' influence on solar irradiation forecasting, data categorization per month for successive years due to the similarity of patterns of solar irradiation per month during the year, and relative seasonal similarity of windspeed patterns have not been taken into consideration in previous work. In this study, three deep learning techniques, i.e., multi-head CNN, multi-channel CNN, and encoder–decoder LSTM, were adopted for medium-term windspeed and solar irradiance forecasting based on a real-time measurement dataset and were compared with two well-known conventional methods, i.e., RegARMA and NARX. Utilization of a walk-forward validation forecast strategy was combined, firstly with a recursive multistep forecast strategy and secondly with a multiple-output forecast strategy, using a specific cloud index introduced for the first time. Moreover, the similarity of patterns of solar irradiation per month during the year and the relative seasonal similarity of windspeed patterns in a timeseries measurements dataset for several successive years demonstrates that they contribute to very high one-day-ahead windspeed and solar irradiation forecasting performance.

Keywords: artificial intelligence; data mining; machine learning; advanced deep learning; windspeed forecasting; solar irradiation forecasting; increased RES penetration

Citation: Blazakis, K.; Katsigiannis, Y.; Stavrakakis, G. One-Day-Ahead Solar Irradiation and Windspeed Forecasting with Advanced Deep Learning Techniques. *Energies* **2022**, *15*, 4361. https://doi.org/10.3390/en15124361

Academic Editor: Hua Li

Received: 30 April 2022
Accepted: 9 June 2022
Published: 15 June 2022

Publisher's Note: MDPI stays neutral with regard to jurisdictional claims in published maps and institutional affiliations.

Copyright: © 2022 by the authors. Licensee MDPI, Basel, Switzerland. This article is an open access article distributed under the terms and conditions of the Creative Commons Attribution (CC BY) license (https://creativecommons.org/licenses/by/4.0/).

1. Introduction

A significant amount of global and domestic energy requirements are covered by fossil fuel consumption. It is widely accepted that consuming fossil fuels such as oil, coal, and natural gas releases a large amount of greenhouse gasses into the atmosphere, leading to extremely negative effects on the environment. The production of "cleaner", carbon-free energy can be achieved by utilizing renewable energy sources such as the wind and sun, which have begun to be used to cover the globe's increasing energy needs. Electric energy market liberalization in conjunction with the increasing need for sustainable energy has turned political and investing interests into further utilizing RES to cover electricity needs [1,2].

Energy produced from the wind and the sun depends largely on local weather conditions, such as temperature, windspeed, air pressure, humidity, sunlight, etc., and their fluctuations. Thus, wind and solar power generation is often difficult to control and predict,

as weather conditions constantly change. This makes integration of wind and solar energy into power grids, especially isolated grids, a significant challenge [3,4].

To tackle the aforementioned challenge, it is essential to improve the performance of windspeed and solar irradiation one-day-ahead forecasting in order to minimize uncertainty about the amount of renewable power that can be generated in any electric grid operational situation. Given the inherent relationship between solar irradiation and the electric power produced from photovoltaics, and between windspeed and wind turbine power generation, it is necessary to create computational models that will accurately predict solar irradiation and windspeed in medium- and/or short-term time scales [5–11].

Windspeed forecasting can be separated into four temporal ranges: very short-term (from a few seconds to 30 min), short-term (from 30 min to 6 h ahead), medium-term (from 6 h to 1 day ahead), and long-term (more than 1 day ahead) [6]. Solar irradiation forecasting can also be divided into four temporal ranges: very short-term (a few minutes to 1 h), short-term (1–4 h), medium-term (1 day ahead), and long-term (more than 1 day ahead) [7].

Over the last few years, various tools have been established to predict windspeed and solar irradiation. These tools can be separated into three main groups: (1) data-driven models, such as statistical models and machine learning models, which are the most prevalent tools used for predicting such timeseries; (2) physical models that use meteorological and topographical data; and (3) hybrid algorithms, which have found great success in a number of research areas [3,6,8].

Regarding data-driven models, statistical methods consist of autoregressive integrated moving average (ARIMA) [9–11], auto-regressive moving average (ARMA) [12–14], Lasso [15], and Markov models [16–18]. The most common machine learning methods are support vector machines (SVM) [19–21], feed forward neural networks (FFNN) [22], recurrent neural networks (RNN) [23–25], convolutional neural networks (CNN) [26,27], long short-term memory networks (LSTM) [28–31], bidirectional long short-term memory neural networks (BiLSTM) [32], deep belief networks (DBN) [33], and artificial neural networks in general (ANN) [34–36].

Physical methods include numerical weather prediction (NWP) forecasting models [37,38], total sky imagery (TSI) [39], cloud-moving-based satellite imagery models [40], and weather research and forecasting (WRF) models [41].

Hybrid methods found in the literature include variational mode decomposition with Gram–Schmidt orthogonal and extreme learning machines, which are enhanced at the same time by a gravitational search algorithm [42], nonlinear neural network architectural models combined with a modified firefly algorithm and particle swarm optimization (PSO) [43], the hybrid model decomposition (HMD) method and online sequential outlier robust extreme learning machine (OSORELM) [44], empirical mode decomposition and Elman neural networks (EMD-ENN) [45], wavelet transform (WT-ARIMA) [46], empirical wavelet transform (EWT) and least-square support vector machines (LSSVM) improved by coupled simulated annealing [47], and variational mode decomposition (VMD) combined with several ML methods, including SVM and back propagation neural networks (BPNN). Moreover, ELMs and ENNs were implemented to perform advanced data preprocessing based on complementary ensemble empirical mode decomposition (CEEMD) [48], while sample entropy and VMD forecasting methods based on ENNs and on a multi-objective "satin bowerbird" optimization algorithm have been introduced [49]. Bidirectional long short-term memory neural networks with an effective hierarchical evolutionary decomposition technique and an improved generalized normal distribution optimization algorithm for hyperparameter tuning, a combined model system including an improved hybrid time-series decomposition strategy (HTD), a novel multi-objective binary backtracking search algorithm (MOBBSA), and an advanced sequence-to-sequence (Seq2Seq) predictor for windspeed forecasting have been presented in [50,51], respectively. Further, recurrent neural network prediction algorithms combined with error decomposition correction methods have also been presented in [52].

The purpose of this paper is to develop models for high-performance, medium-term forecasting (i.e., for the next 24 h) of windspeed and solar irradiation, which will be based on hourly data recorded on Dia Island, which is located north of Heraklion city in Crete, Greece. In order to achieve this, the efficacies of three deep learning techniques, i.e., multi-channel CNN, multi-head CNN, and encoder–decoder LSTM, are investigated and compared with two conventional methods, i.e., RegARMA and NARX, in order, among other things, to demonstrate the improved forecasting performance of the deep learning techniques and to highlight the most effective among them. All the presented methodologies were tested on a benchmarked dataset of real measurements for the purpose of predicting with the highest possible statistical accuracy the windspeed and solar irradiation for a forecasting period of 24 h, i.e., of one day ahead.

The main contributions of this paper are:

- A series of experiments applying advanced deep-learning-based forecasting techniques were conducted, achieving high statistical accuracy forecasts.
- A thorough comparison is conducted successfully among advanced deep learning techniques and well-known conventional techniques for medium-term solar irradiance and windspeed forecasting to highlight the most effective among them.
- A cloud index per hour ($NDD(h,d)$) was introduced and used for the first time in order to improve medium-term solar irradiance forecasting.
- Data were categorized by each month for successive years, firstly due to the similarity of patterns of solar irradiation by month during the year, and secondly because of the relative seasonal similarity of the windspeed patterns, resulting in a monthly timeseries dataset, which is more significant for high-performance forecasting.
- A walk-forward validation forecast strategy in combination first with a recursive multistep forecast strategy and secondly with a multiple-output forecast strategy was successfully implemented in order to significantly improve medium-term windspeed and solar irradiation forecasts.
- The recursive multistep forecast strategy was compared to the multiple-output forecast strategy.

The paper is organized as follows: In Section 2, we present the theory behind the proposed deep learning forecasting methods and the real measurements categorized by each months' dataset, model configurations, the methodology followed, and the algorithms for the medium-term windspeed and solar irradiation forecasting. In Section 3, the simulation results and the discussion of these results are presented, while in Section 4, the conclusions of the paper are summarized.

2. The Proposed Deep Learning Model Framework

2.1. Dataset Presentation

The dataset used in this research is derived from measurements carried out on Dia Island, Crete, Greece. Table 1 includes the required parameters given in hourly values for every day for years 2005–2016 at a height of 10 m from the ground. All these parameters were recorded except for the beam/direct irradiance on a plane always normal to the sun's rays and the diffuse irradiance on the horizontal plane, which were estimated from the global irradiance on the horizontal plane using the anisotropic model described in [53]. The beam/direct irradiance on a plane always normal to the sun rays was considered for two main reasons: (1) it improves the forecasting performance of the examined models, and (2) it is an essential parameter for the estimation of a photovoltaic system's performance in a specific location. Moreover, extraterrestrial irradiation is calculated using the typical solar geometry equations presented in [54]. Table 2 includes some statistical data for solar irradiation and windspeed, including maximum and minimum mean values and standard deviations (Std).

Table 1. Dataset parameters measured.

Parameter	Unit
Air temperature	°C
Relative humidity	%
Windspeed	m/s
Wind direction	°
Surface (air) pressure	Pa
Global irradiance on the horizontal plane	W/m^2
Beam/direct irradiance on a plane always normal to the sun rays	W/m^2
Diffuse irradiance on the horizontal plane	W/m^2
Surface infrared (thermal) irradiance on a horizontal plane	W/m^2
Extraterrestrial irradiation	W/m^2

Table 2. 2005–2016 dataset, Max, Min, Mean, Std values.

	Max	Min	Mean	Std
Solar Irradiation (W/m^2)	1032	0	208	305
Windspeed (m/s)	17.88	0	5.84	3.05
Air temperature (°C)	29.73	5	19.11	4.86
Relative humidity (%)	99.88	48.55	77.23	7.82
Wind direction (°)	360	0	253.2	118.9
Surface (air) pressure (Pa)	103,845	97,349	100,306	576
Beam/direct irradiance on a plane always normal to the suns' rays (W/m^2)	986	0	143	246
Diffuse irradiance on the horizontal plane (W/m^2)	646	0	65	85
Extraterrestrial irradiation (W/m^2)	1294	0	344	429

For solar irradiation forecasting, due to the lack of a cloud index, the normalized discrete index for each day ($NDD(d)$) and for each hour of the day ($NDD(h,d)$) were introduced and calculated by Equations (1) and (2) below, provided the extraterrestrial solar irradiation for Dia Island and the solar irradiation in the horizontal plane [36]. Due to the periodicity of solar irradiation, we constructed two columns: (1) the number of days in the month (31, 30 or 28); and (2) the hour of the day for every observation (1–24). For solar irradiation forecasting, the following parameters were used as inputs from the initial measurements' dataset: air temperature, $NDD(d)$, $NDD(h,d)$, the number of days in the month, and the hour of the day. From the initial dataset of measurements, the nighttime values (zero solar irradiation) were removed due to the fact that night hours do not contribute to solar irradiation forecasting.

The parameters $NDD(d)$ and $NDD(h,d)$ are calculated as follows:

$$NDD(d) = \sqrt{\frac{1}{24}\sum_{i=1}^{24}(G_{on,d}(i) - G_{sn,d}(i))^2} \quad (1)$$

$$NDD(h,d) = G_{on,h,d} - G_{sn,h,d} \quad (2)$$

where "d" is the day of the year (1 to 365), "i" is the hour number of each day (1 to 24), "h" is the specific hour of the day for which the cloud index $NDD(h,d)$ is calculated, G_{on} is the normalized extraterrestrial irradiance, and G_{sn} is the normalized surface irradiance. Global irradiance data on the horizontal plane are presented in Table 1, where extraterrestrial irradiance data were calculated from well-known solar geometry equations, using as parameters the solar constant (1367 W/m^2), day of the year, latitude and longitude of the location, solar hour angle, and declination angle of the Sun [54]. For normalization of G_{on} and G_{sn}, their corresponding maximum values for each year of the dataset were used. Even if the value of extraterrestrial or surface irradiance exceeds its historical maximum

(so the normalized maximum irradiance could slightly exceed 1), this does not affect the performance of the forecasting.

In addition, statistical parameters such as the maxima, minima, means, and standard deviations for windspeed and solar irradiation data are shown in Table 2.

For windspeed forecasting, the following parameters were used as inputs from the initial dataset: air temperature (°C), relative humidity (%), and global irradiance on the horizontal plane (W/m^2) [5].

2.2. Presentation of the Proposed Deep Learning Models

2.2.1. Multi-Channel and Multi-Head CNNs

Convolutional neural networks (CNNs) are a category of artificial deep neural networks that are mainly used for image and video recognition, recommender systems, image and text classification, image analysis, facial recognition, document analysis, natural language processing, financial timeseries data, etc. [27–29].

A typical CNN consists of at least one convolutional layer, fully connected layers, flattened layers, pooling layers, and dropout layers. The purpose of the convolutional layer is to convolve the input image and generate the feature maps. Input image convolving is carried out by sliding a group of small-sized filters (kernels)—each of which contain a sufficient number of learnable weights—over the input image, implementing element-wise multiplication at each possible position. A completely new layer is generated from each kernel, which contains the application results of the particular kernel in the input image. The number of generated feature maps (convolutional layer depth) is defined by the number of kernels and constitutes the CNN hyperparameters, which must be chosen correctly based on available data. Then, this resulting group of layers undergoes a pooling process. Pooling involves a down-sampling operation in which sets of elements in the feature maps are integrated and restricted to a single value based on some criterion or calculation (e.g., maximum value or average of all values). As a result, noise data are eliminated, and better performance is achieved. Repeating the two aforementioned layers multiple times by applying different kernels of different sizes and depths, successive extraction of higher-level features improves, which constitutes one of the assets of CNNs. Dropout layers can be used after convolutional layers and pooling layers to protect neural networks from overfitting.

Finally, the last pooled layer can be converted into a single vector that includes all of its weights and which is connected to a fully connected layer, which is further connected to the output layer that contains a summation of every possible class, thus providing the classification success estimation for the given input [55–58].

The multi-channel approach applied in this paper is based on the aforementioned typical CNN architecture and extends it by adding a further embedding layer into the model in order to raise the number of channels matching the degree of semantic enrichment of the present paper's data. Multi-channel CNNs use each of the solar irradiation inputs and the windspeed forecasting timeseries variables to predict the windspeed and solar irradiation of the next day. This is implemented by entering each one-dimensional timeseries into the model as a separate input channel. A distinct kernel is then used by the CNN, which will read each input sequence onto a separate set of filter maps, essentially learning features from each input timeseries variable. This is useful for situations where the output sequence is some function of the observations at prior timesteps derived from their multiple different features, and also when the output sequence does not contain only the feature to be forecasted [57,59].

Another extension of the CNN model is to obtain a separate sub-CNN model, or, in other words, a head for each input variable, whose structure can be referred to as a multi-headed CNN model. This extension requires transformation of the model preparation, and, in turn, modification of the preparation of the training and test datasets. Regarding the model, a separate CNN model must be defined for each of the input variables: solar irradiation and windspeed. Inserting each input into an independent CNN has a number

of advantages, such as feature extraction that is improved by focusing only on one input, and each convolutional head can be controlled for the specific nature of each input. The configuration of the model, taking into consideration the number of layers and their hyperparameters, was also modified to better suit the new approach presented above [57].

2.2.2. Encoder–Decoder LSTM

Long short-term memory (LSTM) is a modified version of artificial recurrent neural network (RNN) architecture mainly used in deep learning algorithms. LSTMs use feedback connections, in contrast to standard feed forward neural networks, which enhances the memory recovery of a given network. LSTMs can process single data points (such as images) and entire sequences of data (such as speech or video); therefore, LSTMs are suitable for applications such as unsegmented, connected handwriting recognition, speech recognition, anomaly detection in network traffic or intrusion detection systems (IDSs), etc. [60].

A common LSTM unit consists of a cell, an input gate (to investigate which information should be used for memory modification), an output gate, and a forget gate (to decide the information to be dismissed). The cell remembers values over arbitrary time intervals, and the three gates adjust the information flow into and out of the cell.

LSTM networks are appropriate for forecasting, classifying, and processing based on timeseries data, since unknown duration lags may exist between important events when dealing with timeseries problems. LSTMs are able to cope with the vanishing gradient problem that can arise during training of traditional RNNs. Their relative insensitivity to gap lengths is an advantage of LSTMs over RNNs, hidden Markov models, and other sequence learning methods in numerous applications [61].

Encoder–decoder LSTM is a recurrent neural network designed to cope with sequence-to-sequence (seq2seq) problems (text translation, learning program execution, etc.). Due to variations in the number of items in the inputs and outputs, sequence-to-sequence prediction problems have been worth studying. One advantage of an encoder–decoder LSTM is its use of fixed-sized internal representation in the core of the model [59].

The encoder and the decoder are usually LSTM units or gated recurrent units. The purpose of the encoder is to read the input sequence and to summarize the information in the internal state vectors (the hidden state and cell state vectors in the case of LSTMs). The outputs of the encoder can be discarded; only the internal states need to be retained. The decoder is an LSTM whose initial states are initialized to the final states of the encoder LSTM. Using these initial states, the decoder starts to generate the output sequence (see Figure 1).

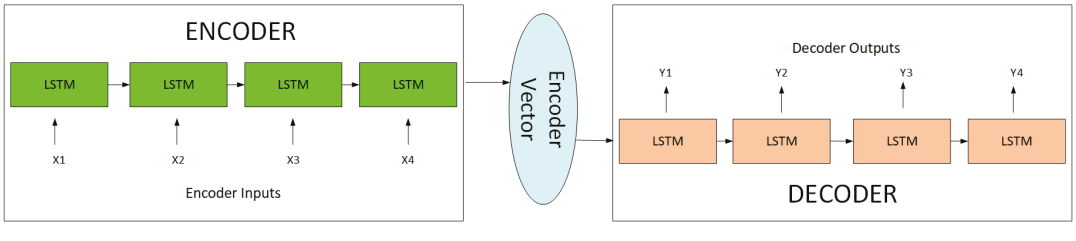

Figure 1. Encoder–decoder LSTM basic architecture.

The decoder operates slightly differently during training and inference. During training, teacher forcing is used, which accelerates decoder training. The input to the decoder at each timestep is the output from the previous timestep.

The encoder transforms the input sequence into state vectors (known as thought vectors), which are then inserted into the decoder in order to start output sequence generation according to the thought vectors. The decoder is just a language model conditioned by the initial states [61].

2.3. Solar and Wind Data Preprocessing and Forecasting Model Configurations

To appropriately train the model, two data preprocessing procedures were carried out. The first procedure normalized the data and the latter procedure accommodated for missing data. As for the latter, the average of nearby values during the same week was calculated to fill missing data values. Furthermore, it is worth noting that data normalization before inserting the input data into the network is a good practice, since inserting variables with both large and small magnitudes will have negative effects on learning algorithm performance. For data normalization, the well-known formula of Equation (3) was used:

$$y = \frac{x_i - x_{min}}{x_{max} - x_{min}} \quad (3)$$

where y is the normalized value, x_i is the current value, and x_{min} and x_{max} are the minimum and the maximum of the original parameters, respectively.

These data were categorized by month, resulting in a monthly timeseries for years 2005–2016, which was then followed by model training and medium-term forecasting. Data were separated by month mainly because of the similarity of solar irradiation patterns, and secondly because of the relative similarity of windspeed patterns.

The most commonly used strategies for making multistep forecasts are [6,28,30,62]:

1. Direct Multistep Forecast Strategy.

For every timestep forecast, a new model is developed. This strategy demands large computational time since there are as many models to learn as the size of the forecasting horizon.

2. Recursive Multistep Forecast Strategy.

The recursive multistep strategy first trains a one-step model and then uses this single model for each horizon, but the prediction of the prior timestep is used as an input in place of the original dataset value for making a prediction at the following timestep. The recursive approach is not so computationally intensive in comparison with the direct strategy, as only one model is fitted. This type of strategy strengthens error accumulation because the predictions of prior steps are inserted into the model instead of the real values. This phenomenon results in poor algorithm performance as the prediction time horizon increases.

3. Direct–Recursive Hybrid Multistep Forecast Strategy.

In this strategy, a combination of direct and recursive strategies is used in order to take advantage of both methods. This method computes the forecasts with different models for every forecasting horizon (direct strategy), and at each timestep it enlarges the set of inputs by adding variables corresponding to the forecasts of the previous step (recursive strategy).

4. Multiple Output Forecast Strategy.

For the multiple output strategy, one model is developed in order to predict the whole forecast sequence in a one-shot manner.

In this study, the walk-forward validation forecast strategy is introduced, with an adaptive training window that expands after the desired forecast horizon (of 24 h) to include each time's recent actual (measured) values, and was applied with improved success for a prediction horizon of 24 h. The walk-forward validation forecast strategy splits the monthly timeseries dataset into preconcerted sub-fragments. Walk-forward validation is based on the sliding window method, where the data are used in ascending order of time rather than randomly shuffling training–test datasets. This validation approach is essential for time-series analysis methods in general, where observations with future timestamp information cannot be used to predict past (old) values. Thus, it is crucial to assess model forecasting performance by recursively augmenting training data with recent observations and reevaluating the model over the extended horizon [62]. The recursive multistep forecast strategy and the multiple-output forecast strategy are applied over expanded timeseries

fragments with a fixed sliding window of 24 h. The recursive multistep forecast strategy computes one-step-ahead forecasts (i.e., 1 h ahead) recursively until the desired forecast horizon (24 h) is achieved, while the multiple-output forecast strategy predicts the whole forecast horizon (i.e., 24 h ahead) in a one-shot manner. Then, the training set is expanded to incorporate recent actual (measured) values. Especially for solar irradiation forecasting, the sliding window magnitude is smaller than 24 h due to the subtraction of zero solar irradiation for every day, and it depends on the variable length of night during the year. Although the sliding window is smaller than 24 h (because of the excluded night hours), it represents, for the forecasting procedure, the window of the previous 24 h. For the training set, the months from the 2005–2014 monthly timeseries dataset were used in order to forecast the values for the corresponding months of 2015 and 2016. For instance, in order to forecast the windspeed and solar irradiation for January of 2015 and January of 2016, the measurements (dataset) for January in the years 2005–2014 were used to train the forecasting model. For every 24 h ahead forecasting, the real measurements (training dataset) available until midnight of the previous day were used to train the forecasting models [59].

The methodologies presented above for solar irradiation and windspeed medium-term forecasting with the recursive multistep forecast strategy and the multiple-output forecast strategy are described formally by the following equations, respectively:

$$\hat{y}\,(h, d) = f(\hat{y}(h-1, d), \ldots, \hat{y}(h-k+1, d), y(h-k, d-1), \ldots, y(h-24, d-1), u_i(h-1, d-1), u_i(h-k+1, d-1), u_i(h-k, d-1), \ldots, u_i(h-24, d-1)) \quad (4a)$$

$$\hat{y}\,(h, d) = f(y(h-1, d-1), \ldots, y(h-k+1, d-1), y(h-k, d-1), \ldots, y(h-24, d-1), u_i(h-1, d-1), u_i(h-k+1, d-1), u_i(h-k, d-1), \ldots, u_i(h-24, d-1)) \quad (4b)$$

where: "$\hat{y}$" is the predicted value for hour "h", . . . ,"$h-(k-1)$ i.e., $h-k+1$" of day "d"; . . . $y(h-k, d-1)$, ... $y(h-24, d-1)$ are the historical measured values, "u_i" represents the other external inputs (i.e., air temperature, relative humidity, global irradiance on the horizontal plane for windspeed forecasting, and air temperature), $NDD(d)$, $NDD(h,d)$ are the number of days in the month and the hour of the day, respectively, for solar irradiation forecasting, and k is the time instant sliding index.

In Table 3, the configuration of each layer for each model used is presented.

Table 3. Model configurations for windspeed and solar irradiation forecasting.

Windspeed and Solar Irradiation Forecasting					
Multi-Head CNN		**Multi-Channel CNN**		**Encoder–Decoder LSTM**	
Layer	**Configuration**	**Layer**	**Configuration**	**Layer**	**Configuration**
Convolution 1	Filters = 32 Kernel size = 3	Convolution 1	Filters = 32 Kernel size = 3	LSTM 1	Units = 200
Convolution 2	Filters = 32 Kernel size = 3	Convolution 2	Filters = 32 Kernel size = 3	Repeat vector	-
Max-pooling 1	Filters = 32	Max-pooling 1	Filters = 32	LSTM 2	Units = 200
Flatten	-	Convolution 3	Filters = 16 Kernel size = 3	Dense 1	Units = 100
Concatenetion	-	Max-pooling 2	Filters = 16	Dense 2	Units = 1
Dense 1	Neurons = 200	Flatten	-	-	-
Dense 2	Neurons = 100	Dense 1	Neurons = 100	-	-
Dense 3	Neurons = 24	Dense 2	Neurons = 24	-	-

Concerning the data shapes of encoder–decoder LSTM, multi-channel CNN, and multi-head CNN, one sample consists of 24 timesteps (i.e., 24 h ahead), with three features for windspeed forecasting and five features for solar irradiation. The training dataset has 300 days (7200 h) or 310 days (7440 h) of data, so the shape of the training dataset would be: [7200/7440, 24, 3/5].

The encoder–decoder LSTM model consists of two sub-models, the encoder and the decoder. The purpose of the encoder is to read and encode the input sequence, and then the decoder reads the encoded input sequence and makes a one-step prediction for each element in the output sequence. After the input sequence reading by the encoder, a 200-element vector output is constructed (one output per unit) that captures features from the input sequence. At first, the internal representation of the input sequence is iterated multiple times, once for each timestep in the output sequence. This sequence of vectors is carried forward to the LSTM decoder. Then, the decoder is defined as an LSTM hidden layer with 200 units. It is worth mentioning that the decoder will output the entire sequence, not just the output at the end of the sequence, as was done with the encoder. This means that each of the 200 units will output a value for each of the 24 h, representing the basis of what to predict for each hour in the output sequence. Then, a fully connected layer to interpret each timestep in the output sequence is used before the final output layer. It is important to note that the output layer predicts a single step in the output sequence, not all of the 24 h at a time.

In multi-head CNN, a different CNN sub-model reads each input with two convolutional layers with 32 filters with a kernel size of 3, a max pooling layer, and a flattened layer. The internal representations come together before them to be interpreted by two fully connected layers of 200 and 100 nodes, respectively, and used to make a prediction.

In multi-channel CNN, a separate channel is linked to each input, similar to different image channels (e.g., red, green, and blue). A model that shows excellent performance consists of two convolutional layers with 32 filter maps with a kernel size of 3 followed by pooling, then another convolutional layer with 16 feature maps and pooling. The fully connected layer that interprets the features consists of 100 nodes.

The choice of hyperparameter values is of great importance [63–66]; for this reason, the well-known grid search method was adopted [49,67,68]. In this study, a grid search took place for the number of prior inputs, training epochs, and samples to include in each mini-batch, optimizer type, type of activation function, and learning rate. In more detail, for number of prior inputs, a set of {6, 12, 24, 48} was examined; for number of training epochs, a set of {5–100} was examined; for mini-batch size, a set of {8–512} was examined; optimizer types {RMSProp, ADAM, SGD, AdaGrad, AdaDelta, AdaMax, NADAM} were applied; activation functions {Relu, Elu, Tanh, Sigmoid} were applied; the learning rate takes values within $\{10^{-5}–10^{-1}\}$; see refs [49,67,68]. The grid search ended up with the optimal hyperparameters shown in Table 4.

Table 4. Optimal hyperparameters of the models.

Multi-Channel CNN/Multi-Head CNN Encoder–Decoder LSTM
Optimizer: Adam
Activation function: Tanh
Mini-batch size: 16
Learning Rate: 10^{-4}
Epochs for windspeed forecasting: 15
Epochs for solar irradiation forecasting: 50
Prior inputs: 24

In this research, 12 monthly models were applied for each deep learning technique for solar irradiation and windspeed one-day-ahead forecasting, and were developed with their corresponding optimal parameter configurations. Each model was run 20 times by performing several experiments in order to reduce the forecasting error statistics, which was found to be sufficient for the present work's case studies. Then, the findings were recorded according to the mean values of the forecasting performance statistical metrics. Computations were carried out on a desktop computer with the following characteristics:

64 bit OS, CPU i5 2.30 GHz, and 8.00 GB of RAM. The forecasting run time for each test set was about 8 min.

3. Deep Learning and Conventional Forecasting Model Performance and Discussion

3.1. Deep Learning Forecasting Performance Evaluation Using Well-Established Error Metrics

Having arrived at the optimal hyperparameters of the forecasting models, evaluation of the results of windspeed and solar irradiation forecasting was based on well-known relationships to calculate the deviation (error) between predicted and real (measured) values, i.e., the well-known forecasting error statistical metrics [1]. These well-known relationships that are used extensively to evaluate forecasting methods in such prediction problems are shown in Table 5, where Y is the actual value and $\hat{Y}$ is the forecasted value.

Table 5. The performance metrics used.

Mean Squared Error (MSE)	$MSE = \frac{1}{N}\sum\left(Y-\hat{Y}\right)^2$
Root Mean Squared Error (RMSE)	$RMSE = \sqrt{MSE}$
Mean Absolute Percentage Error (MAPE)	$MAPE = \frac{100\%}{N}\sum\left\|\frac{Y-\hat{Y}}{Y}\right\|$
Mean Absolute Error (MAE)	$MAE = \frac{1}{N}\sum\left\|Y-\hat{Y}\right\|$
Normalized Root Mean Squared Error (nRMSE)	$nRMSE = \frac{RMSE}{\overline{Y}}$
Coefficient of Determination (r^2)	$1-\frac{Var\left(Y-\hat{Y}\right)}{Var\left(\hat{Y}\right)}$

In Figures 2–5, solar irradiation hourly predictions and windspeed hourly predictions are presented for July and November of 2016 for all the deep learning models that were applied in this survey. The figures followed with the letter 'a' (e.g., Figure 2a) refer to the recursive multistep forecast strategy, while the figures followed with the letter 'b' refer to the multiple-output forecast strategy. It is clarified that in Figures 2–5 in the horizontal axes the time unit is 'hour', but obviously this is not possible to show graphically; thus, the time interval appearing is 'day', so within each interval of 'one day', 24 hourly values are depicted. The fluctuations in solar irradiation observed in Figure 3a,b are due to the cloudy weather during November, in contrast with Figure 2a,b, where the clear sky during July gives an almost periodical curve. In both Figure 4a,b and Figure 5a,b, small and high variations in the windspeed were observed.

The average daily performance metrics for each of the three deep learning algorithms applied for each month of 2015 and 2016 for solar irradiation forecasting and windspeed forecasting are presented in Tables 6 and 7, respectively, in order to determine which method is more appropriate for solar irradiation and windspeed forecasting. In Tables 6 and 7, CNN1 and CNN2 refer to multi-head CNN and multi-channel CNN, respectively.

Concerning the three deep learning techniques, the encoder–decoder LSTM method showed improved forecasting performance for solar irradiation forecasting, while multi-head CNN (CNN1) gave higher success rates for windspeed forecasting according to the performance metrics shown above for both strategies. Comparing the recursive multistep forecast strategy with the multiple-output forecast strategy, the latter outperformed the former in all cases studied. Moreover, Table 6 clearly shows that for the summer months the deep learning models had better forecasting rates than for the remaining months of the year for solar irradiation forecasting due to the absence of clouds, which is somewhat expected. Encoder–decoder LSTM presents a strong competitive advantage, especially in summer months, while in the remaining months encoder–decoder LSTM performs slightly better in comparison with CNN1 and CNN2. In Table 7, CNN1 performs a little better in all the months of the year in comparison with the encoder–decoder LSTM and CNN2 for windspeed forecasting. Taking into account the increased variability of windspeed in contrast to solar irradiation and the 24 h forecasting horizon, the MAPE index values are justified (see similar results in refs [69–71]). Moreover, April and March are the windiest months of the year, which justifies the high MAPE index values of these months compared to the other months of the year.

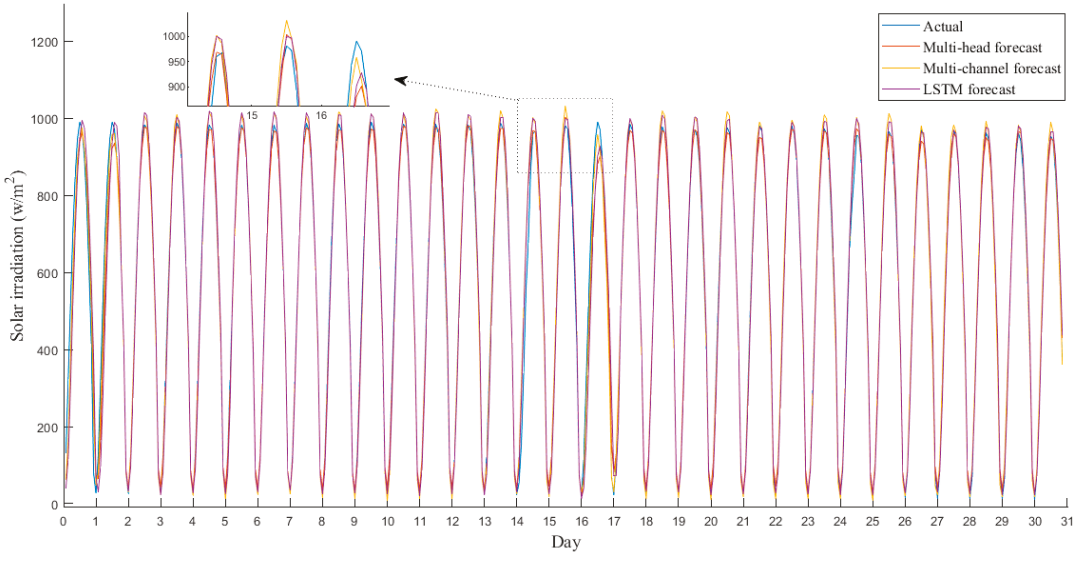

(**a**)

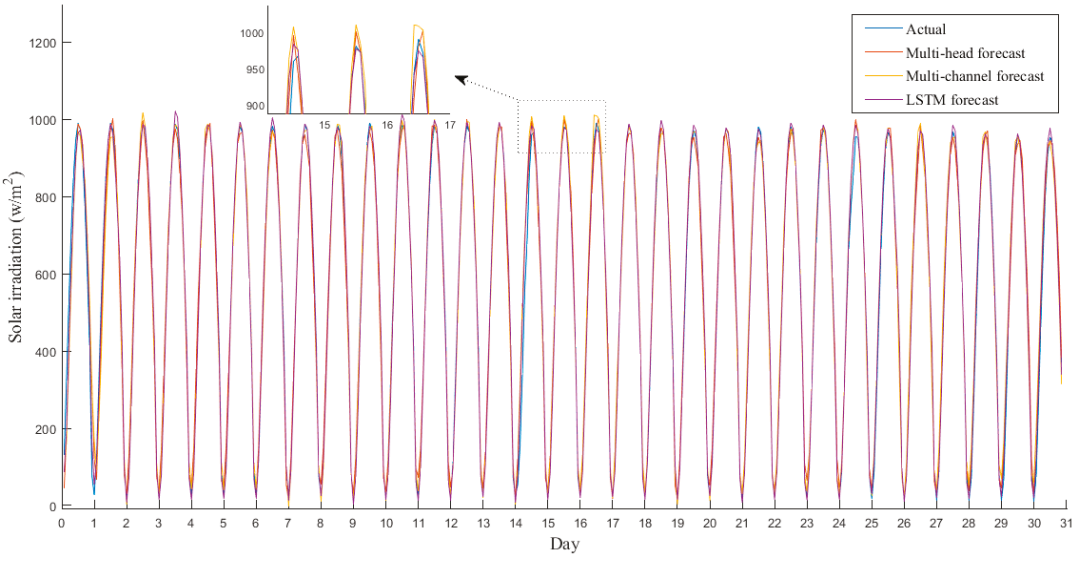

(**b**)

Figure 2. Solar irradiation forecasting during July 2016. (**a**) recursive multistep forecast strategy; (**b**) multiple-output forecast strategy.

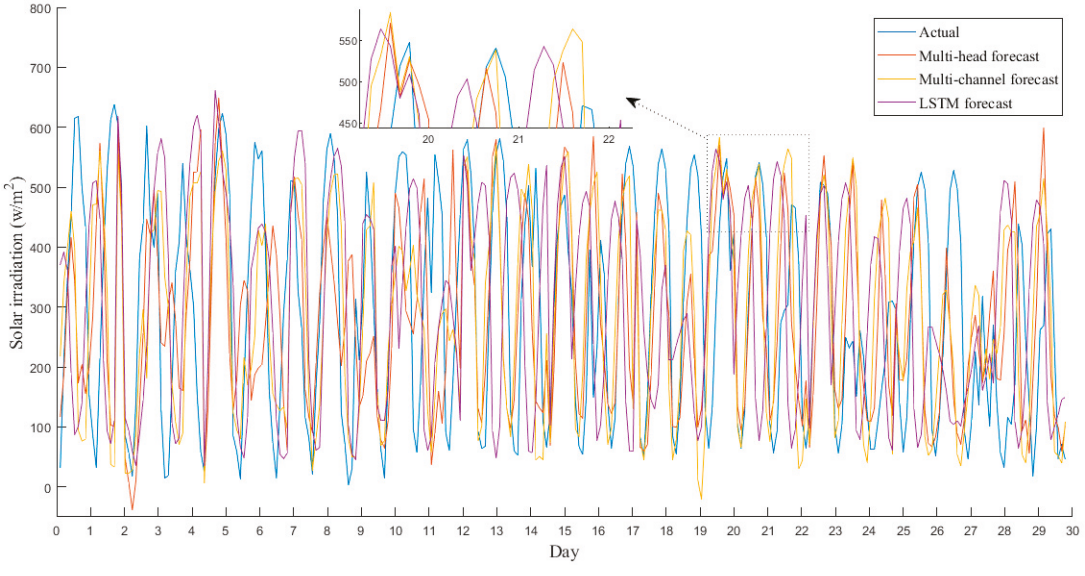

(**a**)

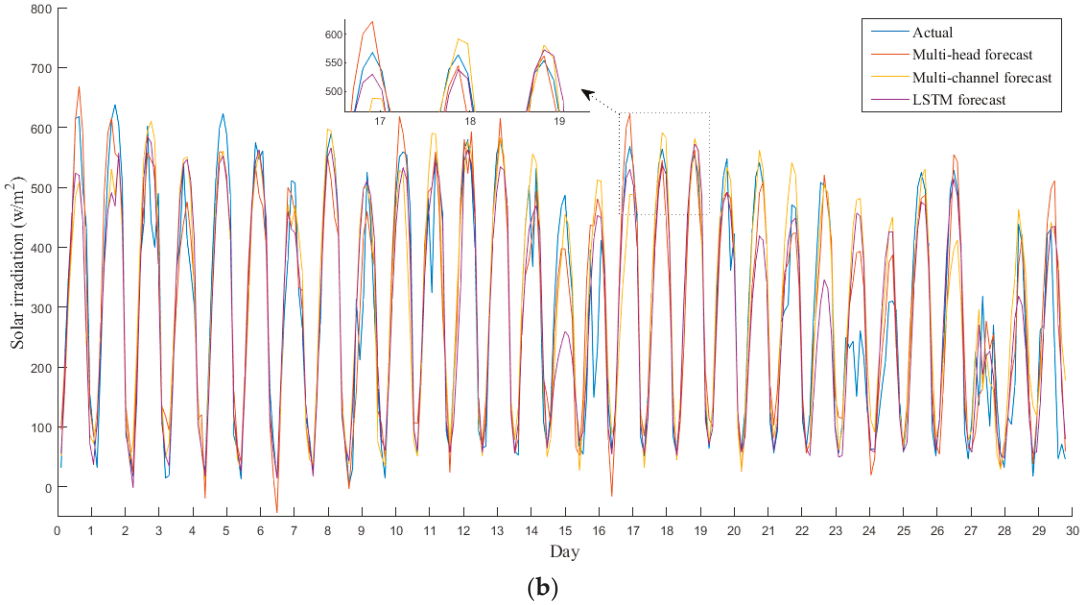

(**b**)

Figure 3. Solar irradiation forecasting during November 2016. (**a**) recursive multistep forecast strategy; (**b**) multiple-output forecast strategy.

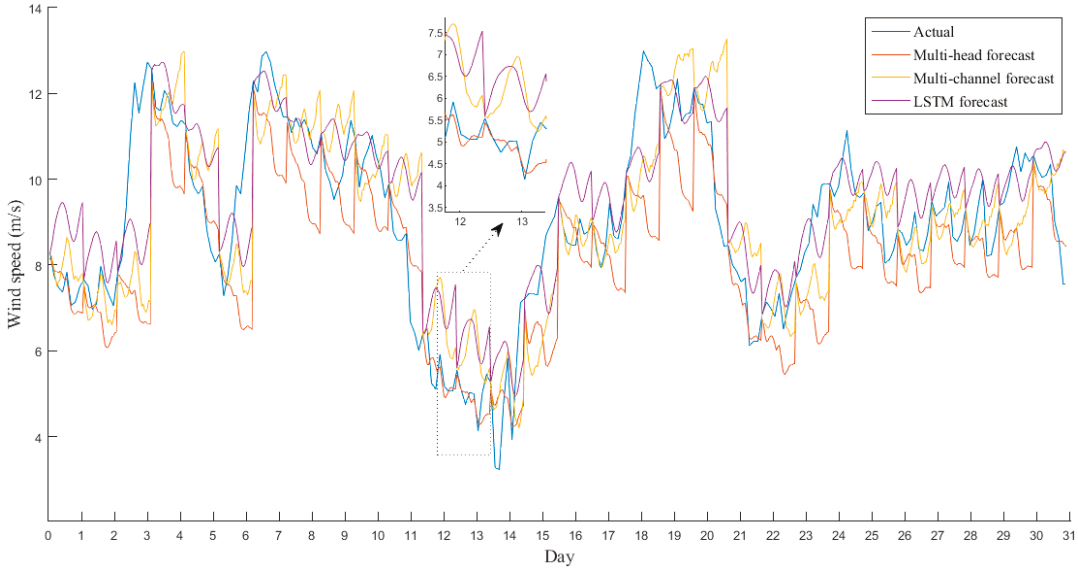

(**a**)

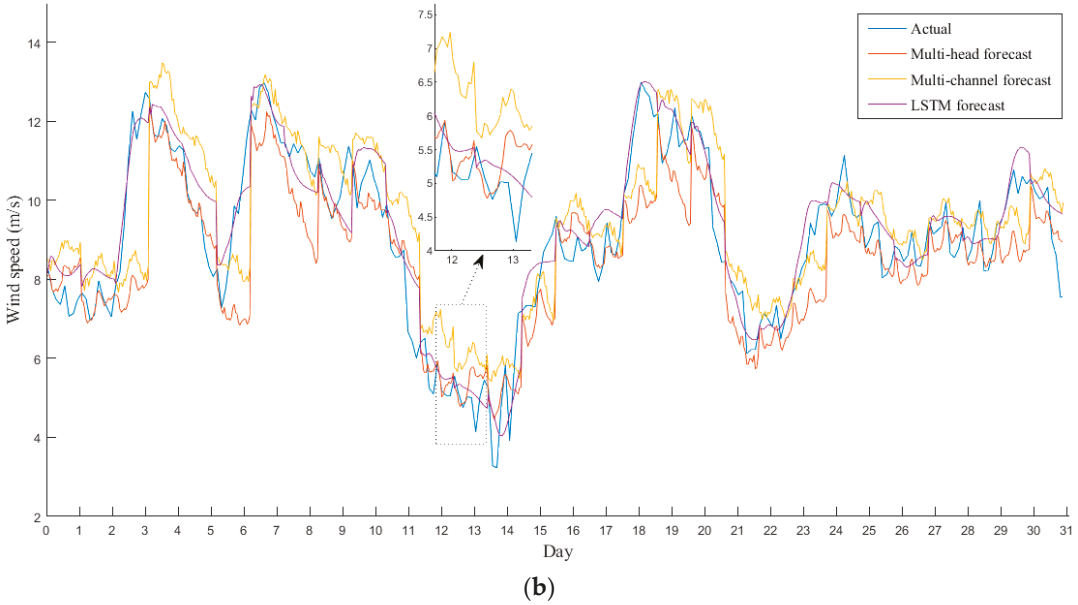

(**b**)

Figure 4. Windspeed forecasting during July 2016. (**a**) recursive multistep forecast strategy; (**b**) multiple-output forecast strategy.

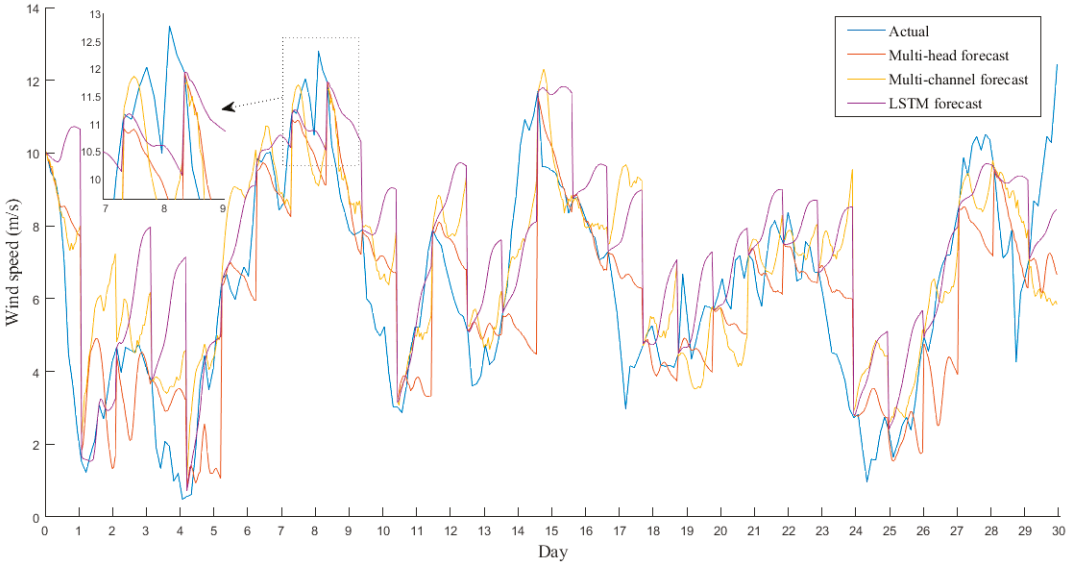

(**a**)

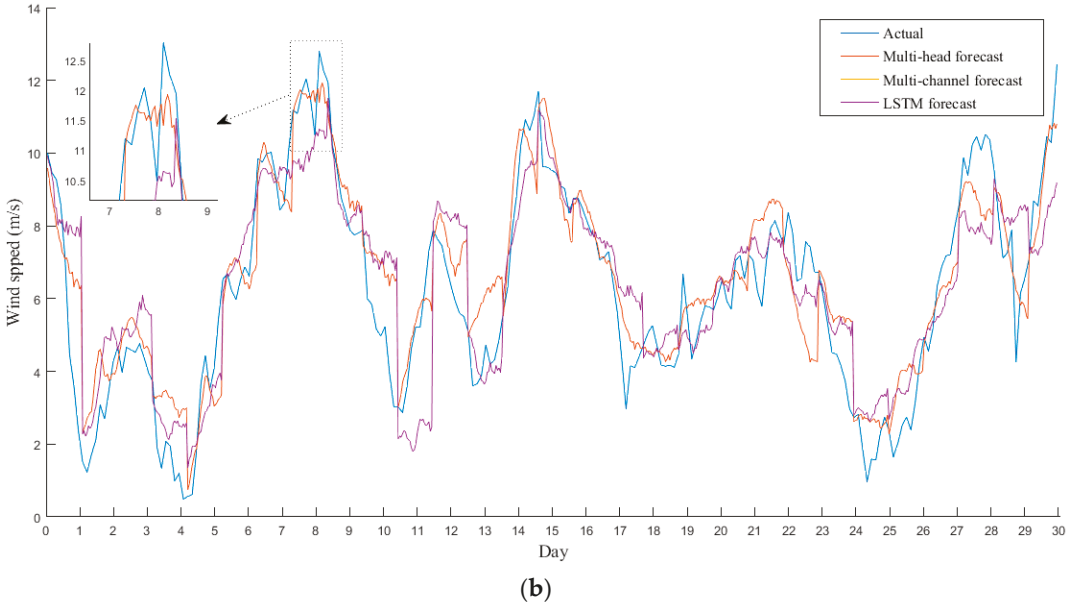

(**b**)

Figure 5. Windspeed forecasting during November 2016. (**a**) recursive multistep forecast strategy; (**b**) multiple-output forecast strategy.

Table 6. Solar irradiation forecasting results: (**a**) average daily forecasting results for 2015 and 2016 with the recursive multistep forecast strategy. (**b**) average daily forecasting results for 2015 and 2016 with the multiple-output forecast strategy.

(**a**)

	MAPE (%)			RMSE (W/m^2)			MAE (W/m^2)			nRMSE		
	CNN1	**CNN2**	**LSTM**	**CNN1**	**CNN2**	**LSTM**	**CNN1**	**CNN2**	**LSTM**	**CNN1**	**CNN2**	**LSTM**
January	114.35	93.35	91.57	195.09	186.68	180.37	140.01	133.16	125.55	0.79	0.74	0.72
February	81.93	64.95	58.33	208.35	187.78	185.58	157.42	136.27	128.82	0.61	0.54	0.51
March	144.02	132.22	129.16	282.32	265.99	251.70	186.67	179.94	176.40	0.69	0.68	0.64
April	48.67	42.16	41.49	153.18	145.49	141.83	117.96	102.00	98.78	0.31	0.28	0.29
May	88.36	75.90	73.99	216.97	206.20	201.86	138.29	126.18	122.88	0.40	0.37	0.35
June	24.70	19.06	17.09	88.48	84.92	79.83	35.41	31.94	27.71	0.14	0.14	0.12
July	16.19	17.10	12.26	50.08	47.75	43.84	25.56	27.32	22.31	0.07	0.05	0.05
August	8.61	8.21	5.86	25.25	25.12	22.30	18.23	19.55	15.82	0.05	0.05	0.04
September	44.29	40.34	23.99	100.33	95.60	85.73	74.04	57.74	53.77	0.24	0.25	0.17
October	69.65	59.54	49.40	146.39	141.26	116.15	113.15	105.63	93.00	0.49	0.46	0.43
November	79.15	68.20	65.89	155.85	145.30	137.58	119.54	106.59	104.28	0.51	0.48	0.43
December	77.23	72.54	63.77	156.00	149.17	133.44	124.83	109.38	103.32	0.65	0.60	0.58
Average	66.43	57.80	**52.73**	148.19	140.11	**131.69**	104.26	94.64	**89.39**	0.41	0.39	**0.36**

(**b**)

	MAPE (%)			RMSE (W/m^2)			MAE (W/m^2)			nRMSE		
	CNN1	**CNN2**	**LSTM**	**CNN1**	**CNN2**	**LSTM**	**CNN1**	**CNN2**	**LSTM**	**CNN1**	**CNN2**	**LSTM**
January	84.47	66.10	66.14	139.15	130.41	129.63	102.31	93.96	89.80	0.58	0.54	0.54
February	50.36	44.98	42.23	148.53	133.71	132.86	99.92	97.15	93.55	0.40	0.39	0.37
March	96.12	91.10	90.16	188.46	182.16	171.50	126.69	124.85	120.74	0.47	0.47	0.45
April	36.18	32.10	32.32	122.56	109.86	112.59	88.81	80.30	78.78	0.23	0.22	0.23
May	71.72	57.89	59.36	177.83	153.57	155.56	109.37	96.98	99.07	0.34	0.31	0.29
June	20.21	15.51	13.99	72.53	71.31	65.64	28.64	26.65	23.40	0.11	0.12	0.11
July	12.39	13.25	9.74	38.53	37.25	35.57	19.90	21.16	17.78	0.06	0.04	0.04
August	6.42	6.59	4.72	19.05	19.97	17.74	14.30	15.50	12.64	0.04	0.04	0.03
September	31.20	33.23	20.03	81.23	80.80	72.77	53.05	47.50	44.61	0.17	0.21	0.15
October	48.21	41.27	37.98	98.56	98.01	90.85	76.27	72.40	71.21	0.35	0.33	0.31
November	57.30	54.29	51.37	116.36	116.39	109.34	82.57	83.54	84.39	0.37	0.38	0.33
December	58.40	51.00	45.59	107.10	107.95	96.64	84.88	77.35	76.35	0.46	0.44	0.42
Average	47.75	42.28	**39.47**	109.16	103.45	**99.23**	73.89	69.78	**67.69**	0.30	0.29	**0.27**

Table 7. Windspeed forecasting results: (**a**) average daily forecasting results for 2015 and 2016 with the recursive multistep forecast strategy. (**b**) average daily forecasting results for 2015 and 2016 with the multiple-output forecast strategy.

(**a**)

	MAPE (%)			RMSE (m/s)			MAE (m/s)			nRMSE		
	CNN1	**CNN2**	**LSTM**	**CNN1**	**CNN2**	**LSTM**	**CNN1**	**CNN2**	**LSTM**	**CNN1**	**CNN2**	**LSTM**
January	30.3	34.06	31.56	2.9	3.04	3.04	2.05	2.28	2.16	0.33	0.35	0.35
February	31.68	38.11	32.79	2.74	2.92	2.83	1.99	2.22	2.02	0.35	0.37	0.36
March	39.31	41.83	41.67	2.87	3.10	3.10	1.98	2.19	2.19	0.39	0.40	0.40
April	44.63	63.19	48.27	1.21	1.63	1.33	1.00	1.38	1.00	0.22	0.31	0.24
May	37.50	40.8	39.9	2.16	2.39	2.29	1.64	1.85	1.79	0.35	0.39	0.38
June	35.59	36.23	38.72	1.83	2.05	2.06	1.45	1.53	1.55	0.26	0.28	0.30
July	13.02	13.53	14.11	1.69	1.75	1.76	1.09	1.14	1.14	0.18	0.19	0.19
August	17.36	18.87	18.74	1.75	2.13	2.00	1.14	1.32	1.28	0.25	0.29	0.26

Table 7. *Cont.*

(**a**)

	MAPE (%)			RMSE (m/s)			MAE (m/s)			nRMSE		
	CNN1	**CNN2**	**LSTM**	**CNN1**	**CNN2**	**LSTM**	**CNN1**	**CNN2**	**LSTM**	**CNN1**	**CNN2**	**LSTM**
September	17.67	20.37	19.81	1.78	2.07	1.83	1.12	1.36	1.31	0.23	0.27	0.24
October	31.35	41.98	41.27	2.26	2.68	2.55	1.41	1.76	1.73	0.31	0.37	0.36
November	36.45	40.96	39.73	2.33	2.77	2.69	1.63	2.00	1.82	0.36	0.44	0.42
December	25.86	27.8	29.16	2.59	2.65	2.63	1.92	2.09	2.04	0.29	0.30	0.30
Average	**30.06**	34.81	32.98	**2.18**	2.43	2.34	**1.54**	1.76	1.67	**0.29**	0.33	0.32

(**b**)

	MAPE (%)			RMSE (m/s)			MAE (m/s)			nRMSE		
	CNN1	**CNN2**	**LSTM**	**CNN1**	**CNN2**	**LSTM**	**CNN1**	**CNN2**	**LSTM**	**CNN1**	**CNN2**	**LSTM**
January	24.98	26.23	25.94	2.48	2.40	2.49	1.78	1.78	1.77	0.29	0.28	0.29
February	26.47	27.44	27.19	2.32	2.33	2.33	1.71	1.77	1.68	0.31	0.31	0.31
March	34.78	34.91	37.85	2.55	2.58	2.61	1.79	1.88	1.86	0.33	0.33	0.35
April	37.48	48.03	36.88	1.03	1.28	1.07	0.88	1.08	0.80	0.19	0.24	0.19
May	33.70	34.92	34.30	1.93	2.06	1.97	1.44	1.56	1.59	0.33	0.33	0.33
June	31.20	34.11	35.01	1.46	1.65	1.65	1.07	1.20	1.21	0.23	0.26	0.27
July	11.02	10.47	11.52	1.44	1.41	1.44	0.95	0.90	0.93	0.16	0.16	0.16
August	13.14	13.37	13.20	1.35	1.52	1.43	0.91	0.94	0.93	0.19	0.21	0.20
September	13.41	15.01	14.62	1.40	1.56	1.37	0.88	0.98	0.97	0.18	0.21	0.18
October	27.58	35.36	35.26	2.00	2.26	2.20	1.28	1.48	1.49	0.27	0.31	0.30
November	30.67	33.39	31.43	1.93	2.24	2.15	1.38	1.58	1.53	0.30	0.35	0.33
December	25.11	25.83	27.25	2.42	2.49	2.44	1.78	1.91	1.91	0.29	0.29	0.28
Average	**25.79**	28.26	27.54	**1.86**	1.98	1.93	**1.32**	1.42	1.39	**0.26**	0.27	0.27

3.2. Evaluation of Conventional Forecasting Performance Methods Using Error Metrics

In Tables 8 and 9, respectively, the average daily performance metrics for the two well-proven conventional methods examined (RegARMA and NARX) and the deep learning technique with the more accurate forecasting performance for solar irradiation (i.e., encoder–decoder LSTM) and windspeed (i.e., CNN1) are presented [72–77].

Table 8. Solar irradiation forecasting results: (**a**) average daily forecasting results for 2015 and 2016 with the conventional methods and the best deep learning technique via the recursive multistep forecast strategy. (**b**) average daily forecasting results for 2015 and 2016 with the conventional methods and the best deep learning technique via the multiple-output forecast strategy.

(**a**)

	Solar irradiation results											
	MAPE (%)			RMSE (W/m^2)			MAE (W/m^2)			nRMSE		
	Reg ARMA	**NARX**	**LSTM**	**Reg ARMA**	**NARX**	**LSTM**	**Reg ARMA**	**NARX**	**LSTM**	**Reg ARMA**	**NARX**	**LSTM**
January	146.08	127.72	91.57	221.53	206.23	180.37	154.25	149.91	125.55	0.91	0.82	0.72
February	83.38	73.79	58.33	242.46	209.54	185.58	175.77	154.48	128.82	0.77	0.61	0.51
March	176.89	160.73	129.16	291.50	280.21	251.70	200.03	195.26	176.40	0.76	0.73	0.64
April	50.63	48.47	41.49	177.97	160.80	141.83	145.95	131.45	98.78	0.37	0.33	0.29
May	88.58	84.86	73.99	231.43	224.74	201.86	140.49	136.35	122.88	0.46	0.41	0.35
June	26.40	22.31	17.09	84.96	85.76	79.83	36.84	34.23	27.71	0.17	0.15	0.12
July	18.57	15.84	12.26	49.12	48.01	43.84	30.54	27.95	22.31	0.11	0.08	0.05
August	12.30	9.42	5.86	28.85	23.18	22.30	21.55	19.05	15.82	0.09	0.07	0.04
September	51.03	42.04	23.99	111.34	98.45	85.73	77.06	65.22	53.77	0.32	0.28	0.17

Table 8. *Cont.*

(**a**)

	Solar irradiation results											
	MAPE (%)			RMSE (W/m^2)			MAE (W/m^2)			nRMSE		
	Reg ARMA	NARX	LSTM	Reg ARMA	NARX	LSTM	Reg ARMA	NARX	LSTM	Reg ARMA	NARX	LSTM
October	81.09	73.79	49.40	156.65	144.43	116.15	125.53	115.67	93.00	0.55	0.51	0.43
November	87.39	74.39	65.89	177.22	158.83	137.58	123.56	107.99	104.28	0.61	0.55	0.43
December	87.00	82.15	63.77	174.47	159.71	133.44	136.24	123.61	103.32	0.80	0.75	0.58
Average	75.78	67.96	**52.73**	162.29	149.99	**131.69**	113.98	105.10	**89.39**	0.49	0.44	**0.36**

(**b**)

	Solar irradiation results											
	MAPE (%)			RMSE (W/m^2)			MAE (W/m^2)			nRMSE		
	Reg ARMA	NARX	LSTM	Reg ARMA	NARX	LSTM	Reg ARMA	NARX	LSTM	Reg ARMA	NARX	LSTM
January	105.26	95.25	66.14	158.32	151.70	129.63	113.13	110.70	89.80	0.69	0.63	0.54
February	55.12	54.17	42.23	162.22	160.52	132.86	118.01	114.86	93.55	0.54	0.46	0.37
March	124.37	115.31	90.16	204.58	202.59	171.50	144.22	140.60	120.74	0.55	0.55	0.45
April	39.78	39.55	32.32	140.35	130.17	112.59	115.05	108.27	78.78	0.30	0.27	0.23
May	74.63	68.87	59.36	194.54	179.89	155.56	120.10	111.14	99.07	0.40	0.36	0.29
June	22.45	19.08	13.99	72.48	74.46	65.64	31.38	29.93	23.40	0.14	0.13	0.11
July	14.75	13.01	9.74	39.57	39.80	35.57	24.54	23.02	17.78	0.09	0.07	0.04
August	9.85	7.89	4.72	23.42	19.14	17.74	17.56	16.01	12.64	0.07	0.06	0.03
September	38.19	35.88	20.03	84.49	85.88	72.77	58.86	56.80	44.61	0.25	0.23	0.15
October	57.16	53.87	37.98	112.32	106.36	90.85	90.22	84.26	71.21	0.40	0.39	0.31
November	63.49	62.14	51.37	132.11	133.82	109.34	90.94	90.33	84.39	0.46	0.45	0.33
December	63.62	61.68	45.59	126.60	120.25	96.64	99.81	93.75	76.35	0.60	0.57	0.42
Average	55.72	52.23	**39.47**	120.92	117.05	**99.22**	85.32	81.64	**67.69**	0.37	0.35	**0.27**

Table 9. Windspeed forecasting results: (**a**) average daily forecasting results for 2015 and 2016 with the conventional methods and the best deep learning technique via the recursive multistep forecast strategy. (**b**) average daily forecasting results for 2015 and 2016 with the conventional methods and the best deep learning technique via the multiple-output forecast strategy.

(**a**)

	Windspeed results											
	MAPE(%)			RMSE (m/s)			MAE (m/s)			nRMSE		
	Reg ARMA	NARX	CNN1	Reg ARMA	NARX	CNN1	Reg ARMA	NARX	CNN1	Reg ARMA	NARX	CNN1
January	48.81	40.09	30.30	3.41	3.23	2.90	2.71	2.40	2.05	0.39	0.37	0.33
February	45.27	37.52	31.68	2.99	2.94	2.74	2.28	2.37	1.99	0.39	0.40	0.35
March	49.48	47.56	39.31	3.27	3.26	2.87	2.30	2.30	1.98	0.43	0.42	0.39
April	72.15	66.14	44.63	1.92	1.69	1.21	1.55	1.40	1.00	0.36	0.32	0.22
May	44.37	42.37	37.50	2.61	2.48	2.16	1.96	1.89	1.64	0.43	0.41	0.35
June	38.20	36.10	35.59	1.95	1.84	1.83	1.55	1.52	1.45	0.29	0.27	0.26
July	19.06	15.21	13.02	2.44	2.05	1.69	1.71	1.32	1.09	0.27	0.23	0.18
August	25.03	22.05	17.36	2.22	2.16	1.75	1.62	1.41	1.14	0.30	0.29	0.25
September	25.83	22.43	17.67	2.23	2.22	1.78	1.70	1.58	1.12	0.30	0.29	0.23
October	56.67	50.04	31.35	2.87	2.82	2.26	1.95	1.90	1.41	0.39	0.39	0.31
November	52.14	49.50	36.45	2.88	2.88	2.33	2.10	2.07	1.63	0.45	0.44	0.36
December	33.75	31.12	25.86	2.78	2.74	2.59	2.17	2.15	1.92	0.31	0.32	0.29
Average	42.56	38.34	**30.06**	2.63	2.53	**2.18**	1.97	1.86	**1.54**	0.36	0.35	**0.29**

Table 9. *Cont.*

(**b**)												
	Windspeed results											
	MAPE(%)			**RMSE (m/s)**			**MAE (m/s)**			**nRMSE**		
	Reg ARMA	**NARX**	**CNN1**	**Reg ARMA**	**NARX**	**CNN1**	**Reg ARMA**	**NARX**	**CNN1**	**Reg ARMA**	**NARX**	**CNN1**
January	38.58	33.92	24.98	2.78	2.76	2.48	2.15	2.06	1.78	0.32	0.33	0.29
February	34.02	31.14	26.47	2.51	2.58	2.32	1.87	2.04	1.71	0.34	0.35	0.31
March	42.18	40.96	34.78	2.82	2.82	2.55	2.02	2.13	1.79	0.37	0.37	0.33
April	58.19	52.33	37.48	1.59	1.39	1.03	1.24	1.16	0.88	0.29	0.27	0.19
May	40.05	38.17	33.70	2.33	2.22	1.93	1.73	1.70	1.44	0.38	0.37	0.33
June	43.96	38.94	31.20	1.90	1.82	1.46	1.44	1.34	1.07	0.30	0.29	0.23
July	15.47	12.73	11.02	1.99	1.73	1.44	1.41	1.11	0.95	0.22	0.20	0.16
August	18.23	15.99	13.14	1.60	1.62	1.35	1.19	1.05	0.91	0.22	0.23	0.19
September	19.42	16.87	13.41	1.70	1.74	1.40	1.31	1.21	0.88	0.23	0.24	0.18
October	48.86	45.15	27.58	2.51	2.50	2.00	1.71	1.69	1.28	0.34	0.34	0.27
November	43.60	40.93	30.67	2.36	2.40	1.93	1.73	1.87	1.38	0.37	0.37	0.30
December	32.36	30.44	25.11	2.69	2.68	2.42	2.07	2.04	1.78	0.31	0.30	0.29
Average	36.24	33.13	**25.80**	2.23	2.19	**1.86**	1.66	1.62	**1.32**	0.31	0.30	**0.26**

NARX is a nonlinear autoregressive exogenous model that has become popular in the last few years for its performance in timeseries forecasting problems, and RegARMA is a model that is based on regression with autoregressive-moving average (ARMA) time-series errors.

The architecture that was developed based on NARX is series–parallel. This architecture is used when the output of the NARX network is considered to be an estimate of the output of a nonlinear dynamic system. Specifically, the model was created with the following parameters: input delays (1:24), feedback delays (1:24), hidden layer size: 20, and training learning algorithm (Levenberg–Marquardt).

The parameters used in RegARMA are: autoregressive order: 10, moving average order: 24, autoregressive lags (1:10), and moving average lags: 24.

The inputs used for NARX and RegARMA were the same as those used in the deep learning techniques. Regarding the comparison of the conventional methods (Tables 8 and 9), NARX had slightly better performance than RegARMA for the majority of cases.

The comparison between these two categories of forecasting methods (conventional vs. deep learning, as presented in Tables 8 and 9) clearly showed the improved forecasting performance of the deep learning techniques in all of the cases presented and for both forecasting strategies (i.e., recursive multistep forecast strategy and multiple-output forecast strategy). Tables 10 and 11 compare the MAPE performance of these methods with the best performance in each category with respect to turbulence intensity (TI) and clearness index (CI). TI is defined as the ratio of standard deviation of fluctuating wind velocity to the mean windspeed, and it represents the intensity of wind velocity fluctuation [78]. CI is defined as the ratio of the monthly average daily irradiation on a horizontal surface to the monthly average daily extraterrestrial irradiation, and its value (which lies between 0 and 1) represents a measure of the clearness of the atmosphere: higher CI values appear under clear and sunny conditions, and lower CI values appear under cloudy conditions [54].

Table 10. CNN1 and NARX forecasting performance comparison: (a) windspeed average daily forecasting MAPE with respect to the turbulence intensity (TI) monthly average for years 2015–2016 via the recursive multistep forecast strategy. (**b**) windspeed average daily forecasting MAPE with respect to the turbulence intensity (TI) monthly average for years 2015–2016 via the multiple-output forecast strategy.

(**a**)												
	January	**February**	**March**	**April**	**May**	**June**	**July**	**August**	**September**	**October**	**November**	**December**
CNN1 MAPE	30.3	31.68	39.31	44.63	37.5	35.59	13.02	17.36	17.67	31.35	36.45	25.86
CNN1 MAPE improvement over NARX	24.42%	15.57%	17.35%	32.52%	11.49%	1.41%	14.40%	21.27%	21.22%	37.35%	26.36%	16.90%
Average TI	0.402	0.459	0.429	0.592	0.388	0.434	0.226	0.303	0.333	0.519	0.461	0.408
(**b**)												
	January	**February**	**March**	**April**	**May**	**June**	**July**	**August**	**September**	**October**	**November**	**December**
CNN1 MAPE	24.98	26.47	34.78	37.48	33.7	31.2	11.02	13.14	13.41	27.58	30.67	25.11
CNN1 MAPE improvement over NARX	26.36%	15.00%	15.09%	28.38%	11.71%	19.88%	13.43%	17.82%	20.51%	38.91%	25.07%	17.51%
Average TI	0.402	0.459	0.429	0.592	0.388	0.434	0.226	0.303	0.333	0.519	0.461	0.408

Table 11. LSTM and NARX forecasting performance comparison: (**a**) solar irradiation average daily forecasting MAPE with respect to the clearness index (CI) monthly average for years 2015–2016 via the recursive multistep forecast strategy. (**b**) solar irradiation average daily forecasting MAPE with respect to the clearness index (CI) monthly average for years 2015–2016 via the multiple-output forecast strategy.

(**a**)												
	January	**February**	**March**	**April**	**May**	**June**	**July**	**August**	**September**	**October**	**November**	**December**
LSTM MAPE	91.57	58.33	129.16	41.49	73.99	17.09	12.26	5.86	23.99	49.4	65.89	63.77
LSTM MAPE improvement over NARX	28.30%	20.95%	19.64%	14.40%	12.81%	23.40%	22.60%	37.79%	42.94%	33.05%	11.43%	22.37%
Average CI	0.42	0.45	0.49	0.56	0.60	0.64	0.65	0.64	0.62	0.55	0.50	0.43
(**b**)												
	January	**February**	**March**	**April**	**May**	**June**	**July**	**August**	**September**	**October**	**November**	**December**
LSTM MAPE	66.14	42.23	90.16	32.32	59.36	13.99	9.74	4.72	20.03	37.98	51.37	45.59
LSTM MAPE improvement over NARX	30.56%	22.04%	21.81%	18.28%	13.81%	26.68%	25.13%	40.18%	44.18%	29.50%	17.33%	26.09%
Average CI	0.42	0.45	0.49	0.56	0.60	0.64	0.65	0.64	0.62	0.55	0.50	0.43

More specifically, Table 10 compare the performance improvement of CNN1 over NARX (i.e., the conventional method with the best average forecasting performance) with respect to the TI value for the windspeed data of 2015–2016. From Table 10, it can be seen that CNN1 tends to have lower MAPE values with slight MAPE index improvement compared to NARX for the months with lower TI (i.e., July to September) and high MAPE index improvement for the months with higher TI (i.e., April and October). Table 11 compares the performance improvement of encoder–decoder LSTM over NARX (i.e., the conventional method with the best average forecasting performance) with respect to the CI value for solar irradiation data of 2015–2016. Regarding Table 11, it can be seen that for months with higher CI (i.e., summer months), MAPE index improvement is significantly lower.

As a result, the modified deep learning methods presented above perform much better than the conventional methods for the months with higher windspeed fluctuation. Moreover, comparing multi-head CNN for windspeed forecasting and encoder–decoder LSTM for solar irradiation forecasting with other popular deep learning techniques with the same one-day-ahead forecasting horizon (see the results of refs [69–71,79] has demonstrated that the presented modified deep learning models in this paper perform better.

Finally, Table 12 shows the efficiency of the forecasting models applied based on the coefficient of determination (r^2).

Table 12. Coefficient of determination (r^2): (**a**) for deep learning techniques with the best average daily forecasting performance via recursive multistep forecast strategy. (**b**) for deep learning techniques with the best average daily forecasting performance via the multiple-output forecast strategy.

(**a**)													
	Method	**January**	**February**	**March**	**April**	**May**	**June**	**July**	**August**	**September**	**October**	**November**	**December**
Windspeed forecasting	CNN1	0.74	0.72	0.71	0.68	0.7	0.72	0.8	0.78	0.78	0.73	0.7	0.74
Solar irradiation forecasting	LSTM	0.64	0.71	0.59	0.75	0.68	0.86	0.87	0.92	0.85	0.76	0.72	0.72
(**b**)													
	Method	**January**	**February**	**March**	**April**	**May**	**June**	**July**	**August**	**September**	**October**	**November**	**December**
Windspeed forecasting	CNN1	0.80	0.78	0.77	0.75	0.78	0.79	0.87	0.85	0.85	0.81	0.78	0.81
Solar irradiation forecasting	LSTM	0.71	0.78	0.67	0.84	0.74	0.95	0.95	0.97	0.93	0.85	0.80	0.79

4. Conclusions

In this paper, a multi-channel CNN, a multi-head CNN, and an encoder–decoder LSTM were implemented for one-day-ahead windspeed and solar irradiation forecasting for an isolated site on Dia Island, Crete, Greece. For the optimal sizing of a microgrid based mainly on RES, advancements in medium-term windspeed and solar irradiation forecasting will play a crucial role in the development of power systems. Moreover, they can be easily integrated into power system design and control, especially for isolated ones, as in the case study above. Increasingly accurate one-day-ahead solar irradiation and windspeed forecasting opens up opportunities for grid operators to predict and optimally balance energy generation and consumption, especially in isolated grids.

From the results of the one-day-ahead windspeed forecasts presented in this paper, it is clear that the worst forecast accuracy was observed during the winter months, as expected due to the increased variability of the windspeed, whereas during the summer months, there was a considerable improvement in forecasting accuracy, as the prediction errors were smaller. The multi-head CNN (CNN1) model gave better forecasting results than the other deep learning methods examined in this paper for windspeed forecasting. For solar irradiation forecasting, all models gave much better results during the summer months due to the absence of clouds relative to the other months, which was somewhat expected. Moreover, it was shown that the encoder–decoder LSTM network outperforms multi-head CNN (CNN1) and multi-channel CNN (CNN2) for solar irradiation forecasting, in contrast with windspeed forecasting, where multi-head CNN gave more accurate results. Additionally, the superiority of the multiple-output forecast strategy versus the recursive multistep forecast strategy is apparent in all cases of windspeed and solar irradiation forecasting.

Concerning the two well-proven conventional forecasting methodologies examined, NARX had slightly better performance than RegARMA in the majority of cases.

This study has also clearly demonstrated based on long historical data (i.e., 2005–2016) and extended comparative simulations the more accurate forecasting performance of the deep learning techniques in all the cases examined compared with the two well-proven

conventional forecasting methods also examined. However, given the extremely large differences in the number of parameters and in the use of information between deep learning and conventional forecasting techniques, this result was somewhat expected. Finally, comparison of the recursive multistep forecast strategy versus the multiple-output forecast strategy was thoroughly performed.

The improved, with the slight modifications proposed above, deep learning forecasting models presented in this paper were shown to perform better than conventional deep learning and autoregressive methods [69–73]. Moreover, they can also be applied to photovoltaic panel- and wind turbine-generated electric power forecasting. It must be noted that errors of the measuring equipment were not taken into account. If their measurements are available, additional meteorological and site determination factors such as the amount of rain, azimuth for solar irradiation, wind direction, and the terrain's form and roughness for windspeed forecasting could also be considered for further improvement of forecasting performance. Accurate solar irradiation and windspeed one-day-ahead forecasting constitutes the first indispensable module, together with the energy storage and management module, to form smart energy management system (SEMS) to optimize the operation of a microgrid incorporating RES.

Author Contributions: Conceptualization, K.B. and G.S.; Data curation, K.B., Y.K., and G.S.; Formal analysis, K.B. and Y.K.; Funding acquisition, Y.K. and G.S.; Investigation, K.B., Y.K. and G.S.; Methodology, K.B., Y.K. and G.S.; Project administration, Y.K. and G.S.; Resources, K.B., Y.K., and G.S.; Software, K.B.; Supervision, Y.K. and G.S.; Validation, K.B. and G.S.; Visualization, K.B. and Y.K.; Writing—original draft, K.B., Y.K. and G.S.; Writing—review and editing, Y.K. and G.S. All authors have read and agreed to the published version of the manuscript.

Funding: This work was funded in part by the "Centre for the study and sustainable exploitation of Marine Biological Recourses (CMBR)", which is implemented under the Action "Reinforcement of the Research and Innovation Infrastructure", funded by the Operational Program "Competitiveness, Entrepreneurship and Innovation" (NSRF 2014–2020, MIS Code 5002670) and co-financed by Greece and the European Union (European Regional Development Fund).

Institutional Review Board Statement: Not applicable.

Informed Consent Statement: Not applicable.

Data Availability Statement: The data are available at: konst.blazakis@gmail.com.

Acknowledgments: The authors would like to thank Nikolaos Efstathopoulos, graduate of the School of Electrical and Computer Engineering, Technical University of Crete, Greece, for his support.

Conflicts of Interest: The authors declare no conflict of interest.

Abbreviations and Nomenclature

Variable	Definition
ANN	Artificial neural networks
ARIMA	Autoregressive integrated moving average model
ARMA	Autoregressive moving average model
BiLSTM	Bidirectional long short-term memory neural network
BPNN	Back propagation neural network
CEEMD	Complementary ensemble empirical mode decomposition
CI	Clearness index
CNN	Convolutional neural network
DBN	Deep belief network
EMD-ENN	Empirical mode decomposition and Elman neural network
EWT	Empirical wavelet transform
FFNN	Feed forward neural networks
G_{on}	Normalized extraterrestrial irradiance
G_{sn}	Normalized surface irradiance

HTD	Hybrid timeseries decomposition strategy
GSRT	General Secretariat for Research and Technology
HFRI	Hellenic Foundation for Research and Innovation
HMD	Hybrid model decomposition method
K	Number of hours of each day
LSSVM	Least-square support vector machine
LSTM	Long short-term memory
MAE	Mean absolute error
MAPE	Mean absolute percentage error
ML	Machine learning
MOBBSA	Multi-objective binary backtracking search algorithm
MSE	Mean squared error
NARX	Nonlinear autoregressive exogenous model
NDD(d)	Normalized discrete difference per day
NDD(h)	Normalized discrete difference per hour
nMAE	Normalized mean absolute error
nRMSE	Normalized root mean squared error
NWP	Numerical weather prediction forecasting model
obs	Observation
OSORELM	Online sequential outlier robust extreme learning machine method
RegARMA	Regression model with autoregressive moving average errors
RES	Renewable energy sources
RMSE	Root mean squared error
RNN	Recurrent neural networks
seq2seq	Sequence-to-sequence
SEMS	smart energy management system
SVM	Support vector machine
TI	Turbulence intensity
VMD	Variational mode decomposition
WRF	Weather research and forecasting model
WT-ARIMA	Wavelet transform-autoregressive integrated moving average model
x_i	Current value
x_{max}	Maximum original value
x_{min}	Minimum original value
y	Normalized value

References

1. Brahimi, T. Using Artificial Intelligence to Predict Wind Speed for Energy Application in Saudi Arabia. *Energies* **2019**, *12*, 4669. [CrossRef]
2. Akarslan, E.; Hocaoglu, F.O. A novel method based on similarity for hourly solar irradiance forecasting. *Renew. Energy* **2017**, *112*, 337–346. [CrossRef]
3. Kariniotakis, G.N.; Stavrakakis, G.S.; Nogaret, E.F. Wind power forecasting using advanced neural networks models. *IEEE Trans. Energy Convers.* **1996**, *11*, 762–767. [CrossRef]
4. Wang, Y.; Wu, L. On practical challenges of decomposition-based hybrid forecasting algorithms for wind speed and solar irradiation. *Energy* **2016**, *112*, 208–220. [CrossRef]
5. Zhang, Y.; Pan, G.; Chen, B.; Han, J.; Zhao, Y.; Zhang, C. Short-term wind speed prediction model based on GA-ANN improved by VMD. *Renew. Energy* **2020**, *156*, 1373–1388. [CrossRef]
6. Wang, J.; Song, Y.; Liu, F.; Hou, R. Analysis and application of forecasting models in wind power integration: A review of multi-step-ahead wind speed forecasting models. *Renew. Sustain. Energy Rev.* **2016**, *60*, 960–981. [CrossRef]
7. Husein, M.; Chung, I.Y. Day-ahead solar irradiance forecasting for microgrids using a long short-term memory recurrent neural network: A deep learning approach. *Energies* **2019**, *12*, 1856. [CrossRef]
8. Wang, Y.; Zou, R.; Liu, F.; Zhang, L.; Liu, Q. A review of wind speed and wind power forecasting with deep neural networks. *Appl. Energy* **2021**, *304*, 117766. [CrossRef]
9. Wu, B.; Wang, L.; Zeng, Y.R. Interpretable wind speed prediction with multivariate time series and temporal fusion transformers. *Energy* **2022**, *252*, 123990. [CrossRef]
10. Liu, Z.; Jiang, P.; Wang, J.; Zhang, L. Ensemble forecasting system for short-term wind speed forecasting based on optimal sub-model selection and multi-objective version of mayfly optimization algorithm. *Expert Syst. Appl.* **2021**, *177*, 114974. [CrossRef]

11. Bellinguer, K.; Girard, R.; Bontron, G.; Kariniotakis, G. Short-term Forecasting of Photovoltaic Generation based on Conditioned Learning of Geopotential Fields. In Proceedings of the 55th International Universities Power Engineering Conference—Virtual Conference UPEC 2020—"Verifying the Targets", Torino, Italy, 1–4 September 2020; pp. 1–6.
12. Mora-Lopez, L.I.; Sidrach-De-Cardona, M. Multiplicative ARMA models to generate hourly series of global irradiation. *Sol. Energy* **1998**, *63*, 283–291. [CrossRef]
13. Erdem, E.; Shi, J. ARMA based approaches for forecasting the tuple of wind speed and direction. *Appl. Energy* **2011**, *88*, 1405–1414. [CrossRef]
14. Wang, F.; Xu, H.; Xu, T.; Li, K.; Shafie-Khah, M.; Catalao, J.P.S. The values of market-based demand response on improving power system reliability under extreme circumstances. *Appl. Energy* **2017**, *193*, 220–231. [CrossRef]
15. Yang, D.; Ye, Z.; Lim, L.H.I.; Dong, Z. Very short term irradiance forecasting using the lasso. *Sol. Energy* **2015**, *114*, 314–326. [CrossRef]
16. Maafi, A.; Adane, A. A two-state Markovian model of global irradiation suitable for photovoltaic conversion. *Sol. Wind Technol.* **1989**, *6*, 247–252. [CrossRef]
17. Shakya, A.; Michael, S.; Saunders, C.; Armstrong, D.; Pandey, P.; Chalise, S.; Tonkoski, R. Solar Irradiance Forecasting in Remote Microgrids Using Markov Switching Model. *IEEE Trans. Sustain. Energy* **2017**, *8*, 895–905. [CrossRef]
18. Jiang, Y.; Long, H.; Zhang, Z.; Song, Z. Day-Ahead Prediction of Bihourly Solar Radiance with a Markov Switch Approach. *IEEE Trans. Sustain. Energy* **2017**, *8*, 1536–1547. [CrossRef]
19. Ekici, B.B. A least squares support vector machine model for prediction of the next day solar insolation for effective use of PV systems. *Measurement* **2014**, *50*, 255–262. [CrossRef]
20. Bae, K.Y.; Jang, H.S.; Sung, D.K. Hourly Solar Irradiance Prediction Based on Support Vector Machine and Its Error Analysis. *IEEE Trans. Power Syst.* **2017**, *32*, 935–945. [CrossRef]
21. Zhang, X.; Wang, J. A novel decomposition-ensemble model for forecasting short term load-time series with multiple seasonal patterns. *Appl. Soft Comput.* **2018**, *65*, 478–494. [CrossRef]
22. Yadab, A.K.; Chandel, S.S. Solar radiation prediction using Artificial Neural Network techniques: A review. Renew. Sustain. *Energy Rev.* **2014**, *33*, 772–781.
23. Srivastava, S.; Lessmann, S. A comparative study of LSTM neural networks in forecasting day-ahead global horizontal irradiance with satellite data. *Sol. Energy* **2018**, *162*, 232–247. [CrossRef]
24. Shi, Z.; Member, S.; Liang, H.; Dinavahi, V.; Member, S. Direct Interval Forecast of Uncertain Wind Power Based on Recurrent Neural Networks. *IEEE Trans. Sustain. Energy* **2018**, *9*, 1177–1187. [CrossRef]
25. Cao, Q.; Ewing, B.T.; Thompson, M.A. Forecasting wind speed with recurrent neural networks. *Eur. J. Oper. Res.* **2012**, *221*, 148–154. [CrossRef]
26. Liu, H.; Duan, Z.; Chen, C.; Wu, H. A novel two-stage deep learning wind speed forecasting method with adaptive multiple error corrections and bivariate Dirichlet process mixture model. *Energy Convers. Manag.* **2019**, *199*, 111975. [CrossRef]
27. Zhu, A.; Li, X.; Mo, Z.; Wu, H. Wind Power Prediction Based on a Convolutional Neural Network. In Proceedings of the International Conference on Circuits, Devices and Systems, Tibet Hotel Chengdu, Chengdu, China, 5–8 September 2017; pp. 133–135.
28. Li, Y.; Wu, H.; Liu, H. Multi-step wind speed forecasting using EWT decomposition, LSTM principal computing, RELM subordinate computing and IEWT reconstruction. *Energy Convers. Manag.* **2018**, *167*, 203–219. [CrossRef]
29. Qing, X.; Niu, Y. Hourly day-ahead solar irradiance prediction using weather forecasts by LSTM. *Energy* **2018**, *148*, 461–468. [CrossRef]
30. Liu, H.; Mi, X.; Li, Y. Smart multi-step deep learning model for wind speed forecasting based on variational mode decomposition, singular spectrum analysis, LSTM network and ELM. *Energy Convers. Manag.* **2018**, *159*, 54–64. [CrossRef]
31. Liu, H.; Mi, X.-W.; Li, Y.-F. Wind speed forecasting method based on deep learning strategy using empirical wavelet transform, long short term memory neural network and Elman neural network. *Energy Convers. Manag.* **2018**, *156*, 498–514. [CrossRef]
32. Kotlyar, O.; Kamalian-Kopae, M.; Pankratova, M.; Vasylchenkova, A.; Prilepsky, J.E.; Turitsyn, S.K. Convolutional long short-term memory neural network equalizer for nonlinear Fourier transform-based optical transmission systems. *Opt. Express* **2021**, *29*, 11254–11267. [CrossRef]
33. Wang, H.; Wang, G.; Li, G.; Peng, J.; Liu, Y. Deep belief network based deterministic and probabilistic wind speed forecasting approach. *Appl. Energy* **2016**, *182*, 80–93. [CrossRef]
34. Zhou, Q.; Wang, C.; Zhang, G. Hybrid forecasting system based on an optimal model selection strategy for different wind speed forecasting problems. *Appl. Energy* **2019**, *250*, 1559–1580. [CrossRef]
35. Viet, D.T.; Phuong, V.V.; Duong, M.Q.; Tran, Q.T. Models for short-term wind power forecasting based on improved artificial neural network using particle swarm optimization and genetic algorithms. *Energies* **2020**, *13*, 2873. [CrossRef]
36. Wang, F.; Mi, Z.; Su, S.; Zhao, H. Short-Term Solar Irradiance Forecasting Model Based on Artificial Neural Network Using Statistical Feature Parameters. *Energies* **2012**, *5*, 1355–1370. [CrossRef]
37. Arbizu-Barrena, C.; Ruiz-Arias, J.A.; Rodríguez-Benítez, F.J.; Pozo-Vázquez, D.; Tovar-Pescador, J. Short-term solar radiation forecasting by adverting and diffusing MSG cloud index. *Sol. Energy* **2017**, *155*, 1092–1103. [CrossRef]
38. Voyant, C.; Muselli, M.; Paoli, C.; Nivet, M.-L. Numerical weather prediction (NWP) and hybrid ARMA/ANN model to predict global radiation. *Energy* **2012**, *39*, 341–355. [CrossRef]

39. Wang, F.; Zhen, Z.; Liu, C.; Mi, Z.; Hodge, B.M.; Shafie-khah, M.; Catalão, J.P.S. Image phase shift invariance based cloud motion displacement vector calculation method for ultra-short-term solar PV power forecasting. *Energy Convers. Manag.* **2018**, *157*, 123–135. [CrossRef]
40. Wang, F.; Li, K.; Wang, X.; Jiang, L.; Ren, J.; Mi, Z.; Shafie-khah, M.; Catalão, J.P.S. A Distributed PV System Capacity Estimation Approach Based on Support Vector Machine with Customer Net Load Curve Features. *Energies* **2018**, *11*, 1750. [CrossRef]
41. Verbois, H.; Huva, R.; Rusydi, A.; Walsh, W. Solar irradiance forecasting in the tropics using numerical weather prediction and statistical learning. *Sol. Energy* **2018**, *162*, 265–277. [CrossRef]
42. Li, C.; Xiao, Z.; Xia, X.; Zou, W.; Zhang, C. A hybrid model based on synchronous optimization for multi-step short-term wind speed forecasting. *Appl. Energy* **2018**, *215*, 131–144. [CrossRef]
43. Begam, K.M.; Deepa, S. Optimized nonlinear neural network architectural models for multistep wind speed forecasting. *Comput. Electr. Eng.* **2019**, *78*, 32–49. [CrossRef]
44. Zhang, D.; Peng, X.; Pan, K.; Liu, Y. A novel wind speed forecasting based on hybrid decomposition and online sequential outlier robust extreme learning machine. *Energy Convers. Manag.* **2019**, *180*, 338–357. [CrossRef]
45. Wang, J.; Zhang, W.; Li, Y.; Wang, J.; Dang, Z. Forecasting wind speed using empirical mode decomposition and Elman neural network. *Appl. Soft. Comput.* **2014**, *23*, 452–459. [CrossRef]
46. Singh, S.N.; Mohapatra, A. Repeated wavelet transform based ARIMA model for very short-term wind speed forecasting. *Renew. Energy* **2019**, *136*, 758–768.
47. Hu, J.; Wang, J.; Ma, K. A hybrid technique for short-term wind speed prediction. *Energy* **2015**, *81*, 563–574. [CrossRef]
48. Wang, J.; Zhang, N.; Lu, H. A novel system based on neural networks with linear combination framework for wind speed forecasting. *Energy Convers. Manag.* **2019**, *181*, 425–442. [CrossRef]
49. Tian, C.; Hao, Y.; Hu, J. A novel wind speed forecasting system based on hybrid data preprocessing and multi-objective optimization. *Appl. Energy* **2018**, *231*, 301–319. [CrossRef]
50. Neshat, M.; Nezhad, M.M.; Abbasnejad, E.; Mirjalili, S.; Tjernberg, L.B.; Garcia, D.A.; Wagner, M. A deep learning-based evolutionary model for short-term wind speed forecasting: A case study of the Lillgrund offshore wind farm. *Energy Convers. Manag.* **2021**, *236*, 114002. [CrossRef]
51. Lv, S.X.; Wang, L. Deep learning combined wind speed forecasting with hybrid time series decomposition and multi-objective parameter optimization. *Appl. Energy* **2022**, *311*, 118674. [CrossRef]
52. Duan, J.; Zuo, H.; Bai, Y.; Duan, J.; Chang, M.; Chen, B. Short-term wind speed forecasting using recurrent neural networks with error correction. *Energy* **2021**, *217*, 119397. [CrossRef]
53. Muneer, T. Solar radiation model for Europe. *Build. Serv. Eng. Res. Technol.* **1990**, *11*, 153–163. [CrossRef]
54. Duffie, J.; Beckman, W.; Blair, N. *Solar Engineering of Thermal Processes, Photovoltaics and Wind*, 5th ed.; Wiley: Hoboken, NJ, USA, 2020; pp. 3–44.
55. Voyant, C.; Notton, G.; Kalogirou, S.; Nivet, M.L.; Paoli, C.; Motte, F.; Fouilloy, A. Machine learning methods for solar radiation forecasting: A review. *Renew. Energy* **2017**, *105*, 569–582. [CrossRef]
56. Chung, H.; Shin, K.-s. Genetic algorithm-optimized multi-channel convolutional neural network for stock market prediction. *Neural Comput. Appl.* **2020**, *32*, 7897–7914. [CrossRef]
57. Karatzoglou, A. *Multi-Channel Convolutional Neural Networks for Handling Multi-Dimensional Semantic Trajectories and Predicting Future Semantic Locations. International Workshop on Multiple-Aspect Analysis of Semantic Trajectories*; Springer: Cham, Switzerland, 2019; pp. 117–132.
58. Wikipedia. Available online: https://en.wikipedia.org/wiki/Convolutional_neural_network (accessed on 20 January 2021).
59. Brownlee, J. Deep Learning for Time Series Forecasting: Predict the Future with MLPs, CNNs and LSTMs. In *Python*; Machine Learning Mastery: New York, NY, USA, 2018.
60. Wikipedia. Available online: https://en.wikipedia.org/wiki/Long_short-term_memory (accessed on 23 January 2021).
61. Medium. Available online: https://medium.com/ (accessed on 25 January 2021).
62. Suradhaniwar, S.; Kar, S.; Durbha, S.S.; Jagarlapudi, A. Time Series Forecasting of Univariate Agrometeorological Data: A Comparative Performance Evaluation via One-Step and Multi-Step Ahead Forecasting Strategies. *Sensors* **2021**, *21*, 2430. [CrossRef] [PubMed]
63. Neshat, M.; Nezhad, M.M.; Mirjalili, S.; Piras, G.; Garcia, D.A. Quaternion convolutional long short-term memory neural model with an adaptive decomposition method for wind speed forecasting: North aegean islands case studies. *Energy Convers. Manag.* **2022**, *259*, 115590. [CrossRef]
64. Pareek, V.; Chaudhury, S. Deep learning-based gas identification and quantification with auto-tuning of hyper-parameters. *Soft Comput.* **2021**, *25*, 14155–14170. [CrossRef]
65. Koutsoukas, A.; Monaghan, K.J.; Li, X.; Huan, J. Deep-learning: Investigating deep neural networks hyper-parameters and comparison of performance to shallow methods for modeling bioactivity data. *J. Cheminformatics* **2017**, *9*, 1–13. [CrossRef]
66. Kwon, D.H.; Kim, J.B.; Heo, J.S.; Kim, C.M.; Han, Y.H. Time series classification of cryptocurrency price trend based on a recurrent LSTM neural network. *J. Inf. Processing Syst.* **2019**, *15*, 694–706.
67. Qu, Z.; Xu, J.; Wang, Z.; Chi, R.; Liu, H. Prediction of electricity generation from a combined cycle power plant based on a stacking ensemble and its hyperparameter optimization with a grid-search method. *Energy* **2021**, *227*, 120309. [CrossRef]
68. Lederer, J. Activation Functions in Artificial Neural Networks: A Systematic Overview. *arXiv* **2021**, arXiv:2101.09957.

69. Wang, J.; Qin, S.; Zhou, Q.; Jiang, H. Medium-term wind speeds forecasting utilizing hybrid models for three different sites in Xinjiang, China. *Renew. Energy* **2015**, *76*, 91–101. [CrossRef]
70. Cai, H.; Jia, X.; Feng, J.; Yang, Q.; Hsu, Y.M.; Chen, Y.; Lee, J. A combined filtering strategy for short term and long term wind speed prediction with improved accuracy. *Renew. Energy* **2019**, *136*, 1082–1090. [CrossRef]
71. Zhu, Q.; Chen, J.; Shi, D.; Zhu, L.; Bai, X.; Duan, X.; Liu, Y. Learning temporal and spatial correlations jointly: A unified framework for wind speed prediction. *IEEE Trans. Sustain. Energy* **2019**, *11*, 509–523. [CrossRef]
72. Hošovský, A.; Piteľ, J.; Adámek, M.; Mižáková, J.; Židek, K. Comparative study of week-ahead forecasting of daily gas consumption in buildings using regression ARMA/SARMA and genetic-algorithm-optimized regression wavelet neural network models. *J. Build. Eng.* **2021**, *34*, 101955. [CrossRef]
73. López, G.; Arboleya, P. Short-term wind speed forecasting over complex terrain using linear regression models and multivariable LSTM and NARX networks in the Andes Mountains, Ecuador. *Renew. Energy* **2022**, *183*, 351–368. [CrossRef]
74. Github. Available online: https://github.com/tristanga/Machine-Learning (accessed on 21 January 2021).
75. Github. Available online: https://github.com/vishnukanduri/Time-series-analysis-in-Python (accessed on 21 January 2021).
76. Github. Available online: https://github.com/husnejahan/Multivariate-Time-series-Analysis-using-LSTM-ARIMA (accessed on 21 January 2021).
77. Github. Available online: https://github.com/Alro10/deep-learning-time-series (accessed on 21 January 2021).
78. Li, F.; Ren, G.; Lee, J. Multi-step wind speed prediction based on turbulence intensity and hybrid deep neural networks. *Energy Convers. Manag.* **2019**, *186*, 306–322. [CrossRef]
79. Lan, H.; Zhang, C.; Hong, Y.Y.; He, Y.; Wen, S. Day-ahead spatiotemporal solar irradiation forecasting using frequency-based hybrid principal component analysis and neural network. *Appl. Energy* **2019**, *247*, 389–402. [CrossRef]

energies

MDPI

Article

Scalability and Replicability for Smart Grid Innovation Projects and the Improvement of Renewable Energy Sources Exploitation: The FLEXITRANSTORE Case

Georgios Fotis [1], Christos Dikeakos [1], Elias Zafeiropoulos [2], Stylianos Pappas [2] and Vasiliki Vita [2,3,*]

[1] IPTO (Independent Power System Operator), Dyrrachiou 89 & Kifissou, 10443 Athens, Greece; gfotis@admie.gr (G.F.); c.dikeakos@admie.gr (C.D.)
[2] Institute of Communications and Computer Systems, School of Electrical and Computer Engineering (ECE), National Technical University of Athens (NTUA), 9 Iroon Polytechniou Street, 15780 Athens, Greece; eagle74@gmail.com (E.Z.); steliospappas74@gmail.com (S.P.)
[3] Department of Electrical and Electronics Engineering Educators, ASPETE—School of Pedagogical and Technological Education of Athens, Stathmos "ISAP", 14121 N. Heraklion, Greece
* Correspondence: vasvita@aspete.gr; Tel.: +30-210-289-6955

Abstract: In this paper, detailed scalability and replicability plans have been developed to facilitate the adoption of innovation technologies in the pan-EU market. Smart grid development must enable both information and power exchange between suppliers and customers, thanks to the enormous innovation in intelligent communication, monitoring, and management systems. Implementing physical infrastructure alone is not enough, but a smart grid must include new business models and new regulations. In recent years, the number, participants, and scope of smart grid initiatives have increased, with different goals and results. FLEXITRANSTORE project integrates hardware and software solutions in all areas of the transmission system and wholesale markets, unleashing the potential for full flexibility of power systems and promoting the penetration of renewable energy sources and pan-EU markets. Full deployment of these demonstrated solutions requires a reasonable level of scalability and replicability to prevent project demonstrators from continuing local experimental exercises. Scalability and replicability are fundamental requirements for successful scaling-up and replication. Therefore, scalability and replicability enable or at least reduce barriers to the growth and reuse of project demonstrator results.

Keywords: smart grid; scalability; replicability; FLEXITRANSTORE

Citation: Fotis, G.; Dikeakos, C.; Zafeiropoulos, E.; Pappas, S.; Vita, V. Scalability and Replicability for Smart Grid Innovation Projects and the Improvement of Renewable Energy Sources Exploitation: The FLEXITRANSTORE Case. *Energies* **2022**, *15*, 4519. https://doi.org/10.3390/en15134519

Academic Editor: George S. Stavrakakis

Received: 1 June 2022
Accepted: 20 June 2022
Published: 21 June 2022

Publisher's Note: MDPI stays neutral with regard to jurisdictional claims in published maps and institutional affiliations.

Copyright: © 2022 by the authors. Licensee MDPI, Basel, Switzerland. This article is an open access article distributed under the terms and conditions of the Creative Commons Attribution (CC BY) license (https://creativecommons.org/licenses/by/4.0/).

1. Introduction

1.1. Smart Grids and Renewable Energy Sources

Smart grid technology is enabling the effective distribution and management of Renewable Energy Sources (RES) such as wind, solar, and hydrogen. Renewable energy integration aims to improve the electric grid's system design, planning, and operation in order to reduce carbon emissions and other air pollutants by increasing the use of renewable energy, storage systems, and other clean distributed generation.

A great variety of distributed energy resource assets are connected to the power grid via the smart grids. Utilities can rapidly detect and manage service issues by leveraging the Internet of Things (IoT) to collect data on the smart grid [1–3]. This self-healing capability is critical to the smart grid because utilities no longer rely on customers to report problems. Wind farms, for example, rely on mechanical gears with several sensors in each connection. Every sensor can record current weather and ambient conditions. These data are then promptly routed through the grid to alert the utility of any problems, improving both service quality and safety.

Electric vehicles, storage systems, and distributed generation of RES are transforming distribution grid characteristics around the world [4,5]. Under certain operational settings,

these novel components could create bidirectional energy flows. This has an impact on grid planning since they are optimized for one direction flows. In these conditions, even if the existing processes for organizing distribution networks on radial layouts are very straightforward and extensively verified, they cannot be implemented holistically.

FLEXITRANSTORE (An Integrated Platform for Increased FLEXIbility in smart TRANSmission grids with STORage Entities and large penetration of Renewable Energy Sources) contributes to the development of a pan-European transmission grid with high flexibility and high interconnection [6]. This will accelerate the transformation of the current energy production mix by increasing the share of renewable energy sources. In order to bring flexibility to the European power system, new control and storage methods, smart grid technologies, and new market approaches will be developed, installed, and demonstrated.

1.2. Smart Grids and FLEXITRANSTORE

Currently, most smart grid projects are still in the phase of Research and Development (R&D) or demonstration. In [7], it is confirmed that regardless of how quickly various utilities embrace smart grid concepts, technologies, and systems, this massive transformation is inevitable, and at the same time, many researchers across the globe are working to make this transition by developing the next-generation technologies required to realize the smart grid easier. Working on this direction in March 2011, the European Commission and the European Free Trade Association (EFTA) issued the Smart Grid Mandate M/490 which requested CEN, CENELEC, and ETSI to develop a framework to enable ESOs to perform continuous standard enhancement and development in the smart grid field [8]. Research work in [9] analyses the state-of-the-art of smart grids, in their technical, management, security, and optimization aspects, providing also a brief overview of the regulatory aspects involved in the development of a smart grid, mainly from the viewpoint of the European Union.

In [10], the smart grid development in Brazil is performed, presenting the policy and regulation efforts beyond investments, taking into account a pattern for smart grid development, since the smart grid implementation is very high. Moreover, in [11] a review of the current research on smart grids is carried out, shedding light on the development of smart grids in China, which is then analyzed to identify the obstacles and barriers in the development process. Reference [12] presents a survey of smart grid projects in Europe bringing together input and feedback from a variety of stakeholders through a cooperative and transparent process. D. Novosel makes clear in [13] that smart grid technologies are required to manage grid complexity, addressing a holistic smart grid approach and experiences with deploying smart grid projects. Research work in [14] indicates that demand response services or vehicle-to-grid and grid-to-vehicle services will be offered in conjunction with the supply of RES.

The work in [15] deals with the assessment of the flexibility benefits coming from smart grid innovations, developed in the H2020 project FLEXITRANSTORE. The project includes pilots in various sites across the Europe, where appropriate technologies have been developed in an effort to enhance the flexibility of the systems examined in the context of the project. Research work in [16] demonstrates the trading and flexibility of services amongst TSOs, DSOs, and Prosumers in a transparent, secure, and cost-effective manner using Blockchain-based TSO-DSO flexibility marketplace. In [17] a flexibility adequacy assessment of the countries of South-East Europe is presented, and in [18,19] a novel technology integration is considered in order to provide more flexibility resources to the power system to absorb more renewable energy.

In [20] a flexibility-oriented day-ahead market model that accounts for renewable sources and storage units where no incentive is provided to the renewable sources is developed, and its results demonstrate how a system can cope with renewable sources with no incentive in the presence of storage. Moreover, in [21] a detailed survey conducted during FLEXITRANSTORE on identifying stakeholders' opinion on electricity networks'

challenges is presented and commented and in [22] grid flexibility solutions for transmission networks with increased RES penetration are examined.

The operational flexibility potential of individual power system assets and their aggregation at the system level is examined in [23] and a similar work in [24] present a methodology to assess the flexibility of a power system while explicitly considering the limitations of the transmission network. Researchers in [25] evaluate the operational flexibility for power system with energy storage, while in [26] a framework to efficiently characterize the available operational flexibility in a multi-area power system is presented and in [27] the flexibility of a test system with increasing penetrations of variable generation is assessed.

Electricity, natural gas, water, and district heating/cooling systems are predominantly planned and operated independently. The work presented in [28] centers on residential city districts as source of flexible electrical energy demand and generation, while [29] presents an integrated optimization and control of such systems at multiple spatiotemporal scales that can bring significant socioeconomic, operational efficiency, and environmental benefits. In [30], an in-depth review of the modeling and implementation of flexible ramping products that have been proposed in the industry to improve the availability of ramp capacity is presented.

The European Commission in its effort to speed the clean energy transition supports the development of flexible energy efficiency and renewable financing platforms at national or regional level [31]. In [32], the Smart Grids Task Force reviews the value which demand side flexibility could be able to bring to the energy system and its possible impact to the future market development in Europe.

Due to a lack of practical experience, the outcome of implementing smart grids on a large scale remains questionable. Many projects have been launched around the world to evaluate various smart grid solutions in real-world systems [33–36]. These projects provide extremely significant information, but the findings obtained are dependent on the precise setting in which the tests are carried out. As a result, the testing conclusions may not be immediately applicable to the deployment of the same solutions on a bigger scale or in other regions. To understand the impact of the context on the outcomes of deploying a smart grid solution, a thorough investigation must be undertaken. It is required to assess the effects of various smart grid systems on existing networks in greater scale for various DEMOs, and this is the main goal of the current work.

FLEXITRANSTORE develops a next-generation Flexible Energy Grid (FEG) that will be integrated into the European Internal Energy Market (IEM) through the flexibility services [15–32]. The project includes pilots in various sites across Europe, where appropriate technologies have been developed in an effort to enhance the flexibility of the systems examined in the context of the project. The work presented here takes both national and regional approaches and recognizes the need to seamlessly integrate the national markets. Networks in Southeast Europe, in particular, do not yet have the high levels of interconnectivity that other European networks have. Full deployment of the tested solutions requires a reasonable level of scalability and replicability to prevent the project demonstrator from continuing local experimental exercises. This paper focuses on analyzing the scalability, replicability, and implementation conditions of the FLEXITRANSTORE concept.

This FEG supports the capabilities of power systems to maintain continuous operation in the face of rapid and large fluctuations in supply or demand. Therefore, as shown in Figure 1, within this integrated FEG, new business models and a wholesale market infrastructure must be upgraded to network players, providing incentives to new ones to participate. Moreover, it will demonstrate new energy trading and business perspectives for cross-border resources management.

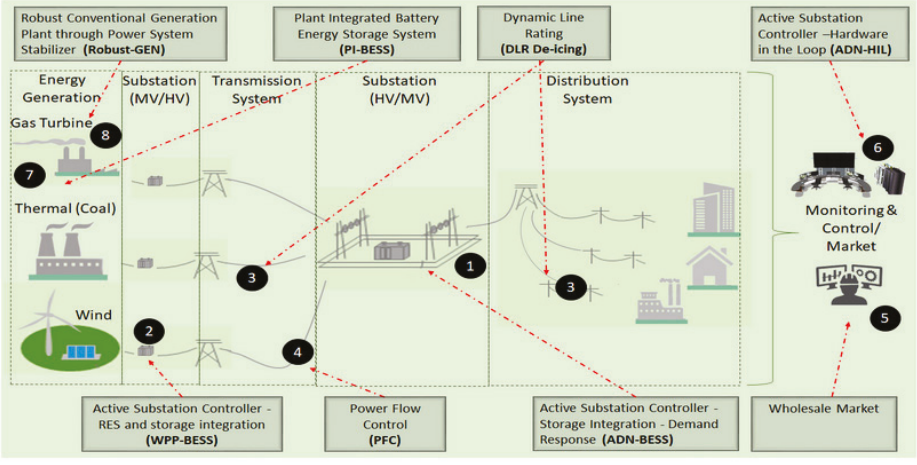

Figure 1. How the European Power System will be transformed by FLEXITRANSTORE through interventions targeting the whole Energy Value Chain [6].

The ability of a process, network, or system to respond to the growth in demand by increasing respectively its scope range or size is called scalability [33–35,37,38]. For FLEXITRANSTORE scalability is crucial, since in different demonstration sites, with different technical requirements development, implementation and validation of several demos have been carried out. The first step to deploy the technological innovation on a large-scale of the FLEXITRANSTORE project in order to meet growing volumes of demand is the scalability analysis. The ability of a process, network, or system to be duplicated in another time or location is called replicability [33–35,37,38]. The replication ability of the FLEXITRANSTORE technological innovations has been studied due to the application of different technologies and costs for different countries.

The focus of this work is to evaluate the experience and the demonstration results, gathered during the period of research, implementation, and testing in order to develop at EU level a detailed scalability and replicability plan. In order to find the practical problems and major benefits of the proposed actual field technical innovations, the results need to be evaluated. Moreover, it is extremely important to find how these innovations meet both the challenges of the variable integration of renewable energy sources and the interconnection of production capacity by increasing the awareness of the grid's flexibility. Two sets of questionnaires one for scalability and the other for replicability have been developed. The project partners are the responders of this survey, who have been involved as a team leader or contributors in the development of functionalities.

FLEXITRANSTORE provides technical innovations that are weighed against the EU energy targets and specific scalability and replicability factors. These factors affect the following four common areas of interest: regulatory, economic, technical, stakeholder acceptance. Replicability factors are: Network configuration, Standardization, Macroeconomics, Interoperability, Market design, Business model (economic factors), Regulation, and Acceptance. Scalability factors are: Modularity, Technology evolution, Software integration, Existing infrastructure (technical factors), Interface design, Economy of scale, Profitability (economic factors), Regulation, and Acceptance.

2. The European Commission Bridge—Scalability and Replicability Analysis (SRA)

BRIDGE is a European Commission initiative that integrates the Horizon 2020 Smart Grid and Energy Storage Projects to structure cross-cutting issues that arise in demonstration projects and can be barriers to innovation [39]. The BRIDGE process facilitates ongoing knowledge exchange between projects and draws conclusions and recommendations re-

garding future use of project results through four different Working Groups representing the main areas of interest: Business Models, Data Management, Consumer Engagement, and Regulations.

In BRIDGE, several Task Forces (TF) were created to address topics that could be horizontal to more than one of the above-mentioned working groups. A specific TF was created to investigate how different projects approached the Scalability and Replicability Analysis (SRA) of different project results.

The first objective of the TF was the development of common guidelines for performing SRAs, and the second one the development of ideas on the definition of the scope and implementation of a toolbox/repository of necessary data, best-practices, and past experiences. The steps to perform an SRA of a smart grid project are depicted in Figure 2 and have been followed in the analysis of this work and for each DEMO. The overall approach has five stages, with each stage having several steps. The definition of the SRA methodology and how to carry out the SRA are the most complex stages. These five stages are briefly described below.

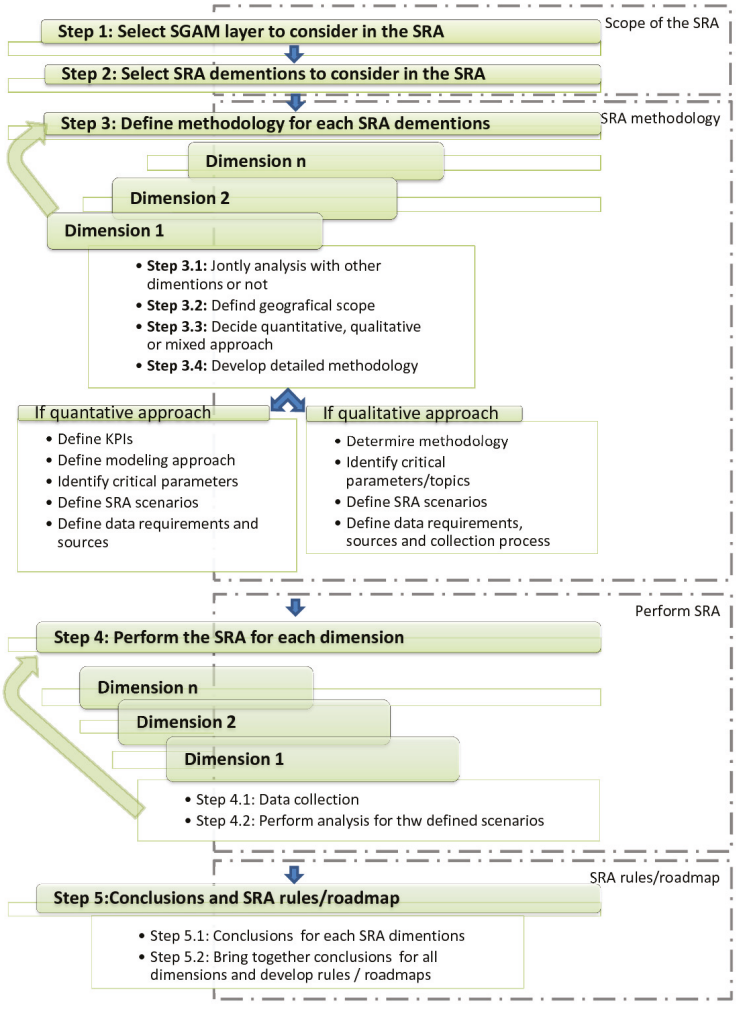

Figure 2. SRA guidelines [39].

Step 1 Definition scope of the SRA: Selection of the SRA dimension or dimensions that will be assessed in the Smart Grid Architecture Models (SGAM) layers and within each SGAM layer.

Step 2 Selection of the SRA dimensions: After the definition of the methodology, SRA developers perform the corresponding qualitative/quantitative analyses for the previously defined scenarios and collect the required input data. During this stage progression it may be necessary to go back and re-assess some aspects of the methodology initial described.

Step 3 Definition of the methodology for each SRA dimension selected: this third stage requires the definition of the methodology for each of the dimensions previously selected. It is recommended to rely on best practices from previous projects, in order to make informed decisions at each one of these steps. SRA developers have to take this into consideration, during the development of quantitative analyses. The proper definition of the relevant Key Performance Indicators (KPIs) and simulation scenarios focusing on the most critical parameters affecting the scalability and replicability is extremely important. In order to avoid delays in the execution of the SRA, an early definition of the input data is required.

Step 4 Performance of the SRA for each dimension: This stage consists of, first, analyzing the results obtained in the SRA for each dimension individually and, then, trying to correlate the results for the various dimensions if relevant.

Step 5 Conclusions and SRA rules/roadmap: The derivation of a set of SRA rules is allowed by this analysis. This can be defined as a conclusion on the most important aspects that affect the scalability and replicability of the technology or solution under investigation. SRA can also be used to provide an implementation roadmap. This can include timelines and milestones for the implementation and/or use of the technology or solution being evaluated.

It must be mentioned that H2020 projects, even if they all address new solutions related to smart grids and storage, are very diverse and consider a wide range of functionalities and technologies at different Technology Readiness Levels (TRLs). Consequently, in this work, the proposed common SRA methodology was applied ensuring that the proposed set of steps can support and speed up the delivery of a high-quality SRA. These steps were as a checklist to ensure that any aspect included or not in the SRA methodology selected by a project has been carefully considered. In any case, there is much room for those in charge of performing the SRA to implement and adapt the proposed guidelines as required by the characteristics of their project.

3. Scalability and Replicability Analysis Approach

Scalability of a system is understood as a set of elements interacting with each other, with similar boundary conditions. In a more restrictive formulation, scalability works to maintain system performance and function, retaining all its required properties when scaling up without correspondingly increasing system complexity [33,40].

Scalability analysis is extremely important for the FLEXITRANSTORE project to do the following:

i. Apply the technical innovations on smart storage and transmission on a large-scale deployment.
ii. Provide the appropriate business models and market strategies.
iii. Integrate flexibility assessment into system planning and power system research.

Replicability refers to the ability of a system to be replicated at another point in time [30]. Due to the difference in proposed technology and cost, replicability of FLEXITRANSTORE (the ability to duplicate the technical innovations in another location) is investigated. Each demo has been implemented, installed, and tested in different locations in the Southeast European (SEE) region, and typically has different technical requirements related to national regulations.

Scalability and replicability are fundamental to successful scaling and replication. Therefore, scalability and replicability enable or at least reduce barriers to growth and reuse of R & D and demonstration project results. This is important for businesses and utilities because scaling and replication offer significant benefits such as cost-effective deployment to a larger customer base and cost-effective reuse of proven solutions.

By examining the scalability and replicability factors that affect the scalability and replicability of FLEXITRANSTORE, scalability and replicability are analyzed, and potential barriers to large-scale deployments are identified.

Specifically, the factors extracted from the literature review were categorized into four main categories.

- Technical factors that determine whether the developed solution in a specific project is inherently scalable and/or replicable, i.e., whether it is feasible for scaling up and/or to replicate.
- Economic factors that reflect whether scaling or replication is feasible. This important step in investing analysis (internal rate of return, net present value, etc.) and ensuring that the business model applies on a larger scale or in different settings than in the original case is often ignored and poses a major barrier.
- Factors related to acceptance and regulation of stakeholders such as authorities, regulators, end users, etc., reflect the extent to which the social environment and current regulatory is willing to respond to an expanded version of the project or whether a new environment is suitable for receiving a project.

According to [33,35], in Tables 1 and 2, the scalability and replicability factors are summarized, relating to the economic, technical, regulatory, and stakeholder acceptance categories. Each of these are further categorized in order to identify the remaining/potential issues and to capture specific project achievements that can limit scalability and replication. Moreover, the main limitations and barriers that have an impact on scalability and replicability are identified. The identified issues already describe necessary conditions for scaling-up and replication, and they represent somehow rules to be contemplated for scalability and replicability.

Table 1. Scalability factors.

Area	Sub-Areas	Factors	Limitation Issues
Technical	Technology	Modularity	Communication capacities Computation memory
		Technology Evolution	Expected equipment costs IT/data security Missing standardization of control signal and information flow from/to distributed generation Big data
	Control and communications Interface	Interface design	Depends on nature of the project and focus
	Infrastructure	Software tools integration	Big data
Economic	Economy of scale	Economies of Scale	No detailed cost-benefit analysis
		Profitability	Uncertainty remuneration Focus on feasibility
Regulatory and Stakeholder	Regulation	Regulatory Issues	Data confidentiality Lack of rules to provide service Lack of rules for interaction
	Consent by users, local authorities and public	Acceptance	Change customer behaviour Stakeholder opposition or hesitancy

Table 2. Replicability factors.

Area	Sub-Areas	Factors	Limitation Issues
Technical	Technology	Standardization	New non-standardized services Proprietary standards Ability for standard-conform implementation
		Interoperability	Customized (project/equipment) implementation Provider-specific applications New non-standardized services
	Control and communications Interface	Standardization Interoperability	Depends on nature of the project and focus
	Infrastructure	Network Configuration	Focus/dependency on resource Load/generation mix and situation Infrastructure need Demographics
Economic	Business Model	Business model	Uncertainty remuneration Lack of rules to provide service
	Profitability Analysis	Macro-economic factors Market Design	Lack of analysis on macro-economic factors Lack of plans to export solution
Regulatory and Stakeholder	Regulation	Regulatory Issues	Non-existing or strongly varying regulatory and legal framework
	Acceptance	Acceptance	Change customer and operator behaviour

4. Scalability Factors

The different scalability factors are analyzed in the following subsections below [33–35,38–40].

4.1. Technical Factors

Modularity is a necessary requirement for scaling up. It refers to whether a configuration can be divided into forbidden components or not. A solid layout will be appropriate for larger-scale execution. On the other hand, well specified (and isolated) constituent elements provide the flexibility needed in ordering the setup to be transferred to a larger scale. Consequently, this factor investigates to what extent a solution is modular (e.g., how simple it is to include new components or whether there are limits on including components).

The number of interactions between components is addressed via interface design. If they grow more than linearly, the scaled-up solution may become overly complex and redundant at the target scale, limiting the scaled-up solution's performance. The extent to which interactions between components are managed locally or centrally is investigated through interface design.

Except for the solution's complexity, the software tools required to deploy it (such as simulation models, databases, and so on) must be able to handle the increased size. Note that a favorable technical progress can offset this impact. When the solution size grows, this factor influences how much the performance of software tools is affected.

The solution's compatibility with the technological environment in which it will be implemented, as well as the interaction between its components and the outside world, is taken into account during the compatibility analysis.

4.2. Economic Factors

A project can only be expanded up if it is viable at the required scale. This implies that both costs and income must be improved. This effectively means that the marginal cost and revenue functions of a solution will determine whether scaling-up is possible or not. The variation of the marginal cost curve according to the number of deployed units is particularly noteworthy in this situation, since the most obvious patterns influencing scalability are rise, drop, or stepwise development.

The percentage increase in costs equals at most the percentage increase of the project size. The significance of project size varies greatly depending on the undertaking (e.g., the number of meters, the amount of managed active power, the number of customers, the number of distributed generation units, etc.) This factor then specifies how much costs increase as the solution size grows.

Similarly, the rise in benefits should be proportional to the increase in project size. This is reflected in the profitability factor. This component asks and defines how much advantages grow as the solution size grows.

4.3. Regulatory and Stakeholder

Regulation establishes the framework for transmission, distribution, generation, and supply activities, outlining how the various agents involved (investors, consumers, etc.) behave and interact. The roles and responsibilities of agents, the rules, and requirements for providing services, the rules for remunerating regulated activities, and the rules for agent interaction are all defined by regulation. Regulation is understood in terms of its impact on the size and scope of the project when it comes to scalability. Scalability is usually influenced by the regulations and requirements for providing specific services. The factor regulation then evaluates whether there are any regulatory constraints to the solution's size and scope.

Acceptance refers to the willingness of stakeholders such as regulators, policymakers, and end users to accept an expanded project. It is vital to examine if the concerned stakeholders will accept the proposed changes. Although a project's solution may have overcome regulatory and legal constraints (for example, by changing the regulatory framework), it is critical that other stakeholders accept the solution. This element decides if stakeholder acceptance has been explored and if any challenges are anticipated.

5. Replicability Factors

The different replicability factors are analyzed in the following subsections below [33–35,38–40].

5.1. Technical Factors

The standardization process and the proper collection of standards by projects are complicated by the large number of players, the required speed, the numerous worldwide activities, and the constantly changing solutions. The standardization factor investigates and determines how standard-compliant the solution is and/or how readily it can be made standard-compliant.

Solutions must also be interoperable. Given the numerous standards available, it is theoretically feasible to have anything standardized that is incompatible with a specific system or environment (that operates according to a different standard). The ability of two or more networks, systems, devices, applications, or components to communicate, exchange, and use information to accomplish essential functions is referred to as interoperability. The factor interoperability determines how interoperable or plug-and-play solutions and their components/functions are.

Within the scope of a project, network configuration refers to aspects that are predetermined and cannot be changed (e.g., climate conditions such as temperature, wind, precipitation levels, terrain conditions, demographics, local generation mix, etc.) This component investigates how dependent the solution is on available resources and infrastructures.

5.2. Economic Factors

The project's solution must be tested in the context of a distinct business model. The original project's business model is unlikely to stand up in a new setting—at least not without modification. However, not all European countries have policies that promote loss reduction, thus a solution that is viable due to loss reduction in one host area may not be desirable in another. The factor business model determines how thoroughly the solution's viability has been investigated and/or whether the solution is viable in various scenarios (e.g., another EU member state).

In addition, a macroeconomic analysis is required to determine whether the proposed solution is (still) profitable in other European countries. This is usually accomplished by doing a brief scenario study on a few key target countries. Inflation carbon cost and interest rates all affect project costs and viability. The factor macroeconomics examines how dependent the answer is on specific macroeconomic factors (e.g., discount rate, inflation rate, etc.)

Additionally, another determining factor is the market design. The definition of products and services, bid or offer requirements, and pricing and financial settlement regulations are all part of market design. It also refers to the responsibilities and roles of various market actors, as well as the interactions among them. This includes questions about the market model utilized, the tariff structure in place, who the players are, how they interact, and whether there are any additional restraints such as taxes or subsidy schemes. The factor market design then indicates how dependent the solution is on a certain market design.

5.3. Regulatory and Stakeholder

It is critical for successful replication that regulation in the intended host area allows the project's deployment to be replicated. Regulation is defined broadly in terms of agent roles, rules for providing services, rules for remunerating regulated agents, and rules for agent interaction. Because the project demonstrator works under various regulatory frameworks, the definition is intentionally kept generic and does not focus on a specific regulatory framework. The factor regulation investigates how much the solution depends on current national or local regulation to be feasible and viable, and whether barriers arise because of this dependency.

Furthermore, the solution must be accepted by key stakeholders. This could imply a more fundamental agreement than is required for scalability. After all, stakeholders must be willing to accept something completely new, which may be more challenging than accepting a larger version of what already exists. The factor acceptance inquires and investigates the extent to which acceptance issues are to be expected when exporting solutions to other countries.

6. Scalability and Replicability Analysis

In the following subsections, the key points from each demonstration's scalability and replicability analysis are highlighted. The various factors were quantified into numbers ranging from zero to three in order to conclude how scalable or replicable each solution is, with zero representing the lowest score and three representing the highest [33–35,38–40].

6.1. DEMO 1: Active Substation Controller—Demand/Response and Storage Integration (ADN-BESS)

The Battery Energy Storage System (BESS) unit power rating (1 MW) meets the requirements for a simple grid connection. However, the increase in BESS unitary size is limited in order to avoid large power cable sizes that would make grid connection difficult. To achieve larger plant sizes, several BESS units can be combined to achieve the desired plant size. On the other hand, technological conditions may lead to smaller rack sizes, but system redesign may be required due to technological advances in the short to medium term [41,42].

The standard sizes of the containers that house the batteries limit the size of the BESS. Furthermore, as the total BESS plant size increases, so does the external plant substation, requiring more layout space. To add a new utility, modifications will be required; therefore, some architecture simplification is recommended to facilitate integration in the substations and systems of the Distribution System Operators (DSO) and Transmission System Operators (TSO).

In terms of the cost-benefit ratio, it is expected that short to medium-term changes will be beneficial. However, in order to accommodate the development of BESS, additional mandatory standard compliance should be completed. Adaptation to specific standards in each country must be considered, and BESS grid services must specifically meet the requirements of the country's Grid Code.

In recent years, the Energy Storage market has accelerated along with a significant increase in the production of electric vehicles, potentially affecting the availability of batteries for BESS applications. It is recommended to encourage agreements between BESS developers and battery suppliers, as well as battery recycling policies, to reduce the risk of shortages and reliance on imports. Finally, there are regulatory barriers to replicability that could affect the solution, specifically compliance with country grid code in each project.

The following Figure 3 shows the overall scalability and replicability assessment. Moreover, in Tables 3 and 4, the main remarks regarding the scalability and replicability analysis, respectively, for DEMO 1 are presented in detail.

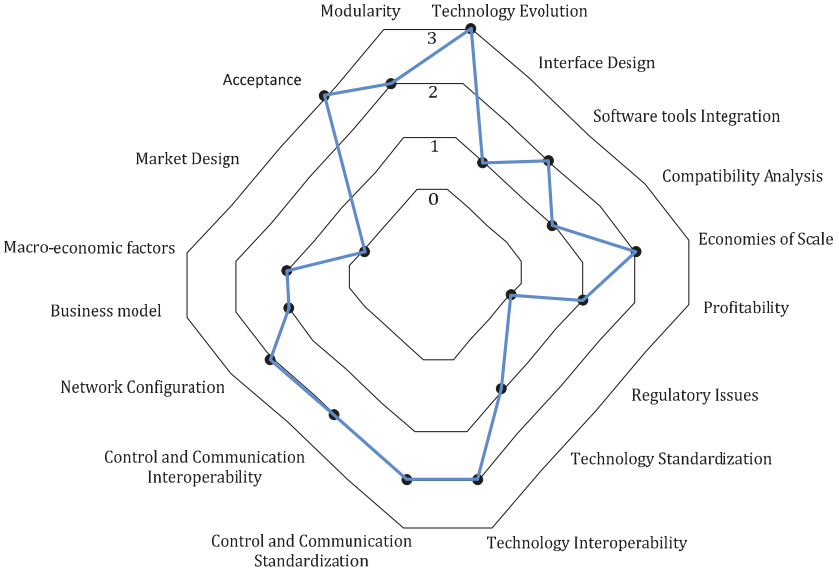

Figure 3. Scalability and replicability assessment DEMO 1: Active Substation Controller.

It can be concluded that DEMO 1: "Active Substation Controller" receives a medium overall score, with strong points for stakeholder acceptance as a key technology for future power grids, as well as the positive impact of technology evolution. The regulatory barriers and market design that do not adequately remunerate the services provided by the Active Substation Controller appear to be the weakest points at this stage.

Table 3. Scalability factors analysis for DEMO 1.

Area	Sub-Areas	Factors	Achievements	Issues
Technical	Technology	Modularity	Independent functional units clearly defined. BESS unit power rating (1 MW) suits the requirements for an easy connection to the grid.	Increase in BESS unitary size is limited to avoid great power cables sizes which would make difficult the connection to the grid. Greater plant sizes are achievable by combining several BESS units to attain the desired plant size.
		Technology Evolution	Technological conditions allow increasing the solution size.	Redesign in the system may be needed due to technological advances in the short to medium term. Some simplification in the architecture would be advisable to facilitate the integration in the substation and DSO/TSO systems. Advances in battery technology could lead to smaller sizes of racks.
	Control and communications Interface	Interface design	Centralized and decentralized.	Modification will be needed for a new utility system to be added.
		Software tools integration	The design of software permits the integration of more elements.	Integration to different operational and market platforms to be further analyzed.
	Infrastructure	Compatibility analysis	Limited physical size limitations.	BESS size is limited by the standard sizes of containers that house the batteries. Increase in total BESS plant size also involves that the external plant substation is also greater thus requiring more space for the layout.
Economic	Economy of scale	Economies of Scale	Evolutions in the short to medium term will have a positive influence on the cost-benefit ratio.	If the size of the solution increases cost and benefit would increase.
		Profitability	The economic indicators of the demo case show that the business model is viable enough to scale up.	Further analysis in business models could be carried out, including scenarios with BESS units supporting wind/solar plants.
Regulatory and Stakeholder	Regulation	Regulatory Issues	Regulation changes under development.	Regulation barriers currently in place.
	Consent by users, local authorities and public	Acceptance	Increasing consent.	Suggested to become more familiar.

Table 4. Replicability factors analysis for DEMO 1.

Area	Sub-Areas	Factors	Achievements	Issues
Technical	Technology	Standardization	The solution is partially standard compliant.	Further mandatory standard compliant should be done. Adaptation to standards particulars in each country needs to be considered Provision of grid services by BESS must specifically match the requirements of the country Grid Code.
		Interoperability	There is the ability to share data via software and hardware.	-
	Control and communications Interface	Standardization	The solution is partially standard compliant (standard communication protocols are used).	Further mandatory standard compliant should be done.
		Interoperability	There is the ability to share data via software and hardware (standard communication protocols are used).	-
	Infrastructure	Network Configuration	The solution is partially standard compliant, by using standard networking devices.	Further mandatory standard compliant should be done. Adaptation to standards particulars in each country needs to be considered.
Economic	Business Model	Business model	Business model exist that could be deployed in different environment.	Some investment would be needed to deploy it in different environment.
	Profitability Analysis	Macro-economic factors	Different options (locations, network topology etc) have been evaluated before the implementation.	Further analysis to study the influence of economic factors on the replicability capacity needed.
		Market Design	Solution can be easily (economically and technically) compliant with a defined different set of standards.	Markets for ADN-BESS currently not existing in many countries.
		Delivery time and availability of batteries suppliers	In the last years Energy Storage market is moving very fast together with a substantial increase in the production of electric vehicles, which could cause affect the availability of batteries for BESS applications.	Encourage agreements between BESS developers and battery suppliers and battery recycling policies to minimize the risk of shortages and reducing the dependence on imports.
Regulatory and Stakeholder	Regulation	Regulatory Issues	Regulation is expected to change that will make the solution feasible and viable.	There exist regulatory barriers with respect to replicability that could affect the solution, regarding specifically compliance with country grid.
	Acceptance	Acceptance	Stakeholders have shown great interest.	The stakeholder acceptance is important regarding replicability potential.

6.2. DEMO 2: Wind Power Plant Connected to Active Substation

The regulatory and institutional environments have a significant impact on the estimation of BESS's potential replicability and scalability. Some countries that have not developed the network codes for the regulation of the integration of BESS systems in their networks are now starting to adapt their regulatory frameworks to the new system needs and generation paradigm.

If the BESS is small in comparison to the size of the grid into which it discharges, detailed power system and production cost models are not required. Large-scale systems, on the other hand, have more data to consider, and the control processes and algorithms include more variables, making the control systems more complex. The task of preparing a BESS economic analysis for appraisal faces two major challenges: (a) the scale of the investment project under consideration influences this; (b) it is necessary to have a sufficient understanding of the unique technical aspects of BESS (technical aspects of battery design, sizing, performance etc.) Overall, there is still a lack of economic experience.

Concerning interoperability, the European Commission (EC) is enabled to develop interoperability standards for communication and control, between different distributed resources. This is in accordance with the delegated act on interoperability published by the EC, in application of the provisions of Directive (EU) 2019/944 [43].

BESS are typically capital-intensive projects, and their viability may necessitate additional assistance. As a result, the existence of financing instruments, both at the European and national levels, aimed entirely or partially at promoting the development of projects and technologies, will play a critical role in scalability.

The following Figure 4 shows the overall scalability and replicability assessment. Moreover, in Tables 5 and 6 the main remarks regarding the scalability and replicability analysis, respectively, for DEMO 2 are presented in detail.

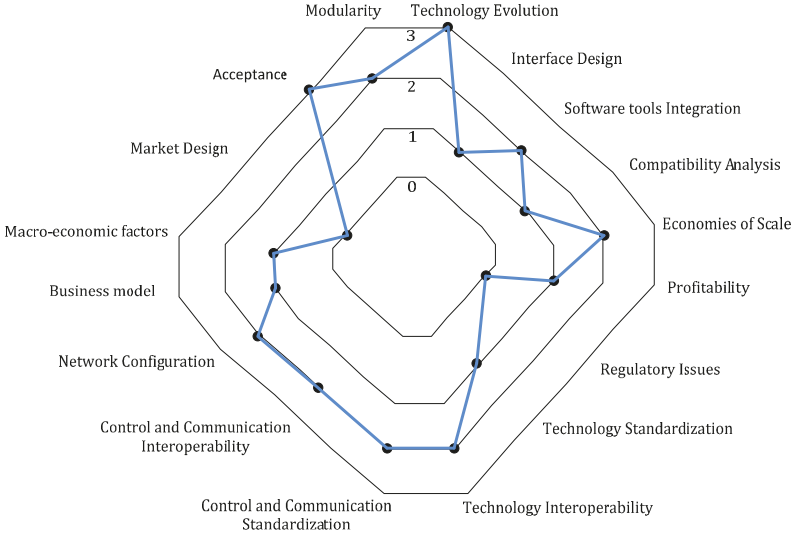

Figure 4. Scalability and replicability assessment DEMO 2: Wind Power Plant connected to Active Substation.

Table 5. Scalability factors analysis for DEMO 2.

Area	Sub-Areas	Factors	Achievements	Issues
Technical	Technology	Modularity	Independent functional units clearly defined.	Some changes would be needed to add components to the solution to increase its size.
		Technology Evolution	Technological conditions allow increasing the solution size.	Redesign in the system may be needed due to technological advances in the short to medium term.
	Control and communications Interface	Interface design	Centralized and decentralized.	Modification will be needed for a new utility system to be added.
		Software tools integration	The design of software permits the integration of more elements	Integration to different operational and market platforms to be further analyzed.
	Infrastructure	Compatibility analysis	Limited physical size limitations.	Some compatibility issues exist.
Economic	Economy of scale	Economies of Scale	Evolutions in the short to medium term will have a positive influence on the cost-benefit ratio.	If the size of the solution increases cost and benefit would increase.
		Profitability	The economic indicators of the demo case show that the business model is viable enough to scale up.	Further analysis in business models could be carried out.
Regulatory and Stakeholder	Regulation	Regulatory Issues	Regulation changes under development.	Regulation barriers currently in place.
	Consent by users, local authorities and public	Acceptance	Increasing consent.	Suggested to become more familiar.

As with DEMO 1, DEMO 2: "Wind Power Plant Connected to Active Substation" receives a medium score, with strong points for stakeholder acceptance as a key technology for future power grids, as well as the positive impact of technology evolution. The regulatory barriers and market design that do not adequately remunerate the services provided by the BESS connected to active substation with wind power plant appear to be the weakest points at this stage.

6.3. DEMO 3: Increase Resilience of the Cross-Border Lines with Sensors for De-Icing Solutions

The Dynamic Line Rating (DLR) [44,45] expert system has several subsystems, including line rating calculation, ice forecasting, sag simulation, and conductor temperature tracking. With model fine-tuning, fractional implementation of the various subsystems is possible. Each subsystem has its own display tab, and each power line necessitates new expert system implementation and adaptation. Furthermore, the incorporation of new sensors into the system increases the number of data records, resulting in increased computational capacity.

Table 6. Replicability factors analysis for DEMO 2.

Area	Sub-Areas	Factors	Achievements	Issues
Technical	Technology	Standardization	The solution is partially standard compliant.	Further mandatory standard compliant should be done.
		Interoperability	There is the ability to share data via software and hardware.	-
	Control and communications Interface	Standardization	The solution is partially standard compliant.	Further mandatory standard compliant should be done.
		Interoperability	There is the ability to share data via software and hardware.	-
	Infrastructure	Network Configuration	The solution is partially standard compliant.	Further mandatory standard compliant should be done.
Economic	Business Model	Business model	Business model exist that could be deployed in different environment.	Some investment would be needed to deploy it in different environment.
	Profitability Analysis	Macro-economic factors	Different options (locations, network topology etc) have been evaluated before the implementation.	Further analysis to study the influence of economic factors on the replicability capacity needed.
		Market Design	Solution can be easily (economically and technically) compliant with a defined different set of standards.	Markets for ADN-BESS currently not existing in many countries.
Regulatory and Stakeholder	Regulation	Regulatory Issues	Regulation is expected to change that will make the solution feasible and viable.	There exist regulatory barriers with respect to replicability that could affect the solution.
	Acceptance	Acceptance	Stakeholders have shown great interest.	The stakeholder acceptance is important regarding replicability potential.

The cost–benefit ratio is determined by the number of integrated sensors and the extra transmission capacity gained. Furthermore, the achieved surplus transmission capacity is dependent on the technical parameters of the line, substation elements, and weather conditions along the line. The demo demonstrated the viability of each subsystem, and the system could be more profitable if used on more power lines.

The technology is widely accepted, and there are no regulatory barriers to scalability or replicability that could jeopardize the solution. However, the TSO's internal regulatory regarding capacity management should be adjusted to the system's dynamic output. The expert system promotes the implementation of the EU's internal electricity market on a market basis.

Finally, sensor communications are standardized, and sensor manufacturers provide standard compliant Supervisory Control and Data Acquisition (SCADA) integration solutions. The interface and overall system communication, however, are dependent on the customers' requests and the system's adaptation to the given TSO's IT security requests for each demonstration.

The following Figure 5 shows the overall scalability and replicability assessment. Moreover, in Tables 7 and 8 the main remarks regarding the scalability and replicability analysis, respectively, for DEMO 3 are presented in detail.

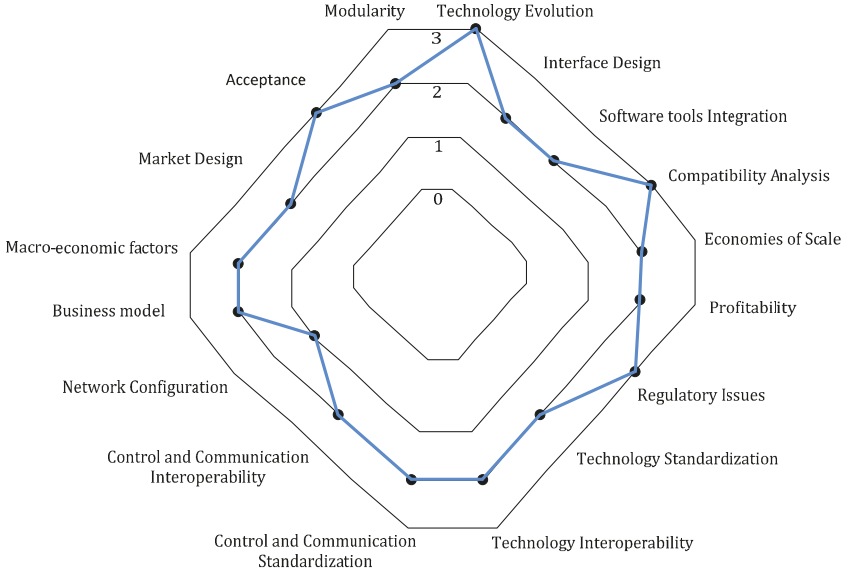

Figure 5. Scalability and replicability assessment DEMO 3: Increase resilience of the cross-border lines with sensors for de-icing solutions.

DEMO 3: "Increase resilience of the cross-border lines with sensors for de-icing solutions" achieves a good score in most of the scalability and replicability factors. There are no significant regulatory barriers, and the expert system can be adapted to any transmission line by knowing its technical parameters, which are both positive aspects of this technology. On the other hand, standardization could be improved further, particularly in terms of TSO security standards.

6.4. DEMO 4: Improve Transfer Capacities and Clean Electricity Flows through Power Flow Control Solutions

The solution can be scaled up or down in response to future changes in system needs. When need is driven by new generation, the solution can be scaled up as more generation connects to the network. As a result, if more generation applies to connect than was originally intended, it is still possible to use the assets and simply increase the impedance as needed. The modularity of this technology is a strong point, with individual units per phase and the ability to scale up and down the number of devices to meet the needs of the network. The ability to control the number of devices connected while in operation is also advantageous because it allows the TSO to scale up and down the functioning deployment as real-time demands change.

Table 7. Scalability factors analysis for DEMO 3.

Area	Sub-Areas	Factors	Achievements	Issues
Technical	Technology	Modularity	The DLR-based expert system includes different subsystems such as line rating calculation, conductor temperature tracking, sag simulation, and ice forecasting subsystems.	-
		Technology Evolution	Fractional implementation possibility for the different subsystems with fine-tuning of the models.	-
	Control and communications Interface	Interface design	Each subsystem has its own display tab.	-
		Software tools integration	The software is implemented on Matlab basis with MS SQL connection.	Each power line requires new implementation of the expert system.
	Infrastructure	Compatibility analysis	The expert system can be adapted to any transmission line by knowing its technical parameters.	Each power line requires new implementation of the expert system.
Economic	Economy of scale	Economies of Scale	Cost-benefit ratio depends on the number of integrated sensors and the gained surplus transmission capacity.	The achieved surplus transmission capacity depends on the technical parameters of the line, substation elements, and prevailing weather conditions along the line.
		Profitability	Quantifiable by the achieved capacity gain/congestion management.	-
Regulatory and Stakeholder	Regulation	Regulatory Issues	Internal regulatory of the TSO regarding the capacity management should be adjusted to the dynamic output of the system.	-
	Consent by users, local authorities, and public	Acceptance	The technology is generally accepted.	-

If the original need is reduced or eliminated, the Power Flow Control (PFC) devices can be easily redeployed to another part of the grid. Because the solution is not tied to the original location, this flexibility allows for a no-regrets investment decision. Because these devices are voltage agnostic, they can be redeployed onto different voltage lines without requiring any changes to the device hardware.

By moving the devices and redeploying them onto the Bulgarian network, the demo demonstrated the replicability of the project deployed in Greece. This could be redeployed to another network with a different voltage level without requiring any changes to the PFC devices. This also demonstrated the deployment's communication interface's ability to integrate into different countries' systems.

The following Figure 6 shows the overall scalability and replicability assessment. Moreover, in Tables 9 and 10, the main remarks regarding the scalability and replicability analysis, respectively, for DEMO 4 are presented in detail.

Table 8. Replicability factors analysis for DEMO 3.

Area	Sub-Areas	Factors	Achievements
Technical	Technology	Standardization	A DLR sensor testing protocol is standardized in the framework of the project.
		Interoperability	The measured field data and the calculated results are stored in the same database.
	Control and communications Interface	Standardization	The sensor communications are standardized; sensor manufacturer offers standard compliant solution regarding SCADA integration.
		Interoperability	The measured field data and the calculated results are stored in the same database.
	Infrastructure	Network Configuration	The system adopted to the given TSO's IT security requests.
Economic	Business Model	Business model	The demo proves the viability of each subsystem.
	Profitability Analysis	Macro-economic factors	The expert system implemented on the most critical power line (from icing and congestion point of view).
		Market Design	The expert system promotes the implementation of internal electricity market at EU level.
Regulatory and Stakeholder	Regulation	Regulatory Issues	No regulatory barriers with respect to replicability that could affect the solution.
	Acceptance	Acceptance	The technology is generally accepted.

It is clear that the highest score is obtained in terms of modularity. Technology evolution ranked high as well, as Smart Wires has evolved this technology further with higher capacity devices with greater controllability, being able to push and pull power from the line by increasing or decreasing the effective impedance rather than simply increasing as was the case with this demo. Because the solution design is determined by the type of transmission lines and towers, compatibility receives a lower score. The business model is viable, but it will vary by network, so individual cases must be investigated. Finally, acceptance could be improved by raising awareness of the devices and their benefit to the network.

6.5. DEMO 5: New Wholesale Market Approach with Flexibility Services

The delivered solution is a new market structure that makes it easier to integrate new flexibility providers. Although the rules of the platform are strict, as is typical of European intraday market platforms, it does not impose any restrictions on national markets to follow other models. The matching algorithm developed for the demonstration has a significant impact on scalability. These algorithms were tested on two markets (Bulgaria and Cyprus) with varying levels of maturity, but not on several coupled markets.

In terms of scaling up the proposed approach, because the matching algorithm is solving a mathematical problem continuously, the required computational capacity grows linearly with the size of the problem. The demonstration, on the other hand, can be replicated in other countries if the necessary data are shared by the relevant market operators. Only the interfaces should be changed; the main components can remain unchanged. It should also be noted that this market is separate from the system operators. Finally, inte-

grating the new order types necessitates a change in the matching algorithm used across Europe, but the solution fits within the overall European market structure.

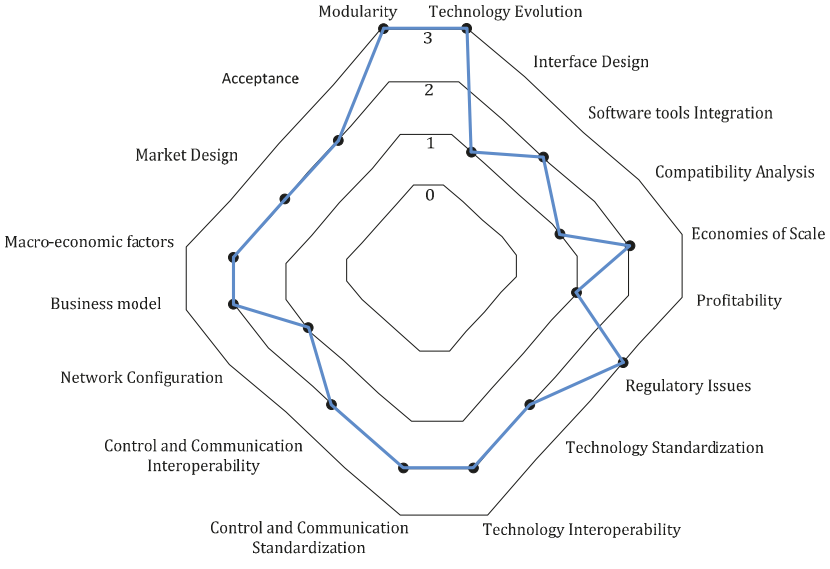

Figure 6. Scalability and replicability assessment DEMO 4: Improve transfer capacities and clean electricity flows through Power Flow Control Solutions.

Concerning the delivered solution's business aspect, the economic impact should be evaluated by taking into account number of trades, market participants, and number of participating flexibility providers.

The following Figure 7 shows the overall scalability and replicability assessment. Moreover, in Tables 11 and 12, the main remarks regarding the scalability and replicability analysis, respectively, for DEMO 5 are presented in detail.

DEMO 5 receives high marks in both scalability and replicability. However, developments on the European markets have taken a turn since the project's inception, and other solutions appear to be emerging. This severely limits the rationale for considering adapting the developed solution to other markets; however, the solution is scalable and replicable.

6.6. DEMO 6: Flexible Substations Advanced Control and Services Demonstration

Demo 6 "Flexible substations advanced control and services demonstration" includes clearly defined independent functional units. However, some modifications would be required to add components to the solution in order to increase its size. Technological conditions permit increasing the size of the solution, but system redesign may be required due to short to medium term technological advance. Finally, the design of software allows for the incorporation of more elements, and there are no physical size constraints.

On the economic side, no economic barriers to scalability and replicability have been identified, and no regulatory barriers that could affect the solution are currently in place. The solution is partially standard compliant, but more standardization is required. Finally, stakeholder acceptance is unimportant in terms of the developed solution's scalability and replicability.

The following Figure 8 shows the overall scalability and replicability assessment. Moreover, in Tables 13 and 14, the main remarks regarding the scalability and replicability analysis, respectively, for DEMO 6 are presented in detail.

Table 9. Scalability factors analysis for DEMO 4.

Area	Sub-Areas	Factors	Achievements	Issues
Technical	Technology	Modularity	The solution can be divided into interdependent components/independent functional units.	If a large impudence is required, design considerations need to be taken to substation space availability. However, as the devices are modular, there is flexibility around how they are deployed on the system.
		Technology Evolution	Technological conditions allow increasing the solution size.	Development of technology means more advanced and capable units now available based on learnings from innovation installations.
	Control and communications Interface	Interface design	Centralized and decentralized.	Modification will be needed for a new utility system to be added.
		Software tools integration	The design of software permits the integration of more elements.	Integration to different operational and market platforms to be further analyzed.
	Infrastructure	Compatibility analysis	Physical size limitations exist.	Solution design depends on the type of transmission lines and towers.
Economic	Economy of scale	Economies of Scale	Evolutions in the short to medium term will have a positive influence on the cost-benefit ratio.	If the size of the solution increases cost and benefit would increase.
		Profitability	The business model should be viable enough to scale up.	This will vary from network to network, so individual cases would need to be investigated.
Regulatory and Stakeholder	Regulation	Regulatory Issues	No regulatory barriers with respect to scalability that could affect the solution.	-
	Consent by users, local authorities, and public	Acceptance	Stakeholder acceptance is of some important regarding scalability potential for your solution.	Being a newer technology preference can sometime lean towards more established technology where concerns around issues such as noise and visual impact are better understood.

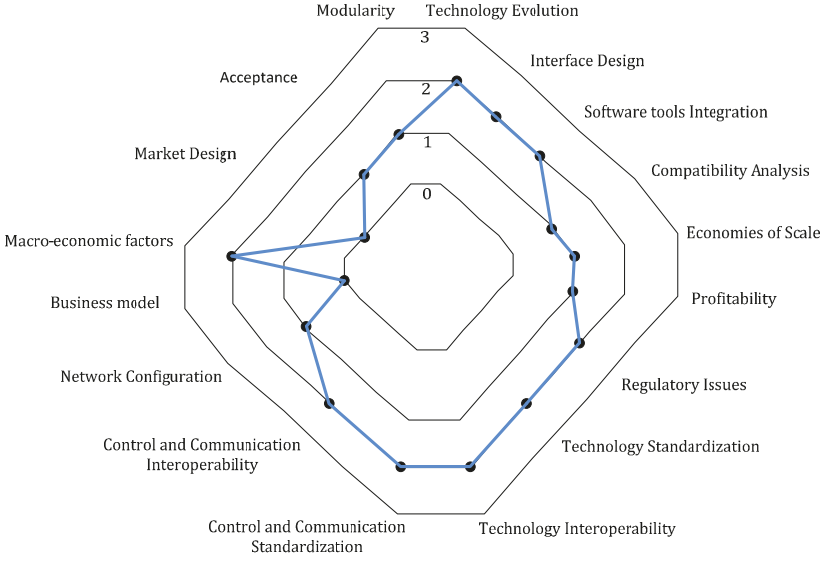

Figure 7. Scalability and replicability assessment DEMO 5: New wholesale market approach with flexibility services.

Table 10. Replicability factors analysis for DEMO 4.

Area	Sub-Areas	Factors	Achievements	Issues
Technical	Technology	Standardization	The solution is standard compliant.	Will still require studies on individual networks to ensure optimal performance
		Interoperability	There is the ability to share data via software and hardware.	-
	Control and communications Interface	Standardization	The solution is partially standard compliant.	Communication with the devices uses radio frequency to ensure ease of installation. Some sites may require the speed of fiber optic as provided by the later models of the technology.
		Interoperability	There is the ability to share data via software and hardware.	-
	Infrastructure	Network Configuration	The solution is partially standard compliant.	-
Economic	Business Model	Business model	The demo case demonstrates that it is viable enough to replicate.	Further analysis on business model exist that could be deployed in different environment.
	Profitability Analysis	Macro-economic factors	Different options (locations, network topology, etc.) have been evaluated before the implementation.	-
		Market Design	Solution can be (economically and technically) compliant with a defined different set of standards.	Further analysis on the use in market environment.
Regulatory and Stakeholder	Regulation	Regulatory Issues	No regulatory barriers with respect to replicability that could affect the solution.	-
	Acceptance	Acceptance	The stakeholder acceptance is of some important regarding replicability potential for your solution.	Being a newer technology preference can sometime lean towards more establish technology.

Table 11. Scalability factors analysis for DEMO 5.

Area	Sub-Areas	Factors	Achievements	Issues
Technical	Technology	Modularity	Independent functional units clearly defined.	Not clear if the solution could be divided.
		Technology Evolution	Technological advances in the short to medium term have positive impact.	-
	Control and communications Interface	Interface design	Centralized and decentralized.	Modification will be needed for a new utility system to be added
		Software tools integration	The design of software permits the integration of more elements.	Integration to different operational and market platforms to be further analyzed.
	Infrastructure	Combability analysis	No physical size limitations.	-
Economic	Economy of scale	Economies of Scale	No economic barriers with respect to scalability that could affect the solution.	-
		Profitability	The business model is viable enough to scale up.	-
Regulatory and Stakeholder	Regulation	Regulatory Issues	No regulatory barriers with respect to scalability that could affect the solution.	-
	Consent by users, local authorities, and public	Acceptance	Major importance	-

Table 12. Replicability factors analysis for DEMO 5.

Area	Sub-Areas	Factors	Achievements	Issues
Technical	Technology	Standardization	The solution is partially standard compliant.	Further standardization to be further developed.
		Interoperability	There is the ability to share data via software and hardware.	-
	Control and communications Interface	Standardization	The solution is partially standard compliant.	-
		Interoperability	There is the ability to share data via software and hardware.	-
	Infrastructure	Network Configuration	The solution is partially standard compliant.	-
Economic	Business Model	Business model	The demo case demonstrates that it is viable enough to replicate.	Further analysis on business model exist that could be deployed in different environment.
	Profitability Analysis	Macro-economic factors	With some effort the solution would be profitable in different countries.	-
		Market Design	Solution can be (economically and technically) compliant with a defined different set of standards.	Further analysis on the use in market environment.
Regulatory and Stakeholder	Regulation	Regulatory Issues	No regulatory barriers with respect to replicability that could affect the solution.	-
	Acceptance	Acceptance	The stakeholder acceptance is important regarding replicability potential for your solution.	-

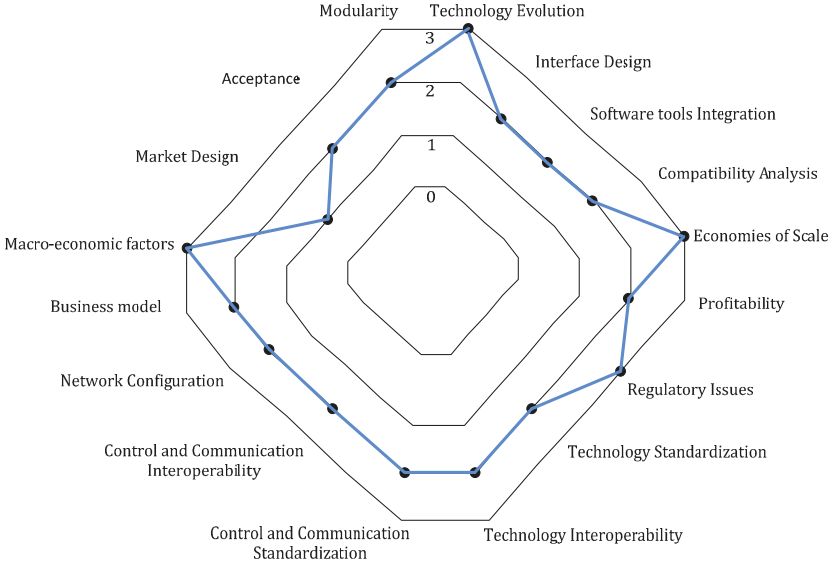

Figure 8. Scalability and replicability assessment DEMO 6: Flexible substations advanced control and services demonstration.

Table 13. Scalability factors analysis for DEMO 6.

Area	Sub-Areas	Factors	Achievements	Issues
Technical	Technology	Modularity	Independent functional units clearly defined.	Some changes would be needed to add components to the solution to increase its size.
		Technology Evolution	Technological conditions allow increasing the solution size.	Redesign in the system may be needed due to technological advances in the short to medium term.
	Control and communications Interface	Interface design	Centralized and decentralized.	Modification will be needed for a new utility system to be added.
		Software tools integration	The design of software permits the integration of more elements.	-
	Infrastructure	Combatibility analysis	No physical size limitations.	-
Economic	Economy of scale	Economies of Scale	No economic barriers with respect to scalability.	-
		Profitability	The business model is viable enough to scale up.	-
Regulatory and Stakeholder	Regulation	Regulatory Issues	No regulatory barriers with respect to scalability that could affect the solution.	-
	Consent by users, local authorities, and public	Acceptance	Not of importance.	-

Table 14. Replicability factors analysis for DEMO 6.

Area	Sub-Areas	Factors	Achievements	Issues
Technical	Technology	Standardization	The solution is partially standard compliant.	Further standardization to be further developed.
		Interoperability	There is the ability to share data via software and hardware.	-
	Control and communications Interface	Standardization	The solution is partially standard compliant.	-
		Interoperability	There is the ability to share data via software and hardware.	-
	Infrastructure	Network Configuration	The solution is partially standard compliant.	-
Economic	Business Model	Business model	The demo case demonstrates that it is viable enough to replicate.	-
	Profitability Analysis	Macro-economic factors	With some effort the solution would be profitable in different countries.	-
		Market Design	Solution can be (economically and technically) compliant with a defined different set of standards.	Further analysis in different market environment.
Regulatory and Stakeholder	Regulation	Regulatory Issues	-	Regulatory barriers with respect to replicability that could affect the solution.
	Acceptance	Acceptance	The stakeholder acceptance is of minor importance regarding replicability potential for your solution.	-

Overall, Demo 6 "Flexible substations advanced control and services demonstration" receives high marks in the various scalability and replicability factors, indicating that

there is no specific barrier to scaling up and replicating the developed technology. Further standardization is recommended, as is the smooth integration of changes brought about by technological evolution.

6.7. DEMO 7: Large Scale Storage System for Combined Cycle Plant

The standard container sizes that include the batteries limit the size of the BESS. Furthermore, an increase in total BESS plant size implies an increase in external space in the power plant. This is usually not a problem because power plants are located in more isolated areas with plenty of open space. To add a new utility, modifications will be required; therefore, some architecture simplification is recommended to facilitate integration in the power plant.

In terms of the cost-benefit analysis, it has yet to be demonstrated that the benefit outweighs the additional cost. Additionally, mandatory standard compliance is recommended. Adaptation to specific standards in each country must be considered, and power plant grid services must specifically meet the requirements of the country grid code.

The following Figure 9 shows the overall scalability and replicability assessment. Moreover, in Tables 15 and 16, the main remarks regarding the scalability and replicability analysis, respectively, for DEMO 7 are presented in detail.

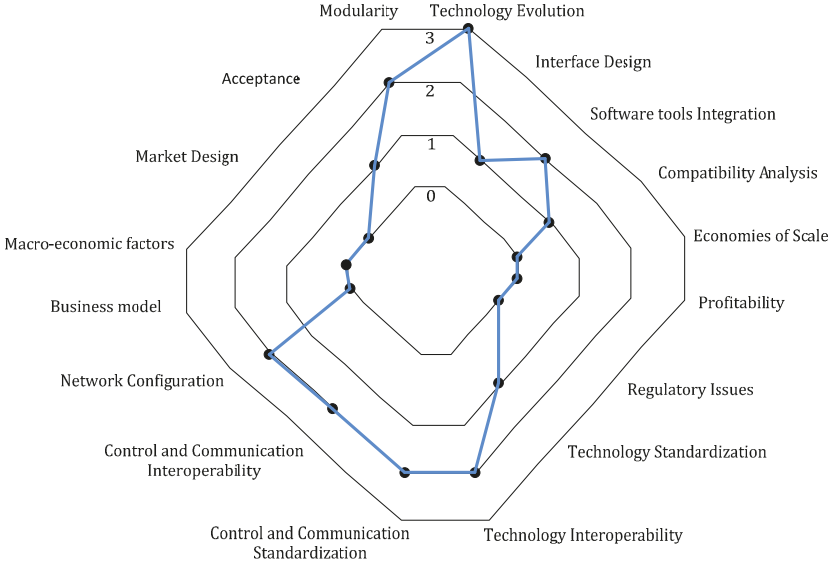

Figure 9. Scalability and replicability assessment DEMO 7: Large Scale Storage System for Combined Cycle Plant.

Even though the developed technology appears to have the potential to be scalable and replicable, GEF has received very few bids for this product/service in the last two years, none of which have been converted into reality. Furthermore, the increased benefits are not currently visible or significant. As a result, one could conclude that this technology is still in its early stages and does not have the potential to be scaled up and replicated.

6.8. DEMO 8: Advanced Control for Flexible Synchronous Generation

The developed system could be used for installations with several generators or larger generators, without increasing computational requirements. However, new computational resources would be required for large plants or when the system is deployed in new plants.

Furthermore, adding new controllers to the system and modelling new generators in the algorithms would be required to scale up the system in other plants.

It would be necessary to analyze the new system to be operated, model it, and appropriately train the control algorithms in order to replicate the demonstration activities. The controller would also have to work with the new Power System Stabilizers (PSS) and area of influence measurements.

PSS technology is well-established and has been in use for many years. The approach to installing a new PSS should be same across all TSOs (PSS is meaningless for DSOs since the plant's capacity must be high to have an influence, and such facilities are normally only found at the TSO level). Beyond what has been indicated, adding the solution to the PSS has no influence on replicability and scalability. Finally, there is currently no compensation available for providing damping.

The following Figure 10 shows the overall scalability and replicability assessment. Moreover, in Tables 17 and 18 the main remarks regarding the scalability and replicability analysis, respectively, for DEMO 8 are presented in detail.

Table 15. Scalability factors analysis for DEMO 7.

Area	Sub-Areas	Factors	Achievements	Issues
Technical	Technology	Modularity	Independent functional units clearly defined.	-
		Technology Evolution	Technological conditions allow increasing the solution size.	-
	Control and communications Interface	Interface design	Centralized and decentralized.	Modification will be needed for a new utility system to be added.
		Software tools integration	The design of software permits the integration of more elements.	Integration to different operational and market platforms to be further analyzed.
	Infrastructure	Combability analysis	Limited physical size limitations.	-
Economic	Economy of scale	Economies of Scale	Evolutions in the short to medium term will have a positive influence on the cost-benefit ratio.	If the size of the solution increases cost and benefit would increase.
		Profitability	The economic indicators of the demo case show that the business model is viable enough to scale up.	-
Regulatory and Stakeholder	Regulation	Regulatory Issues	Regulation changes under development.	Regulation barriers currently in place.
	Consent by users, local authorities, and public	Acceptance	Increasing consent.	-

Table 16. Replicability factors analysis for DEMO 7.

Area	Sub-Areas	Factors	Achievements	Issues
Technical	Technology	Standardization	The solution is partially standard compliant.	Further mandatory standard compliant should be done.
		Interoperability	There is the ability to share data via software and hardware.	-
	Control and communications Interface	Standardization	The solution is partially standard compliant.	Further mandatory standard compliant should be done.
		Interoperability	There is the ability to share data via software and hardware.	-
	Infrastructure	Network Configuration	The solution is partially standard compliant.	Further mandatory standard compliant should be done.
Economic	Business Model	Business model	Business model exist that could be deployed in different environment.	-
	Profitability Analysis	Macro-economic factors	Different options (locations, network topology, etc.) have been evaluated before the implementation.	-
		Market Design	Solution can be easily (economically and technically) compliant with a defined different set of standards.	-
Regulatory and Stakeholder	Regulation	Regulatory Issues	Regulation is expected to change that will make the solution feasible and viable.	There exist regulatory barriers with respect to replicability that could affect the solution.
	Acceptance	Acceptance	Stakeholders have shown great interest.	-

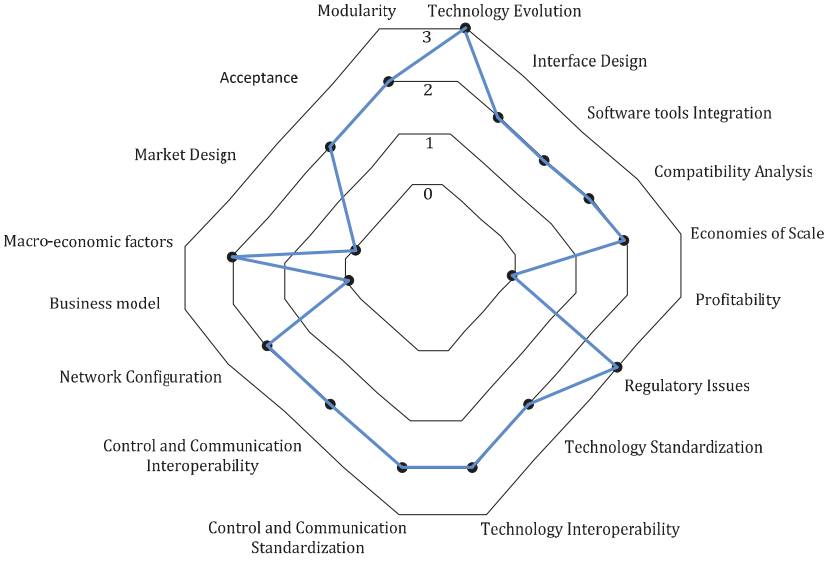

Figure 10. Scalability and replicability assessment DEMO 8: Advanced Control for flexible synchronous generation.

Table 17. Scalability factors analysis for DEMO 8.

Area	Sub-Areas	Factors	Achievements	Issues
Technical	Technology	Modularity	Independent functional units clearly defined.	Replication in a different location would require a new installation. Retraining of prediction models is needed if inputs are changed.
		Technology Evolution	Technological conditions allow increasing the solution size.	-
	Control and communications Interface	Interface design	Centralized	Modification will be needed for new systems under the same location to be added.
		Software tools integration	The design of software permits the integration of more elements.	Integration to different operational and market platforms to be further analyzed.
	Infrastructure	Combability analysis	No physical size limitations.	-
Economic	Economy of scale	Economies of Scale	No economic barriers with respect to scalability.	-
		Profitability	Yet to be determined (by increasing the damping more power can be transferred along the lines which can reduce costs).	No compensation for this kind of service (Damping Oscillations).
Regulatory and Stakeholder	Regulation	Regulatory Issues	No regulatory barriers are known with respect to scalability that could affect the solution.	
	Consent by users, local authorities, and public	Acceptance	Not of importance.	

Table 18. Replicability factors analysis for DEMO 8.

Area	Sub-Areas	Factors	Achievements	Issues
Technical	Technology	Standardization	The solution is partially standard compliant.	-
		Interoperability	There is the ability to share data via software and hardware.	-
	Control and communications Interface	Standardization	The solution is partially standard compliant (standard communication protocols are used).	-
		Interoperability	There is the ability to share data via software and hardware (standard communication protocols are used).	-
	Infrastructure	Network Configuration	The network configuration is standard compliant, by using standard networking devices.	-
Economic	Business Model	Business model	The demo case demonstrates that it is viable enough to replicate.	
	Profitability Analysis	Macro-economic factors	Yet to be determined.	-
		Market Design	Solution can be (economically and technically) compliant with a defined different set of standards.	-
Regulatory and Stakeholder	Regulation	Regulatory Issues	No regulatory barriers are known with respect to replicability that could affect the solution.	
	Acceptance	Acceptance	Minor importance regarding replicability potential for your solution.	

Overall DEMO 8: "Advanced Control for flexible synchronous generation" in the different scalability and replicability factors achieves good score. However, there are significant barriers such as market design and profitability, since currently there is not compensation for providing damping.

7. Results Discussion

The scalability and replicability of FLEXITRANSTORE technology improvements were investigated in this study. Factors that influence the project's scalability and replicability have been researched and identified for this purpose. These criteria include characteristics of technical, economic, regulatory, and stakeholder approval.

The following are the main conclusions for each demonstration:

DEMO 1: "Active Substation Controller" receives a medium overall score, with strong points being the acceptance of stakeholders as a crucial technology for future power grids and the positive impact of technology evolution. The regulatory barriers and the market design that do not satisfactory remunerate the services provided by the Active Substation Controller appear to be the weakest points at this time.

DEMO 2: "Wind Power Plant Connected to Active Substation" receives a medium score, with strong points being the acceptance of stakeholders as a crucial technology for future power grids and the positive impact of technology evolution. Regulatory barriers and market design that do not satisfactory remunerate the services offered by the BESS connected to an active substation with wind power plant appear to be the weakest points at this moment.

DEMO 3: "Increase resilience of the cross-border lines with sensors for de-icing solutions" in most of the scalability and replicability factors achieves a good score. Positive characteristics of this technology include the lack of significant regulatory barriers and the fact that the expert system can be customized to any transmission line by knowing its technical parameters. Standardization, on the other hand, could be further improved, particularly in terms of TSO security standards.

DEMO 4: "Improve transfer capacities and clean electricity flows through Power Flow Control Solutions" in terms of modularity achieves the highest score. Smart Wires has advanced this technology further with higher capacity devices with more controllability, allowing them to push and pull power from the line by increasing or decreasing the effective impedance rather than just increasing it, as was the case with this demo. Compatibility receives a lower grade since the solution design is dependent on the type of transmission lines and towers. The business model is viable, but it will differ from network to network, necessitating further investigation in individual cases. Finally, increasing awareness of the devices and their benefits to the network could help to improve acceptability.

DEMO 5: "New wholesale market approach with flexibility services" achieves high scores in both scalability and replicability. However, since the start of the project, developments on the European markets have taken a turn, and other options appear to be emerging. This severely limits the rationale for considering adapting the developed solution to other markets, yet the approach itself is scalable and reproducible.

DEMO 6: "Flexible substations advanced control and services demonstration" gets high scores on all the scalability and replicability factors, leading to the conclusion that there is no special obstacle to scaling up and replicating the developed technology. Further standardization, as well as the smooth integration of technological developments, would be beneficial.

DEMO 7: "Large Scale Storage System for Combined Cycle Plant" appears to have the potential to be scalable and reproducible; however, GEF has received relatively few bids for this product/service in the last two years, and none have been realized. Furthermore, the increased benefits are not observable or significant now. As a result, one could conclude that this technology is immature and does not have the potential to be scaled up and replicated at this time.

DEMO 8: "Advanced Control for flexible synchronous generation" in the different scalability and replicability factors achieves a good score. However, market design and profitability seem to be significant barriers because there is not compensation for providing damping currently.

8. Conclusions

The scalability and replicability of FLEXITRANSTORE technology innovations were investigated in this study. Factors that influence the project's scalability and replicability have been explored and identified for this purpose. These parameters were chosen based on a thorough literature assessment and include technological, economic, regulatory, and stakeholder acceptance considerations. In a nutshell, technical variables assess if a project's solution is naturally scalable and/or reproducible, whereas economic factors decide whether scaling up or replication is economically viable. Regulation and stakeholder acceptability factors indicate if the current environment is ready to accept a scaled-up version of a project or whether a new environment is appropriate for receiving a project.

Author Contributions: Conceptualization, G.F., C.D., E.Z., S.P. and V.V.; methodology, G.F., C.D., S.P. and V.V.; validation, G.F., V.V. and E.Z.; formal analysis, C.D. and E.Z.; writing—original draft preparation, G.F. and C.D.; writing—review and editing, V.V. and G.F.; visualization, C.D., E.Z., S.P. and G.F.; supervision, V.V. and E.Z. All authors have read and agreed to the published version of the manuscript.

Funding: This research was funded by the European Union's Horizon 2020 research and innovation program under grant agreement No. 824330. The authors acknowledge financial support for the publication of this work from the Special Account for Research of ASPETE.

Conflicts of Interest: The authors declare no conflict of interest.

References

1. Al-Ali, A.; Aburukba, R. Role of Internet of Things in the Smart Grid Technology. *J. Comput. Commun.* **2015**, *3*, 229–233. [CrossRef]
2. Pramudhita, A.N.; Asmara, R.A.; Siradjuddin, I.; Rohadi, E. Internet of Things Integration in Smart Grid. In Proceedings of the International Conference on Applied Science and Technology (iCAST), Manado, Indonesia, 26–27 October 2018; pp. 718–722. [CrossRef]
3. Saleem, Y.; Crespi, N.; Rehmani, M.H.; Copeland, R. Internet of Things-Aided Smart Grid: Technologies. *IEEE Archit. Appl. Prototypes Future Res. Dir.* **2019**, *7*, 62962–63003. [CrossRef]
4. Lazarou, S.; Vita, V.; Christodoulou, C.A.; Ekonomou, L. Calculating operational patterns for electric vehicle charging on a real distribution network based on renewables' production. *Energies* **2018**, *11*, 2400. [CrossRef]
5. Lazarou, S.; Vita, V.; Ekonomou, L. Protection schemes of meshed distribution networks for smart grids and electric vehicles. *Energies* **2018**, *11*, 3106. [CrossRef]
6. FLEXITRANSTORE. An Integrated Platform for Increased FLEXIbility in Smart TRANSmission grids with STORage Entities and Large Penetration of Renewable Energy Sources. Available online: http://flexitranstore.eu/content/home (accessed on 13 May 2022).
7. Farhangi, H. The path of the smart grid. *IEEE Power Energy Mag.* **2010**, *8*, 18–28. [CrossRef]
8. CEN-CENELEC-ETSI. Smart Grid Reference Architecture; CEN-CENELEC-ETSI Smart Grid Coordination Group; Brussels, Belgium, 2012. Available online: https://www.cencenelec.eu/areas-of-work/cen-cenelec-topics/smart-grids-and-meters/smart-grids/ (accessed on 2 May 2022).
9. Ardito, L.; Procaccianti, G.; Menga, G.; Morisio, M. Smart grid technologies in Europe: An overview. *Energies* **2013**, *6*, 251–281. [CrossRef]
10. Di Santo, K.G.; Kanashiro, E.; di Santo, S.G.; Saidel, M.A. A review on smart grids and experiences in Brazil. *Renew. Sustain. Energy Rev.* **2015**, *52*, 1072–1082. [CrossRef]
11. Yu, Y.; Yang, J.; Chen, B. The smart grids in China—A review. *Energies* **2012**, *5*, 1321–1338. [CrossRef]
12. Jiménez, M.S.; Onyeji, I.; Colta, A.; Papaioannou, I.; Mengolini, A.; Alecu, C.; Maschio, I. *Smart Grid Projects in Europe: Lessons Learned and Current Developments*; JRC: Luxembourg, 2012; Available online: https://ses.jrc.ec.europa.eu/sites/ses/files/documents/smart_grid_projects_in_europe_lessons_learned_and_current_developments.pdf (accessed on 15 May 2022).
13. Novosel, D. Experiences with deployment of smart grid projects. In Proceedings of the 2012 IEEE PES Conference on Innovative Smart Grid Technologies (ISGT), Washington, DC, USA, 16–20 January 2012.
14. Niesten, E.; Alkemade, F. How is value created and captured in smart grids? A review of the literature and an analysis of pilot projects. *Renew. Sustain. Energy Rev.* **2016**, *53*, 629–638. [CrossRef]

15. Vita, V.; Christodoulou, C.; Zafeiropoulos, I.; Gonos, I.; Asprou, M.; Kyriakides, E. Evaluating the flexibility benefits of smart grid innovations in transmission networks. *Appl. Sci.* **2021**, *11*, 10692. [CrossRef]
16. Mladenov, V.; Chobanov, V.; Seritan, G.C.; Porumb, R.F.; Enache, B.-A.; Vita, V.; Stănculescu, M.; Van, T.V.; Bargiotas, D. A flexibility market platform for electricity system operators using blockchain technology. *Energies* **2022**, *15*, 539. [CrossRef]
17. Vita, V.; Christodoulou, C.A.; Zafeiropoulos, E.; Mladenov, V.; Chobanov, V.; Asprou, M.; Kyriakides, E. Flexibility adequacy assessment in the SEE region with new technology integration. *WSEAS Trans. Power Syst.* **2022**, *17*, 76–83. [CrossRef]
18. Mladenov, V.; Chobanov, V.; Zafeiropoulos, E.; Vita, V. Characterisation and evaluation of flexibility of electrical power system. In Proceedings of the 10th Electrical Engineering Faculty Conference (BulEF), Sozopol, Bulgaria, 11–14 September 2018. [CrossRef]
19. Zafiropoulos, E.; Christodoulou, C.A.; Vita, V.; Dikaiakos, C.; Gonos, I.F.; Zubieta, E.; Santamaria, G.; Lai, N.B.; Baltas, N.G.; Rodriguez, P. Smart grid flexibility solutions for transmission networks with increased RES penetration. In Proceedings of the CIGRE Paris Seeion 2022 (CIGRE 2022), Paris, France, 28 August–2 September 2022.
20. Mazidi, P.; Baltas, G.N.; Eliassi, M.; Rodriguez, P.; Pastor, R.; Michael, M.; Tapakis, R.; Vita, V.; Zafiropoulos, E.; Dikeakos, C.; et al. Zero renewable incentive analysis for flexibility study of a grid. In Proceedings of the 21st International Symposium on High Voltage Engineering (ISH 2019), Budapest, Hungary, 26–30 August 2019. [CrossRef]
21. Vita, V.; Zafiropoulos, E.; Gonos, I.F.; Mladenov, V.; Chobanov, V. Power system studies in the clean energy era: From capacity to flexibility adequacy through research and innovation. In Proceedings of the 21st International Symposium on High Voltage Engineering (ISH 2019), Budapest, Hungary, 26–30 August 2019. [CrossRef]
22. Mladenov, V.; Chobanov, V.; Zafeiropoulos, E.; Vita, V. Flexibility assessment studies worldwide-bridging with the adequacy needs. In Proceedings of the 11th Electrical Engineering Faculty Conference (BulEF), Varna, Bulgaria, 11–14 September 2019. [CrossRef]
23. Nosair, H.; Bouffard, F. Flexibility Envelopes for Power System Operational Planning. *IEEE Trans. Sustain. Energy* **2015**, *6*, 800–809. [CrossRef]
24. Lannoye, E.; Flynn, D.; O'Malley, M. Transmission, variable generation, and power system flexibility. *IEEE Trans. Power Syst.* **2015**, *30*, 57–66. [CrossRef]
25. Yang, J.; Zhang, L.; Han, X.; Wang, M. Evaluation of operational flexibility for power system with energy storage. In Proceedings of the International Conference on Smart Grid and Clean Energy Technologies (ICSGCE), Chengdu, China, 19–22 October 2016. [CrossRef]
26. Bucher, M.A.; Chatzivasileiadis, S.; Andersson, G. Managing Flexibility in Multi-Area Power Systems. *IEEE Trans. Power Syst.* **2016**, *31*, 1218–1226. [CrossRef]
27. Lannoye, E.; Flynn, D.; O'Malley, M. Evaluation of power system flexibility. *IEEE Trans. Power Syst.* **2012**, *27*, 922–931. [CrossRef]
28. Molitor, C.; Monti, A.; Moser, A. *Residential City Districts as Flexibility Resource: Analysis, Simulation and Decentralized Coordination Algorithms*; RWTH Aachen University: Aachen, Germany, 2015.
29. Dall'Anese, E.; Mancarella, P.; Monti, A. Unlocking Flexibility: Integrated Optimization and Control of Multienergy Systems. *IEEE Power Energy Mag.* **2017**, *15*, 43–52. [CrossRef]
30. Wang, Q.; Hodge, B.M. Enhancing power system operational flexibility with flexible ramping products: A review. *IEEE Trans. Ind. Inform.* **2017**, *13*, 1652–1664. [CrossRef]
31. European Commission. Clean Energy for All Europeans: Communication from the Commission to the European Parliament, the Council, the European Economic and Social Committee, the Committee of the Regions and the European Investment Bank. Available online: https://eur-lex.europa.eu/legal-content/EN/TXT/?uri=COM:2016:0860:FIN (accessed on 15 May 2022).
32. Smart Grid Task Force. Regulatory Recommendations for the Deployment of Flexibility—EG3 REPORT. Available online: https://ec.europa.eu/energy/sites/ener/files/documents/EG3%20Final%20-%20January%202015.pdf (accessed on 15 May 2022).
33. Sigrist, L.; May, K.; Morch, A.; Verboven, P.; Vingerhoets, P.; Rouco, L. On Scalability and Replicability of Smart Grid Projects—A Case Study. *Energies* **2016**, *9*, 195. [CrossRef]
34. Calvo, A.R.; Cossent, R.; Frías, P. Scalability and replicability analysis of large-scale smart grid implementations: Approaches and proposals in Europe. *Renew. Sustain. Energy Rev.* **2018**, *93*, 1–15. [CrossRef]
35. May, K.; Vingerhoets, P.; Sigrist, L. Barriers regarding Scalability and Replicability of Smart Grid Projects. In Proceedings of the 12th International Conference on the European Energy Market (EEM), Lisbon, Portugal, 19–22 May 2015. [CrossRef]
36. Colak, I.; Fulli, G.; Sagiroglu, S.; Yesilbudak, M.; Covrig, C.F. Smart grid projects in Europe: Current status, maturity and future scenarios. *Appl. Energy* **2015**, *152*, 58–70. [CrossRef]
37. Bonnefoy, P.A. Scalability of the Air Transportation System and Development of Multi-Airport Systems: A Worldwide Perspective. Ph.D. Dissertation, Engineering Systems Division, Massachusetts Institute of Technology, Boston, MA, USA, 2008.
38. Menci, S.P.; Herndler, B.; Kupzog, F.; Zweistra, M.; Steegh, R.; Willems, M. Scalability and Replicability Analysis of Grid Management Services in Low Voltage Networks in Local Flexibility Markets: An InterFlex analysis. In Proceedings of the IEEE Madrid PowerTech, Madrid, Spain, 28 June–2 July 2021. [CrossRef]
39. Bridge Horizon 2020. Task Force Replicability & Scalability Analysis, Draft Methodological Guidelines to Perform a Scalability and Replicability Analysis. Available online: https://www.h2020-bridge.eu/download/ (accessed on 13 May 2022).
40. Centre for Coordination of Agricultural Research and Development for Southern Africa (CCARDESA). Scaling Up and Scalability: Concepts, Frameworks and Assessment—Research Report Commissioned by Vuna. Available online: https://www.ccardesa.org/knowledge-products/scaling-and-scalability-concepts-frameworks-and-assessment (accessed on 13 May 2022).

41. Rocabert, J.; Capo-Misut, R.; Munoz-Aguilar, R.S.; Candela, J.I.; Rodriguez, P. Control of Energy Storage System Integrating Electrochemical Batteries and SC for Grid-connected Applications. *IEEE Trans. Ind. Appl.* **2018**, *55*, 1853–1862. [CrossRef]
42. Meng, L.; Zafar, J.; Khadem, S.K.; Collinson, A.; Murchie, K.C.; Coffele, F.; Burt, G.M. Fast Frequency Response From Energy Storage Systems—A Review of Grid Standards, Projects and Technical Issues. *IEEE Trans. Smart Grid* **2020**, *11*, 1566–1581. [CrossRef]
43. European Parliament. *Directive (EU) 2019/944 of the European Parliament and of the Council of 5 June 2019 on Common Rules for the Internal Market for Electricity and Amending Directive 2012/27/EU*; OJ L 158, 14.6.2019; European Parliament: Strasbourg, France, 2019.
44. Khoo, W.C.; The, J.; Lai, C.M. Demand Response and Dynamic Line Ratings for Optimum Power Network Reliability and Ageing. *IEEE Access* **2020**, *8*, 175319–175328. [CrossRef]
45. Numan, M.; Khan, A.Z.; Asif, M.; Majeed, M.S.; Imran, K. Exploiting the Inherent Flexibility in Transmission Network for Optimal Scheduling, Wind Power Utilization, and Network Congestion Management. *IEEE Access* **2021**, *9*, 88746–88758. [CrossRef]

energies

MDPI

Article

A Deep Learning and GIS Approach for the Optimal Positioning of Wave Energy Converters

Georgios Batsis [1], Panagiotis Partsinevelos [2,*] and Georgios Stavrakakis [1]

[1] School of Electrical and Computer Engineering, Technical University of Crete, 73100 Chania, Greece; georgebatsis95@gmail.com (G.B.); gstavr@electronics.tuc.gr (G.S.)
[2] Senselab Research, School of Mineral Resources Engineering, Technical University of Crete, 73100 Chania, Greece
* Correspondence: ppartsi@mred.tuc.gr

Abstract: Renewable Energy Sources provide a viable solution to the problem of ever-increasing climate change. For this reason, several countries focus on electricity production using alternative sources. In this paper, the optimal positioning of the installation of wave energy converters is examined taking into account geospatial and technical limitations. Geospatial constraints depend on Land Use classes and seagrass of the coastal areas, while technical limitations include meteorological conditions and the morphology of the seabed. Suitable installation areas are selected after the exclusion of points that do not meet the aforementioned restrictions. We implemented a Deep Neural Network that operates based on heterogeneous data fusion, in this case satellite images and time series of meteorological data. This fact implies the definition of a two-branches architecture. The branch that is trained with image data provides for the localization of dynamic geospatial classes in the potential installation area, whereas the second one is responsible for the classification of the region according to the potential wave energy using wave height and period time series. In making the final decision on the suitability of the potential area, a large number of static land use data play an important role. These data are combined with neural network predictions for the optimizing positioning of the Wave Energy Converters. For the sake of completeness and flexibility, a Multi-Task Neural Network is developed. This model, in addition to predicting the suitability of an area depending on seagrass patterns and wave energy, also predicts land use classes through Multi-Label classification process. The proposed methodology is applied in the marine area of the city of Sines, Portugal. The first neural network achieves 98.7% Binary Classification accuracy, while the Multi-Task Neural Network 97.5% in the same metric and 93.5% in the F1 score of the Multi-Label classification output.

Keywords: wave energy converters; deep neural networks; renewable energy sources; spatial planning; sentinel satellite imagery

Citation: Batsis, G.; Partsinevelos, P.; Stavrakakis, G. A Deep Learning and GIS Approach for the Optimal Positioning of Wave Energy Converters. *Energies* **2021**, *14*, 6773. https://doi.org/10.3390/en14206773

Academic Editor: Mohamed Benbouzid

Received: 11 August 2021
Accepted: 10 October 2021
Published: 17 October 2021

Publisher's Note: MDPI stays neutral with regard to jurisdictional claims in published maps and institutional affiliations.

Copyright: © 2021 by the authors. Licensee MDPI, Basel, Switzerland. This article is an open access article distributed under the terms and conditions of the Creative Commons Attribution (CC BY) license (https://creativecommons.org/licenses/by/4.0/).

1. Introduction

Currently, the multifaceted phenomenon of climate change is a matter of increasing concern. Despite the fact that the rapid technological progress leads to the improvement of human well-being, some of the industrial sectors are responsible for a significant part of greenhouse gas emissions. More specifically, industry emits 37% of the total gas emissions and a significant part of this percentage represents the environmental cost of producing the required electrical energy for the operation of industrial activities [1]. The need to meet the growing energy demand combined with the least possible environmental consequences, leads to the emergence of renewable energy plants [2]. A challenge for Europe is the ability to generate electricity from renewable sources at high and increasing, over time, levels. Particularly, the objective of EU is to cover the 32% of the total European energy demand from renewable sources by 2030 and to reduce the greenhouse gas emissions by 40% compared to 1999 [3]. It is necessary for various renewable energy plants to be

developed in order to achieve the aforementioned objectives. Many countries are looking for an efficient way to use the ocean as a renewable energy source. Wave energy systems are characterized by high efficiency and their contribution to Europe's energy demand is estimated to be 15% by 2050 [4]. Towards this end, Wave Energy Converters (WEC) are systems that exploit the wave energy, converting it into electricity and they can be installed either independently or in combination with Offshore Wind Generators [5].

Optimal positioning of WECs, is a crucial issue for the marine environment, human activities and the wave energy potential. Suitable areas for WEC installation are selected after the exclusion of points that do not meet certain restrictions. WEC planning limitations are determined by a specific set of rules included in the Marine Spatial Planning (MSP) [6]. In this way, the negative aspect of these systems on the marine activities and the natural environment (i.e., algae, beaches, protected areas and coastal agriculture activities) is prevented. In addition, it is necessary to exclude regions in which the operation of WEC is not efficient (i.e., weather conditions and seabed morphology). Thus, WEC positioning constitutes a decision-making problem in which multiple constraints should be taken into account.

The first step for the optimal positioning of WEC devices is the assessment of the wave energy resource. The most recent research in potential wave energy characterization is based on in situ, satellite and reanalysis data or wave model simulations. Farkas et al. [7], used the third-generation wave model (WAM) combined with altimetry data and characterised the annual, monthly and seasonal wave energy for two specific devices. Authors compared Wave Energy Potential at seven different locations. Additionally, Nilsson et al. [8] utilized WAM evaluated by bouy data and calculated the wave energy potential of the Exclusive Economic Zone (EEZ). They performed wave energy classification in five categories comparing the energy resource of selected locations to the mean wave energy and standard deviation of other sites at similar distance to the shoreline. An additional wave model is the Simulating Waves Nearshore (SWAN) which is developed at Delft University of Technology. Veigas et al. [9] utilized SWAN to find out the offshore wave conditions near the shoreline. Wave energy resource characterization is carried out according to the wave power matrix of the Sea Slot-cone Generator (SSG) data [10] of an offshore bouy and the calculation of the mean annual energy values. Amarouche et al. [11] developed a historical dataset using the SWAN model. Authors classified the potential wave energy flux through the calculation of different temporal variations of wave energy, the probability of distribution, the wave energy development index and the yearly wave energy. Fairley et al. [12] presented a novel method for the wave energy resource characterization. One of the main results of this study are the consequences of the different temporal variability at wave power time series of two locations. Despite the fact that these time series have the same mean value, the standard deviation is different. Thus, the traditional methods for the wave energy resource assessment (i.e., Annual Wave Energy Flux) lead to inefficient results because they cannot handle temporal variability differences. The authors proposed a novel clustering-based method to evaluate wave height and period time series.

Additional to the aforementioned analysis, optimal locations for WEC installation are carried out through geospatial analysis. Researchers and practitioners use Geographic Information Systems (GIS), Multiple-criteria, or a combination of them to deal with optimal positioning of Renewable Energy Systems. Aydin et al. [13], used a GIS-based method in order to find optimal locations for hybrid renewable energy plants in Turkey. Regarding the WEC positioning, Castro-Santos et al. [14], proposed a GIS-based approach under which data were collected for the corresponding geospatial limitations, the seabed morphology, as well as the meteorological conditions and developed four GIS tools. After the combination of corresponding GIS layers, the final decision is made by identifying the available areas on the resulting map. Galparsoro Iza et al. [15], developed a decision making system that combines the MSP approach and GIS. Authors calculated Suitability Index in order to find optimal locations for WEC installation. Apart from the aforementioned methods, some researchers have used Multiple-criteria decision-making (MCDM) systems. Vasileiou

et al. [16] developed a combined GIS-MCDM system to select cites for a hybrid offshore wind-wave farm in Greece. Ghosh et al. [17] proposed a system for WEC positioning. Limitations of WEC planning are defined with the corresponding weights and the MCDM System derives the Feasibility Index (FI) for each of the potential installation regions. An Artificial Neural Network (ANN) is also used to predict the FI value according to the criteria.

The state-of-the-art methods for wave energy resource assessment and for optimal positioning of WEC including geospatial analysis are summarized on Tables 1 and 2, respectively. As a rule, both geospatial and technical limitations criteria for WEC positioning can be modeled using the traditional GIS-based methods. However, in some cases it is essential to examine restrictions related to dynamically changing patterns in marine areas. This is the major limitation of the state of the art methods for WEC positioning, including geospatial analysis (Table 2). For instance, algae are important for the environmental balance and cannot be identified using a GIS database. Geographic datasets entail only historical algae presence records for specific dates. Towards this end, Effrosynidis et al. [18] proposed a Machine Learning (ML) based method to identify seagrass presence according to environmental variables. In addition, satellite imagery is an efficient method for seagrass mapping [19] and Deep Neural Networks (DNN) are used to automate this process. More precisely, Li et al. [20] trained a Convolutional Neural Network (CNN) for the seagrass segmentation of satellite images. Thus, in our study we use Deep Learning methods and remote sensing data in order to identify dynamically changing patterns such as algae in marine areas. Last but not least, relying on Fairley's et al. [12] study, one may highlight the major limitation of the state of the art methods for wave energy resource characterization. According to their results, traditional studies lead to inefficient results due to the difference in time variability of separated locations. In order to deal with this limitation, we expand Fairley's et al. [12] method for the assessment of wave energy potential through the generation of a wave energy dataset with the corresponding suitability labels of wave height and period time series, in order to implement a Deep Learning based algorithm for time series classification. Using this method, we handle differences of temporal variability and we are able to use the proposed model for other case studies.

Based on the above information, in the present study we address the optimal positioning of WEC establishments using a DNN approach. Machine learning techniques are widely used in Renewable Energy Systems in order to estimate the maximum energy production [21], to predict production and load time series [22–24] or to identify potential space for new installations such as photovoltaic systems [25,26]. The heterogeneity and dynamic nature of data and the desire for automation are the main driving forces to undertake the proposed methodology. Thus, we divide the necessary data into static (i.e., land use classes) and dynamic (i.e., algae and wave energy potential). We propose a Deep Learning-based decision system that detects dynamic geospatial limitations, while it evaluates the wave energy potential with respect to time variability. Particularly, we developed a DNN that operates on heterogeneous data fusion [27], in this case satellite images and time series of meteorological data. This fact implies the definition of a two-branches architecture. The branch that is trained with image data provides the localization of dynamic geospatial classes in the potential installation area, whereas the second one is responsible for the classification of the region according to the potential wave energy. The proposed Neural Network is the core of the system that we implemented to automate the process of WEC optimal positioning. Our system operates in two modes: in Mode I, the image recognition branch of DNN only detects algae. The land use classes are received from a land use database and are combined with DNN predictions for the WEC optimizing positioning.

Table 1. Related work for the assessment of wave energy resource.

Authors	Method	Wave Energy Resource Assessment	Results
Farkas et al.	Numerical Method and Wave Model	Annual, Monthly and Seasonal Wave Energy. Comparison with Offshore Wind Energy potential.	Authors compared Wave Energy Potential at seven different locations. Highest values are obtained during winter and lowest at summer.
Nilsson et al.	Numerical Method and Wave Model	Wave energy resource classification through the comparison of mean wave energy potential and its standard deviation of sites at similar distance to the shoreline.	Areas with the highest Wave Energy potential located within the Exclusive Economic Zone of Sweden.
Veigas et al.	Numerical Method, Wave Model and SSG Wave Power Matrix	Comparison with offshore buoy data and SSD Wave Power Matrix.	Authors selected the three best locations. In addition, they calculated the WEC capacity factor (33% or 2628 equivalent hours).
Amarouche et al.	Numerical Method and Wave Model	Temporal variations of different scales, probability of distribution, wave energy development index and annual wave energy.	Authors characterized Eastern Algerian coast as one of the highest energy potential locations in the Mediterranean.
Fairley et al.	Multivariate Clustering	K-means for wave energy resource clustering.	Traditional methods for the wave energy resource assessment (i.e., Annual Wave Energy Flux) lead to inefficient results because they cannot handle temporal variability.

Table 2. Related work for WEC positioning assuming geospatial analysis.

Authors	Plant	Method	Geospatial Analysis	Renewable Energy Resource Assessment
Aydin et al.	Hybrid Solar and Wind Farms	GIS and MCDM	Data Collection, Objectives as fuzzy sets, Environmental performance index	Energy Performance Index
Castro-Santos et al.	Hybrid Offshore Wind and Wave Farms	GIS	Data Collection and GIS techniques	Annual Energy Production
Vasileiou et al.	Hybrid Offshore Wind and Wave Farms	GIS and MCDM	Data Collection, Exclusion of unsuitable areas, AHP for site selection	Average Power
Ghosh et al.	Wave Farm	MCDM and ANN that predicts index for decision-making.	Historical Data	Significant Wave Height and Wind Speed Average
Galparsoro Iza et al.	Wave Farm	Marine Spatial Planning and GIS. Suitability Index.	Data Collection and GIS techniques	Local Wave Atlas

On the other hand, in Mode II, the image recognition branch classifies land use as well as the algae patterns. Thus, the potential regions classified as suitable or as not suitable for WEC installation are exclusively processed via DNN predictions. In both cases, final classification is based upon feature extraction from both image and time series datasets. Overall, the main contributions of this paper include:

- Automation of WEC optimal positioning through Deep Learning algorithms.
- Recognition of dynamically changing patterns—geospatial WEC planning constraints.
- Wave energy potential assessment using time series classification.
- Recognition of dynamic spatial constrains and characterization of wave height and period time series simultaneously via Data Fusion DNN.

In the next section, the methodology and architecture of both implementation modes are described, along with the data used. Section 3 presents the results of both methodological modes and concludes with a real-life case study paradigm. Section 4 discusses the findings of the proposed work and suggests further development paths.

2. Methodology

In this section, we present the proposed methodology for WEC positioning. At first, we describe how we developed our heterogeneous dataset. More precisely, we created a Geographic Information Tool with the usage of which we receive satellite imagery and time series data. In addition, we present the labeling method, in order to develop the training, validation and test dataset for Deep Learning models. The Deep Learning algorithm consists of two modes and for each of them two different DNN architectures are shown. In conclusion, we can use this algorithm after the training process to develop a decision-making system for WEC positioning. All procedure was carried out with the use of our code written in Python programming language and GeoPandas, GDAL and Tensorflow libraries.

2.1. Dataset Generation—Geographic Information Tool

The extraction of specific geographic datasets is necessary in order to implement the proposed method. We developed a Geographic Information Tool, which is necessary to generate the training dataset and apply the methodology to the selected area of interest. In its general form, this tool uses bounding box coordinates of the area of interest as an input and defines the grid of the potential WEC installation points, as well as it incorporates the necessary data. The flowchart of this tool is shown in Figure 1. Initially, we acquire the Sentinel-2 Tile [28] for the corresponding geographical coordinate using the Open Access Hub API. Then, we define the grid of the potential points for WEC installation and we create the georeferenced patch of Sentinel-2 images for each of the patches using the geometric buffer operation. We receive bathymetric data from GEBCO [29] and 12-year Wave Height and Period time series using 3 h time-step from ERA-5 dataset [30] via the Climate Data Store (CDS) API. In addition, we interpolate bathymetric and time series data to our grid, via the CDS Toolbox. For nearshore potential regions we extract land use classes and their polygons from Corine Land Cover (CLC) dataset [31].

The output of our Geographic Information Tool is two databases connected via an information file. The first database contains the georeferenced image patches and the other one the historical wave height and period time series. In Figure 2, an example of a potential WEC installation point is shown. In time series plot the x-axis represents the 3-h time step for the past 12 years and y-axis represents the values of Significant Wave Height (meters) and Peak Wave Period (seconds). Despite the fact that image patches and time series are stored to the corresponding database, the water depth and land use classes are stored in the information file.

Generation of training dataset involves the labeling process of both satellite images and time series. More precisely, we must assign labels to image patches according to algae presence or absence. For this purpose, we use the algae presence observations from UNEP-WCMC dataset [32,33]. By extracting the potential WEC installation points with the aforementioned tool, the event dates from UNEP-WCMC records are used for the region of South Italy to acquire the corresponding Sentinel images. In this way, we used spatial intersection operation between seagrass and patches polygons to assign labels to potential WEC installation regions. On the other hand, time series labeling process is crucial for the assessment of the wave energy potential. In this paper, the novel method of Fairley et al. [12] is used to assign labels about the wave energy. Particularly we implemented the W-based approach. Considering the Significant Wave Height (H_s) and Peak Wave Period (T_p) we calculate the Coefficient of Variation (CV) of $\overline{H_s^2}$, $\overline{T_p}$. Precise, CV is the ratio

of standard deviation of a variable and its mean value. For each of the time series the following variables are calculated:

$$\overline{H_s^2},\ \overline{T_p}$$

$$CV_{H_s^2} = \frac{\sigma_{H_s^2}}{\overline{H_s^2}} \quad (1)$$

$$CV_{T_p} = \frac{\sigma_{T_p}}{\overline{T_p}} \quad (2)$$

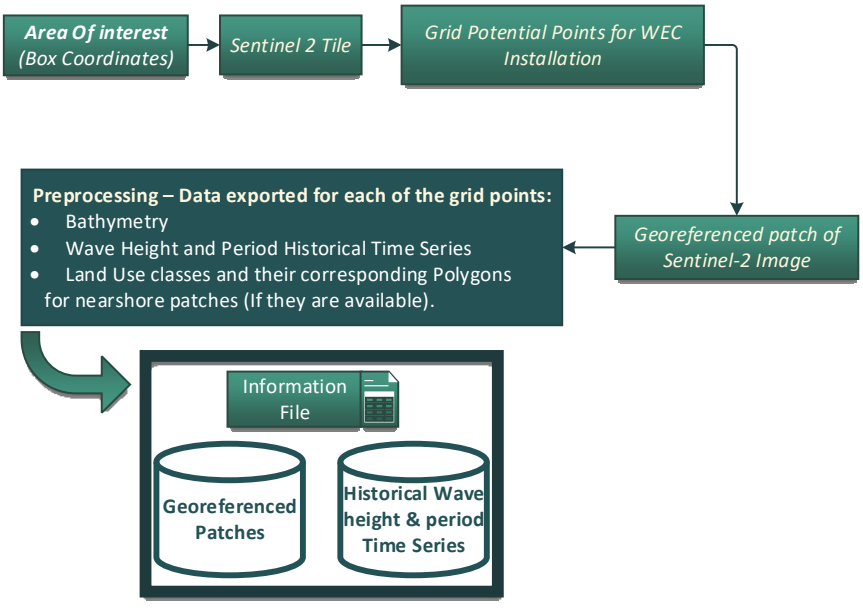

Figure 1. Flowchart of Geographic Information Tool.

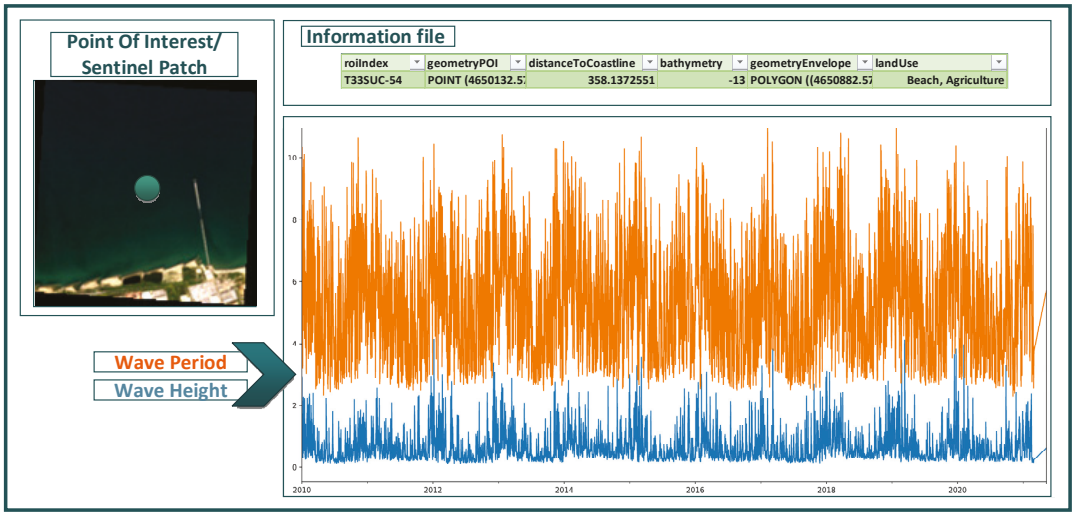

Figure 2. Example of a potential WEC installation point.

The aforementioned variables are used to cluster time series using K-Means (K = 6). According to Significant Wave Height cluster-mean we can sort clusters from 1 to 6 or low wave energy to high wave energy potential, respectively. Thus, we define the clusters 1 to 3 as unsuitable for WEC installation and the clusters from 4 to 6 as suitable. Finally, we can combine the above information in order to assign labels to potential WEC installation points as follows:

- High Wave energy potential and Algae Absence means Suitable Area;
- High Wave energy potential and Algae Presence means Unsuitable Area;
- Low Wave energy potential and Algae Absence means Unsuitable Area;
- Low Wave energy potential and Algae Presence means Unsuitable Area.

2.2. Deep Learning Algorithm

The proposed Deep Learning algorithm is the core of the system that we implemented to automate the process of WEC optimal positioning. As mentioned above, our system operates in two modes: In Mode I, we developed a Data Fusion based Neural Network. The image recognition branch only detects algae. The land use classes are received from a land use dataset. On the other hand, in Mode II, the image recognition branch classifies land use as well as the algae patterns. Thus, the potential regions classified as suitable or as not suitable for WEC installation is performed exclusively via DNN predictions. In this mode, we have implemented a Multitask Data Fusion based Neural Network. In both modes, we used heterogeneous data fusion techniques because the second branch of proposed architecture classifies wave height and period time series.

The Deep Learning model that we implemented is a Convolutional Neural Network (CNN), which is widely used for image recognition and is trained using the Backpropagation algorithm like the traditional ANN [34–37]. Besides this, CNN are efficient for time series classification [38,39]. Consequently, we developed a Convolutional architecture for each of two branches.

2.2.1. Data Fusion Based Neural Network

Consequently, we developed a Convolutional architecture for each of two branches. In order to create Multimodal DNN, its two branches are developed as individual Neural Networks. The reason leading to the specific implementation is to find the optimal architecture for each branch. One of the popular neural networks that work efficiently in the process of identifying marine algae in satellite imagery is the U-Net [20]. This architecture is used for the Semantic Segmentation of an image. However, since we aim to classify images on the presence or absence of algae, an architecture inspired by the Encoder of U-Net is created, due to its efficiency in extracting features from images.

According to Figure 3, the image recognition branch of the Neural Network has three convolutional blocks, in each of which two consecutive Convolutional Layers with the Relu activation function followed by Max Pooling are placed. The number of feature Maps defined per block is 32–64–128, respectively with a 3×3 filter. The Max Pooling process runs in 2×2 regions. At the final step, a Global Average Pooling (GAP) layer is used instead of the flatten operation. In this way, the average value is extracted from each feature map of the last convolutional node. GAP can replace the Fully Connected Layer, while helping to avoid overfitting because it reduces the number of training parameters. The time series branch of DNN consists of 1-D Convolutional and Pooling Layers. As it is shown in Figure 3, this branch has one Convolution of 32 feature maps with a kernel size 5, followed by Max Pooling and then another Convolutional Layer with Filter size 7 from which 64 Feature Maps are extracted, followed again by Max Pooling of size 2. GAP Layer is used instead of Dense Layer too. The extracted features of the two branches are merged via the Concatenation Layer and this layer is fed to a Fully Connected Layer of 256 neurons which are activated via ReLU. Because the task is a Binary Classification problem, the Activation Function that is defined for the final neuron is the Sigmoid. The DNN is implemented on the Tensorflow and Keras Python libraries.

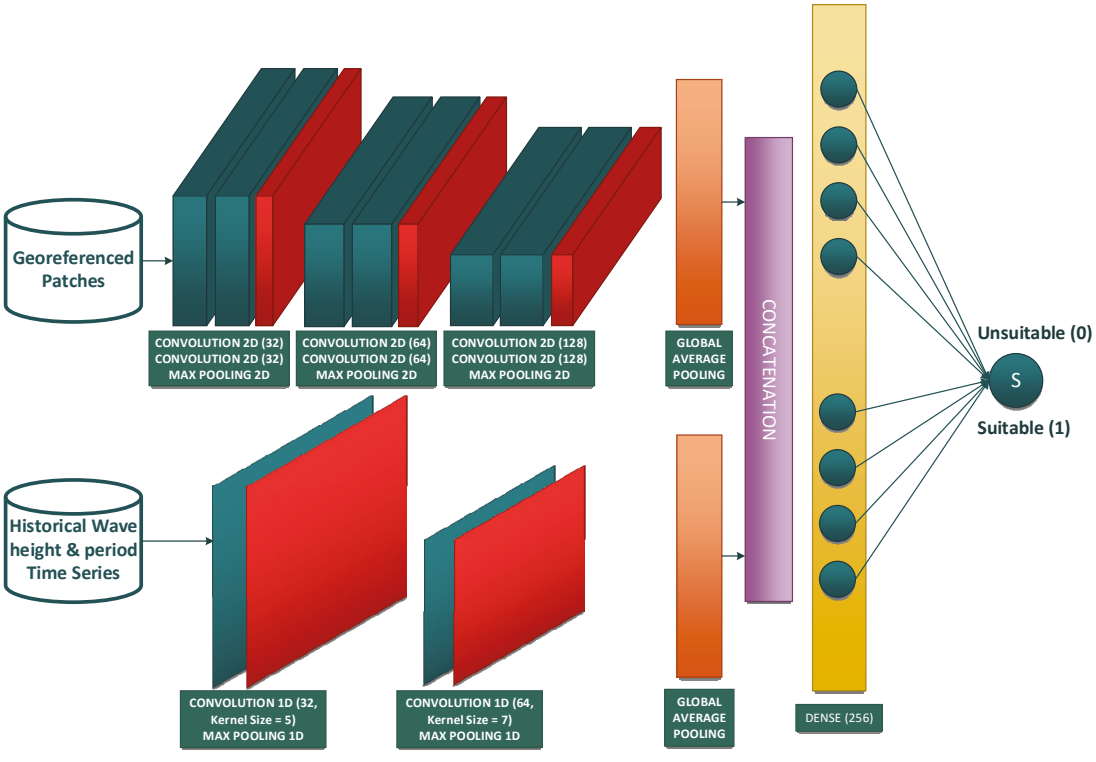

Figure 3. Data fusion Neural Network Architecture—Mode I.

During the training process we need a heterogeneous-data fetching tool, which is developed using the Custom Data Generator of Keras and its input is the information file that connects the two databases (Section 2.1). Satellite images are normalized, dividing each pixel value with 255. The secondary input of Neural Network is a multivariate time series, in particular with two variables, for wave height and period, respectively. Thus, time series are modeled as a 2-D matrix, which consists of two columns, while the number of rows corresponds to the time-steps. Before starting the training process, we split the dataset using 60% for training, 20% for validation and 20% for testing. The validation dataset is fed to the Neural Network at the end of each epoch and when the value of the loss function during the prediction of the data does not improve further, Early Stopping occurs. The Dataset Test is used after the end of the training in order to verify the ability of Neural Network to be generalized. Finally, we use the Adam optimizer [40], 16 batch size, Binary Cross Entropy (BCE) loss function and we estimate model performance according to Accuracy, Precession, Recall and F1 metrics. This Neural Network represents Mode I.

2.2.2. Multitask Data Fusion Based Neural Network

In this section, we present the Neural Network that constitutes the core of Mode II. Particularly, the process of land use classification via the image recognition branch is integrated. This implementation requires the adaptation of both the Neural Network architecture and the training dataset. At the first stage, we determined a One-Hot label for each of the potential WEC installation points. The first four cells of the corresponding table describe the geospatial constraints (Agriculture Activities, Beaches/Dunes, Forest Pattern and Algae) and the last cell is the suitability label of wave energy potential. We provide an example of One-Hot label in Figure 4.

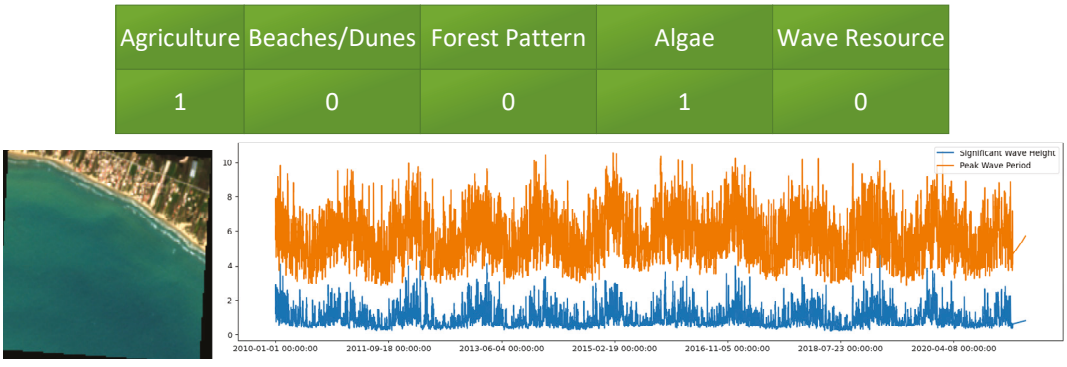

Figure 4. Example of One-Hot vector for unsuitable region.

When the table has the value 1, then the corresponding class exists in the area. The last cell of the table concerns the wave energy assessment, and values 0 or 1 correspond to low or high wave energy, respectively. Based on the One-Hot table, each point is labelled as suitable or not for WEC installation. In this case, the encoding that implies a suitable point (Label equal to 1) is [0,0,0,0,1]. In any other case, the potential region is not suitable and the final label is equal to 0. In Figure 4, an example of an unsuitable region for WEC installation is shown. In this case, we need to build a Neural Network for the solution of two tasks: Multi-label classification and Binary Classification.

When a neural network consists of two outputs, during backpropagation, the common weights are modified in order to optimize two loss functions in parallel. In other words, the model learns to recognize the suitability of a region based on which classes are recognized.

The architecture of Multimodal DNN is modified, initially, as the to the depth of the satellite image recognition branch. In particular, one more Convolution Block is added, and as a result, the number of Feature Maps defined per block are 32–64–128–256, respectively. The time series classification branch remains unchanged. After combining the extracted features from two branches through the Concatenation Layer, a Fully Connected Layer of 256 neurons is used. The first output is for the Binary Classification problem (suitable or not suitable WEC installation point), while the second is used to predict the above One-Hot table. We use BCE loss function on both outputs and we define the Accuracy metric and F1 score in order to estimate the performance of the Binary Classification and Multi-Label classification, respectively. Figure 5 shows the Neural Network Mode II architecture.

2.3. Optimal Positioning of WECs Using Deep Learning—System Implementation

As mentioned before, the decision-making system for WEC positioning, is implemented through two modes, which differ in how the information related to the land use of coastal areas is obtained. In Mode I, the satellite imagery branch recognizes exclusively algae patterns which constitutes the dynamic component. Therefore, the prediction of the suitability of each potential point is based on both the presence or absence of algae and the energy availability of the region, which is classified through the time series branch. The output of the Multimodal DNN is combined with the CLC data in order to avoid additional geographic limitations. The variant in Mode II, is the recognition of land use/cover classes by the satellite image branch. In this case, the suitability of each potential WEC installation point is predicted via the DNN.

Common processes for both modes are the definition of potential installation points and the integration of the corresponding data (Section 2.1). In addition, points that are not in the depth range between 10 and 200 m are excluded.

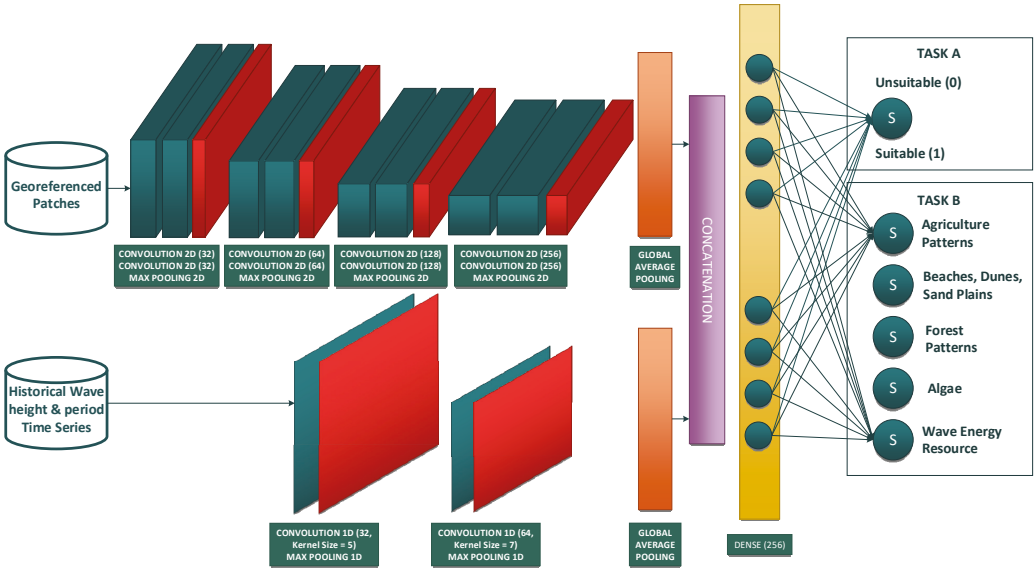

Figure 5. Multitask Data Fusion based Neural Network Architecture.

2.3.1. Mode I

The first implementation of the WEC installation positioning system is modeled according to the flowchart in Figure 6. The Data Fusion based DNN of Section 2.2.1 takes the georeferenced Sentinel patch and time series as input and predicts the corresponding binary label. If the latter is zero, then the point is considered as not suitable for WEC installation. In contrast, prediction of suitable points implies both the absence of algae and high wave energy potential. In this case, the system further processes some information in order to make the final decision. In particular, if the potential region is offshore, then it is considered suitable for WEC installation, while if it is a nearshore point, it is required to avoid additional spatial restrictions related to the use/coverage of the closest coastal land. If in the latter beaches, swimming zones, dunes, woodland or agricultural facilities are located, then the point is automatically rejected. Finally, decisions of each of the potential WEC installation sites are combined, in order to construct the suitability map of the overall area of interest.

2.3.2. Mode II

The second mode of the WEC optimal positioning methodology contains the Multitask data fusion based Neural Network analyzed in Section 2.2.2 as a core unit. In this way, the decision for each point is taken directly through the corresponding output of DNN, that is, the one that implements the Binary Classification problem. In addition, the output of the Multi-label Classification process is used to monitor how the final decision is formed, since as a result, the land use classes identified, including algae, as well as the energy suitability results are given. The flowchart of this process is in Figure 7.

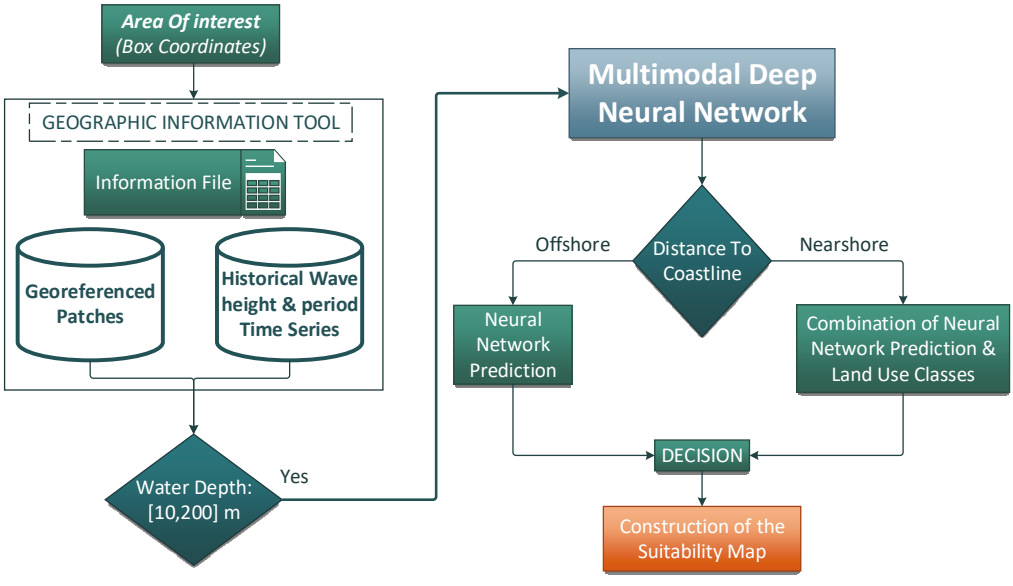

Figure 6. Decision-making system flowchart in Mode I.

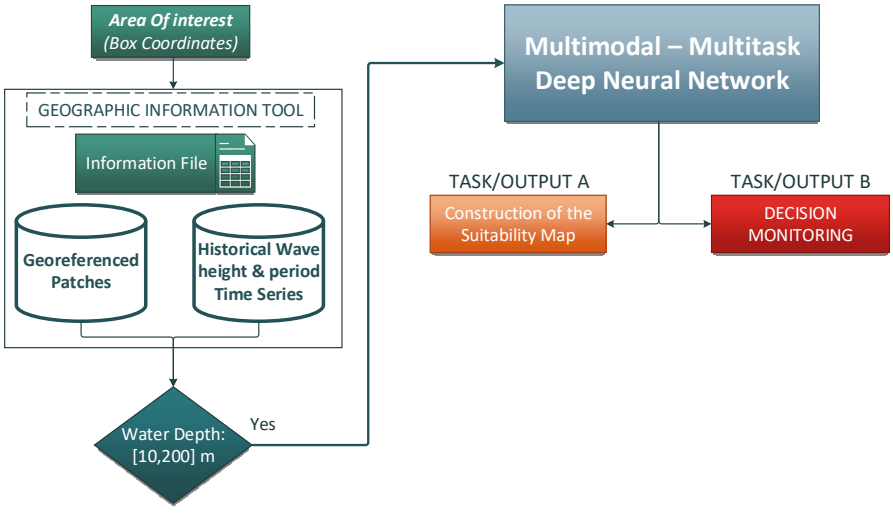

Figure 7. Decision-making system flowchart in Mode II.

3. Results

In this section, we present the results of our approach. At first, we analyze the training diagrams and the performance of Deep Learning models. Then, we showcase the proposed methodology to the selected geographical area. We trained our models using the NVDIA GTX 1650 GPU and we used TensorBoard for training process monitoring.

3.1. Performance Metrics

In Binary Classification problems, we can estimate the performance of our classifier calculating the number of samples that are classified correctly or incorrectly. If the value of the final neuron output is greater than 0.5, our sample belongs to positive class, whereas our

sample belongs to the negative one. Regions that are suitable for the installation of WEC device correspond to class one, whereas the unsuitable locations are marked as samples of negative class. Thus, we calculate True Positive (*TP*), True Negative (*TN*), False Positive (*FP*) and False Negative (*FN*) classified samples. Using these statistical variables, we can see how many of testing samples are classified correctly or not. In order to visualize the aforementioned statistical approach, we define the Confusion Matrix as follows:

$$Confusion\ Matrix = \begin{bmatrix} TP & FP \\ FN & TN \end{bmatrix} \tag{3}$$

Far from these, we examine effectiveness of the proposed model using Recall and Precision. Recall is the ratio of actual positive predictions divided by the number of actual positive samples. In other words, is a metric that shows the effectiveness of our model to accomplish true predictions of positive labels. On the other hand, Precision is the ratio of actual positive samples divided by the number of all positive predictions. Thus, Precision is the proportion of actually correct positive predictions [41].

$$Recall = \frac{TP}{TP + FN} \tag{4}$$

$$Precission = \frac{TP}{TP + FP} \tag{5}$$

Precision and Recall combined in a single performance metric. *F*1 score is the harmonic mean of both. We defined *F*1 as the actual model performance metric during training process. *F*1 is using in Binary Classification problems [42].

$$F1 = 2 * \frac{Precision * Recall}{Precission + Recall} \tag{6}$$

3.2. Data Fusion Based Neural Network

Searching about the optimal architecture of the Data Fusion-Based Neural Network, we implemented each branch of it as an individual DNN. Particularly, we added a sigmoid neuron after the GAP layer. Thus, two binary classifiers have developed, for algae and time series classification, respectively. Compared to other methods for algae classification and detection based on remote sensing data [18,20,43], our approach achieves 98.5% (Table 3). F1 score on test dataset according to the Confusion Matrix. The equivalent percentage for testing samples of time series classification CNN is 98.8% (Table 4).

Table 3. Confusion Matrix for algae detection problem.

	Predicted—Class 0	**Predicted—Class 1**
Actual—Class 0	TN: 2071	FP: 14
Actual—Class 1	FN: 30	TP: 1959

Table 4. Confusion Matrix for time series classification problem.

	Predicted—Class 0	**Predicted—Class 1**
Actual—Class 0	TN: 1053	FP: 6
Actual—Class 1	FN: 18	TP: 1023

The combination of the above Deep Learning implementations leads to the development of the Data Fusion based Neural Network, which is shown in Figure 3. Training curves are presented in Figure 8. Training process ends in the 19th Epoch due to the Early Stopping condition, because there is no improvement of the loss function, while in the 16th the minimum value of BCE is observed. The F1 metric performance results in test Dataset are 98.7%, while Table 5 presents the confusion matrix on test dataset. Therefore, the DNN

can be used to classify the potential regions as suitable or not for WEC installation. The final decision depends upon the combination of the presence or absence of algae and wave energy assessment. According to Figure 9, the Binary Classifier works efficiently because it identifies the potential regions of the test dataset with high accuracy. In particular, it correctly classifies both suitable sites, and non-suitable ones that they are points with algae presence or with low wave energy. Both the prediction of DNN and the actual labels are shown in order to understand the final decision.

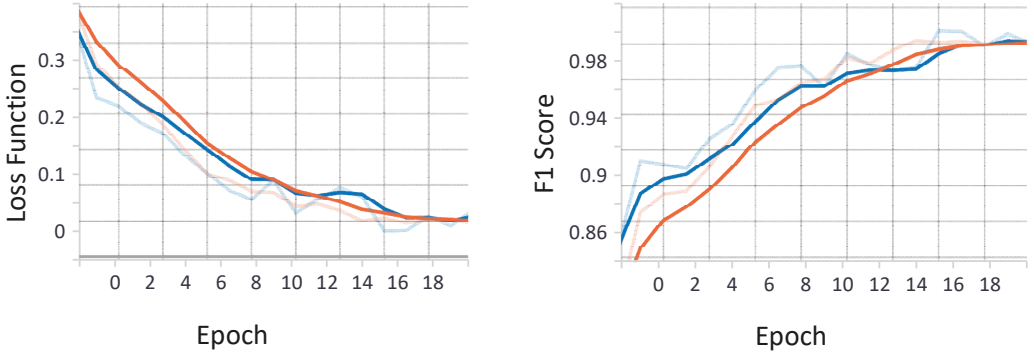

Figure 8. Data Fusion based Neural Network performance during training process. (**a**) Binary Cross Entropy Loss for both training (orange) and validation (blue) datasets; (**b**) F1 score for both training and validation datasets.

Table 5. Confusion Matrix of Neural Network that classifies the suitability of potential WEC installation regions.

	Predicted—Class 0	**Predicted—Class 1**
Actual—Class 0	TN: 799	FP: 10
Actual—Class 1	FN: 7	TP: 847

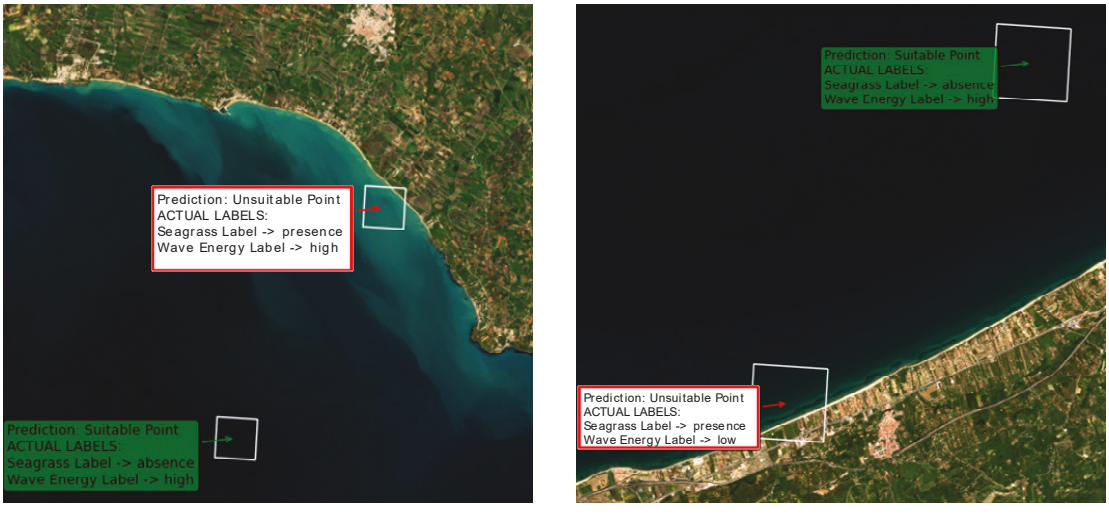

Figure 9. Data Fusion based Neural Network predictions on test dataset.

3.3. Multitask Data Fusion Based Neural Network

Proceeding to the development of Multitask Data Fusion based Neural Network (Figure 5), we integrate the land cover classification task to our model. The architecture consists of two outputs. The first output is for the binary prediction of the potential region as suitable or not suitable for the WEC system installation and the second for the prediction of One-Hot vector of limitations, in this case land use classes, algae detection and the wave energy class. Regarding Figure 10, in the 24th Epoch the training ends, while in the 15th the lower value of the BCE is observed. We defined as the loss function and metric for both outputs BCE-F1 Score. The overall F1 Score is 94%.

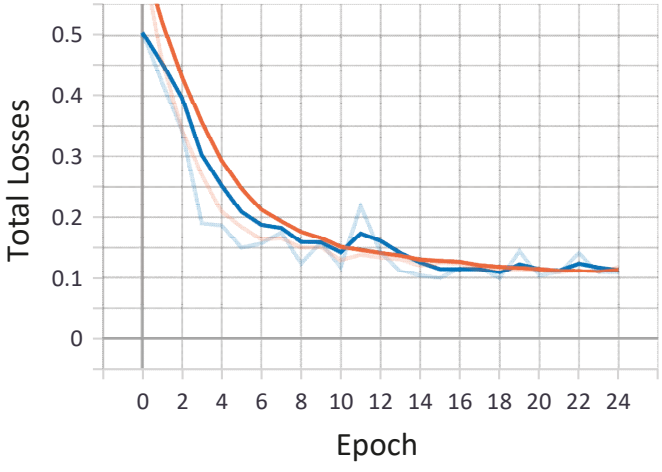

Figure 10. Total training and validation losses for Multitask Data Fusion based Neural Network.

For potential WEC installation points classified as True Positive or True Negative, the corresponding One-Hot Label is predicted correctly as well. Figure 11 shows the results on test data. As observed, for each region, both the Multilabel vector containing the detected classes is predicted, as well as the designation as suitable or not. As the two loss functions are optimized at the same time, there is an interdependence between the outputs, which is the objective of our approach. The difference between the F1 score of the two Neural Networks arises because in Mode II we have larger prediction complexity due to the dependence of the two outputs and the recognition of land use classes.

3.4. Expreriments of Methodology Application

Case Study

We applied the proposed methodology to the geographical area of Figure 12a. By defining the geographical coordinates of the selected bounding box on the map, data extraction and preprocessing is performed, as shown in Section 2.1. In particular, we receive the Sentinel-2 images and we define the Grid of the potential WEC installation points. For each point, the Patch of the image is extracted and the wave height and period time series are obtained from the Era-5 dataset. In Figure 12b, the gaps observed, are regions that were automatically excluded because they are out of the desired water depth range.

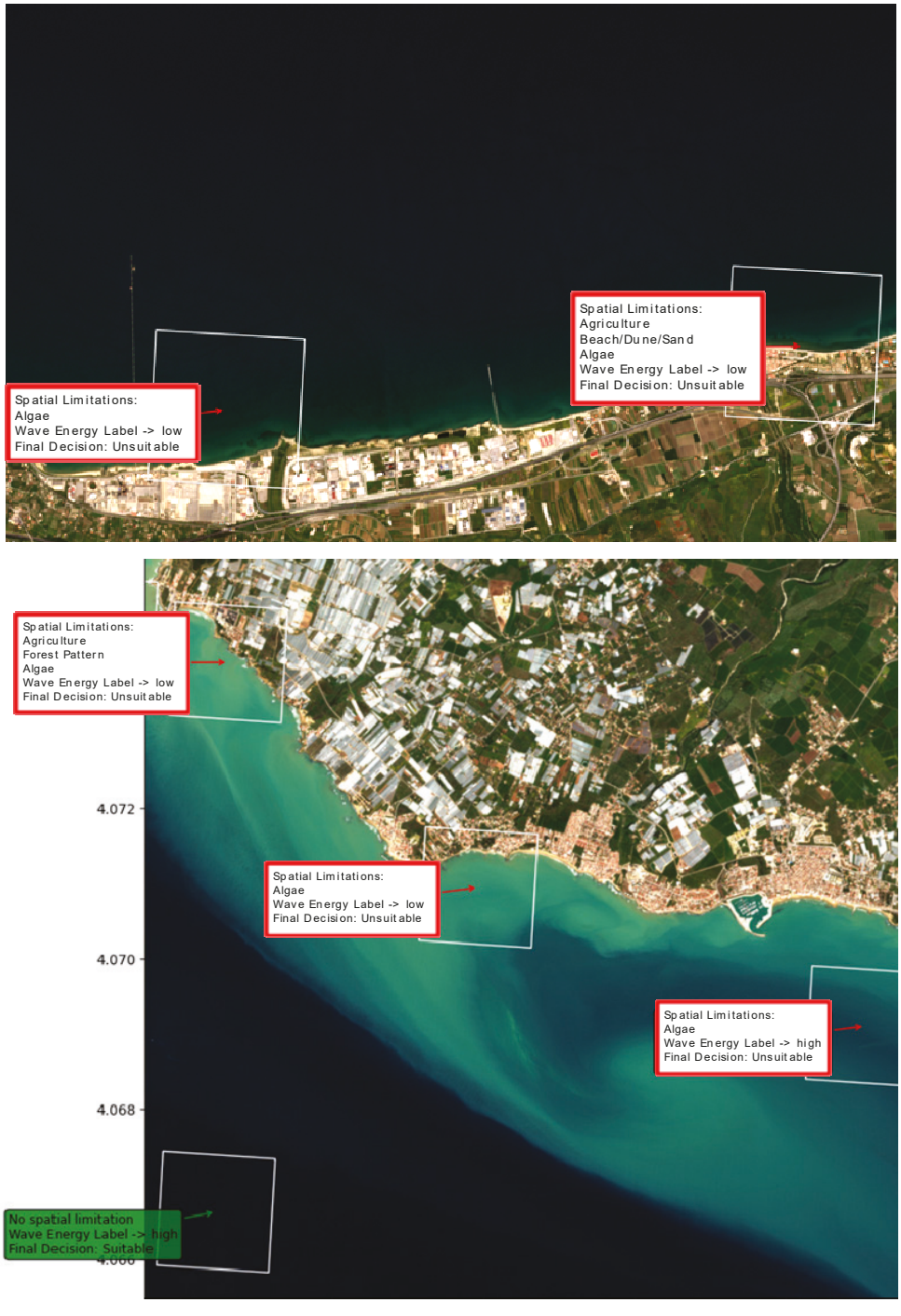

Figure 11. Multitask Data Fusion based Neural Network predictions on test dataset.

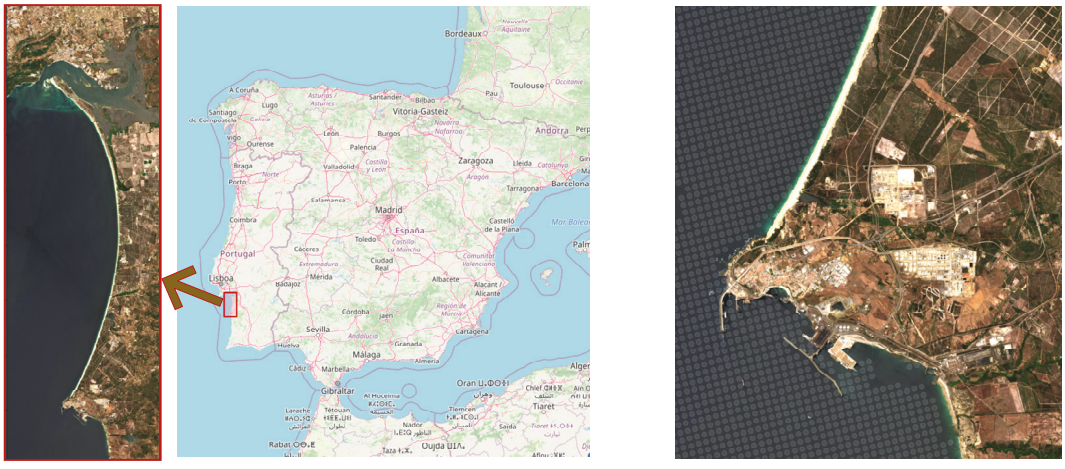

(**a**) (**b**)

Figure 12. (**a**) Case study; Sines, Portugal; (**b**) potential WEC installation points of interest.

In Mode I, the suitability map is first derived based on the algae detection and wave energy assessment. Neural Network predictions are presented in Figures 13a and 14a. Then, the available land use/land cover data are fetched from the CLC dataset and depending on the geographical constraints that arise, the final decision is formed, as Figures 13b and 14b show. The areas highlighted in red color are excluded, while in green the suitable for WEC system sites are shown.

(**a**) (**b**)

Figure 13. (**a**) Neural Network Prediction; (**b**) final decision considering land use data.

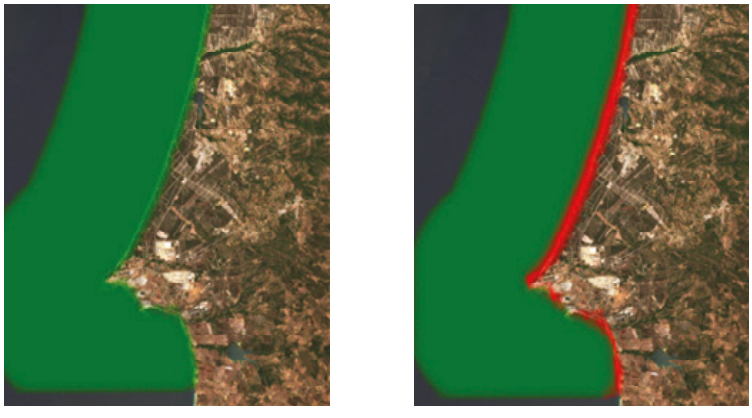

(**a**) (**b**)

Figure 14. (**a**) Neural Network Prediction; (**b**) final decision considering land use data.

Utilizing the Multitask Data Fusion based Neural Network in Mode II, the suitability map is generated directly from the DNN predictions and specially the output of Binary Classification task (Figures 15a and 16a). In addition, One-Hot label, which results from the second output of the Neural Network, appears for each of the potential regions. In this way, the cause for which the area was excluded from the study becomes known. In Figures 15b and 16b there is a sample of predictions of the second task.

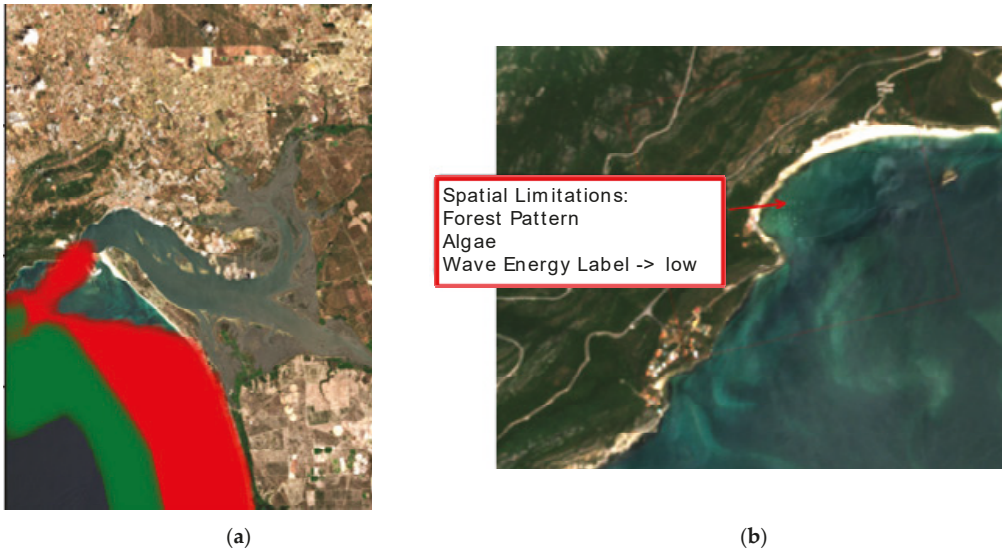

(**a**) (**b**)

Figure 15. (**a**) Suitability map—Neural Network Predictions; (**b**) zoom to observe Multilabel Classification results.

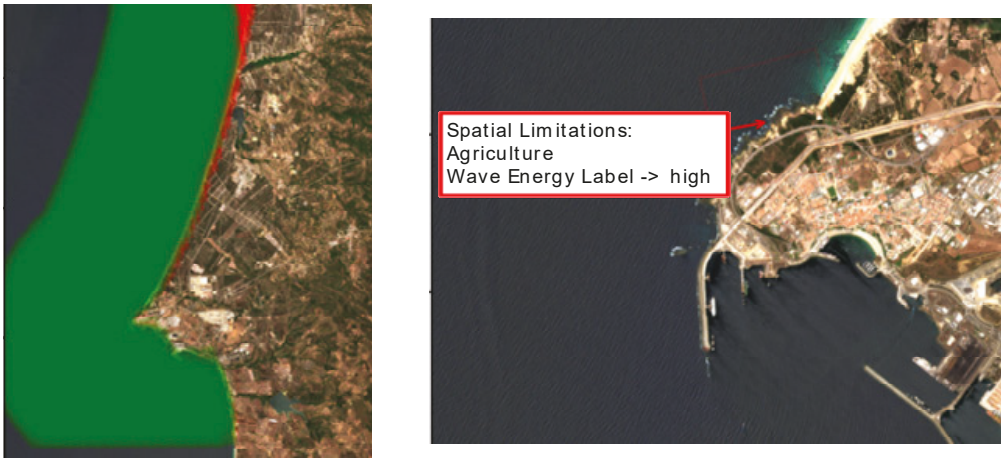

(**a**) (**b**)

Figure 16. (**a**) Suitability map—Neural Network Predictions; (**b**) zoom to observe Multilabel Classification results.

Both Modes make common predictions of offshore points of interest with algae presence. In Figures 13a and 15a our models classify differently the wave energy potential in some offshore points of interest due to FN predictions of Neural Network in Mode II, because the Binary Classification task depends on the Multilabel Classification task. In the majority of nearshore regions, which are affected by land use, there is an agreement between the two approaches. Nevertheless, we notice in Figures 14a and 16a that the Multitask DNN does not properly classify coastal areas in the southern part, because in order to identify a land use class in the satellite image, the latter must correspond to a significant percentage of the coast and be clearly visible. When using Mode I, land use classes are found using the spatial intersection operation, which always implies their correct detection. Nobre et al. [44] focus in this geographical area during their study. Comparison of the results with the proposed approach can only be done for offshore points, because the authors reject the areas near the coast. Although the estimate of the potential wave energy is made in a different way and in the present paper we detect seagrass in marine areas, there is an agreement of the results to a very large extent.

4. Conclusions and Discussion

This paper presents a new, Deep Learning-based methodology to automate the process of WEC optimal positioning. The presented models work with freely available satellite images, as well as Climate Reanalysis data. The methodology is applied through two different approaches. In Mode I, land use data are received from CLC dataset, while in the second method they are extracted from the satellite images in order to avoid additional geographic limitations. At the end of the training process, the model being developed is capable of identifying the spatial restrictions in satellite images, including algae patterns that are dynamically changing features. At the same time, the system estimates the wave energy potential by treating it as a dynamic phenomenon, which is characterized by non-predictable temporal variability. In addition, our model can identify the differences in temporal variability of multiple locations. In this way, it is confirmed that merging heterogeneous data works efficiently in solving complex problems. Thus, it turns out that CNNs are efficient in both image and time series recognition.

In this paper, we initiate a new method for the spatial positioning of WEC that is based in recognition of geospatial constraints which are dynamically changing patterns in marine areas. Thus, the main limitation of this study is the fact that additional dynamic classes can be added to satellite image recognition task. Under this rationale, the proposed

model can be generalized to include several image-related dynamic phenomena. In marine areas there are characteristics that change in time, so their identification is difficult without Machine Learning or costly monitoring. In addition, the main technical challenge of this study is the fact that the examination of dynamic geospatial and technical restrictions should be combined in terms of Levelized Cost of Energy (LCOE) of wave energy and GIS methods [45]. Regarding land use, the interconnection of the proposed system with an API such as Google Maps/Places or Open Street Map could be efficient because these platforms contain data that are frequently updated. Finally, in addition to assessing climatic conditions, a third branch can be added to the proposed Neural Network for time series forecasting.

Author Contributions: Conceptualization, G.B., G.S. and P.P.; methodology, G.B., G.S. and P.P.; software, G.B.; validation, G.B. and G.S.; formal analysis, G.B.; resources, G.B. and P.P.; data curation, G.B.; writing—original draft preparation, G.B.; writing—review and editing, G.B., G.S. and P.P.; supervision, G.S. and P.P.; All authors have read and agreed to the published version of the manuscript.

Funding: This research received no external funding.

Institutional Review Board Statement: Not applicable.

Informed Consent Statement: Not applicable.

Data Availability Statement: UN Environment Programme World Conservation Monitoring Centre provides open-access data about the global distribution of seagrass. Copernicus Land Monitoring Service produced the Corine Land Cover Dataset within the frame of CORINE Land Cover Programme, which is coordinated by the European Environment Agency (EEA) (https://land.copernicus.eu/pan-european/corine-land-cover, accessed on 10 September 2021). Furthermore, Copernicus Proramme and Open Acess Hub provide publicly available Sentinel 2 satellite imagery (https://scihub.copernicus.eu/, accessed on 10 September 2021). Concerning time series data, the ERA5 is the ECMWF reanalysis dataset for the global climate and weather. These data are available through the Climate Data Store (https://cds.climate.copernicus.eu/cdsapp#!/dataset/reanalysis-era5-single-levels?tab=overview, accessed on 10 September 2021).

Conflicts of Interest: The authors declare no conflict of interest.

Index of Abbreviations

WEC	Wave Energy Converters
MSP	Marine Spatial Planning
EEZ	Exclusive Economic Zone
SWAN	Simulating Waves Nearshore
GIS	Geographic Information Systems
MCDM	Multiple-criteria decision-making
FI	Feasibility Index
ANN	Artificial Neural Network
ML	Machine Learning
DNN	Deep Neural Networks
CNN	Convolutional Neural Network
CDS	Climate Data Store
CLC	Corine Land Cover
CV	Coefficient of Variation
GAP	Global Average Pooling
BCE	Binary Cross Entropy
TP	True Positive
TN	True Negative
FP	False Positive
FN	False Negative
LCOE	Levelized Cost of Energy

References

1. Panwar, N.; Kaushik, S.; Kothari, S. Role of renewable energy sources in environmental protection: A review. *Renew. Sustain. Energy Rev.* **2011**, *15*, 1513–1524. [CrossRef]
2. Bilgen, S. Global warming and renewable energy sources for sustainable development: A case study in Turkey. *Renew. Sustain. Energy Rev.* **2008**, *12*, 372–396. [CrossRef]
3. Commision, E. *The 2030 Climate and Energy Framework*; Palgrave Macmillan: Cham, Switzerland, 2013.
4. The European Ocean Energy Association (EU-OEA). *Oceans of Energy-European Ocean Energy Roadmap 2010–2050*; EU-OEA: Brussels, Belgium, 2010.
5. Pérez-Collazo, C.; Greaves, D.; Iglesias, G. A review of combined wave and offshore wind energy. *Renew. Sustain. Energy Rev.* **2015**, *42*, 141–153. [CrossRef]
6. Commision, E. *Maritime Spatial Planning in the EU-Achievements and future development. Communication from the Commision to the European Parliament, the Council, the European Economic and Social Commitee and the Committe of the Regions*; European Commission: Brussels, Belgium, 2010.
7. Farkas, A.; Degiuli, N.; Martić, I. Assessment of Offshore Wave Energy Potential in the Croatian Part of the Adriatic Sea and Comparison with Wind Energy Potential. *Energies* **2019**, *12*, 2357. [CrossRef]
8. Nilsson, E. Characterization of Wave Energy Potential for the Baltic Sea with Focus on the Swedish Exclusive Economic Zone. *Energies* **2019**, *12*, 793. [CrossRef]
9. Veigas, M.; Lopez, M.; Iglesias, G. Assessing the optimal location for a shoreline wave energy converter. *Appl. Energy* **2014**, *132*, 404–411. [CrossRef]
10. Vicinanza, D. The SSG Wave Energy Converter: Performance, Status and Recent Developments. *Energies* **2012**, *5*, 193–226. [CrossRef]
11. Amarouche, K. Wave energy resource assessment along the Algerian coast based on 39-year wave hindcast. *Renew. Energy* **2020**, *153*, 840–860. [CrossRef]
12. Fairley, I. A classification system for global wave energy resources based on multivariate clustering. *Appl. Energy* **2020**, *262*, 114515. [CrossRef]
13. Aydin, N.Y.; Kentel, E.; Duzgun, H.S. GIS-based site selection methodology for hybrid renewable energy systems: A case study from western Turkey. *Energy Convers. Manag.* **2013**, *70*, 90–106. [CrossRef]
14. Castro-Santos, L. Planning of the installation of offshore renewable energies: A GIS approach of the Portuguese roadmap. *Renew. Energy* **2019**, *132*, 1251–1262. [CrossRef]
15. Galparsoro Iza, I. A Marine Spatial Planning Approach to Select Suitable Areas for Installing Wave Energy Converters (WECs), on the Basque Continental Shelf (Bay of Biscay). *Coast. Manag.* **2012**, *40*, 1–19. [CrossRef]
16. Vasileiou, M.; Loukogeorgaki, E.; Vagiona, D.G. GIS-based multi-criteria decision analysis for site selection of hybrid offshore wind and wave energy systems in Greece. *Renew. Sustain. Energy Rev.* **2017**, *73*, 745–757. [CrossRef]
17. Ghosh, S. Wave Energy Potential Site Selection Based on MCDM and Neural Network Analysis. In *Application of Geographical Information Systems and Soft Computation Techniques in Water and Water Based Renewable Energy Problems*; Springer: Singapore, 2018; pp. 107–120.
18. Effrosynidis, D.; Arampatzis, A.; Sylaios, G. Seagrass detection in the mediterranean: A supervised learning approach. *Ecol. Inform.* **2018**, *48*, 158–170. [CrossRef]
19. Traganos, D. Towards Global-Scale Seagrass Mapping and Monitoring Using Sentinel-2 on Google Earth Engine: The Case Study of the Aegean and Ionian Seas. *Remote Sens.* **2018**, *10*, 1227. [CrossRef]
20. Li, X. Deep-learning-based information mining from ocean remote-sensing imagery. *Natl. Sci. Rev.* **2020**, *7*, 1584–1605. [CrossRef]
21. Kalogerakis, C.; Koutroulis, E.; Lagoudakis, M.G. Global MPPT Based on Machine-Learning for PV Arrays Operating under Partial Shading Conditions. *Appl. Sci.* **2020**, *10*, 700. [CrossRef]
22. Jayalakshmi, N. Novel Multi-Time Scale Deep Learning Algorithm for Solar Irradiance Forecasting. *Energies* **2021**, *14*, 2404. [CrossRef]
23. Jin, X.-B. Deep-Learning Forecasting Method for Electric Power Load via Attention-Based Encoder-Decoder with Bayesian Optimization. *Energies* **2021**, *14*, 1596. [CrossRef]
24. Peng, X. Short-Term Wind Power Prediction for Wind Farm Clusters Based on SFFS Feature Selection and BLSTM Deep Learning. *Energies* **2021**, *14*, 1894. [CrossRef]
25. Castello, R. Deep learning in the built environment: Automatic detection of rooftop solar panels using Convolutional Neural Networks. *J. Physics Conf. Ser.* **2019**, *1343*, 012034. [CrossRef]
26. Lee, S. Deep Roof: A Data-driven Approach For Solar Potential Estimation Using Rooftop Imagery. In Proceedings of the 25th ACM SIGKDD International Conference on Knowledge Discovery & Data Mining, Anchorage, AK, USA, 8 August 2019; pp. 2105–2113.
27. Cao, R. Deep learning-based remote and social sensing data fusion for urban region function recognition. *ISPRS J. Photogramm. Remote Sens.* **2020**, *163*, 82–97. [CrossRef]
28. ESA. *Copernicus Sentinel Data 2018–2021*; ESA: Paris, France; pp. 2018–2021.
29. British Oceanographic Data Centre. *GEBCO Digital Atlas: Digital version of the IOC/IHO General Bathymetric Chart of the Oceans (GEBCO)*; British Oceanographic Data Centre: Liverpool, UK, 1994.

30. Hersbach, H.; Bell, B.; Berrisford, P.; Biavati, G.; Horányi, A.; Muñoz Sabater, J.; Nicolas, J.; Peubey, C.; Radu, R.; Rozum, I.; et al. ERA5 hourly data on single levels from 1979 to present. *Copernic. Clim. Chang. Serv. Clim. Data Store* **2018**.
31. EEA. *Corine Land Cover (CLC)*; EEA: Copenhagener, Denmark, 2018.
32. Short, F.; Green, E. *World Atlas of Seagrasses*; University of California Press: Berkeley, CA, USA, 2003; ISBN 0-520-24047-2.
33. UNEP-WCMC; Short, F. *Global Distribution of Seagrasses (Version 7.1). Seventh Update to the Data Layer Used in Green and Short (2003)*; UN Environment World Conservation Monitoring Centre; Cambridge, UK, 2021.
34. DiCarlo, J.J.; Zoccolan, D.; Rust, N.C. How Does the Brain Solve Visual Object Recognition? *Neuron* **2012**, *73*, 415–434. [CrossRef] [PubMed]
35. Gonzalez, R.C.; Woods, R.E. *Digital Image Processing*; Pearson: London, UK, 2018; ISBN 0133356728/9780133356724.
36. LeCun, Y. Backpropagation Applied to Handwritten Zip Code Recognition. *Neural Comput.* **1989**, *1*, 541–551. [CrossRef]
37. Yamashita, R. Convolutional neural networks: An overview and application in radiology. *Insights Imaging* **2018**, *9*, 611–629. [CrossRef] [PubMed]
38. Fawaz, H.I.; Forestier, G. Deep learning for time series classification: A review. *Data Min. Knowl. Discov.* **2019**, *33*, 917–963. [CrossRef]
39. Zhao, B. Convolutional neural networks for time series classification. *J. Syst. Eng. Electron.* **2017**, *28*, 162–169. [CrossRef]
40. Kingma, D.P.; Ba, J. Adam: A method for stochastic optimization. In Proceedings of the International Conference Learn. Represent. (ICLR), San Diego, CA, USA, 5–8 May 2015.
41. Sokolova, M.; Lapalme, G. A systematic analysis of performance measures for classification tasks. *Inf. Process. Manag.* **2009**, *45*, 427–437. [CrossRef]
42. Goutte, C.; Gaussier, E. A Probabilistic Interpretation of Precision, Recall and F-Score, with Implication for Evaluation. In Proceedings of the 27th European Conference on IR Research, ECIR 2005, Santiago de Compostela, Spain, 21–23 March 2005; Volume 3408, pp. 345–359.
43. Arellano-Verdejo, J.; Hernandez, H.E.L.; Cabanillas-Terán, N. ERISNet: Deep neural network for Sargassum detection along the coastline of the Mexican Caribbean. *PeerJ* **2019**, *7*, e6842. [CrossRef]
44. Nobre, A. Geo-spatial multi-criteria analysis for wave energy conversion system deployment. *Renew. Energy* **2009**, *34*, 97–111. [CrossRef]
45. Castro-Santos, L. The Levelized Cost of Energy (LCOE) of wave energy using GIS based analysis: The case study of Portugal. *Int. J. Electr. Power Energy Syst.* **2015**, *65*, 21–25. [CrossRef]

energies

MDPI

Article

Hybridizing Lead–Acid Batteries with Supercapacitors: A Methodology

Xi Luo [1], Jorge Varela Barreras [2], Clementine L. Chambon [3], Billy Wu [4] and Efstratios Batzelis [1,*]

[1] Department of Electrical and Electronic Engineering, Imperial College London, London SW7 2AZ, UK; xi.luo19@imperial.ac.uk
[2] Department of Mechanical Engineering, Imperial College London, London SW7 2AZ, UK; j.varela-barreras@imperial.ac.uk
[3] Department of Chemical Engineering, Imperial College London, London SW7 2AZ, UK; c.chambon13@imperial.ac.uk
[4] Dyson School of Design Engineering, Imperial College London, London SW7 2AZ, UK; billy.wu@imperial.ac.uk
* Correspondence: e.batzelis@imperial.ac.uk

Abstract: Hybridizing a lead–acid battery energy storage system (ESS) with supercapacitors is a promising solution to cope with the increased battery degradation in standalone microgrids that suffer from irregular electricity profiles. There are many studies in the literature on such hybrid energy storage systems (HESS), usually examining the various hybridization aspects separately. This paper provides a holistic look at the design of an HESS. A new control scheme is proposed that applies power filtering to smooth out the battery profile, while strictly adhering to the supercapacitors' voltage limits. A new lead–acid battery model is introduced, which accounts for the combined effects of a microcycle's depth of discharge (DoD) and battery temperature, usually considered separately in the literature. Furthermore, a sensitivity analysis on the thermal parameters and an economic analysis were performed using a 90-day electricity profile from an actual DC microgrid in India to infer the hybridization benefit. The results show that the hybridization is beneficial mainly at poor thermal conditions and highlight the need for a battery degradation model that considers both the DoD effect with microcycle resolution and temperate impact to accurately assess the gain from such a hybridization.

Keywords: hybrid energy storage system; supercapacitor; lead–acid battery; energy management system; battery degradation; depth of discharge; techno-economic analysis

Citation: Luo, X.; Barreras, J.V.; Chambon, C.L.; Wu, B.; Batzelis, E. Hybridizing Lead–Acid Batteries with Supercapacitors: A Methodology. *Energies* **2021**, *14*, 507. https://doi.org/10.3390/en14020507

Received: 18 December 2020
Accepted: 13 January 2021
Published: 19 January 2021

Publisher's Note: MDPI stays neutral with regard to jurisdictional claims in published maps and institutional affiliations.

Copyright: © 2021 by the authors. Licensee MDPI, Basel, Switzerland. This article is an open access article distributed under the terms and conditions of the Creative Commons Attribution (CC BY) license (https://creativecommons.org/licenses/by/4.0/).

1. Introduction

Among the Sustainable Development Goals (SDGs) established by the United Nations General Assembly in 2015 [1], SDG 7 aims at affordable, reliable, sustainable and modern energy access for all. Microgrids are a key technology to this end, and have seen recently remarkable expansion in isolated rural areas around the world with limited or no access to the main electric grid. The typical standalone microgrid utilizes renewable or other local energy sources to provide electricity in places where long-distance power transmission and substantial grid investments are deemed uneconomical [2]. An irreplaceable component of these miniature power grids is the energy storage system (ESS), whose main role is to ensure power quality and energy balance between the intermittent supply and demand [3,4]. Batteries are the most widely used energy storage technology in microgrids, mainly due to their scalability, modularity and limited maintenance needs. Lead–acid batteries, in particular, remain to this day the most commonly found battery technology in operating microgrids, being the most commercially mature. A big challenge in these ESS, however, is battery degradation due to deep discharge and surge currents often found in standalone microgrids supplied by intermittent renewables supply, such as solar [5]. For example, lead–acid batteries under high charge/discharge rates suffer from the formation of smaller sulphate crystals that lead to inhomogeneous current distribution and

increased internal resistance, all of which have a negative impact on battery life [6]. To this day, the longevity and associated replacement costs of batteries remain one of the most critical factors for the economic viability of an off-grid microgrid investment.

To overcome these challenges, the scientific community has explored in the last decade how to hybridize a battery ESS with other storage technologies, such as supercapacitors [7–14], fuel cells [15,16] and flywheels [17], to come up with a more reliable hybrid energy storage system (HESS) that features longer lifespan and higher resistance to degradation. Supercapacitors (or ultracapacitors) are deemed among the most suitable coupling candidates, as they exhibit high power density (though low energy density) and complementary characteristics to electrochemical batteries [18,19]. They can readily support high charge/discharge rates as often as required with negligible impact to their life, which typically exceeds a decade [20]. For this reason, they couple nicely with batteries in absorbing the sudden changes in power demand that allows for a smoother power profile to the batteries and reduced deterioration. Furthermore, the two energy storage technologies exhibit relatively similar operating principles as they are both electrochemical devices, which translates to similar low set-up costs [2]. Furthermore, the long-term operation and maintenance (O&M) costs of supercapacitors are lower than those of batteries [21]. This paper takes a deep look on how to hybridize an ESS with lead–acid batteries and supercapacitors, providing recommendations for the topology selection, the design of the control scheme, the battery degradation modeling and economic viability analysis of the investment.

The state of the art in HESS topologies involves mainly three different configurations of batteries and supercapacitors: passive, semi-active and fully active [2,7]. The most appropriate topology for an application is selected based on factors such as the set-up cost, efficiency, controllability, system complexity and utilization rate. The passive HESS is the simplest and cheapest topology, according to which the batteries and supercapacitors are directly coupled in parallel at the DC link without any power electronics or control [8,9]; this approach is widely applied in high voltage ESS, benefiting from low internal losses and reduced system complexity. However, this way the supercapacitors voltage varies little and their capacity is severely underutilized, which entails only limited extension of the battery life. Furthermore, this approach faces also challenges related to impedance matching between the batteries and supercapacitors. The semi-active configuration, on the other hand, employs power electronics in either batteries or supercapacitors—not both—to expand the operating region of the latter [10,11]. With this approach, one of the two storage devices is effectively isolated, thus allowing for more flexible power allocation between the two. Nonetheless, the passive element may suffer from surge currents—if it is the battery—or cause bus voltage fluctuation and negatively impact the power quality—if it is the supercapacitors. The third option of fully active configuration tackles all these issues. Usually a parallel connection is adopted [5,12–14], but cascade implementations are also reported [22]. The big gain with this topology is effective decoupling of the two components permitting independent control during operation and separate sizing at the design phase. Especially for DC standalone microgrids, this is a viable option for getting the energy storage mix right and extending the HESS lifespan as much as possible. It is worth noting that there are some recent alternatives that involve distributed hybridization combined with active balancing, achieved by incorporating supercapacitors into the balancing bus in order to enable cell-level hybridization [23]. However, this is still a new and more complex solution, so far targeted only at Li-ion batteries in e-mobility applications. Therefore, this paper adopts the fully active HESS method as the most appropriate for isolated DC microgrids.

Various philosophies exist in the literature regarding the control strategy of fully active HESS to allocate the power flows between the batteries and supercapacitors and maintain the system stability. These control strategies, commonly referred to as energy management systems (EMS), may involve power filtering [5,14,24–26], deterministic rule-based control [13,27], fuzzy logic [10,28] and optimization-based control [29–31]. In [28], a fuzzy logic rule-based control is applied to a HESS to ensure that the ESS elements operate in the safe

region. Alternatives employing neural networks [29] and model predictive control [30,31] are based on multi-objective or cost functions that aim to optimize the power allocation. A combination of the rule-based concept with optimization algorithms is proposed in [27]. However, the aforementioned approaches employ sophisticated algorithms that require large amounts of input data and complex mathematical calculations, which have acted as barriers towards wider adoption. By contrast, the power filtering approach has proven quite popular, as it is both effective and easy to implement. It has been also shown that a simple filter-based control is effective in off-line sizing applications as well, yielding very similar results to more complex, non-causal, optimization control approaches as long as battery model accounts for sufficiently complex dynamics [32]. Given these considerations, this paper focuses on the power filtering method.

There are many studies on power filtering in the literature. Somayajula et al. in [33] demonstrated an active supercapacitor control scheme to achieve smoothing of intermittent renewables generation; the adopted cascade control comprising an outer voltage loop and an inner current loop has been also applied to battery-supercapacitor hybrid systems to ensure power quality. Decoupling the high frequency part of the power control using a first-order low-pass filter (LPF) is proposed in [5,14,24,25]. However, these studies do not properly consider the safe operating region of the ESS components. Especially for the supercapacitors, their low energy density and high charge/discharge rates lead to highly volatile voltage; if not properly contained within the safety limits, this may result in irreversible damage if overcharged (e.g., voltage exceeding the structural limits) or power converter malfunction if left uncharged (e.g., power converter not managing to step-up the low input voltage). To this end, State of Charge (SoC) controllers are proposed in [26,34], which however aim to maintain the energy of the supercapacitors around the reference level and do not directly control the voltage. This may occasionally result in voltage out of limits due to SoC miscalculation caused by various factors, such as parasitic resistances or capacitance deviation due to aging and deterioration. To this day, a complete control scheme for hybrid batteries-supercapacitors systems based on power filtering that strictly adheres to the supercapacitor voltage limits is missing from the literature.

To evaluate the contribution of the hybridization to the battery lifespan, the battery degradation needs to be captured and modeled. There are three different degradation modeling philosophies in the literature: physical-mechanistic models, empirical models and data-driven models [35–37]. Physical-mechanistic models are generally based on electrochemical aging processes inside the battery and involve physics-inspired differential equations. For example, Dufo-López et al. in [35] consider the phenomena of internal corrosion of the battery and aging of the active material to quantify the capacity loss. Although very well-aligned with the physics, these models require many unknown parameters and laborious computations that limit their applicability only to research purposes. The empirical models, on the other hand, entail simpler mathematical functions and coefficients extracted from fitting to experimental results. This makes this approach more effective and practical, except that it requires lots of experimental data to capture a wide range of operating conditions and degradation factors. Making assumptions for untested conditions, to make up for missing data, may introduce uncertainty in the results [36]. A popular extension of this category are the cycle-counting models [38]; by adopting the principle of fatigue damage, these models measure the degradation for each cycle of use assuming that the aging factors are independent and cumulative. This allows for a more abstract and universal model structure that relies on limited empirical information usually available in the manufacturer datasheet. Examples of such quantitative cycle-counting models may be found in [6,14,22,39–42]. The third category of data-driven degradation models apply statistical analysis and machine learning on a large database to predict the battery status and extract patterns to quantify the lifespan [37,43]. These methods are not yet widely used due to their dependence on large datasets and sophisticated implementation. This paper, therefore, adopts the cycle-counting empirical approach due to practicality and wide acceptance in the field.

The battery ages and degrades over time mainly due to (i) calendar aging, i.e., capacity decrease under idle conditions, and (ii) cycle life aging, i.e., degradation during usage [44]. In standalone microgrids, the ESS is in continuous operation and the latter type of aging prevails; this is why the degradation model of this paper focuses on cycle life aging, as generally done in HESS studies. This type of deterioration can be manifested as corrosion of positive grid, hard/irreversible sulfation and shedding [45]. The most prevalent failure mode for lead–acid batteries in standalone stationary systems is the former, also known as anodic corrosion [46], which used to be a major problem in early design, thereafter overcome by the adoption of improved grid alloys. The corrosion rate is accelerated by high temperatures, extreme voltages and cycling operation (versus constant current operation) [46]. Primary factors of this degradation are the depth of discharge (DoD) (i.e., how deeply the battery is discharged), the charge/discharge rates and the battery's operating temperature [6]. Most relevant models take into account only the DoD factor and employ a cycle-counting method, such as the rainflow counting method [6,40], to capture the number and depth of the cycles [42,47]. However, these models are designed for moderate and deep discharge cycles (e.g., more than 10%) and may fail to accurately capture the effect of smaller cycles, i.e., microcycles, often found in off-grid microgrids with irregular power flows due to intermittent supply and demand [14,22]. The case study of this paper show that it is imperative to employ a microcycles DoD model when there is access to high time-resolution electricity data (e.g., second resolution) in order to accurately capture the DoD degradation. Furthermore, battery temperature is also an important stress factor to battery degradation, usually studied separately from the DoD effect [48]. The investigation in this paper demonstrates that the two factors are strongly related in the presence of microcycles and rapidly changing battery currents. Narayan et al. [38] have proposed a model that combines both DoD and temperature effects, albeit following an alternative dynamic capacity fading approach that is too complicated for classical cycle counting and fundamentally differs from the aforementioned mainstream DoD models. There is still a need in the literature for a lead–acid battery degradation model that accounts for the combined effect of microcycles DoD and temperature.

In applications of lead–acid battery and supercapacitor hybrid systems, the selection of energy storage components mainly depends on the availability, system size and cost. Lead–acid batteries are the industry standard for small-scale standalone photovoltaic (PV) systems, both in valve-regulated and flooded deep-cycle designs [49]. The batteries are usually connected in series to meet the system voltage requirements, and then several strings are added in parallel to meet the required capacity. Twelve-volt batteries are considered the most cost-effective solution for systems comprising up to 4–6 parallel strings, and two-volt batteries are usually preferred for larger systems. Suggestions on the selection of lead–acid battery types in different scenarios are given in [49], where there is a need to strike a balance between lifespan, cost and energy density. The supercapacitors are commercially available in modules, consisting of several cells connected in series; the maximum voltage of a single cell is usually 2.7 V. For the selection of supercapacitors, the capacity is determined by the maximum energy variation required by the system and its operating voltage range [26]. As supercapacitors are much more expensive than batteries, a thorough cost-benefit analysis should take place to come up with the appropriate size of the two components.

The aim of this paper is to propose a complete methodology to hybridize a lead–acid battery ESS with supercapacitors for standalone DC microgrids. A new power allocation control scheme and battery degradation model are proposed to accurately capture and maximize the battery life extension due to hybridization. A thorough techno-economic analysis takes place based on a 90-day electricity dataset from a real-life 4.8 kW standalone microgrid installed in rural India, to determine the viability of the hybridization at six different scenarios. The main novel points of this study are as follows:

- A complete ESS hybridization methodology is developed, including the control design, battery degradation and economic viability analysis, while the results are based on data from a real-life DC microgrid.
- A new power allocation control scheme is proposed, based on power filtering that strictly abides by the supercapacitors' voltage operating limits.
- A new degradation mechanism model for lead–acid batteries (or simply "battery degradation model") is introduced that accounts for the combined effect of microcycles DoD and battery temperature, appropriate for high time-resolution profiles.

The structure of the paper is as follows. Section 2 presents the control scheme and power filtering method that respects the supercapacitors' voltage limits, while the new battery degradation model that accounts for both DoD and temperature impact is given in Section 3. In Section 4, the real-life case study of this paper is detailed, followed by a sensitivity analysis on the thermal parameters. Section 5 discusses the economic benefit from the hybridization at six different scenarios and Section 6 concludes this study.

2. Topology and Control Strategy of the HESS

The HESS under consideration corresponds to the case-study 24 V DC microgrid described in Section 4. Figure 1 shows a simplified diagram with aggregated PV generation and load that involves the proposed parallel, fully-active HESS. Both the battery bank and supercapacitors bank have their own bidirectional DC/DC converter to allow separate power flows according to the controller. The objective of the controller is multi-fold: to regulate the DC link voltage and maintain the power balance in the microgrid, whilst cleverly allocating the power demand between the two storage components to smooth out the battery power profile but respecting the supercapacitor voltage limits. The details of the topology and control strategy follow.

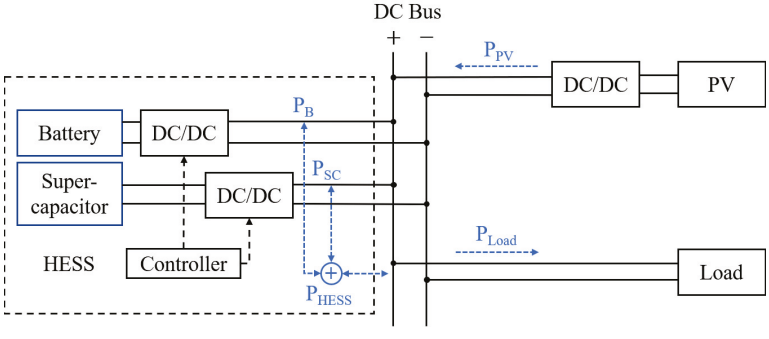

Figure 1. Selected system topology: DC microgrid with a parallel, fully-active hybrid energy storage system (HESS).

2.1. The Fully Active Topology

Among various HESS configurations, the parallel, fully-active topology allows for maximum flexibility when designing and operating the system. This flexibility, however, comes at the cost of an additional DC/DC converter for the supercapacitors on top of the one used for the batteries. Nonetheless, given the low DC bus voltage of 24 V, a simple bidirectional two-quadrant converter is sufficient to step-up the supercapacitors' voltage (8–16 V in this paper), which is an effective and economical solution [5]. It is also worth noting that the power rating of the supercapacitor converter is lower than the batteries' one, here sized at about 30% of the ESS rated power for the case study of Section 4. At any time, the HESS maintains the power balance in the microgrid by supporting any deviation between PV generation P_{PV} and load P_{Load} with power P_{HESS}, the latter consisting of the batteries P_B and supercapacitors P_{SC} contribution. The level of these contributions at any time is determined by the controller detailed in the following section.

2.2. Control Strategy

Figure 2 depicts the overall control strategy designed for the HESS. It comprises three main parts: the outer voltage control loop, the power allocation mechanism and the inner current control loop. The outer voltage control loop regulates the DC bus voltage Vo to the reference Vo^* by calculating the total reference power $Ptot^*$ that the HESS needs to inject (if positive) or consume (if negative) to maintain the power balance in the microgrid. The power allocation scheme then splits $Ptot^*$ to the two components fed into the battery Pb^* and supercapacitor Psc^*; the battery undertakes a low-pass-filtered version of $Ptot^*$, possibly adjusted by ΔP_{sc} when the supercapacitors operate close to their limits, and the remaining goes to the supercapacitors. Finally, these reference power values are converted to reference currents Ib^* and Isc^* that drive the inner loop current controllers in adjusting the duty cycle Db and Dsc of the separate DC/DC converters. The power filtering and supercapacitor voltage limitation scheme are described in more detail below.

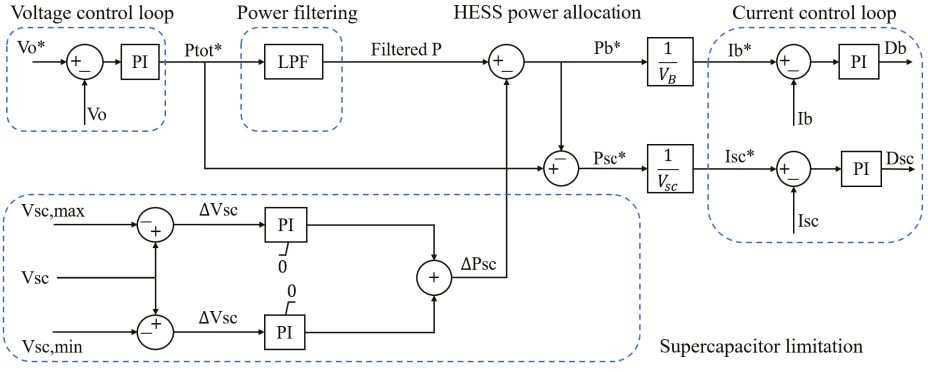

Figure 2. Proposed HESS control scheme.

2.2.1. Power Filtering

Supercapacitors have several features, such as fast dynamics, long cycle life and low internal resistance, which make them ideal to deal with the high-frequency power components of the load. Although some studies indicate capacitance drop for high frequencies of operation [50], they remain very useful in absorbing the high charge/discharge rates to protect the batteries. To this end, a low pass filter (LPF) is employed here to disaggregate $Ptot^*$ to the slow-changing Pb^* and fast-changing Psc^*. The simplest approach for the LPF would be a first-order continuous time filter, with a transfer function

$$H(s) = \frac{1}{1 + T \cdot s} \tag{1}$$

where T is the time constant. The higher the time constant, the better the filtering, albeit requiring larger capacity from the supercapacitors; if it is too high, their capacity may be quickly outspent, effectively disabling them for large periods of time. A discussion on the selection of the time constant follows in Section 2.3.

High-order filters generally perform better in cutting high-frequency signals and have been employed in power filtering of energy storage systems in the literature [24,51]. There are two broad categories of digital filters: finite impulse response (FIR) filters and infinite impulse response (IIR) filters, based on the time domain characteristics of their impulse response functions. Generally, high-order IIR filters are seen to exhibit convergence and stability issues, which is in contrast to FIR filters that feature low phase distortion and are always stable without feedback loops [51–53]. Therefore, the second filter alternative considered in this study is an FIR filter, expressed in the z-domain as

$$H(z) = \sum_{n=0}^{N-1} h[n] z^{-n} \tag{2}$$

and in the discrete time domain as

$$h[n] = h_d[n]\omega[n] = \frac{sin(n\omega_c)}{n\pi}\omega[n] \tag{3}$$

where $\omega[n]$ represents a window function. The window function (e.g., Hamming window [54], Kaiser window [55]) is used in cutting of the low-pass infinite pulse to obtain the FIR coefficients. The design parameters of an FIR filter are the filter length N and the cut-off frequency ω_c.

A important feature of a high-order FIR filter is the group delay, directly related to the length of the window N [52]. High-length windows yield better low-pass filtering performance, albeit with a larger group delay. However, such delays lead to power lags that need to be accommodated by the supercapacitors, which may lead to power oscillations and suboptimal performance in some cases, as shown in Section 2.3. Selection of the FIR filter length and cutoff frequency is a delicate procedure that needs to strike a balance between the filtering effect and group delay.

2.2.2. Supercapacitor Voltage Limitation

The supercapacitors' voltage varies substantially during normal operation due to their strong coupling with the stored energy: to fully charge, the voltage needs to get to the nominal value; to fully discharge, the voltage should decrease as low as possible. This variation, however, must abide by certain safety limits $V_{SC,min} \leq V_{SC} \leq V_{SC,max}$ to account for structural characteristics of the supercapacitors and input voltage limitations of the power converter.

Take the supercapacitor module used in this case study (see Section 4) as an example [56]. The maximum voltage $V_{SC,max}$ is set to the nominal value of 16 V (6 cells in series—about 2.7 V per cell), while the minimum value $V_{SC,min}$ is selected as 8 V, so that the DC/DC converter is required to boost the voltage up to three times to reach the target 24 V. Past experience has shown that the conduction and switching losses of such converters skyrocket for conversion ratios of higher than three [57], which entails inefficient operation or even inability of the power converter to step-up the voltage. Within this voltage range, the usable energy capacity portion of the supercapacitor E_{SC} would be

$$E_{SC} = \frac{\frac{1}{2}CV_{SC,max}^2 - \frac{1}{2}CV_{SC,min}^2}{\frac{1}{2}CV_{SC,max}^2} = \frac{16^2 - 8^2}{16^2} = 75\% \tag{4}$$

Utilizing 75% of the available energy is quite reasonable, especially given the simple and economical power converter employed.

To enforce adherence of these limits, the supercapacitor limitation scheme of Figure 2 is used. The main idea is to compensate for any voltage violation by adjusting the battery power Pb^* by a signal ΔP_{SC}. ΔP_{SC} will be zero while operating within limits, but it will get positive values when the supercapacitors voltage exceed the upper bound (need to discharge) or negative values when it goes below the lower bound (need to charge). To this end, two PI controllers are employed with appropriate saturation limits and anti-windup mechanisms, each undertaking regulation around one of the two voltage limits. While voltage is in the safe region, both PI controllers are driven to their zero saturation bound, thus exporting zero ΔP_{SC}; when $V_{SC} > V_{SC,max}$, the upper PI controller gets activated while the lower controller remains stuck at zero, which brings the voltage back to $V_{SC,max}$; when $V_{SC} < V_{SC,min}$, the opposite happens and the lower PI controller regulates the voltage back into the safe region. Notably, the anti-windup mechanism is crucial for this control scheme, so that the controllers can "unstick" from saturation immediately after the voltage gets

out of bounds. Here, the clamping anti-windup method has been employed, but other anti-windup alternatives will work equally as well.

2.3. Energy Management System Results

This section evaluates the proposed control scheme on a 10,000-s electricity profile from the study-case system detailed in Section 4. The following results have been produced through simulations in MATLAB/Simulink. As a benchmark, the conventional battery-alone ESS is considered first, as shown in Figure 3. The entire power demand P_{ESS} is taken care of solely by the batteries P_B, resulting in high-frequency power fluctuation that accelerates the battery degradation. Please note that positive and negative power values indicate discharging and charging respectively, while small deviations between P_{ESS} and P_B are due to power losses.

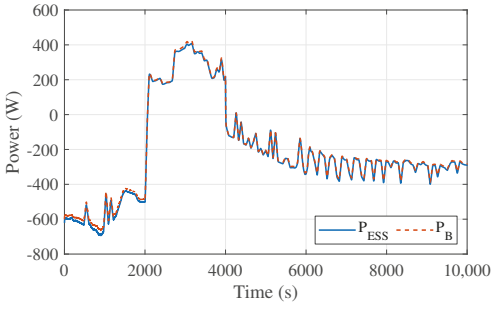

Figure 3. Power profile in the battery-alone ESS system.

The same power profile is applied to a HESS employing different power filters, as shown in Figures 4–6. A simple first-order LPF with a small time constant of 50 s yields a smoother battery power profile P_B in Figure 4a, as the supercapacitors absorb the fast-changing component P_{SC}. It is worth noting that the mean value of P_{SC} is not far from zero, which leads to limited supercapacitor voltage variation in Figure 4b, well within the safe operating region.

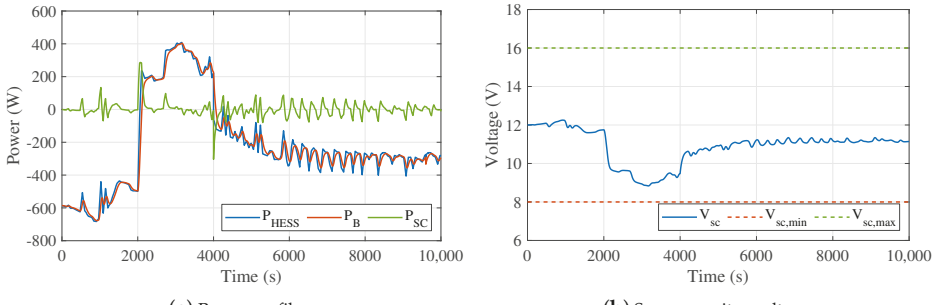

(**a**) Power profile (**b**) Supercapacitor voltage

Figure 4. Power filtering and voltage results for the HESS with a first-order low-pass filter (LPF) ($T = 50$ s).

When increasing the time constant to 300 s, the power profile of the battery becomes clearly smoother in Figure 5a, albeit at the cost of risking voltage going out of limits in Figure 5b. As explained by Equation (4), there is strong relation between the energy stored in the supercapacitors and their terminal voltage. For the selected supercapacitor module [56], the absolute maximum voltage is 17 V, which creates a safety margin of 1 V above the 16 V nominal voltage. In addition, the lower voltage bound of 8 V set is not really a strict limit; the power converter can readily operate slightly lower, e.g., at 7 V, for a short time, temporarily resulting in more losses that will not however risk the system integrity for a few seconds.

This safety margin of 1 V from the upper and lower voltage limits provide the space for the proposed supercapacitor voltage limitation scheme to detect any deviation and act upon in by nullifying P_{SC} whenever V_{SC} is exceeding the limits. In fact, the designed control is very fast in responding to these events, recording an imperceptible voltage overshoot of less than 0.01 V in the example of Figure 5b, well below the 1 V margin.

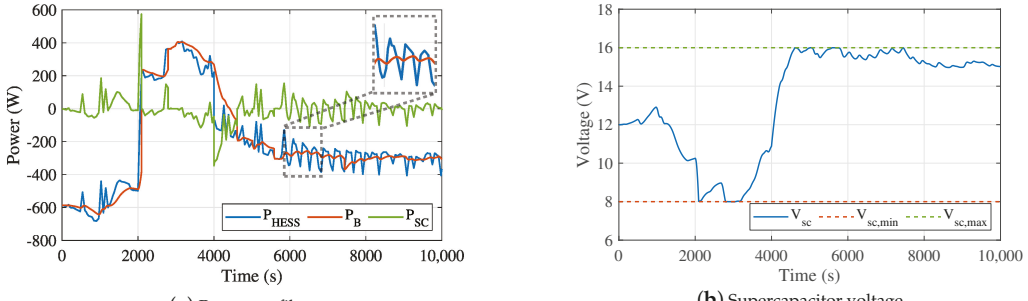

(**a**) Power profile (**b**) Supercapacitor voltage

Figure 5. Power filtering and voltage results for the HESS with a first-order LPF ($T = 300$ s).

A similar smoothing effect is achieved by the high-order FIR filter except for a noticeable group delay, as shown in Figure 6 ($N = 420$, $\omega_c = 0.0005\pi$ rad/sample). This results in a phase delay between P_B and P_{HESS}, seen more clearly by comparing the zoom boxes in Figures 5a and 6a. This group delay may trigger power oscillations and pose control and stability challenges, and use the supercapacitors' capacity in a suboptimal manner. The conclusion from this investigation is that "too much" filtering may lead to the opposite result, with power spikes and oscillations that do not resemble a smooth profile for the battery. There is no golden rule on the selection of the filter parameters, as they strongly depend on the electricity profile and the supercapacitors' capacity. The parameters selection for the case study of this paper is discussed in Section 4.

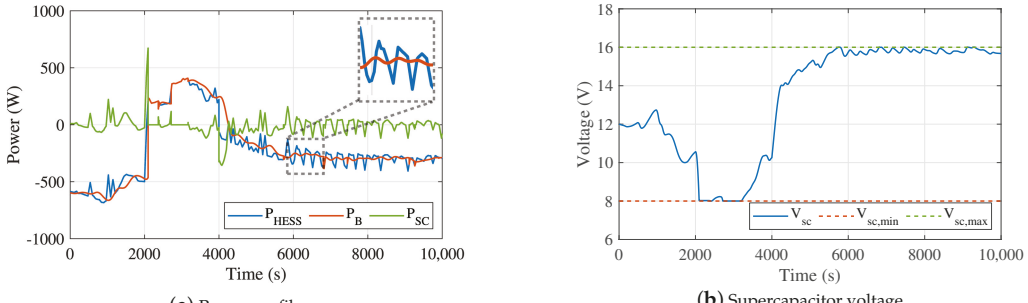

(**a**) Power profile (**b**) Supercapacitor voltage

Figure 6. Power filtering and voltage results for the HESS with a finite impulse response (FIR) filter ($N = 420$ and $\omega_c = 0.0005\pi$ rad/sample).

3. Battery Degradation Model

This section presents a new degradation model for lead–acid batteries used to evaluate the contribution of the hybridization to the battery life. This is a cycle-counting model that accounts for the cumulative fatigue from the most prevalent stress factors: the DoD and battery temperature. Most conventional models explore these effects separately and focus on medium and deep discharge cycles, i.e., DoD higher than 10%, thus neglecting smaller changes in the SoC, i.e., microcycles. However, the ESS in small-scale PV microgrids often experiences irregular charging/discharging patterns that involve lots of microcycles

and rapidly changing currents that have increased DoD-related and temperature-related impact on the battery life. This paper shows that it is important in these cases to use high-resolution time series that allow for accurate approximation of both effects and thus the battery degradation. The objective of the following paragraphs is to describe a methodology for such a degradation model, which can be easily adapted to any lead–acid battery given the appropriate coefficients and inputs.

3.1. Depth of Discharge (DoD) Model

To evaluate the DoD degradation, one needs first to extract the number of cycles and their depth of discharge as explained in Section 3.1.1, to be used afterwards in a cycle life model to quantify their impact on the battery life in Section 3.1.2.

3.1.1. Rainflow Counting Method

The most widely adopted method to capture the DoD profile is the rainflow counting method. Using the SoC variation as an input, this method extracts the number of cycles, their depth and length. An example is given in Figure 7: the plot of SoC over time is rotated 90° clockwise and treated as a roof upon which raindrops fall. Starting from a local maximum point "a", the rainflow reaches the next local minimum point "b" and then drops. The portion of the profile (b-c-b') forms a whole cycle, denoted as "whole-cycle 1". Then, the flow continues dropping till point "d" when it meets the minimum SoC value. The transition (a-b-d) is counted as a half-cycle. Thereafter, "d" is set as the new initial point for the next raindrop and these steps are repeated to identify the remaining whole and half cycles, as illustrated in Figure 7. More details on the implementation of the Rainflow counting method may be found in [6,40].

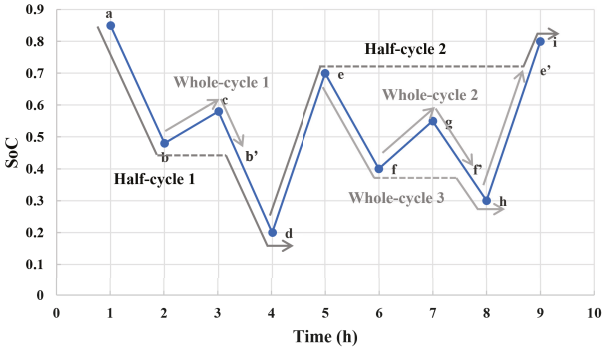

Figure 7. Example application of the rainflow counting algorithm based on a SoC profile.

3.1.2. Cycle Life Model—CL(DoD)

Given the extracted cycles pattern, the next step is to evaluate their effect on the battery life. This is done by calculating the cycle life CL(d), i.e., the number of cycles that the battery will last if the DoD of all cycles is d. Usually, $CL(d)$ is a mathematical expression that is unique for every battery and is derived based on information from the manufacturer datasheet.

An example of such datasheet information is given with the purple star markers in Figure 8a for Trojan's deep-cycle gel lead–acid battery [58]: the cycle life heavily depends on the DoD, with higher DoD resulting in shorter cycle life. Since only a few such data points are typically provided in the datasheet, there is a need for a mathematical model to capture the cycle life for all possible DoDs. One commonly used such model, thereafter referred to as the conventional model, is given by [40–42]

$$CL(d) = a_5 d^5 + a_4 d^4 + a_3 d^3 + a_2 d^2 + a_1 d + a_0 \quad (5)$$

where a_i are coefficients extracted by fitting Equation (5) on the given data points. For the study-case battery, the fitted model is shown with a blue line in Figure 8a in regular scale and in Figure 8b in logarithmic scale, while the a_i coefficients are given in Table 1.

However, a major limitation of this method is that it does not accurately capture the effect of microcycles with DoD less than 10%. Since the datasheet rarely includes information for so low DoD, the Conventional model may overestimate the impact of the microcycles, projecting low cycle life even for near-zero DoD (see how to blue line meets the y-axis in Figure 8a). This proves to be problematic when there is access to high resolution time series that permits visibility on the numerous existing microcycles. For these cases, a microcycles model is required, such as [14,22]

$$CL(d) = b_4 d^{-4} + b_3 d^{-3} + b_2 d^{-2} + b_1 d^{-1} + b_0 \tag{6}$$

where b_i are again coefficients extracted from the datasheet. Accurate identification of these coefficients would normally require data points for smaller DoD; in absence of this information, this paper assumes additional extrapolated points using a linear relationship in the logarithmic scale, as shown with green markers in Figure 8b (coefficients in Table 1). This way, the cycle life is very high for small DoD, providing a more realistic approximation of the limited microcycles effect.

In fact, without sufficient input data at low DoD, both models are approximations of the microcycles impact: a pessimistic one with the Conventional model and an optimistic one with the microcycle model. However, the case study of Section 4 shows that the former is clearly unsuitable in presence of microcycles, while the latter yields reasonable results. In addition, with the microcycle model the supercapacitor's contribution to the battery life extension is more limited, which makes it a conservative benchmark when evaluating the economic viability of the hybridization. Therefore, this paper recommends adoption of the microcycle model as the safest approach in the design of a HESS.

Table 1. Coefficients of conventional and microcycle models.

Model	Coefficients		
Conventional model	$a_5 = -46{,}573$	$a_4 = 187{,}495$	$a_3 = -288{,}854$
	$a_2 = 212{,}925$	$a_1 = -76{,}291$	$a_0 = 11{,}761$
Microcycle model	$b_4 = -1.345 \times 10^{-12}$	$b_3 = 1.495 \times 10^{-7}$	$b_2 = -1.507 \times 10^{-3}$
	$b_1 = 601.5$	$b_0 = -122.5$	

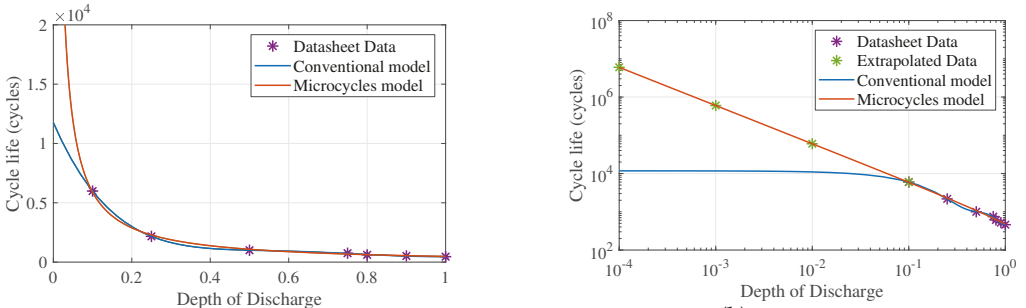

(**a**) in regular scale (**b**) in log-log scale

Figure 8. Battery cycle life vs. depth of discharge (DoD) curve.

3.2. Temperature Model

The battery's operating temperature is also an important factor to the battery life. In the following, Section 3.2.1 explains how to calculate the battery temperature and Section 3.2.3 how to evaluate its effect on the cycle life.

3.2.1. Battery Temperature Calculation

The battery temperature T depends mainly on the ambient temperature T_a and the power losses P_{loss}. Taking into account the thermal inertia of the system, their combined effect can be expressed in the Laplace domain by the transfer function of a first-order low pass filter

$$T(s) = \frac{P_{loss} \cdot R_{th} + T_a}{1 + t_c \cdot s} \tag{7}$$

where R_{th} is the thermal resistance and t_c is the thermal time constant. Equation (7) reflects the fact that any change in T_a or P_{loss} will not be transferred to the battery temperature immediately. T_a is an input to the model, while P_{loss} is the aggregate power losses on the battery $P_{loss\_battery}$ and on the power converter $P_{loss\_converter}$ (assuming they are both placed in the same cabinet):

$$P_{loss} = P_{loss\_battery} + P_{loss\_converter} \tag{8}$$

The converter power losses are found directly from the DC/DC converter efficiency. Typical efficiencies vary around 95% [59], thus $P_{loss\_converter}$ is assumed here to be 5% of the actual power output at any time. The internal losses of the battery is described in detail in Section 3.2.2 below.

3.2.2. Battery Electrical Equivalent Circuit Model

The battery internal losses $P_{loss\_battery}$ are calculated using the equivalent circuit of the battery shown in Figure 9. This circuit involves the following parasitic elements [60]: (i) an internal series resistance R_{serial} that reflects losses due to ohmic polarization of instantaneous nature; (ii) a pair of resistance/capacitance R_{t_fast}, C_{t_fast} that accounts for activation polarization (or charge-transfer) phenomena with fast dynamics; and (iii) another pair R_{t_slow}, C_{t_slow} that models slower concentration polarization effects. The parameter values used in this paper are listed in Table 2, taken from [61]. The power losses were found by solving the algebraic and differential equations of this circuit for the given input battery current I_{bat}:

$$P_{loss\_battery} = I_{bat}^2 R_{serial} + \frac{V_{t\_fast}^2}{R_{t\_fast}} + \frac{V_{t\_slow}^2}{R_{t\_slow}} \tag{9}$$

$$I_{bat} = C_{t\_fast} \frac{dV_{t\_fast}}{dt} + \frac{V_{t\_fast}}{R_{t\_fast}} \tag{10}$$

$$I_{bat} = C_{t\_slow} \frac{dV_{t\_slow}}{dt} + \frac{V_{t\_slow}}{R_{t\_slow}} \tag{11}$$

Table 2. Parameters of lead–acid battery equivalent circuit [61].

Parameter	Value
R_{serial}	$0.0401 \times e^{0.0908 \times SoC} + 0.0366\ \Omega$
R_{t_fast}	$3.041 \times 10^{-10} \times e^{0.1874 \times SoC} + 0.0344\ \Omega$
R_{t_slow}	$0.101 \times e^{0.0203 \cdot SoC} + 0.0219\ \Omega$
C_{t_fast}	1200 F
C_{t_slow}	5000 F

It is worth noting that the relation between $P_{loss\_battery}$ and I_{bat} is non-linear; there is a quadratic dependence of the I^2R losses on the current, which means that the charg-

ing/discharging pattern matters for the losses. For example, charging the battery with a constant current yields lower power losses than with a fluctuating current with the same mean value. However, the equivalent model of Figure 9 does not consider any dependence of the parasitic elements on the operating frequency, which some experimental studies have shown to be apparent.

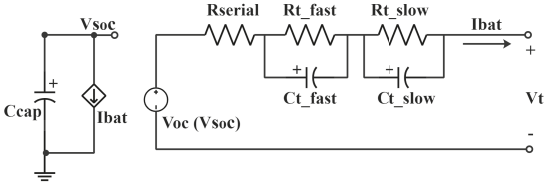

Figure 9. Equivalent electrical model of the lead–acid battery [61,62].

3.2.3. Temperature's Effect on Cycle Life

The temperature mainly affects the corrosion of the lead–acid battery's positive electrode [6]: the higher the temperature, the faster the corrosion process. An investigation in [38] has shown that there is a linear relationship between the battery temperature and the cycle life for the same DoD, as shown in Figure 10. This means that the cycle life of the battery $CL(d)$ calculated in Section 3.1 is only valid at 20 °C and needs to be translated to the actual operating temperature T by multiplying with a coefficient $nCL(T)$ given here by

$$nCL(T) = -0.0225 \cdot T + 1.45 \tag{12}$$

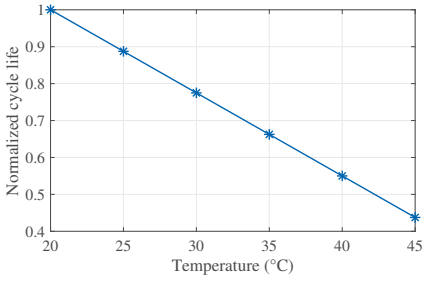

Figure 10. Normalized cycle life with temperature in a lead–acid battery [38].

This equation taken from [38] refers to a flooded lead–acid battery, but it is assumed here that it applies more or less to deep-cycle gel-type lead–acid batteries as well. The typical gel battery datasheet does not provide any information on the cycle life-temperature relationship, but it includes data on the dependence of the battery capacity loss on the temperature, which is also linear [58,63]. Therefore, in absence of datasheet information or other relevant knowledge on the battery, this paper deems it better to use Equation (12) to model the temperature effect rather than to ignore it completely, as often done in the literature.

3.3. The Complete Battery Degradation Model

Given the cycles profile and operating temperature calculated in the previous paragraphs, the battery fatigue damage D is given by the Palmgren-Miner rule [64]:

$$D = \sum_{d=0\%}^{d=100\%} \frac{count(d)}{CL(d) \cdot nCL(T)} \tag{13}$$

where $count(d)$ is the number of cycles with a DoD equal to d, and $CL(d) \cdot nCL(T)$ the respective battery cycle life at battery temperature T. Equation (13) reflects that D comes

essentially from the weighted average of the various cycles depending on their frequency in the profile. It is worth noting that during a particular cycle, the temperature T is not constant and may vary; here the maximum temperature recorded during each cycle is selected for T.

The fatigue damage D gives by how much the battery has degraded for the particular charging/discharging profile, e.g., 5%. To get an estimate of the life expectancy L_{bat} assuming that the battery will operate under that profile, one needs to simply divide the duration of the study-case profile N_{days} by D:

$$L_{bat} = \frac{N_{days}}{D} \tag{14}$$

For example, if a 90-day profile is used that yields 5% aging, the estimated lifespan of the battery will be 1800 days or equivalently 4.9 years. The full picture of the proposed battery degradation model is given in Figure 11.

- First, the input SoC profile is analyzed using the rainflow counting method to identify the various cycles, which are then grouped together based on their DoD.
- Then, the microcycle model (Equation (6)) is applied to every DoD captured to determine the respective cycle life $CL(d)$.
- Next, the battery temperature variation is calculated from Equations (7)–(11) for the entire profile.
- For every cycle, the temperature coefficient $nCL(T)$ is determined based on the respective temperature through Equation (12).
- Finally, applying Equations (13) and (14) yields the fatigue damage D and lifespan of the battery L_{bat}.

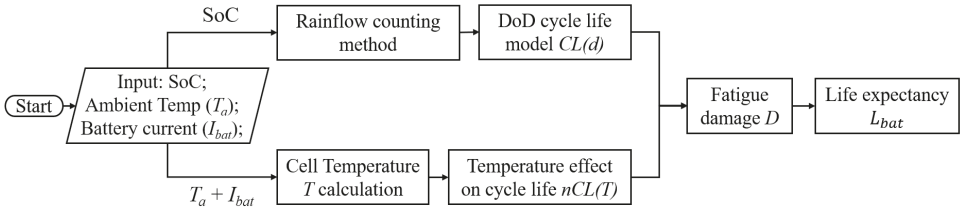

Figure 11. Flowchart of the proposed battery life estimation method.

4. Case Study and Analysis

This section outlines the case study adopted in this paper to evaluate the proposed hybridization methodology. The electricity profile from a real-life standalone DC microgrid is used, followed by a sensitivity analysis on the impact of various thermal factors. It is worth noting that many parameters related to the ESS are assumed or taken from the literature and do not necessarily correspond to the case-study microgrid. The purpose of this section is to extract general conclusions on how different factors influence the battery life and hybridization benefit, rather than to be contained to a specific system.

4.1. The Case Study

The system under consideration is a DC microgrid installed in rural India (Bahraich district, Uttar Pradesh) that supplies electricity to 43 households. The microgrid comprises a total of 4.6 kWp of solar PV generation, 24 lead–acid batteries of 12 V/100 Ah each, and a 24 V distribution network over 1 km distance. The household loads are LED bulbs (1 W or 4 W), fans (15 W) and mobile phone chargers (max 5 W). Two profiles were provided over a period of 2 days and 90 days that include information on generation, load and ambient temperature at 1 s time resolution. It is worth noting that the acquired profiles refer to a subset only of the entire system.

Figure 12a depicts the PV generation and load profiles for two days in April 2019, extracted from the 90-day dataset. Solar generation expectedly varies slowly during the day, although it occasionally features high-frequency oscillations due to intermittent clouding. The domestic load profile exhibits its peak in the evening hours, when the people finish their agricultural activities and return back to their home. This deviation between supply and demand is the net power profile seen by the ESS. Figure 12b shows the ambient temperature profile during that period.

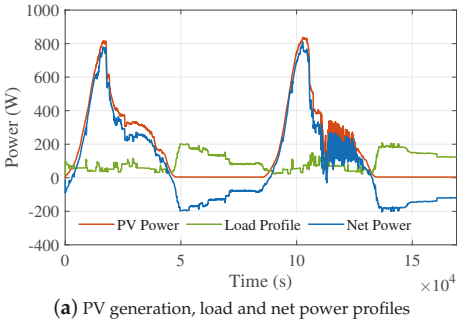

(**a**) PV generation, load and net power profiles

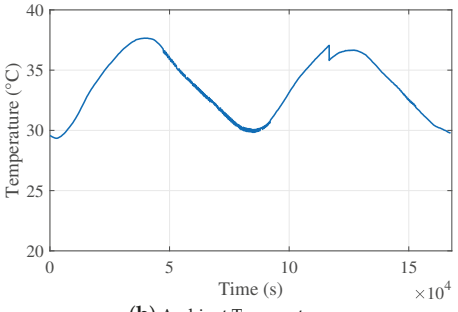

(**b**) Ambient Temperature

Figure 12. Two-day electricity and temperature profiles.

Figure 13 depicts the 90-day profile referring to 20 February to 20 May in 2019. The electricity and ambient temperature variation is given in Figure 13a,b, both featuring the anticipated daily fluctuation; the temperature also exhibits an interseasonal variation, increasing from about 20 °C to 35 °C on average. The power distribution is further studied in the histogram of Figure 13c: the load varies usually from 0 to 200 W, while solar generation is often zero or very low during the the night-time and low-light hours. The mismatch between the two is the net power accommodated by the ESS, varying here from −311 W to 993 W. To investigate how quickly the net power changes, the distribution of the rate of change of net power (RoCoP) is given in Figure 13d. It is apparent that rates of ±50–200 W/s are not rare at all; such high power rates for the scale of the system have a negative impact on the battery life both in terms of DoD and battery temperature.

The following sections explore how the supercapacitors can mitigate these power fluctuations, and how this improvement relates to the thermal parameters. The default parameters of the system used as a benchmark below are given in Table 3. The battery-alone ESS is assumed to comprise 6 batteries, while the HESS has also 1 supercapacitor module. The rest of the parameters are based on reasonable assumptions taken from the literature [61,65,66] and do not necessarily reflect the case study system. For the remainder of the analysis, the 90-day profile is used.

Table 3. Default HESS parameters.

Parameter	Value
Number of lead–acid batteries	6 (2 × 3 strings; 100 Ah; 12 V)
Number of supercapacitor modules	1 (BMOD0500 P016: 500 F; 16 V)
HESS LPF time constant	45 s (1st order LPF)
Cycle life model of DoD	Microcycle model
Thermal resistance R_{th}	0.6 °C/W
Thermal time constant t_c	18,000 s (5 h)
Internal series resistance R_{serial}	$0.0401 \times e^{0.0908 \times SoC} + 0.0366\ \Omega$
Converter power losses $P_{loss\_converter}$	5%

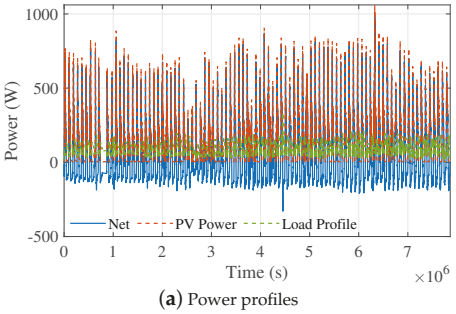

(a) Power profiles

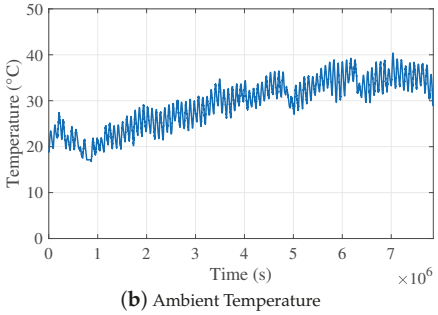

(b) Ambient Temperature

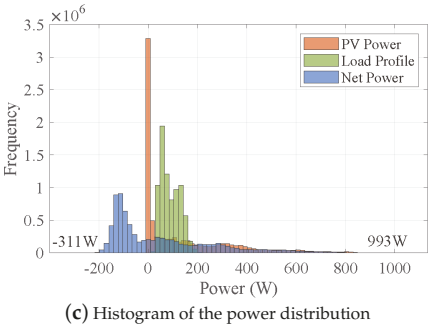

(c) Histogram of the power distribution

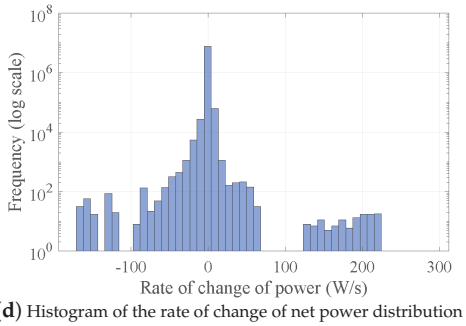

(d) Histogram of the rate of change of net power distribution

Figure 13. Ninety-day electricity and temperature profiles.

4.2. Power Filtering Results and Analysis

Based on the given 90-day profile and design specifications of Table 3, the optimal parameters for the two power filter alternatives are extracted through exhaustive search (testing wide ranges for each of the parameters, and select the ones that deliver the most favorable performance) and are appended in Table 4. Apparently, both filters increase the expected battery lifespan by almost the same amount. The first-order filter effectively smooths out the power profile resulting in much lower standard deviation in battery RoCoP and number of microcycles compared to the battery-alone system. The FIR filter yields approximately the same life extension but by squeezing more the number of microcycles while allowing for more deep cycles with higher DoD compared to the first-order LPF. Given that the FIR filter comes also with some stability and control issues related to the group delay, the first-order LPF is selected as more preferable and used in the remainder of the paper.

Table 4. Hybridization benefit with the two power filters.

Parameter	Battery-Alone	1st Order LPF	FIR Filter
LPF parameters	N/A	T = 45 s	N = 350; $\omega_c = 0.007\pi$ rad/sample
Expected battery life	1858 days	2009 days	2003 days
Standard deviation of the P_B RoCoP	1.7 W/s	0.3 W/s	1.3 W/s
Number of microcycles (<10% DoD)	1675	499	212
Number of deep cycles (≥10% DoD)	89	89	91

For a closer look at the filtering effect on the battery life, Figure 14 compares the battery RoCoP and DoD distribution between the battery-alone and HESS cases. Clearly, the hybridized batteries are exposed to a much more narrow RoCoP spectrum with substantially smaller power rates in Figure 14a, which translates to much fewer microcycles in

Figure 14b (logarithmic scale). Please note also the large proportion of microcycles over the total number of cycles in each case in Table 4. This analysis consolidates the importance of an accurate battery degradation model with microcycles DoD resolution in order to properly assess the hybridization benefit.

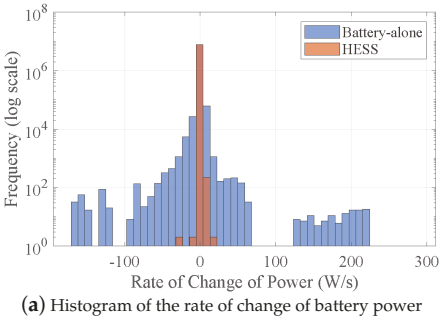

(**a**) Histogram of the rate of change of battery power

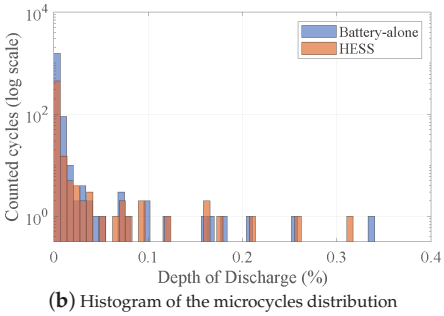

(**b**) Histogram of the microcycles distribution

Figure 14. Hybridization effect on the battery operation.

4.3. Sensitivity Analysis of Thermal Parameters

Although the importance of the battery temperature on the battery life is a well-known fact, it is still somewhat unclear how the supercapacitors can influence this phenomenon and therefore the hybridization benefit. For this reason, the following paragraphs present a sensitivity analysis, in which some of the most prevalent thermal parameters, i.e., thermal resistance R_{th}, thermal time constant t_c and converter power losses $P_{loss\_converter}$, are varied over a wide range to capture their effect on the temperature and battery life with and without the hybridization. The default parameters of Table 3 are used as a benchmark.

4.3.1. The Effect of Thermal Resistance

The thermal resistance R_{th} reflects how the power losses from the battery and power converter translate to battery temperature. Figure 15a shows the resulting HESS battery temperature for R_{th} varying from 0 to 1 °C/W in the form of sorted curves (i.e., the temperature values of the entire profile are sorted from high to low). Clearly, R_{th} is a crucial factor, which may lead to very high temperatures for large values.

Figure 15b illustrates how this relates to the battery life with and without the hybridization. The R_{th} impact is indeed negative, but the HESS seems to be much more resilient compared to the battery-alone ESS. This is because the hybridization effectively reduces the battery internal power losses $P_{loss\_battery}$ due to a smoother battery current I_{bat}, as explained in Section 3.2.2; this entails lower battery temperature, and fewer number of cycles in total. As a result, the life extension from hybridization in Figure 15c increases in an exponential manner with R_{th}. The conclusion from this investigation is that the supercapacitors not only alleviate some of the DoD degradation, but they also bring a thermal benefit which proves to be substantial when the thermal resistance is high.

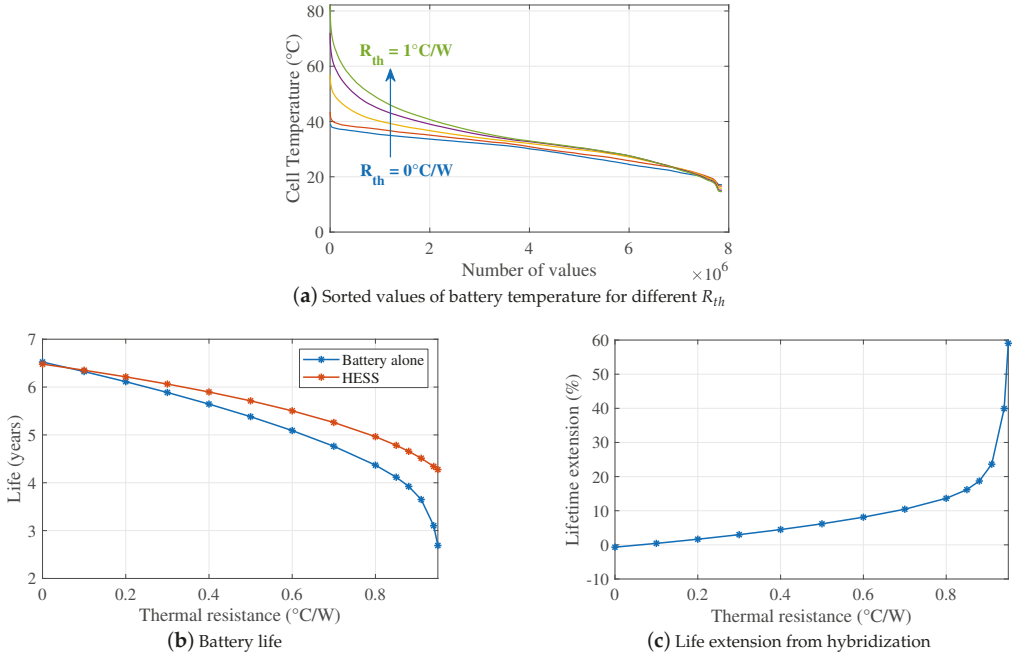

(**a**) Sorted values of battery temperature for different R_{th}

(**b**) Battery life

(**c**) Life extension from hybridization

Figure 15. Thermal resistance's effect on battery life.

4.3.2. The Effect of the Thermal Time Constant

The thermal time constant t_c plays essentially the role of inertia for the battery temperature (see Equation (7)), typically few hours [66,67]. Small values entail steep temperature rise during short-term power peaks, whereas large values effectively flatten out the temperature distribution. This is why a $t_c = 1$ h in Figure 16a results in occasional very high temperatures, but most of the time the temperature is slightly lower than the $t_c = 10$ h case. This effect is reflected to the battery life and hybridization benefit as Figure 16b,c show; the trend is somewhat similar to the R_{th} effect but with a reversed x-axis. Again, the supercapacitors may prove of little or major importance depending on the time constant value.

4.3.3. The Effect of Converter Power Losses

The converter power losses $P_{loss\_converter}$ have a rather limited impact on the battery temperature as shown in Figure 17a: higher losses lead to higher temperatures, but the difference is not as significant as with the previous factors. This translates to a more limited effect on the battery life in Figure 17b and to a linear life extension from the hybridization in Figure 17c. The general conclusion from this sensitivity analysis is: the more severe the thermal conditions of the ESS, the more useful the supercapacitors are. This gives an additional perspective on the hybridization benefits, apart from the most commonly considered DoD impact.

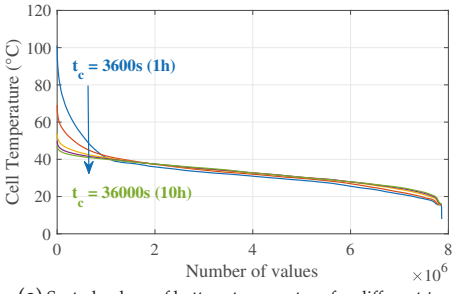

(**a**) Sorted values of battery temperature for different t_c

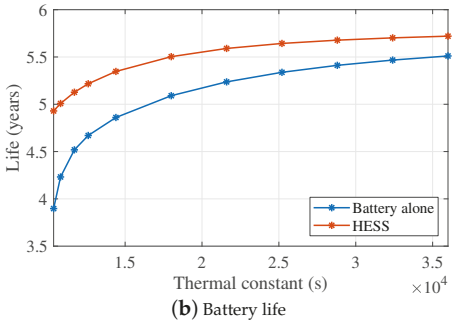

(**b**) Battery life

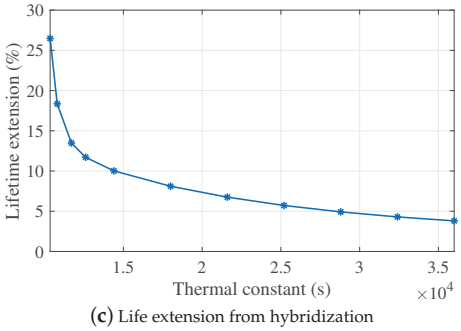

(**c**) Life extension from hybridization

Figure 16. The thermal time constant's effect on battery life.

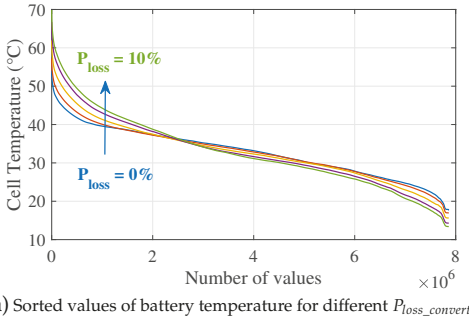

(**a**) Sorted values of battery temperature for different $P_{loss\_converter}$

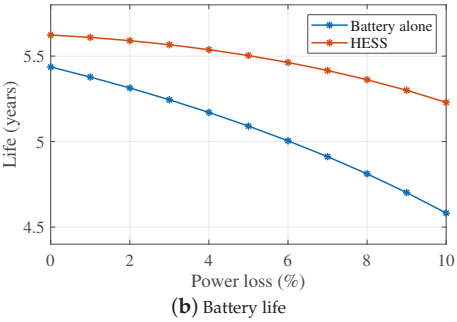

(**b**) Battery life

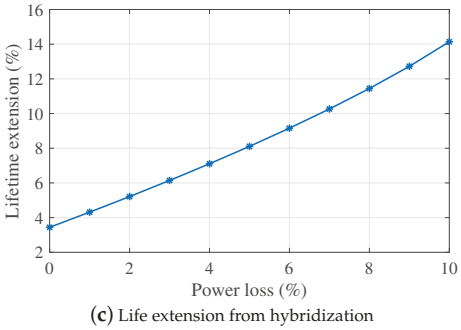

(**c**) Life extension from hybridization

Figure 17. Converter power losses' effect on battery life.

5. Economic Analysis and Discussion

Although the previous section shows that hybridization is more or less beneficial to the battery's life, it is not clear when it makes sense in terms of economic viability. Here, the benefit of more long-lived batteries is weighted against the additional investment burden of the supercapacitors and their power converter to evaluate the overall economic benefit of the hybridization. The case study of the previous section is used as an example, assessed in six different scenarios to understand when the investment is viable and when it is not.

The net present cost (NPC) metric is adopted in this paper to evaluate the total investment required for the two alternative ESS over the entire project life. NPC involves the initial one-time investment I_0, any replacement costs R and operation and maintenance (O&M) costs OM during the lifetime of the project [22,68]:

$$NPC = I_0 + R + OM \tag{15}$$

In the battery-alone system, I_0 comprises the costs for the batteries $C_{bat}E_{bat}$ and their converter $C_{conv}E_{conv}^{bat}$, while the HESS involves additionally the supercapacitors costs $C_{sup}E_{sup}$ and their own converter costs $C_{conv}E_{conv}^{sup}$. Equation (16) shows the full picture for the HESS case.

$$I_0 = C_{bat}E_{bat} + C_{sup}E_{sup} + C_{conv}(E_{conv}^{bat} + E_{conv}^{sup}) \tag{16}$$

The parameters used in this paper are given in Table 5. The capital cost accounts for the main investment. According to [21], the capital cost of lead–acid batteries in 2018 was approximately 260 \$/kWh and it was predicted to drop to 220 \$/kWh by 2025. Assuming that this project starts in 2020, a battery capital cost of 250 \$/kWh is considered, with a discount rate of 2.4%. The capital cost of supercapacitors is typically 10,000 \$/kWh [69], as adopted for example in the case study of [70]. The O&M costs of supercapacitors are generally lower than that of batteries, selecting here 0.1% and 0.45% of the investment, respectively, based on [21]. The cost of the power converters is taken from [21,68].

Assuming a project lifetime of 15 years, the replacement costs R in both battery-alone ESS and HESS refer only to the batteries, since the supercapacitors and converters lifespan typically reaches or exceeds 15 years [21,68]. Given the battery lifespan L_{bat} calculated in years by the proposed degradation model in Section 3, the batteries need to be replaced $r = 15/L_{bat} - 1$ times during the project lifetime; every replacement will cost $C_{bat}E_{bat}$ adjusted by the annual market discount rate d_r that reflects the fact that technology becomes cheaper over time. As r may not be an integer, the equation below involves the cost of full replacements $\lfloor r \rfloor$ (rounded down) plus the cost of the final replacement that accounts only for the remaining years and is adjusted by $r - \lfloor r \rfloor$. The latter intervention is a simple way to account for capital recovery after the project life.

$$R = \sum_{n=1}^{\lfloor r \rfloor} \frac{C_{bat}E_{bat}}{(1+d_r)^{nL_{bat}}} + (r - \lfloor r \rfloor)\frac{C_{bat}E_{bat}}{(1+d_r)^{\lceil r \rceil L_{bat}}} \tag{17}$$

Finally, the O&M costs increase every year due to aging of the equipment, reflected in the actual discount rate d. During the first battery lifetime, the annual maintenance costs will be an adjusted version of OM_0^{bat} based on d, where OM_0^{bat} is a percentage of the initial investment (see Table 5). When the batteries are replaced, the maintenance costs will be a discounted value of OM_1^{bat}, which is again a percentage but of the respective replacement cost (see Equation (17)). The final O&M expression is given below for the HESS.

$$OM = \sum_{n=1}^{15/L_{bat}} \sum_{t=1}^{L_{bat}} \frac{OM_{n-1}^{bat}}{(1+d)^t} + \sum_{t=1}^{15} \frac{OM_0^{sup}}{(1+d)^t} + \sum_{t=1}^{15} \frac{OM_0^{conv}}{(1+d)^t} \tag{18}$$

Table 5. Economic parameters [21,68,69].

Parameter	Lead Acid Battery	Supercapacitor	Power Converters
Capital cost C_{bat}, C_{sup}, C_{conv}	250 $/kWh	10,000 $/kWh	0.25 $/W
Capacity E_{bat}, E_{sup}, $E_{conv}^{bat}/E_{conv}^{sup}$	7200 Wh	18 Wh	1000 W/ 300 W
Initial O&M costs OM_0^{bat}, OM_0^{sup}, OM_0^{conv}	0.45% of invest.	0.11% of invest.	1 $/kW
Other Economic Parameters			
Market discount rate d_r		2.4%	
O&M actual discount rate d		−5%	

It is worth noting that the O&M costs of the hybridized system will not fundamentally differ from the battery-alone ESS. Being both electrochemical storage devices, the battery and supercapacitor require simple and straightforward maintenance, i.e., keeping the surface clean and the connectors sealed etc. [71]. The skillset required by the local technicians for installation, operation and maintenance is practically the same in the two systems, which does not create any additional barriers in adopting the HESS in isolated rural communities. However, it should be noted that supercapacitors consumables are not as readily available as lead–acid batteries in local markets in rural India, although currently the market size of Indian supercapacitor manufacturing industry grows steadily every year [72].

5.1. Base Scenario

The base scenario refers to the default HESS parameters of Table 3 and the economic considerations of Table 5. This includes a set of reasonable assumptions corresponding to a realistic system, used thereafter as a benchmark for the remaining scenarios. The results of the techno-economic analysis are given in Table 6. The battery life in the basic scenario is estimated to be 5–5.5 years, which is well-aligned with industry's expectations for real-life microgrids [71]. The supercapacitors' contribution reduces the total number of cycles by 2/3, mainly the microcycles, which translates to about 8% longer lifespan for the batteries. However, given the additional investment costs in the HESS, the economic benefit is much more limited at 1.9%. This makes the hybridization economically viable, albeit very marginally. The following scenarios explore how these numbers change for different thermal and economic considerations.

Table 6. Results of the base scenario.

Parameters	Battery-Alone	HESS
Total number of cycles	1754	579
Life estimation	1858 days	2009 days
Life estimation	5.09 years	5.50 years
Number of battery replacements	1.95	1.73
Invest. on Supercapacitor	0	184 $
Invest. on Battery	4734 $	4386 $
Invest. on Converters	250 $	325 $
O&M	140 $	132 $
Total invest.	5124 $	5027 $
Life extension		8.1%
Economic benefit		1.9%

5.2. Scenario 2: Conventional Cycle Life DoD Model

The discussion in Section 3.1.2 outlines two cycle life models that evaluate the DoD degradation effect: the conventional model designed for cycles with substantial DoD, and the microcycle model that accounts also for the cycles with very little DoD. Given that

the case-study electricity profile is of high time-resolution and the numerous microcycles are visible, it is of paramount importance to use the latter model in all analyses, as has been done throughout this paper. To support this claim, scenario 2 employs the conventional model instead, with the results given in Table 7. Clearly, the battery degradation is severely overestimated, yielding about 1 year lifespan for the battery-alone and 3 years for the HESS. Although, hybridization seems very beneficial indeed in this case, the results of 1-3 years are not realistic [71], highlighting that this type of model can not reflect reality and should not be used to inform an investment. In fact, the main conclusion from this scenario is how important is to use a microcycles life model when the SoC profile is of high time-resolution and the microcycles are visible. In cases that a microcycle model is not available, it is preferable to completely disregard the microcycles from the profile when evaluating the DoD degradation.

Table 7. Results of scenario 2.

Parameters	Battery-Alone	HESS
Life estimation	1.05 years	3.04 years
Number of battery replacements	13.33	3.93
Total invest.	22,346 $	8382 $
Life extension	190.6%	
Economic benefit	62.5%	

5.3. Scenario 3: Poor Thermal Characteristics

The thermal parameters of Table 3 are indicative and strongly depend on the specific system and environment. Their influence on the battery life is discussed in Section 4.3; here, the respective economic impact is assessed in a scenario with worse thermal characteristics (e.g., poor ventilation and thermal management system): thermal resistance 0.8 °C/W, thermal time constant 14,400 s (4 h) and converter losses 8%. For example, [66] shows that the thermal resistance can be in some cases as high as 1.1 °C/W and the thermal constant around 3–4 h. The results of Table 8 show a lifespan reduction of more than a year in both systems compared to the base scenario due to the higher battery temperature. These severe thermal conditions result in a battery life falling short of the industrial targets [71], but hybridization manages to mitigate this impact to a large extent. The contribution of the hybridization is considerable indeed, extending the battery longevity by more than 20%, which translates to about 12% economic benefit. Clearly, hybridization is highly beneficial in this case, which indicates that a HESS is a good solution under poor thermal conditions.

Table 8. Results of different scenarios of thermal characteristics.

Parameters	Scenario 3 (Poor Thermal Char.)		Scenario 4 (Good Thermal Char.)	
	Battery-Alone	HESS	Battery-Alone	HESS
Life estimation	3.80 years	4.59 years	5.72 years	5.93 years
Number of battery replacements	2.95	2.27	1.62	1.53
Total invest.	6627 $	5840 $	4605 $	4716 $
Life extension	20.7%		3.7%	
Economic benefit	11.9%		−2.4%	

5.4. Scenario 4: Good Thermal Characteristics

On the other hand, improved thermal characteristics should affect the results in the opposite way. Here, the thermal parameters are: thermal resistance 0.4 °C/W; thermal time constant 21,600 s (6 h); [67,73] and converter losses remain at 5%. For example, [73] shows that with a properly designed cooling system, the thermal resistance will almost

be lower than 0.4 °C/W, or even be reduced to 0.2 °C/W. Table 8 shows that the battery life of the only-battery system meets and exceeds the industry expectations, which entails marginal only life improvement from hybridization and a negative economic benefit indeed. In other words, the hybridization contribution is too little to overcome the relevant financial overhead. This highlights once again the importance to consider both temperature and DoD factors in a battery degradation model to yield reliable conclusions.

5.5. Scenario 5: Economic Parameters in Favor of Hybridization

In order to assess the influence of the economic parameters on the viability of the hybridization, this section repeats the analysis assuming conditions more favorable to the supercapacitors. Specifically, the supercapacitors' capital cost is reduced by 20% to 8000 $/kWh, the batteries are priced 12% higher at 280 $/kWh, the market discount rate d_r drops to 0.4% and the O&M discount rate d is assumed to be −1% (see Table 5 for comparison). The resulting Table 9 differs from the base case Table 6 only in the financial figures, now increasing the economic benefit of the hybridization to 3.6%. Apparently, this is not fundamentally different from the 1.9% in the base case, which entails that the hybridization viability is more sensitive on the thermal parameters, rather than the economic ones.

Table 9. Results of different scenarios of economic parameters.

Parameters	Scenario 5 (In Favor of Hybr.)		Scenario 6 (Against Hybr.)	
	Battery-Alone	**HESS**	**Battery-Alone**	**HESS**
Life estimation	5.09 years	5.50 years	5.09 years	5.50 years
Number of battery replacements	1.95	1.73	1.95	1.73
Invest. on Supercapacitor	0	147 $	0	224 $
Invest. on Battery	5824 $	5388 $	3732 $	3467 $
O&M	150 $	140 $	139 $	132 $
Total invest.	6224 $	5999 $	4122 $	4148 $
Life extension	8.1%		8.1%	
Economic benefit	3.6%		−0.6%	

5.6. Scenario 6: Economic Parameters against Hybridization

By contrast, this scenario explores economic parameters that stand against the hybridization: supercapacitors cost $12,000/kWh, battery costs $220/kWh, 5% battery market discount rate and −10% O&M discount rate. Table 9 shows a slightly negative economic benefit which renders the hybridization marginally inviable. Still, a drop from 1.9% in the base case to −0.6% here is very limited considering the substantial variations in the capital costs, which essentially confirms the relative insensitivity of the hybridization to the economic parameters.

In fact, the main conclusion from this investigation is that the main factors to assess whether a lead–acid battery ESS should be hybridized with supercapacitors are the thermal parameters, rather than the economic ones. The poorest the thermal conditions, the more likely the hybridization to be beneficial.

6. Conclusions

This paper describes a methodology to hybridize a battery-based energy storage system using supercapacitors for a smoother power profile, presenting a new control scheme, a new battery degradation mechanism model and an economic viability analysis. Compared to a system with only lead–acid batteries, the hybrid system features longer battery life. The results showed that a simple first-order low-pass filter is an effective and reliable solution for the power filtering, performing more favorably than higher order FIR filters given the limited supercapacitors capacity and strict voltage limits. Apparently, the supercapacitors result in fewer microcycles, but also in lower average battery temperature

due to the smoother current profile that yields less power losses compared to a fluctuating current in the battery-alone case. This also highlights the importance in capturing both DoD and temperature effects in a battery degradation model, such as in the one proposed.

Especially when there is access to second-resolution time series that allows visibility to numerous microcycles, an appropriate microcycles cycle life DoD model should be used; if not available, the microcycles should instead be completely disregarded from the profile to avoid erroneous battery life estimation. A sensitivity analysis showed that the thermal parameters of the system not only affect the battery life, but play a major role in the hybridization benefit: poorer or better thermal conditions render the hybridization more or less useful respectively. This is confirmed by the economic analysis, which concludes that the financial benefit of the hybridization depends more on the thermal conditions rather than the economic parameters of the investment.

The methodology and findings of this study may be useful when exploring hybridization options for battery ESS in standalone microgrids. In addition, this type of hybrid ESS has great grid-connected potential as well, mainly in facilitating high levels of renewables integration. It is nowadays seen as a credible way to absorb generation and load intermittency and provide ancillary services to the power system, such as frequency response and inertia emulation, functions that again result in irregular charge/discharge battery profiles that hint towards a hybrid ESS.

Furthermore, it is worth noting that the core of the proposed methodology applies to Li-ion battery systems as well, which is increasingly gaining popularity due to longer life, smaller size and less weight. Most steps of this paper's methodology will be common in this case, but with substantially different characteristics and parameters that do not allow for straightforward extrapolation of this study findings to Li-ion battery systems.

Author Contributions: Conceptualization, X.L. and E.B.; methodology, X.L., J.V.B. and E.B.; investigation, X.L.; writing—original draft preparation, X.L.; writing—review and editing, J.V.B., B.W., C.L.C. and E.B.; supervision, E.B. All authors have read and agreed to the published version of the manuscript.

Funding: This research has been supported by the Royal Academy of Engineering under the Engineering for Development Research Fellowship scheme (number RF\201819\18\86) and EPSRC Faraday Institution's Multi-Scale Modelling Project (EP/S003053/1, grant number FIRG003).

Institutional Review Board Statement: Not applicable.

Informed Consent Statement: Not applicable.

Data Availability Statement: No new data were created or analyzed in this study. Data sharing is not applicable to this article.

Acknowledgments: The authors would like to thank Oorja Development Solutions Limited and BBOXX for their kind provision of the electricity profile of the case study, and Mr Hamish Beath and Mr Philip Sandwell for assisting with acquiring the data.

Conflicts of Interest: The authors declare no conflict of interest.

Abbreviations

The following abbreviations are used in this manuscript:

DoD	Depth of Discharge
ESS	Energy Storage System
FIR	Finite Impulse Response (filter)
HESS	Hybrid Energy Storage System
LPF	Low-Pass Filter
NPC	Net Present Cost
O&M	Operation and Maintenance (costs)
PV	Photovoltaic
SoC	State of Charge

References

1. United Nations Sustainable Development Goals (SDGs). Ensure Access to Affordable, Reliable, Sustainable and Modern Energy. Available online: https://www.un.org/sustainabledevelopment/energy/ (accessed on 11 December 2020).
2. Jing, W.; Lai, C.H.; Wong, S.H.W.; Wong, M.L.D. Battery-supercapacitor hybrid energy storage system in standalone DC microgrids: Areview. *IET Renew. Power Gener.* **2016**, *11*, 461–469. [CrossRef]
3. Serban, E.; Serban, H. A control strategy for a distributed power generation microgrid application with voltage-and current-controlled source converter. *IEEE Trans. Power Electron.* **2010**, *25*, 2981–2992. [CrossRef]
4. Zhang, Y.; Wang, J.; Berizzi, A.; Cao, X. Life cycle planning of battery energy storage system in off-grid wind–solar–diesel microgrid. *IET Gener. Transm. Distrib.* **2018**, *12*, 4451–4461. [CrossRef]
5. Kollimalla, S.K.; Mishra, M.K.; Narasamma, N.L. Design and Analysis of Novel Control Strategy for Battery and Supercapacitor Storage System. *IEEE Trans. Sustain. Energy* **2014**, *5*, 1137–1144. [CrossRef]
6. Bindner, H.; Cronin, T.; Lundsager, P.; Manwell, J.F.; Abdulwahid, U.; Baring-Gould, I. Lifetime modelling of lead acid batteries. *Risø Natl. Lab.* **2005**, *12*, 1629–1639.
7. Kuperman, A.; Aharon, I. Battery–ultracapacitor hybrids for pulsed current loads: A review. *Renew. Sustain. Energy Rev.* **2011**, *15*, 981–992. [CrossRef]
8. Sarwar, W.; Engstrom, T.; Marinescu, M.; Green, N.; Taylor, N.; Offer, G.J. Experimental analysis of Hybridised Energy Storage Systems for automotive applications. *J. Power Sources* **2016**, *324*, 388–401. [CrossRef]
9. Dezza, F.C.; Musolino, V.; Piegari, L.; Rizzo, R. Hybrid battery–supercapacitor system for full electric forklifts. *IET Electr. Syst. Transp.* **2018**, *9*, 16–23. [CrossRef]
10. Zhang, Q.; Li, G. Experimental study on a semi-active battery-supercapacitor hybrid energy storage system for electric vehicle application. *IEEE Trans. Power Electron.* **2019**, *35*, 1014–1021. [CrossRef]
11. Choi, M.; Lee, J.; Seo, S. Real-time optimization for power management systems of a battery/supercapacitor hybrid energy storage system in electric vehicles. *IEEE Trans. Veh. Technol.* **2014**, *63*, 3600–3611. [CrossRef]
12. Yoo, H.; Sul, S.; Park, Y.; Jeong, J. System integration and power-flow management for a series hybrid electric vehicle using supercapacitors and batteries. *IEEE Trans. Ind. Appl.* **2008**, *44*, 108–114. [CrossRef]
13. Carter, R.; Cruden, A.; Hall, P.J. Optimizing for efficiency or battery life in a battery/supercapacitor electric vehicle. *IEEE Trans. Veh. Technol.* **2012**, *61*, 1526–1533. [CrossRef]
14. Mohammadi, E.; Rasoulinezhad, R.; Moschopoulos, G. Using a Supercapacitor to Mitigate Battery Microcycles Due to Wind Shear and Tower Shadow Effects in Wind-Diesel Microgrids. *IEEE Trans. Smart Grid* **2020**, *11*, 3677–3689. [CrossRef]
15. Garcia, P.; Fernandez, L.M.; Garcia, C.A.; Jurado, F. Energy management system of fuel-cell-battery hybrid tramway. *IEEE Trans. Ind. Electron.* **2009**, *57*, 4013–4023. [CrossRef]
16. Carignano, M.; Roda, V.; Costa-Castelló, R.; Valiño, L.; Lozano, A.; Barreras, F. Assessment of energy management in a fuel cell/battery hybrid vehicle. *IEEE Access* **2019**, *7*, 16110–16122. [CrossRef]
17. Zhang, F.; Hu, Z.; Meng, K.; Ding, L.; Dong, Z.Y. Sequence control strategy for hybrid energy storage system for wind smoothing. *IET Gener. Transm. Distrib.* **2019**, *13*, 4482–4490. [CrossRef]
18. Lemofouet, S.; Rufer, A. Hybrid energy storage system based on compressed air and super-capacitors with maximum efficiency point tracking (MEPT). *IEEJ Trans. Ind. Appl.* **2006**, *126*, 911–920. [CrossRef]
19. Mamun, A.; Liu, Z.; Rizzo, D.M.; Onori, S. An integrated design and control optimization framework for hybrid military vehicle using lithium-ion battery and supercapacitor as energy storage devices. *IEEE Trans. Transp. Electrif.* **2018**, *5*, 239–251. [CrossRef]
20. German, R.; Sari, A.; Briat, O.; Vinassa, J.; Venet, P. Impact of voltage resets on supercapacitors aging. *IEEE Trans. Ind. Electron.* **2016**, *63*, 7703–7711. [CrossRef]
21. Mongird, K.; Viswanathan, V.V.; Balducci, P.J.; Alam, M.J.E.; Fotedar, V.; Koritarov, V.S.; Hadjerioua, B. *Energy Storage Technology and Cost Characterization Report*; Pacific Northwest National Lab. (PNNL): Richland, WA, USA, 2019.
22. Gee, A.M.; Robinson, F.V.P.; Dunn, R.W. Analysis of battery lifetime extension in a small-scale wind-energy system using supercapacitors. *IEEE Trans. Energy Convers.* **2013**, *28*, 24–33. [CrossRef]
23. de Castro, R.; Pinto, C.; Varela Barreras, J.; Araújo, R.E.; Howey, D.A. Smart and Hybrid Balancing System: Design, Modeling, and Experimental Demonstration. *IEEE Trans. Veh. Technol.* **2019**, *68*, 11449–11461. [CrossRef]
24. Oriti, G.; Julian, A.L.; Anglani, N.; Hernandez, G.D. Novel economic analysis to design the energy storage control system of a remote islanded microgrid. *IEEE Trans. Ind. Appl.* **2018**, *54*, 6332–6342. [CrossRef]
25. Kurm, S.; Agarwal, V. Hybrid Energy Storage System based on a Novel Reduced Rating Multi Input Converter. *IEEE Trans. Power Electron.* **2020**, *35*, 12133–12142. [CrossRef]
26. Abeywardana, D.B.W.; Hredzak, B.; Agelidis, V.G.; Demetriades, G.D. Supercapacitor Sizing Method for Energy-Controlled Filter-Based Hybrid Energy Storage Systems. *IEEE Trans. Power Electron.* **2016**, *32*, 1626–1637. [CrossRef]
27. Mesbahi, T.; Rizoug, N.; Bartholomeüs, P.; Sadoun, R.; Khenfri, F.; Le Moigne, P. Optimal energy management for a li-ion battery/supercapacitor hybrid energy storage system based on a particle swarm optimization incorporating Nelder–Mead simplex approach. *IEEE Trans. Intell. Veh.* **2017**, *2*, 99–110. [CrossRef]
28. Khan, M.M.S.; Faruque, M.O.; Newaz, A. Fuzzy logic based energy storage management system for MVDC power system of all electric ship. *IEEE Trans. Energy Convers.* **2017**, *32*, 798–809. [CrossRef]

29. Shen, J.; Khaligh, A. A supervisory energy management control strategy in a battery/ultracapacitor hybrid energy storage system. *IEEE Trans. Transp. Electrif.* **2015**, *1*, 223–231. [CrossRef]
30. Ravada, B.R.; Tummuru, N.R. Control of a Supercapacitor/Battery/PV based Stand-Alone DC-Microgrid. *IEEE Trans. Energy Convers.* **2020**, *35*, 1268–1277. [CrossRef]
31. Zhang, S.; Xiong, R.; Sun, F. Model predictive control for power management in a plug-in hybrid electric vehicle with a hybrid energy storage system. *Appl. Energy* **2017**, *185*, 1654–1662. [CrossRef]
32. Pinto, C.; Varela Barreras, J.; de Castro, R.; Araújo, R.E.; Schaltz, E. Study on the combined influence of battery models and sizing strategy for hybrid and battery-based electric vehicles. *Energy* **2017**, *137*, 272–284. [CrossRef]
33. Somayajula, D.; Crow, M.L. An ultracapacitor integrated power conditioner for intermittency smoothing and improving power quality of distribution grid. *IEEE Trans. Sustain. Energy* **2014**, *5*, 1145–1155. [CrossRef]
34. Kotra, S.; Mishra, M.K. Design and stability analysis of dc microgrid with hybrid energy storage system. *IEEE Trans. Sustain. Energy* **2019**, *10*, 1603–1612. [CrossRef]
35. Dufo-López, R.; Lujano-Rojas, J.M.; Bernal-Agustín, J.L. Comparison of different lead–acid battery lifetime prediction models for use in simulation of stand-alone photovoltaic systems. *Appl. Energy* **2014**, *115*, 242–253. [CrossRef]
36. Reniers, J.M.; Mulder, G.; Howey, D.A. Review and performance comparison of mechanical-chemical degradation models for lithium-ion batteries. *J. Electrochem. Soc.* **2019**, *166*, A3189–A3200. [CrossRef]
37. Liao, L.; Köttig, F. Review of hybrid prognostics approaches for remaining useful life prediction of engineered systems, and an application to battery life prediction. *IEEE Trans. Reliab.* **2014**, *63*, 191–207. [CrossRef]
38. Narayan, N.; Papakosta, T.; Vega-Garita, V.; Qin, Z.; Popovic-Gerber, J.; Bauer, P.; Zeman, M. Estimating battery lifetimes in Solar Home System design using a practical modelling methodology. *Appl. Energy* **2018**, *228*, 1629–1639. [CrossRef]
39. Dudézert, C.; Reynier, Y.; Duffault, J.; Franger, S. Fatigue damage approach applied to Li-ion batteries aging characterization. *Mater. Sci. Eng. B* **2016**, *213*, 177–189. [CrossRef]
40. Schaltz, E.; Khaligh, A.; Rasmussen, P.O. Influence of battery/ultracapacitor energy-storage sizing on battery lifetime in a fuel cell hybrid electric vehicle. *IEEE Trans. Veh. Technol.* **2009**, *58*, 3882–3891. [CrossRef]
41. He, G.; Chen, Q.; Kang, C.; Pinson, P.; Xia, Q. Optimal bidding strategy of battery storage in power markets considering performance-based regulation and battery cycle life. *IEEE Trans. Smart Grid* **2015**, *7*, 2359–2367. [CrossRef]
42. Han, X.; Liang, Y.; Ai, Y.; Li, J. Economic evaluation of a PV combined energy storage charging station based on cost estimation of second-use batteries. *Energy* **2018**, *165*, 326–339. [CrossRef]
43. Li, S.; He, H.; Su, C.; Zhao, P. Data driven battery modeling and management method with aging phenomenon considered. *Appl. Energy* **2020**, *275*, 115340. [CrossRef]
44. Stroe, D.; Świerczyński, M.; Stan, A.; Teodorescu, R.; Andreasen, S.J. Accelerated lifetime testing methodology for lifetime estimation of lithium-ion batteries used in augmented wind power plants. *IEEE Trans. Ind. Appl.* **2014**, *50*, 4006–4017. [CrossRef]
45. Reddy, T.B. *Linden's Handbook of Batteries*, 4th ed.; McGraw-Hill, Inc.: New York, NY, USA, 2011.
46. Sauer, D.U. Secondary Batteries: Lead-acid batteries—Lifetime Determining Processes. *Encycl. Electrochem. Power Sources* **2009**, *4*, 805–815.
47. Layadi, T.M.; Champenois, G.; Mostefai, M.; Abbes, D. Lifetime estimation tool of lead–acid batteries for hybrid power sources design. *Simul. Model. Pract. Theory* **2015**, *54*, 36–48. [CrossRef]
48. Swierczynski, M.; Stroe, D.; Stan, A.; Teodorescu, R.; Kær, S.K. Lifetime Estimation of the Nanophosphate $LiFePO_4$/C Battery Chemistry Used in Fully Electric Vehicles. *IEEE Trans. Ind. Appl.* **2015**, *51*, 3453–3461. [CrossRef]
49. Photovoltaics, D.G.; Storage, E. *IEEE Guide for Selecting, Charging, Testing, and Evaluating Lead-Acid Batteries Used in Stand-Alone Photovoltaic (PV) Systems*; IEEE Std 1361-2014 (Revision of IEEE Std 1361-2003); IEEE: Piscataway, NJ, USA, 2014; pp. 1–39.
50. Wu, B.; Parkes, M.A.; Yufit, V.; De Benedetti, L.; Veismann, S.; Wirsching, C.; Vesper, F.; Martinez-Botas, R.F.; Marquis, A.J.; Offer, G.J. and others Design and testing of a 9.5 kWe proton exchange membrane fuel cell–supercapacitor passive hybrid system. *Int. J. Hydrogen Energy* **2014**, *39*, 7885–7896. [CrossRef]
51. Nazaripouya, H.; Chu, C.; Pota, H.R.; Gadh, R. Battery energy storage system control for intermittency smoothing using an optimized two-stage filter. *IEEE Trans. Sustain. Energy* **2017**, *9*, 664–675. [CrossRef]
52. Al-Alaoui, M.A. Linear phase low-pass IIR digital differentiators. *IEEE Trans. Signal Process.* **2007**, *55*, 697–706. [CrossRef]
53. Mellit, A.; Benghanem, M.; Kalogirou, S.A. Modeling and simulation of a stand-alone photovoltaic system using an adaptive artificial neural network: Proposition for a new sizing procedure. *Renew. Energy* **2007**, *32*, 285–313. [CrossRef]
54. Kumar, S.; Singh, K.; Saxena, R. Analysis of Dirichlet and generalized "Hamming" window functions in the fractional Fourier transform domains. *Signal Process.* **2011**, *91*, 600–606. [CrossRef]
55. Kumar, A.; Singh, G.K.; Anand, R. An improved closed form design method for the cosine modulated filter banks using windowing technique. *Appl. Soft Comput.* **2011**, *11*, 3209–3217. [CrossRef]
56. Supercapacitors/Ultracapacitors BMOD0500 P016 B01 Datasheet, Maxwell Technologies, Inc. 2014. Available online: https://www.maxwell.com/images/documents/datasheet_16v_module.pdf (accessed on 1 July 2020).
57. Wang, Y.; Xue, L.; Wang, C.; Wang, P.; Li, W. Interleaved high-conversion-ratio bidirectional DC–DC converter for distributed energy-storage systems—Circuit generation, analysis, and design. *IEEE Trans. Power Electron.* **2015**, *31*, 5547–5561. [CrossRef]
58. Deep-Cycle Gel Batteries, Trojan Battery Co. 2008. Available online: http://www.trojanbattery.com/pdf/GEL_SS_Web.pdf (accessed on 14 July 2020).

59. U.S. DRIVE. Electrical and electronics technical team roadmap. In *U.S. DRIVE Partnership Plan, Roadmaps, and Accomplishments*; United States Department of Energy: Washington, DC, USA, 2013.
60. Winter, M.; Brodd, R.J. What are batteries, fuel cells, and supercapacitors? *Chem. Rev.* **2004**, *104*, 4245–4270. [CrossRef]
61. Dragičević, T. Hierarchical Control of a Direct Current Microgrid with Energy Storage Systems in a Distributed Topology. Ph.D. Thesis, University of Zagreb, Zagreb, Croatia, 2013.
62. Zou, Y.; Hu, X.; Ma, H.; Li, S.E. Combined state of charge and state of health estimation over lithium-ion battery cell cycle lifespan for electric vehicles. *J. Power Sources* **2015**, *273*, 793–803. [CrossRef]
63. 31GEL Trojan Data Sheets, Trojan Battery Co. 2019. Available online: https://www.trojanbattery.com/pdf/datasheets/31GEL_Trojan_Data_Sheets.pdf (accessed on 14 July 2020).
64. Kauzlarich, J.J. The Palmgren-Miner rule derived. In *Tribology Series*; Dowson, D., Taylor, C., Eds.; Elsevier: New York, NY, USA, 1989; pp. 175–179.
65. Berndt, D. Valve-regulated lead-acid batteries. *J. Power Sources* **2001**, *100*, 29–46. [CrossRef]
66. Barsali, S.; Ceraolo, M. Dynamical models of lead-acid batteries: Implementation issues. *IEEE Trans. Energy Convers.* **2002**, *17*, 16–23. [CrossRef]
67. Ceraolo, M. New dynamical models of lead-acid batteries. *IEEE Trans. Power Syst.* **2000**, *15*, 1184–1190. [CrossRef]
68. Tsai, C.; Beza, T.M.; Molla, E.M.; Kuo, C. Analysis and Sizing of Mini-Grid Hybrid Renewable Energy System for Islands. *IEEE Access* **2020**, *8*, 70013–70029. [CrossRef]
69. Ultracapacitor Overview, Maxwell Technologies, Inc. 2018. Available online: http://www.maxwell.com/products/ultracapacitors (accessed on 28 July 2020).
70. Kim, K.; An, J.; Park, K.; Roh, G.; Chun, K. Analysis of a supercapacitor/battery hybrid power system for a bulk carrier. *Appl. Sci.* **2019**, *9*, 1547. [CrossRef]
71. Sen, R. *A Detailed Manual on Lead Acid Battery Operation & Maintenance for Solar PV Plants*; USAID: Washington, DC, USA, 2018.
72. Kale, B.; Chatterjee, S. Electrochemical energy storage systems: India perspective. *Bull. Mater. Sci.* **2020**, *43*, 1–15. [CrossRef]
73. Divakaran, A.M.; Hamilton, D.; Manjunatha, K.N.; Minakshi, M. Design, development and thermal analysis of reusable Li-ion battery module for future mobile and stationary applications. *Energies* **2020**, *13*, 1477. [CrossRef]

energies

MDPI

Article

Parallel PV Configuration with Magnetic-Free Switched Capacitor Module-Level Converters for Partial Shading Conditions

Georgios Kampitsis [1,*], Efstratios Batzelis [1], Remco van Erp [2] and Elison Matioli [2]

[1] Department of Electrical and Electronic Engineering, Imperial College London, London SW7 2AZ, UK; e.batzelis@imperial.ac.uk
[2] Power and Wide-Band-Gap Electronics Research Laboratory, École Polytechnique Fédérale de Lausanne, 1015 Lausanne, Switzerland; remco.vanerp@epfl.ch (R.v.E.); elison.matioli@epfl.ch (E.M.)
* Correspondence: g.kampitsis@imperial.ac.uk

Abstract: In this paper, a module-level photovoltaic (PV) architecture in parallel configuration is introduced for maximum power extraction, under partial shading (PS) conditions. For the first time, a non-regulated switched capacitor (SC) nX converter is a used at the PV-side conversion stage, whose purpose is just to multiply the PV voltage by a fixed ratio and accordingly reduce the input current. All the control functions, including the maximum power point tracking, are transferred to the grid-side inverter. The voltage-multiplied PV modules (VMPVs) are connected in parallel to a common DC-bus, which offers expandability to the system and eliminates the PS issues of a typical string architecture. The advantage of the proposed approach is that the PV-side converter is relieved of bulky capacitors, filters, controllers and voltage/current sensors, allowing for a more compact and efficient conversion stage, compared to conventional per-module systems, such as microinverters. The proposed configuration was initially simulated in a 5 kW residential PV system and compared against conventional PV arrangements. For the experimental validation, a 10X Gallium Nitride (GaN) converter prototype was developed with a flat conversion efficiency of 96.3% throughout the power range. This is particularly advantageous, given the power production variability of PV generators. Subsequently, the VMPV architecture was tested on a two-module 500 W_P prototype, exhibiting an excellent power extraction efficiency of over 99.7% under PS conditions and minimal DC-bus voltage variation of 3%, leading to a higher total system efficiency compared to most state-of-the-art configurations.

Keywords: gallium nitride; magnetic-free converters; module-level converters; parallel architecture; partial shading; photovoltaic systems; switched capacitor converters

Citation: Kampitsis, G.; Batzelis, E.; van Erp, R.; Matioli, E. Parallel PV Configuration with Magnetic-Free Switched Capacitor Module-Level Converters for Partial Shading Conditions. *Energies* **2021**, *14*, 456. https://doi.org/10.3390/en14020456

Received: 15 December 2020
Accepted: 11 January 2021
Published: 15 January 2021

Publisher's Note: MDPI stays neutral with regard to jurisdictional claims in published maps and institutional affiliations.

Copyright: © 2021 by the authors. Licensee MDPI, Basel, Switzerland. This article is an open access article distributed under the terms and conditions of the Creative Commons Attribution (CC BY) license (https://creativecommons.org/licenses/by/4.0/).

1. Introduction

Low-power residential rooftop and façade photovoltaic (PV) systems (in the range of a few kW) are expected to dominate in future distributed energy resources (DERs) and smart grid applications [1]. However, partial shading (PS) in such low-power PV systems, caused by moving clouds, neighboring buildings, trees and other objects, hinders their maximum energy production, especially in urban areas with low installation height [2,3]. In these conditions, the highly shaded panels are bypassed by the integrated antiparallel diodes that protect the panels against hotspot formation and degradation, as described in [4]. According to [5–7], PS is responsible for a reduction of the annual energy yield by 10–20% (depending on the installation type) in building-integrated PVs (BIPVs).

To increase the PV energy production under PS conditions, various software and hardware solutions have been proposed over recent decades. More specifically, building-integrated PV enhanced maximum power point tracking (MPPT) algorithms have been developed, such as particle swarm optimization [8] and artificial bee colony [9], which are

able to distinguish global from local optima of the P-V characteristic. Alternative software techniques presented in [10–12] propose power peak estimation through analytical PV models and parameter extraction via electrical measurements. Although economical and easily applicable, software solutions can only have a limited impact since the shaded modules will still be bypassed or will operate at sub-optimum power point.

On the contrary, hardware solutions can offer a significant improvement in PV generation during PS. Various PV array interconnection schemes have been proposed, namely total-cross-tied (TCT), bridge-link (BL) and honey-comb (HC), that reduce the PS losses in comparison to the conventional series-parallel (SP) architecture [11]. Other studies investigated the physical relocation of individual panels, for applications where the shading pattern is easily predictable [13], or real-time array rearrangement for addressing dynamic changes of the shading conditions [14,15]. These solutions exhibit better performance than the aforementioned static interconnection schemes but require a large number of switching devices and a complex network of voltage/current or irradiance sensors, while local optima will still exist in non-uniform insolation conditions.

The most effective hardware solution for PS loss mitigation relies on module-level power electronics (MLPEs), which aim to maximize the power yield of each individual panel through dedicated MPPT. In this field, micro-inverter topologies have proven commercially successful, since they offer the flexibility to connect any number of PV modules directly to the AC grid [16]. However, they exhibit low power density, due to the large component count and filter requirements imposed by the strict grid-interface regulation [17], and limited capability to provide ancillary services, which is a prerequisite for future DERs [18]. Another popular MLPE alternative uses PV power optimizers (PVPOs), which are buck-boost DC-DC converters, integrated with the solar panels of a typical string arrangement [19]. According to the study performed in [5], PVPOs have lower long-term efficiency compared to micro-inverters and reduced expandability, due to the minimum required string length [20]. The same limitations hold true for the distributed power processors [21] and voltage equalizers [22], that are connected between two panels in a string configuration.

To overcome the aforementioned limitations of the conventional MLPE approaches, an alternative promotes micro-converters that allow parallel connection of the PV modules in a single DC-bus, through high step-up DC-DC converters [23]. This solution aims to exploit the clear advantages of parallel configuration for addressing PS effects [24]. Converter topologies with a large voltage boost ratio have been proposed for the interface between the low-voltage PV module and the high-voltage DC-bus, including cascade boost [23], coupled inductors [25], switching capacitors [26] and combinations of the above [27–29]. However, these topologies are known to require complicated control algorithms [15] and, most importantly, employ electrolytic capacitors and magnetic components that limit the power density and the lifetime of the system, as found in [16,17]. They also exhibit a significant efficiency drop in low loading conditions, which is a drawback, given that a PV generator operates within 30–80% of its nominal power for 80% of the time [30].

Therefore, there is a clear need for a new MLPE system that addresses PS effects in rooftop PV systems and façade BIPVs, with a high boost ratio, high efficiency throughout the power range and simple structure and controllability. In this paper, we aim to satisfy these requirements by introducing a new PV architecture, based on the parallel connection of fixed-step, per-panel micro-converters. To the best of the authors' knowledge, it is the first time that a magnetic-free switched capacitor (SC) "*voltage amplifier*" has been used as a front-end conversion stage of a parallel PV configuration. It is a hybrid solution that combines the expandability of micro-inverters and the control simplicity of a single-stage grid-side inverter. The new approach exhibits (a) a high conversion efficiency of 96.3% even at low loading, (b) an excellent extraction efficiency of 99.7% under severe partial shading, (c) a high power density due to the omission of magnetic components and electrolytic capacitors and (d) limited DC-bus voltage variation with the operating conditions.

The operating principles of the novel PV architecture are explained in Section 2, followed by simulation results on a 5 kW grid-connected residential PV system in Section 3. The design, development and experimental validation of a 500 W prototype are presented in Section 4. The main conclusions of this work are summarized in Section 5.

2. Proposed Module-Level PV Architecture

The foundation of the new approach relies on the combinations of a non-regulated high step-up micro-converter with each PV panel, to form a high-voltage/low-current building block. All the voltage-multiplied PV (VMPV) modules are connected in parallel at the input of the grid-side inverter, which simultaneously regulates the operating point of all PV panels with a central MPPT. A simplified block diagram of the proposed VMPV architecture against the centralized and conventional MLPE configurations, such as microinverters and PVPOs, is presented in Figure 1a. For every architecture, the converter responsible for the MPPT is highlighted with a yellow background. This reveals a unique feature of the proposed system: that the MPPT is not performed by the DC-side converter, but is shifted to the grid-side inverter, as will be explained in Section 2.2. The schematic of the SC converter, which will be described in detail in the following subsection, is shown in Figure 1b.

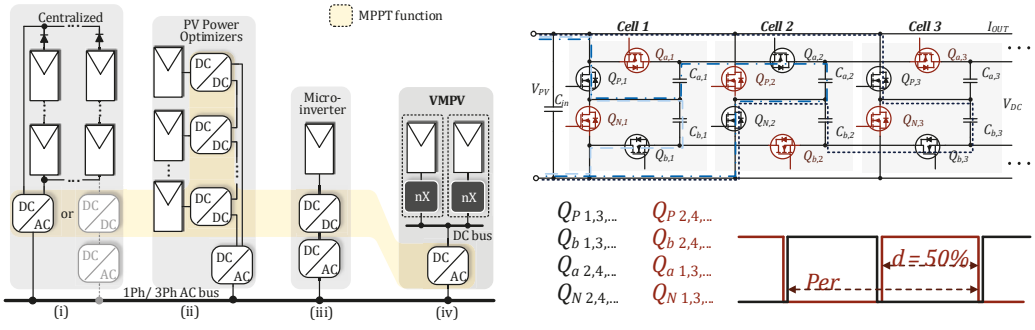

(**a**) (**b**)

Figure 1. (**a**) PV architectures, including (**i**) central inverter, (**ii**) PVPOs (**iii**) micro-inverters and (**iv**) the proposed VMPV architecture. (**b**) Schematic diagram of the magnetic-free SC voltage amplifier.

The effect of the PV module voltage amplification can be viewed as "*stretching*" the output I-V characteristic to higher voltages and lower currents, while keeping the produced power constant, as shown in Figure 2. The multiplication factor, n, should be higher than the V_{DC}/V_{MP} ratio, where V_{DC} is the required DC-link voltage for grid integration (e.g., 400 V) and V_{MP} is the nominal PV panel voltage at MPP (e.g., 40 V). Each module contributes additively to the total system output by injecting the power that corresponds to the common DC-voltage, i.e., $P_{PV\text{-}j}(V_{PV\text{-}j} = V_{DC}/n)$, where $P_{PV\text{-}j}$ and $V_{PV\text{-}j}$ are the output power and voltage, respectively, of the j panel.

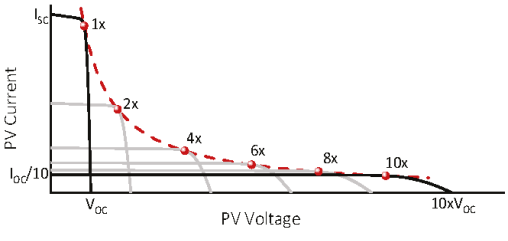

Figure 2. Modified I-V characteristic at the output of the voltage-multiplied PV module.

The operating principles of the two stages are presented in the following subsections, along with a short discussion on the advantageous features of the new layout.

2.1. PV-Side Voltage Multiplier

The voltage amplification function can theoretically be performed by any topology from the high step-up converter family mentioned in the Introduction. However, these solutions would add unnecessary complexity to the system and increase its size and weight, given that no voltage regulation is required. As an alternative, we propose the use of the nX converter, first introduced in [31], which combines high power density with high conversion efficiency and a fixed voltage ratio. This feature come with the omission of all magnetic components and the modular structure. The fixed boost ratio is not a limitation for this application, given the inherently small voltage variation of the MPP with the environmental conditions, as will be shown in the simulation and experimental results.

An example of a six-times boost nX converter ($n = 6$) is depicted in Figure 1b. The power devices constituting the nX converter can be grouped in two sets: the Q_P and Q_N that are always connected to the input and form a bridge leg configuration, and the ones at the top and bottom rail, Q_a and Q_b, that form a series connection between the different cells. The transistors are driven by a complementary switching pattern with a fixed 50% duty cycle, as indicated in Figure 1b, corresponding to the two operating modes: transistors in black conduct in the first operating mode, while the ones depicted in red conduct in the second operating mode. The same pattern holds for any number of cells.

The different current paths during the first operating mode are indicated with blue lines in Figure 1b. More specifically, when transistors $Q_{P\ 1,3}$, $Q_{b\ 1,3}$, $Q_{N\ 2}$ and $Q_{a\ 2}$ are conducting, three current paths are formed simultaneously:

1. the input voltage source is directly connected across C_{b1} (dashed blue line),
2. the source is connected in series with C_{a1} to charge capacitor C_{a2} (dash–dot blue line), and
3. the source is connected in series with C_{b2} to charge capacitor C_{b3} (dotted blue line).

In general, the output capacitors of each cell, $C_{a(i)}$ and $C_{b(i)}$, are charged by connecting the capacitor of the previous cell $(i - 1)$ in series with the input voltage, V_{PV}, as described in (1).

$$V_C(i) = V_C(i - 1) + V_{PV}, \qquad 1 < i \leq n/2 \tag{1}$$

Applying (1) to successive cells, the voltage stress across the top and bottom rail power devices can be deduced and is equal to $2{\cdot}V_{PV}$. The only exception to this rule holds for the first cell, in which $V_{DS\text{-}a,b}(1) = V_{PV}$. On the other hand, transistors Q_P and Q_N are always connected to the input power source, hence $V_{DS\text{-}P,N}(\mathrm{i}) = V_{PV}$. Provided that the current flowing through each path is equal to the output current, I_{OUT}, it can be easily observed that the current stress of the top and bottom rail transistors is $I_{D\text{-}a,b}(i) = I_{OUT} = I_{PV}/n$ and for transistors Q_P and Q_N it is $I_{D\text{-}P,N}(i) = 2{\cdot}I_{OUT} = 2{\cdot}I_{PV}/n$. An exception to this rule is the last cell, where $I_{D\text{-}P,N}(n/2) = I_{OUT}$. These equations give an indication of the devices' stress and help select the components for the experimental validation in Section 4.1.

An advantage of the nX converter topology is that there is no need for a feedback control loop and, thus, no requirements for voltage/current sensors, micro-controllers and communication links. Additionally, the simplicity of the pulse width modulation (PWM) strategy allows for a cost-effective PWM integrated circuit (IC) generator, as opposed to a costly microprocessor. Further, the converter inherently operates under soft switching conditions, resulting in low switching losses, as explained in [32,33].

In its current form, the presented nX converter has a high transistor count ($2{\cdot}n$). However, state-of-the-art Gallium Nitride (GaN) technology offers a unique potential for the monolithic integration of multiple devices on a single power chip [34]. In addition to that, the high switching frequency capability of the high electron mobility transistors (HEMTs) allows for the replacement of electrolytic capacitors, which is the most common point of failure [16,17], with robust and efficient ceramic capacitors. This technology migration improves the lifetime of the micro-converter to match that of the solar panels (more than

25 years), an important requirement for rooftop and BIPV systems. The small footprint and low driving requirements of GaN devices further contribute to the miniaturization of the micro-converter, as presented in [35].

By adopting the GaN transistor technology in a magnetic-free converter topology, an ideal platform for future VMPV modules can be developed.

2.2. Grid-Side Inverter

Regulation of the operating point of a PV module, string or system is traditionally performed by the front-end converter, as indicated by the highlighted area in Figure 1a. In this study, the fixed voltage ratio at the PV-side requires that the MPPT function is performed by the grid-side inverter, much like a single-stage system. Therefore, although the proposed topology is fundamentally a two-stage system, it operates like a single-stage centralized system in terms of MPPT function, but with higher MPP tracking efficiency. Specifically, the merits of this new architecture are:

1. The entire PV system always has a single MPP, even under mismatched irradiance and temperature conditions, due to the parallel connection of the VMPVs. As a result, no PV module is bypassed and the MPP is always successfully tracked, as opposed to the multi-peak P-V curves in centralized architectures, leading to almost 100% power extraction efficiency under any partial shading conditions.
2. The DC-link voltage variation is limited due to the inherently small deviation of V_{MP} with the environmental conditions. This makes it easy for the inverter to extract the maximum power while meeting the input voltage requirements, in contrast to single-stage systems under PS.
3. Having a single grid-side inverter permits the implementation of sophisticated control functions, such as ancillary services to the grid (e.g., fault ride through, reactive power injection, frequency regulation), as opposed to the micro-inverters that cannot afford such complexity.

3. Modeling and Simulation

In this section, the power extraction efficiency of the proposed architecture under PS conditions is assessed against conventional PV configurations, through simulations in Matlab/Simulink. First, it is important to define the total system efficiency, η_{sys}, as the product of conversion efficiency, η_c, and extraction efficiency, η_{ext} (also found in the literature as tracking or MPPT efficiency):

$$\eta_{sys} = \eta_c \cdot \eta_{ext}. \tag{2}$$

$$\eta_{ext} = P_{PV}/P_{TOT} = P_{PV}/\left(\Sigma_1^N P_{MPj}\right) \tag{3}$$

η_c represents the hardware's efficiency to convert the power from the PV-side to the grid-side and will be discussed in Section 4. η_{ext} is given as the ratio of the average output power of the PV system, P_{PV}, to the total available power from all individual modules, P_{TOT}, as shown in (3), for N panels. This efficiency factor represents the ability of the architecture to extract as much of the available power as possible, regardless of the converters/electronics used. The reduction of η_{ext} is usually attributed to three factors: (a) shaded modules operating at a sub-optimal operating point or completely bypassed, (b) MPPT locked on a local maximum and (c) MPPT oscillating around the normal operating point. For a fair comparison of the VMPV with other conventional architectures, only component (a) of η_{ext} should be considered. Thus, for the rest of the paper, it is assumed that the MPPT algorithm can always find the global maximum, even in the case of multiple power peaks at PS, with negligible oscillation around the MPP.

To extract η_{ext} for any PV configuration in real time, the PV model described in [10] is used, that expresses the module voltage and current in explicit form.

3.1. PV Generator Configuration Comparison

The focus of this sub-section is to study the extraction efficiency of the parallel-connected VMPV architecture under PS conditions against the conventional SP and TCT interconnection schemes, the TCT configuration with dynamic rearrangement capability [14] and the ideal MLPE architecture. A 5 kW_P residential (rooftop or façade) PV system of 20 panels is considered. Each PV module consists of 72 cells and has V_{OC}(STC) = 53 V and V_{MP}(STC) = 44.3 V, to match the characteristics of the commercial VBHN245SJ25 panel. A 10X step-up conversion ratio for the VMPV architecture is adequate for integration to the single-phase grid.

Two realistic shading patterns are examined, inspired by [14] and depicted in Figure 3. Solid lines show the SP configuration and dashed lines represent the TCT interconnection scheme.

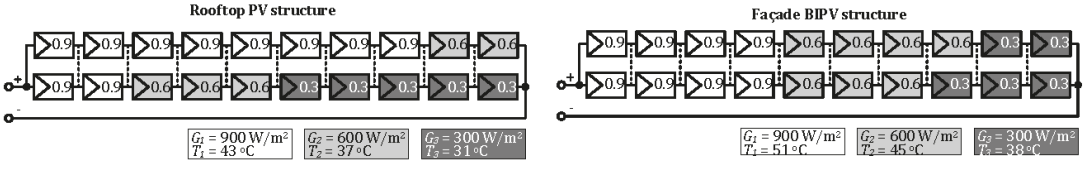

Figure 3. Indicative PS scenarios. (**a**) Long–narrow shading pattern A and (**b**) short–wide shading pattern B.

3.1.1. Shading Pattern A: Long–Narrow

In this case, the shadow covers the majority of one string of a rooftop PV structure, giving rise to three irradiance intensity levels, G_1 = 900 W/m^2, G_2 = 600 W/m^2 and G_3 = 300 W/m^2, as shown in Figure 3a. An ambient temperature of 20 °C and wind speed of 1 m/s are considered, according to the international standard IEC-61215. The nominal operation cell temperature (NOCT) has been extracted from [36], considering both the photoelectrical and photothermal conversion effect, and is included in Figure 3. Solid lines show the SP configuration and dashed lines represent the TCT interconnection scheme.

The simulation results for this case study are presented in Figure 4. The gray dashed line in Figure 4b corresponds to the total PV system available power, P_{TOT}, calculated by adding the maximum available power of all modules, P_{MPj}, j = 1, . . . , 20, as in (4) and (5) for the shading patterns A and B, respectively. P_{TOT} is used as a benchmark in the architecture comparison.

$$P_{TOT-A} = \Sigma_1^{20} P_{MPj} = 10 \cdot P_{MP(0.9)} + 5 \cdot P_{MP(0.6)} + 5 \cdot P_{MP(0.3)} = 3.17 \text{ kW} \quad (4)$$

$$P_{TOT-B} = \Sigma_1^{20} P_{MPj} = 8 \cdot P_{MP(0.9)} + 7 \cdot P_{MP(0.6)} + 5 \cdot P_{MP(0.3)} = 3.04 \text{ kW} \quad (5)$$

It is evident that both SP and TCT configurations exhibit poor extraction efficiencies of 73.59% and 74.94%, respectively, due to the bypassing of the shaded modules. On the other hand, the dynamic rearrangement of the panels significantly improves the efficiency to 93.12% and reduces the number of local maxima to two. However, it is the proposed VMPV architecture that achieves the best extraction efficiency of 99.86% with just a single global MPP.

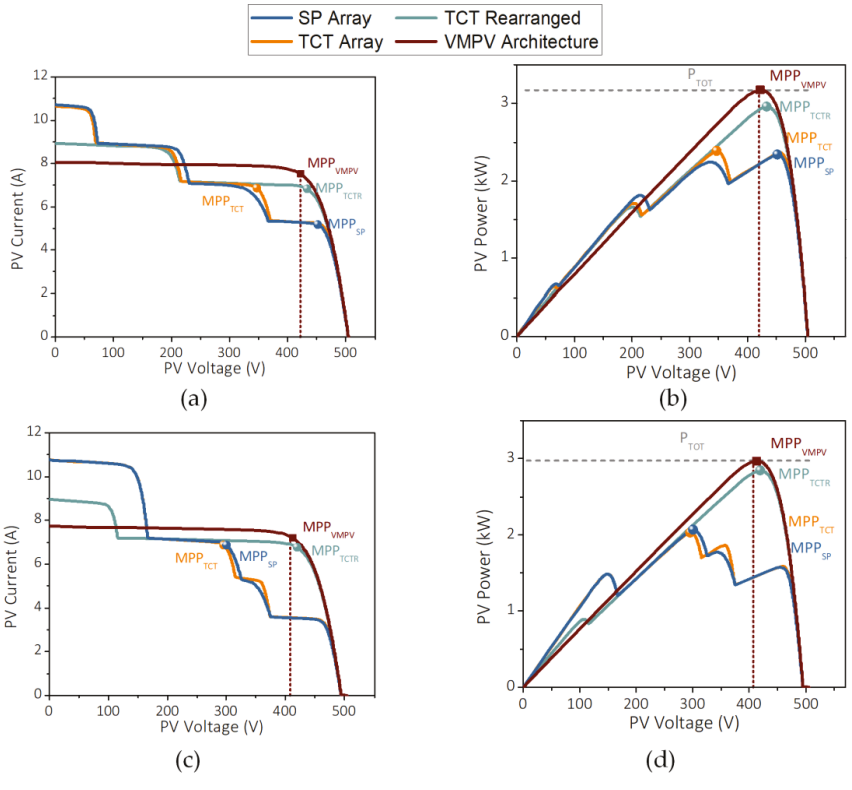

Figure 4. I-V and P-V curves of the examined PV architectures under (**a**,**b**) the shading pattern A and (**c**,**d**) the shading pattern B.

3.1.2. Shading Pattern B: Short–Wide

This scenario concerns a façade PV system, partially shaded by the pattern illustrated in Figure 3b. In contrast to an open rack rooftop structure, the BIPVs are characterized by a higher temperature (included in Figure 3b), since only one side of the panel is in contact with the air. The output I-V and P-V characteristics for the shading pattern B are presented in Figure 4c,d. Even under these highly non-uniform irradiance and temperature conditions, the VMPV architecture still exhibits a near-perfect efficiency of 99.8%. As a comparison, the SP and TCT interconnection schemes have η_{ext}(SP) = 69.4% and η_{ext}(TCT) = 68.3%, respectively, while the electrically rearranged TCT array has η_{ext}(TCTR) = 95.5%.

3.2. Grid-Connected VMPV System

To evaluate the time response of the whole system under variation of the atmospheric conditions, the proposed PV architecture is connected to a single-phase grid-side inverter. Two scenarios are simulated, where the PV structure is initially uniformly insolated (G_1 = 900 W/m^2) and gradually shaded to match shading pattern A or shading pattern B. A linear drop of the irradiance is considered (see Figure 5), at a rate of 25 W/m^2 per second, which is a representative value for rapidly changing environmental conditions [18]. The temperature variation of the individual PV groups is shown in Figure 5b, for both investigated shading patterns A (continuous lines) and B (dashed lines).

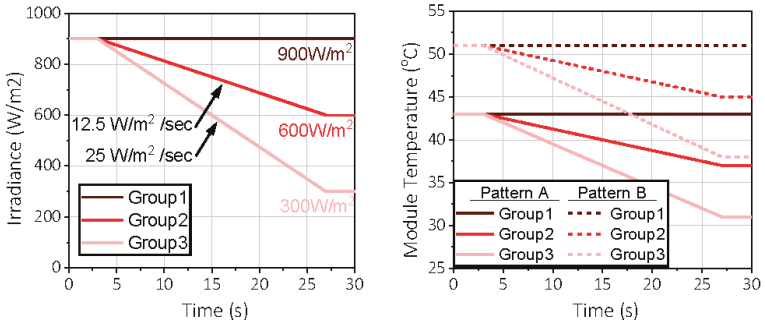

(**a**) (**b**)

Figure 5. (**a**) Irradiance and (**b**) temperature variation with time for the three PV groups of the VMPV architecture.

The inverter control is structured in three nested control loops, as outlined in Figure 6, [37]. The outer control loop is a perturb and observe (P&O) MPPT that is applied at the common high-voltage DC-bus and produces the reference DC-voltage, V_{DC}*. In the middle control loop, a PI controller regulates the active and reactive power reference to be injected to the grid, P* and Q*, respectively. A proportional resonant (PR) current controller is implemented in the inner control loop and the grid frequency is extracted by a second-order generalized integrator phase locked loop (SOGI-PLL).

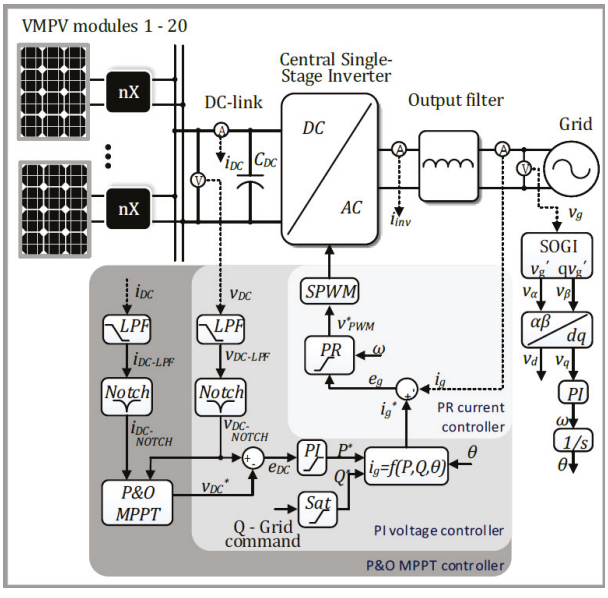

Figure 6. Complete control scheme of the proposed grid-connected PV system, consisting of three nested control loops.

Figure 7a shows the active power fed to the grid, P_{OUT}, with respect to the total available PV power, P_{TOT}. The new VMPV architecture follows closely the benchmark curve, even when all the shaded panels have reached their steady state conditions (Time > 27 s). For comparison purposes, the output power of the conventional SP interconnection is also included in the same figure. Notably, the DC-link voltage variation is limited to a range of

just 4 V (from 420 V to 424 V) in the VMPV case, as can be seen in Figure 7b, despite the significant variation of the produced power. In contrast, the voltage variation of the SP configuration is 33 V for the same shading pattern.

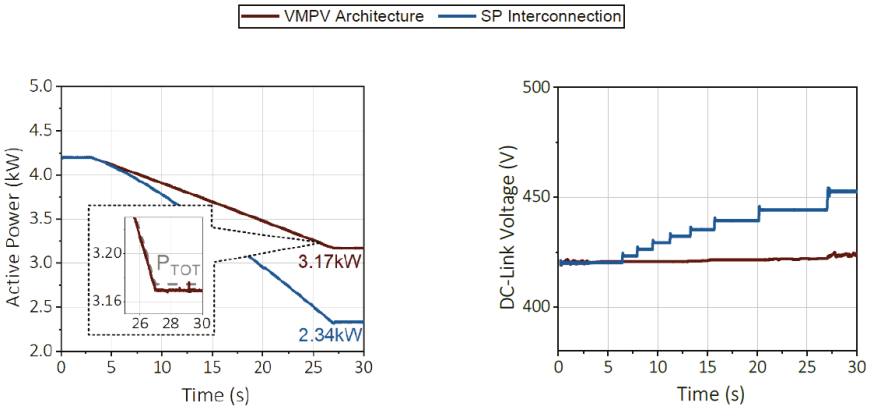

Figure 7. (**a**) Active power fed to the grid and (**b**) DC-bus voltage variation with time for the proposed VMPV under shading pattern A.

Similarly, Figure 8 shows the power and voltage variation of the proposed VMPV and standard SP architectures when the shading evolves towards shading pattern B. This scenario better highlights the merits of a single MPP in the proposed parallel connection against the multiple peak formation in conventional SP configurations and the challenges in identifying the global one. Even if a sophisticated MPPT algorithm is employed that always converges to the global MPP (yellow dashed curves), the respective DC-link voltage (300 V in Figure 8b) may be outside the inverter limits, thus not allowing operation at the MPP, leading to even lower extraction efficiency.

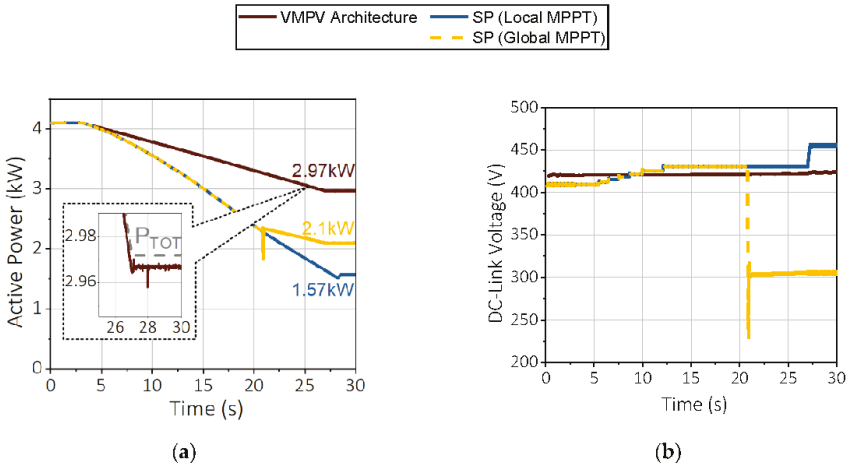

Figure 8. (**a**) Active power fed to the grid and (**b**) DC-bus voltage variation with time for the proposed VMPV under shading pattern B.

The simulation results show that the proposed VMPV architecture combines the best of MLPE and centralized topologies: it yields near-optimal power extraction (like MLPE, in contrast to centralized) while allowing for sophisticated control functions in the inverter (like centralized, as opposed to micro-inverters).

4. Experimental Validation

In this section, the favorable operation of the VMPV architecture under uniform and PS conditions is experimentally validated and compared to a conventional string configuration.

4.1. Experimental Setup

Two 245 W_P PV modules of the same type, VBHN245SJ25, are used as inputs to two nX converters that are connected in parallel at the high-voltage side, as depicted in Figure 9. Throughout the experiment, both PV panels are placed close to each other on a structure of fixed inclination with respect to the horizon. Semi-transparent fabric is used to cover one PV module completely and uniformly to emulate PS conditions.

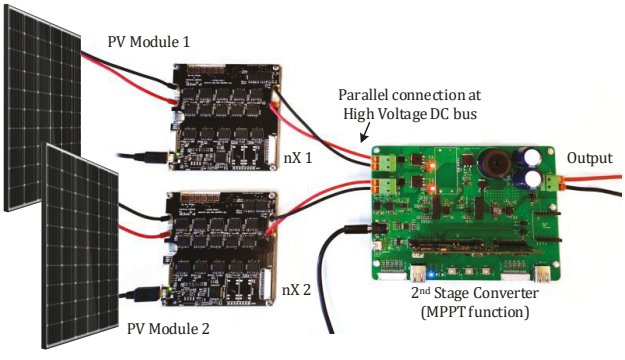

Figure 9. Experimental setup consisting of two VMPV modules.

The objective of these experiments is to study the first stage of the system independently from the topology of the second stage. To this end, a DC-DC converter that performs all control functions, including scanning of the PV curves and MPPT, feeding a resistive load, was used as a simple substitute of the grid-tied inverter. This setup allows for safe and repetitive testing of the new architecture, while the results are also valid for the grid-connected system. The switching frequency of the buck converter was set to 20 kHz and the MPPT period to 250 ms. All voltage and current measurements were continuously monitored with a sampling rate of 4 k samples/s and then filtered via a digital low-pass filter (LPF) with a cutoff frequency of 100 Hz to reject the switching noise. The key components and parameters of the experimental setup are summarized in Table 1.

4.2. PV-Side nX Converter

The backbone of the new architecture is the GaN-based magnetic-free nX converter, depicted in Figure 10. It has a 10-times step-up ratio to match the simulation conditions in Section 3. The developed prototype consists of two separate printed circuit boards (PCBs): the drive board, shown in Figure 10a, and the power board, in Figure 10b. One side of the power PCB is reserved only for the GaN HEMTs, a design aspect that provides flexibility to mount the board on any flat surface, such as a heat sink or the backside of the PV panel. Four parallel-connected multilayer ceramic capacitors (MLCCs) of 2.2 μF each, with low internal series resistance (ESR), constitute the output capacitance of each cell.

Table 1. List of components of the experimental setup.

Component	Parameter	Value
PV modules	Part Type	VBHN245SJ25
	V_{MP}	44.3 V
	I_{MP}	5.53 A
	V_{OC}	53 V
	I_{SC}	5.86 A
Module-level nX converter	Transistors in $Q_{P/N}$ position	GS61008T
	Transistors in $Q_{a/b}$ position	GS66508T
	Switching capacitors	4 × 2.2 µF, X6S
	Gate driver	LM5114
	Digital/Power isolator	ISOW7842F
2nd-stage DC-DC converter	Series diodes	S10KC
	$L_{DC\text{-}DC}$	1.5 mH
	$C_{DC\text{-}DC}$	50 µF
	Transistor	IPB65R190CFD
	Switching diode	C3D08065E
	Micro-controller	TMS320F28379D
	Switching frequency ($F_{SW\text{-}B}$)	20 kHz
	MPPT period (T_{MPPT})	250 ms
	Voltage/Current sampling rate	4 k samples/s
	LPF cutoff frequency (F_0)	100 Hz
Output Resistor	R_{out}	0–240 Ω

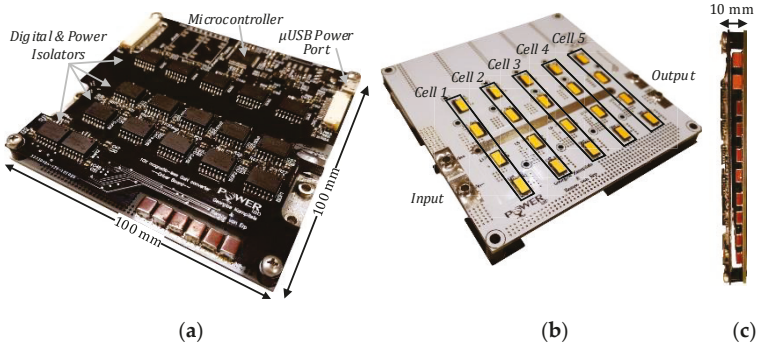

Figure 10. (**a**) Front side—drive board, (**b**) back side—power board and (**c**) side view of the magnetic-free nX converter prototype.

The switching frequency is tuned to match the circuit resonant frequency, $F_{SW\text{-}nX}$ = 200 kHz, to achieve zero current switching (ZCS) operation and, thus, minimize the switching losses. The entire converter occupies just 100 mL of volume (100 mm × 100 mm × 10 mm) and has a fixed conversion efficiency of 96.3%, throughout the power range, as shown in Figure 11a. This is a strong point of this converter that ensures a high energy yield, even under low irradiance conditions. In contrast, other high step-up micro-converters exhibit efficiencies that peak from 94–98% [25,27,29], but drop significantly (below 90%) in low loading conditions, due to higher switching losses from entering discontinuous conduction mode or exiting the soft switching window. On the other hand, the magnetic-free nX converter is always operating at a fixed 50% duty cycle, and is inherently operating under soft switching, as explained in [32]. Please note that the calculated conversion efficiency does not account for any losses from the grid-side inverter or the output filter, which is expected to introduce a non-linearity to the total system efficiency curve at light loads. It should be mentioned

that the conversion efficiency can be further improved by choosing GaN HEMTs with even lower on-resistance and faster switching transients.

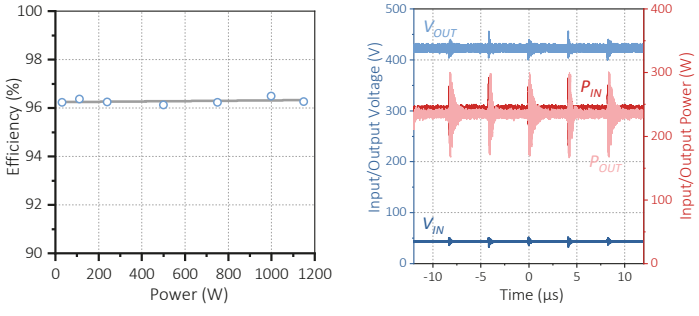

(**a**) (**b**)

Figure 11. Experimental results of the developed 10X converter. (**a**) Efficiency curve over operating power and (**b**) voltage and power waveforms during operation at 250 W.

Voltage and power waveforms of the system operating at 250 W are illustrated in Figure 11b. Under these conditions, the temperature increase in the transistors was maintained below 15 °C, avoiding the use of bulky heat sinks. More design details and considerations regarding the component selection and test conditions can be found in [35]. The high power density (greater than 11 kW/l) and the low cooling requirements are both key factors that enable the integration of the nX converter with the solar panel.

4.3. Output Characteristics of the VMPV System

The I-V and P-V characteristics of the proposed PV system were recorded in two shading patterns: (A) uniform irradiance and temperature conditions and (B) partial shading, where one panel is uniformly shaded while the other one remains unshaded. The curves are captured by slowly changing the operating point within 5 s (scanning), which guarantees that the measurements are not affected by transient phenomena attributed to the second-stage inductance and output capacitance.

Figure 12a,b show the characteristic curves of the two individual PV modules (dashed and dash–dot lines) and the combined curve of the proposed VMPV architecture (solid red line), under uniform irradiance and temperature conditions. It should be noted that, although the parallel connection takes place at the high-voltage side of the nX converters, the I-V and P-V characteristics are translated to the PV-side for consistency with the string topology (blue line).

As shown in Table 2, the two modules are not identical and their MPPs differ by 3.4 W and are spaced by 1.17 V. However, the power loss of the VMPV approach is just 0.4 W, resulting in an excellent extraction efficiency of 99.9%. In fact, both modules operate at 99.9% of their respective MPPs. In this scenario, the string arrangement also has near-perfect extraction efficiency but no conversion losses. It should be noted that the total available PV power $P_{TOT} = P_{MP1} + P_{MP2}$ and the actual extracted power P_{PV} are measured in successive experiments within a short time duration to ensure equal irradiance and temperature conditions; it is impossible to measure the maximum available power of the individual modules when they form a PV string that operates at a different operating point.

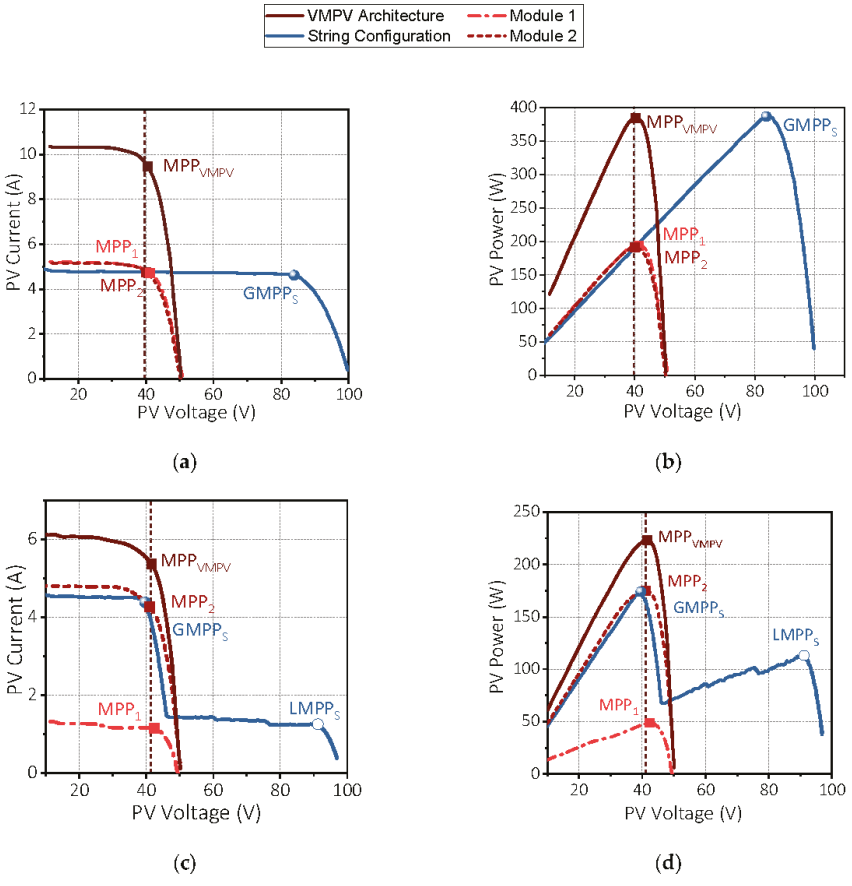

Figure 12. Experimentally extracted I-V and P-V characteristics of the PV modules under (**a**,**b**) the shading pattern A: uniform irradiance and (**c**,**d**) the shading pattern B: PS conditions.

Table 2. MPP data from the experimentally extracted characteristics.

Test Conditions	PV Module/PV System	V_{PV} (V)	I_{PV} (A)	P_{PV} (W)	Extraction eff. (%)
Pattern A: Uniform Conditions	Module 1 (MPP_1)	41.25	4.705	194.1	-
	Module 2 (MPP_2)	40.08	4.757	190.7	-
	VMPV Architecture (MPP_{VMPV})	40.52	9.475	384.4	99.9
	Module 1 (@MPP_{VMPV})	40.52	4.785	193.9	99.9
	Module 2 (@MPP_{VMPV})	40.52	4.702	190.5	99.9
Pattern B: PS Conditions	Module 1 (MPP_1)	42.5	1.145	48.7	-
	Module 2 (MPP_2)	41.05	4.26	174.9	-
	VMPV Architecture (MPP_{VMPV})	41.6	5.36	223	99.74
	Module 1 (@MPP_{VMPV})	41.6	1.161	48.3	99.18
	Module 2 (@MPP_{VMPV})	41.6	4.20	174.7	99.89
	Series Connection ($GMPP_S$)	39.65	4.38	174	77.8
	Series Connection ($LMPP_S$)	91.3	1.255	113	50.5

Figure 12c,d show the experimentally extracted I-V and P-V traces under the shading pattern B: Module 1 is entirely shaded, while Module 2 remains unshaded. Although

$P_{PV}(\mathrm{MPP}_1)$ = 48.7 W is more than 3.5 times smaller than $P_{PV}(\mathrm{MPP}_2)$ = 174.9 W, their respective voltage difference is just 1.45 V, leading to an almost perfect η_{ext} = 99.74% for the VMPV system. Taking the effect of η_c into account, the total system efficiency is η_{sys} = 96.05%. On the other hand, the global MPP of the series connection is $P_{PV}(\mathrm{GMPP_S})$ = 174 W, equal to MPP_2 minus the power dissipated at the bypass diode of Module 1, resulting in an extraction efficiency of just 77.8%. Still, it is highly possible that a simple MPPT algorithm would converge at a local MPP (LMPP), in which case half of the PV power would be lost ($\eta_{ext}(\mathrm{LMPP_S})$ = 50.5%).

4.4. Real-Time MPPT of the VMPV Architecture

For this experiment, a P&O algorithm was executed by the second-stage converter, with a period of 250 ms and an MPPT duty cycle step of 1%. The two PV modules were subjected to the two shading patterns of the previous subsection (uniform and PS conditions).

Figure 13 shows the output power and DC-bus voltage variation under real-time tracking of the MPP. The MPPT algorithm always converges to the single MPP, guaranteeing near-perfect extraction efficiency in any conditions and effectively addressing the tracking challenges of SP configurations. In addition, the DC-link voltage is insignificantly affected by PS (only a 3% deviation), which allows for a narrow predetermined input voltage range for the grid-side inverter, in contrast to the single-stage PV systems.

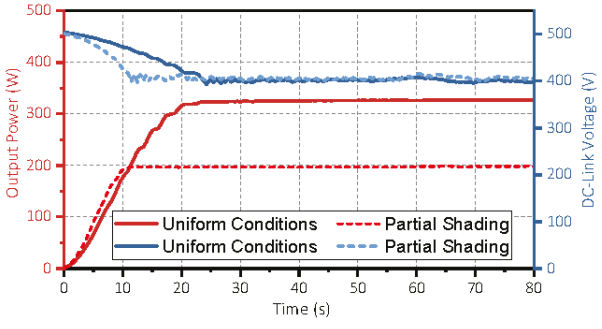

Figure 13. Response of the new VMPV architecture during real-time MPPT, under uniform and PS conditions. Output power (in red) and DC-bus voltage (in blue) variation with time.

The experimental results show that the proposed VMPV architecture combines the near-perfect extraction efficiency of MLPE with a flat conversion efficiency in any conditions; this leads to a higher total system efficiency than most state-of-the-art configurations, including other MLPE architectures.

5. Conclusions

In this paper, a new highly efficient architecture for residential grid-connected PV systems has been demonstrated and experimentally verified. The PV modules are connected in parallel through fixed-step high step-up nX converters (voltage multipliers), thus eliminating the partial shading challenges of typical series connections and delivering almost 100% extraction efficiency. At the same time, the nX converter features a high flat conversion efficiency of more than 96.3% irrespective of the power level, leading to better total system efficiency at partial shading than most centralized and distributed PV architectures.

The developed magnetic-free nX converters use GaN HEMTs that are switching at high frequency which, in turn, allow for longer lifetime ceramic capacitors in place of the conventional bulky electrolytic capacitors. This, along with the omissions of all magnetic components and the low cooling requirements, lead to a very compact solution that can be integrated with the backside of the PV panel, forming a new voltage-multiplied PV module.

All control functions, including MPPT, are transferred to the inverter, simplifying the DC-DC micro-converter requirements for micro-controllers and voltage/current sensors. The high-voltage parallel connection results in a small variation of the DC-link voltage with the environmental conditions which, in turn, simplifies the requirements for the grid-side inverter, as in two-stage string inverters.

Author Contributions: Conceptualization, G.K. and E.B.; methodology and investigation, G.K.; experimental validation, G.K. and R.v.E.; writing—original draft preparation, G.K.; writing—review and editing, E.B., R.v.E. and E.M.; project administration, supervision and funding acquisition, E.M. All authors have read and agreed to the published version of the manuscript.

Funding: This research was funded by the Swiss Office of Energy, Grant No. SI501568-01, the European Research Council under the European Union's H2020 program/ERC Grant Agreement No. 679425 and the Royal Academy of Engineering under the Engineering for Development Research Fellowship scheme, Grant No. RF\201819\18\86.

Institutional Review Board Statement: Not applicable.

Informed Consent Statement: Not applicable.

Data Availability Statement: No new data were created or analyzed in this study. Data sharing is not applicable to this article.

Conflicts of Interest: The authors declare no conflict of interest.

Abbreviations

BIPV	Building-integrated photovoltaic
BL	Bridge-link interconnection scheme
DER	Distributed energy resources
ESR	Capacitor's internal series resistance
GMPP	Global maximum power point
HC	Honey-comb interconnection scheme
HEMT	High electron mobility transistor
IC	Integrated circuit
LMPP	Local maximum power point
LPF	Low-pass filter
MLCC	Multi-layer ceramic capacitors
MLPE	Module-level power electronics
MPPT	Maximum power point
NOCT	Nominal operation cell temperature
P&O	Perturb and observe algorithm
PCB	Printed circuit board
PLL	Phase locked loop
PR	Proportional resonant controller
PS	Partial shading
PV	Photovoltaic
PVPO	Photovoltaic power optimizer
PWM	Pulse width modulation
SC	Switched capacitor
SOGI	Second order generalized integrator
SP	Series-parallel interconnection scheme
STC	Standard test conditions
TCT	Total-cross-tied interconnection scheme
TCTR	Electrically rearranged TCT array
VMPV	Voltage-multiplied photovoltaic system
ZCS	Zero current switching

References

1. Eftekharnejad, S.; Vittal, V.; Heydt, G.T.; Keel, B.; Loehr, J. Impact of Increased Penetration of Photovoltaic Generation on Power Systems. *IEEE Trans. Power Syst.* **2013**, *28*, 893–901. [CrossRef]
2. Batzelis, E.I.; Georgilakis, P.S.; Papathanassiou, S.A. Energy Models for Photovoltaic Systems under Partial Shading Conditions: A Comprehensive Review. *IET Renew. Power Gener.* **2015**, *9*, 340–349. [CrossRef]
3. Atmaja, T.D. Façade and Rooftop PV Installation Strategy for Building Integrated Photo Voltaic Application. *Energy Procedia* **2013**, *32*, 105–114. [CrossRef]
4. Karatepe, E.; Boztepe, M.; Çolak, M. Development of a Suitable Model for Characterizing Photovoltaic Arrays with Shaded Solar Cells. *Solar Energy* **2007**, *81*, 977–992. [CrossRef]
5. Strache, S.; Wunderlich, R.; Heinen, S. A Comprehensive, Quantitative Comparison of Inverter Architectures for Various PV Systems, PV Cells, and Irradiance Profiles. *IEEE Trans. Sustain. Energy* **2014**, *5*, 813–822. [CrossRef]
6. Hanson, A.J.; Deline, C.A.; MacAlpine, S.M.; Stauth, J.T.; Sullivan, C.R. Partial-Shading Assessment of Photovoltaic Installations via Module-Level Monitoring. *IEEE J. Photovolt.* **2014**, *4*, 1618–1624. [CrossRef]
7. Drif, M.; Pérez, P.J.; Aguilera, J.; Aguilar, J.D. A New Estimation Method of Irradiance on a Partially Shaded PV Generator in Grid-Connected Photovoltaic Systems. *Renew. Energy* **2008**, *33*, 2048–2056. [CrossRef]
8. Li, H.; Yang, D.; Su, W.; Lu, J.; Yu, X. An Overall Distribution Particle Swarm Optimization MPPT Algorithm for Photovoltaic System Under Partial Shading. *IEEE Trans. Ind. Electron.* **2019**, *66*, 265–275. [CrossRef]
9. Sundareswaran, K.; Sankar, P.; Nayak, P.S.R.; Simon, S.P.; Palani, S. Enhanced Energy Output From a PV System Under Partial Shaded Conditions Through Artificial Bee Colony. *IEEE Trans. Sustain. Energy* **2015**, *6*, 198–209. [CrossRef]
10. Batzelis, E.I.; Kampitsis, G.E.; Papathanassiou, S.A.; Manias, S.N. Direct MPP Calculation in Terms of the Single-Diode PV Model Parameters. *IEEE Trans. Energy Convers.* **2015**, *30*, 226–236. [CrossRef]
11. Moballegh, S.; Jiang, J. Modeling, Prediction, and Experimental Validations of Power Peaks of PV Arrays Under Partial Shading Conditions. *IEEE Trans. Sustain. Energy* **2014**, *5*, 293–300. [CrossRef]
12. Jeyaprabha, S.B.; Selvakumar, A.I. Model-Based MPPT for Shaded and Mismatched Modules of Photovoltaic Farm. *IEEE Trans. Sustain. Energy* **2017**, *8*, 1763–1771. [CrossRef]
13. Shams El-Dein, M.Z.; Kazerani, M.; Salama, M.M.A. An Optimal Total Cross Tied Interconnection for Reducing Mismatch Losses in Photovoltaic Arrays. *IEEE Trans. Sustain. Energy* **2013**, *4*, 99–107. [CrossRef]
14. Babu, T.S.; Ram, J.P.; Dragicevic, T.; Miyatake, M.; Blaabjerg, F.; Rajasekar, N. Particle Swarm Optimization Based Solar PV Array Reconfiguration of the Maximum Power Extraction Under Partial Shading Conditions. *IEEE Trans. Sustain. Energy* **2018**, *9*, 74–85. [CrossRef]
15. Shams El-Dein, M.Z.; Kazerani, M.; Salama, M.M.A. Optimal Photovoltaic Array Reconfiguration to Reduce Partial Shading Losses. *IEEE Trans. Sustain. Energy* **2013**, *4*, 145–153. [CrossRef]
16. Kjaer, S.B.; Pedersen, J.K.; Blaabjerg, F. A Review of Single-Phase Grid-Connected Inverters for Photovoltaic Modules. *IEEE Trans. Ind. Appl.* **2005**, *41*, 1292–1306. [CrossRef]
17. Meneses, D.; Blaabjerg, F.; García, Ó.; Cobos, J.A. Review and Comparison of Step-Up Transformerless Topologies for Photovoltaic AC-Module Application. *IEEE Trans. Power Electron.* **2013**, *28*, 2649–2663. [CrossRef]
18. Batzelis, E.I.; Kampitsis, G.E.; Papathanassiou, S.A. Power Reserves Control for PV Systems With Real-Time MPP Estimation via Curve Fitting. *IEEE Trans. Sustain. Energy* **2017**, *8*, 1269–1280. [CrossRef]
19. Chen, S.-M.; Liang, T.-J.; Hu, K.-R. Design, Analysis, and Implementation of Solar Power Optimizer for DC Distribution System. *IEEE Trans. Power Electron.* **2013**, *28*, 1764–1772. [CrossRef]
20. Vinnikov, D.; Chub, A.; Liivik, E.; Kosenko, R.; Korkh, O. Solar Optiverter—A Novel Hybrid Approach to the Photovoltaic Module Level Power Electronics. *IEEE Trans. Ind. Electron.* **2019**, *66*, 3869–3880. [CrossRef]
21. Stauth, J.T.; Seeman, M.D.; Kesarwani, K. Resonant Switched-Capacitor Converters for Sub-Module Distributed Photovoltaic Power Management. *IEEE Trans. Power Electron.* **2013**, *28*, 1189–1198. [CrossRef]
22. Tahmasbi-Fard, M.; Tarafdar-Hagh, M.; Pourpayam, S.; Haghrah, A.-A. A Voltage Equalizer Circuit to Reduce Partial Shading Effect in Photovoltaic String. *IEEE J. Photovolt.* **2018**, *8*, 1102–1109. [CrossRef]
23. Li, W.; He, X. Review of Nonisolated High-Step-Up DC/DC Converters in Photovoltaic Grid-Connected Applications. *IEEE Trans. Ind. Electron.* **2011**, *58*, 1239–1250. [CrossRef]
24. Gao, L.; Dougal, R.A.; Liu, S.; Iotova, A.P. Parallel-Connected Solar PV System to Address Partial and Rapidly Fluctuating Shadow Conditions. *IEEE Trans. Ind. Electron.* **2009**, *56*, 1548–1556. [CrossRef]
25. Tseng, K.-C.; Huang, C.-C.; Shih, W.-Y. A High Step-Up Converter With a Voltage Multiplier Module for a Photovoltaic System. *IEEE Trans. Power Electron.* **2013**, *28*, 3047–3057. [CrossRef]
26. Ahmed, M.E.; Mousa, M.; Orabi, M. Development of High Gain and Efficiency Photovoltaic System Using Multilevel Boost Converter Topology. In Proceedings of the IEEE 2nd International Symposium on Power Electronics for Distributed Generation Systems (PEDG), Hefei, China, 16–18 June 2010; pp. 898–903.
27. Molavi, N.; Farzanehfard, H.; Adib, E. Soft-Switched Non-Isolated High Step-up DC–DC Converter with Reduced Voltage Stress. *IET Power Electron.* **2016**, *9*, 1711–1718. [CrossRef]

28. Revathi, B.S.; Prabhakar, M. High Gain High Power DC-DC Converter for Photovoltaic Application. In Proceedings of the 2013 Annual International Conference on Emerging Research Areas and 2013 International Conference on Microelectronics, Communications and Renewable Energy, Kanjirapally, India, 4–6 June 2013; pp. 1–6.
29. Gu, B.; Dominic, J.; Lai, J.-S.; Zhao, Z.; Liu, C. High Boost Ratio Hybrid Transformer DC–DC Converter for Photovoltaic Module Applications. *IEEE Trans. Power Electron.* **2013**, *28*, 2048–2058. [CrossRef]
30. Nanakos, A.C.; Christidis, G.C.; Tatakis, E.C. Weighted Efficiency Optimization of Flyback Microinverter Under Improved Boundary Conduction Mode (i-BCM). *IEEE Trans. Power Electron.* **2015**, *30*, 5548–5564. [CrossRef]
31. Qian, W.; Cao, D.; Cintron-Rivera, J.G.; Gebben, M.; Wey, D.; Peng, F.Z. A Switched-Capacitor DC–DC Converter With High Voltage Gain and Reduced Component Rating and Count. *IEEE Trans. Ind. Appl.* **2012**, *48*, 1397–1406. [CrossRef]
32. Kampitsis, G.; Chevron, M.; van Erp, R.; Perera, N.; Papathanassiou, S.; Matioli, E. Mixed Simulation-Experimental Optimization of a Modular Multilevel Switched Capacitors Converter Cell. In Proceedings of the 2020 IEEE 21st Workshop on Control and Modeling for Power Electronics (COMPEL), Aalborg, Denmark, 9 November 2020; pp. 1–6.
33. Cao, D.; Peng, F.Z. A Family of Zero Current Switching Switched-Capacitor Dc-Dc Converters. In Proceedings of the Twenty-Fifth Annual IEEE Applied Power Electronics Conference and Exposition (APEC), Palm Springs, CA, USA, 21–25 February 2010; pp. 1365–1372.
34. Uemoto, Y.; Morita, T.; Ikoshi, A.; Umeda, H.; Matsuo, H.; Shimizu, J.; Hikita, M.; Yanagihara, M.; Ueda, T.; Tanaka, T.; et al. GaN Monolithic Inverter IC Using Normally-off Gate Injection Transistors with Planar Isolation on Si Substrate. In Proceedings of the 2009 IEEE International Electron Devices Meeting (IEDM), Baltimore, MD, USA, 7–9 December 2009; pp. 1–4.
35. Kampitsis, G.; van Erp, R.; Matioli, E. Ultra-High Power Density Magnetic-Less DC/DC Converter Utilizing GaN Transistors. In Proceedings of the 2019 IEEE Applied Power Electronics Conference and Exposition (APEC), Anaheim, CA, USA, 17–21 March 2019; pp. 1609–1615.
36. Zhang, Z.; Xiao, T.; Shen, Y.; Wang, L.; Jia, P.; Yu, J. A Method to Test Operating Cell Temperature for BIPV Modules. *IEEE J. Photovolt.* **2016**, *6*, 272–277. [CrossRef]
37. Kampitsis, G.; Batzelis, E.; Papathanassiou, S. Power Balance Control for a Two-Stage Solar Inverter with Low Voltage Ride through Capability. *Eur. Photovolt. Solar Energy Conf. Exhib.* **2016**, *32*, 1646–1650. [CrossRef]

energies

MDPI

Article

Detection of Demagnetization Faults in Axial Flux Permanent-Magnet Synchronous Wind Generators

Apostolos Lamprokostopoulos, Epameinondas Mitronikas * and Alexandra Barmpatza

Department of Electrical and Computer Engineering, University of Patras, 26504 Patras, Greece; a.lamprokostopoulos@upnet.gr (A.L.); abarmpatza@upatras.gr (A.B.)
* Correspondence: e.mitronikas@upatras.gr

Abstract: A new method for detecting demagnetization faults in axial flux permanent magnet synchronous wind generators is presented in this study. Demagnetization faults occur in the case of total or partial loss of the magnetic properties of one or more permanent magnets of the machine. Fault signatures appearing in the current or voltage signal due to a demagnetization fault can often be confused with those produced by eccentricity faults, making the discrimination between the two types of faults difficult. The proposed methodology is based on the analysis of the instant power spectrum of the generator, combined with an estimator to derive the permanent magnet flux, based on the machine equations. Short-Time Fourier Transform is proposed as the means for spectrum analysis to ensure performance during variations of the generator speed. Results derived from the experimental tests are presented, which show that the proposed methodology is capable of detecting demagnetization faults and distinguishing them from eccentricity ones under a wide variety of operating conditions.

Keywords: permanent magnet synchronous machines; generators; fault detection; demagnetization

Citation: Lamprokostopoulos, A.; Mitronikas, E.; Barmpatza, A. Detection of Demagnetization Faults in Axial Flux Permanent-Magnet Synchronous Wind Generators. *Energies* **2022**, *15*, 3220. https://doi.org/10.3390/en15093220

Academic Editor: Terence O'Donnell

Received: 28 March 2022
Accepted: 26 April 2022
Published: 28 April 2022

Publisher's Note: MDPI stays neutral with regard to jurisdictional claims in published maps and institutional affiliations.

Copyright: © 2022 by the authors. Licensee MDPI, Basel, Switzerland. This article is an open access article distributed under the terms and conditions of the Creative Commons Attribution (CC BY) license (https://creativecommons.org/licenses/by/4.0/).

1. Introduction

Permanent magnet synchronous machines are widely used both as motors in a variety of industrial applications and as generators in many areas, including wind power systems. The reasons for their widespread use are their advantages over other types of machines; these advantages include high efficiency, high power density, very good dynamic response, and compact design. However, these machines are affected by demagnetization faults that come from high temperatures and short-circuiting from the coils of the stator. The demagnetization can be partial or total and reduce the electromagnetic force that can be produced by the machine, affecting its performance. Thus, it is very crucial to detect this kind of fault.

Research activity is extensive in this area [1,2] and has been moving towards two directions: (a) modelling the machine, using software tools such as Finite Element Method (FEM), helps to export with accuracy the voltage and current waveforms of the machine, whose spectra will be used subsequently for fault diagnosis purposes, using tools as FFT analysis, etc.; (b) developing methods to detect the fault and its severity in Permanent Magnet Synchronous Machines (PMSM). The latter can be categorized as time-domain methods, frequency-analysis methods such as machine current or back-emf voltage signature analysis, while others use methodologies such as deep learning to enable detection.

Machine current or voltage signature analysis is one of the most common methods for fault detection since it does not require prior knowledge of the characteristics and parameters of the machine. It is based on the current–voltage signals of the machine and simple mathematical time–frequency algorithms such as Fast Fourier Transform (FFT) for stationary conditions or wavelet analysis, Short-Time Fourier Transform (STFT), Hilbert–Huang Transform (HHT), and Empirical Mode Decomposition (EMD) for non-stationary

conditions. This kind of method compares the signals between the healthy and faulty case and detects the fault. Also, a very significant advantage of signal analysis is the small requirement of processing and memory, while in other methods e.g., deep learning or neural networks the requirements for processing and memory are extremely great.

Studies that investigate faults in radial flux permanent magnet synchronous machines are presented in [3–15]. In [3,4] Finite Element Method (FEM) is used to offer cognitive background about the stator currents and back-emf voltages spectrum, which is often extracted using Fast Fourier Transform (FFT), at demagnetization condition.

Referring to methodologies used for demagnetization faults detection, in [5,6] Linear Discriminant Analysis is used to determine which harmonic has the most detailed information for fault classification, distinguishing between eccentricity, inter-turn short circuit and demagnetization. In [7,8], wavelet analysis by implementing wavelet transforms (WT) of stator currents is used for demagnetization fault detection. In [9], an Extended Kalman Filter combined with the FFT algorithm is used to estimate the stator currents of a PMSG. In [10], a comparison between Extended Kalman Filter (EKF) and unscented Kalman Filter for fault diagnosis is presented. In [11], Hilbert–Huang Transform is used for demagnetization fault analysis at stationary and non-stationary conditions of a PMSM. In [12], a convolutional neural network (CNN), which is based on deep learning, has been trained for fault diagnosis. The common drawback of these methods [5–12] is that they require relatively high computational power and memory for implementation.

On the other hand, in [13], a method based on Least Square Method and Structure Analysis of the PMSM inductance is used as demagnetisation fault index. It is known that a demagnetized machine produces lower flux magnet than the normal one, which leads to higher inductances, as proven experimentally by the authors of [13]. In [14], a slightly different method for L_d inductance estimation is presented, which produces good results, but, as the authors conclude, it cannot be used continuously for detection of the demagnetization fault. In [15], a magnet flux estimator based on a synchronously rotating d-q reference frame in combination with FFT is used to detect rotor faults.

However, in all the aforementioned studies, the demagnetization fault in Radial Flux Permanent Magnet (RFPM) synchronous machines is investigated. On the other hand, studies related to demagnetization faults in Axial Flux Permanent Magnet (AFPM) synchronous machines are less in number. In [16–26], the most significant contributions in this area are summarized. In [16], the demagnetization fault in an AFPM synchronous machine, with one stator and two rotors is investigated, using search coils and an analytical model. In [17], both eccentricity and demagnetization faults are studied, using an analytic time harmonic model, in a single stator–double rotor topology too. In [18], the static, dynamic eccentricity and the demagnetization fault are investigated using the 3D field-reconstruction method. In [19], the stator current, output torque, and zero sequence component of the voltage are used for fault-detection purposes. In [20], the flux density and the mean torque are used as diagnostic means, when demagnetization exists in the magnets of the AFPM synchronous machine, due a to short circuit fault. In [21–23], the demagnetization and the combined demagnetization–eccentricity faults are investigated using the voltage and current spectra for fault-diagnosis purposes. In [24], a controller is proposed for the compensation of demagnetization fault in an AFPM synchronous machine with two rotors. In [25], the partial demagnetization fault is detected by monitoring the speed and the induced voltage in a supplementary winding. Finally, in [26], the texture-based analysis is used as a fault diagnosis means.

This paper presents a new method for demagnetization-fault detection in an AFPM synchronous generator, based on the instantaneous power of the machine and the calculation of permanent magnets flux. More specifically, the flux magnitude is calculated using a stationary reference frame, while signatures in the instant power of the generator are investigated to achieve reliable detection of demagnetization faults. The proposed method does not need initial angle calculation, resulting to a very simple algorithm. The signatures in the spectrum of instant power of the machine are evaluated for demagne-

tization diagnosis in both stationary and non-stationary conditions using FFT and STFT analysis respectively, as wind generators are in general variable speed machines. Therefore, the proposed method can provide information about the presence of the demagnetisation fault even under non-stationary conditions, while the majority of the existing articles use methods that can give accurate results only when stationary conditions exist.

2. Theoretical Analysis of the Proposed Fault Detection Method

The equations of the Permanent Magnet Synchronous Generator (PMSG), expressed in the stationary α-β reference frame, are shown in Equations (1)–(6):

$$u_\alpha(t) = R_S i_\alpha(t) + \frac{d\lambda_\alpha(t)}{dt} \quad (1)$$

$$u_\beta(t) = R_S i_\beta(t) + \frac{d\lambda_\beta(t)}{dt} \quad (2)$$

$$\lambda_\alpha(t) = L_S i_\alpha(t) + \lambda_{m\alpha}(t) \quad (3)$$

$$\lambda_\beta(t) = L_S i_\beta(t) + \lambda_{m\beta}(t) \quad (4)$$

$$T_e(t) = p\left(\lambda_\alpha(t) i_\alpha(t) - \lambda_\beta(t) i_\beta(t)\right) \quad (5)$$

$$T_e(t) - T_m(t) = \mathrm{J}\frac{d\omega_m(t)}{dt} - \beta_C \omega_m(t) \quad (6)$$

where $u_\alpha, u_\beta, i_\alpha, i_\beta$ are the machine voltage and current components expressed in the α-β reference frame, ω_r is the reference frame angular frequency, ω_m is the rotating shaft angular frequency, T_e is the electromagnetic torque produced by the machine, T_m is the torque applied to the shaft of the machine, λ_m is the magnetic flux established by the permanent magnets, p is the number of pole pairs, and β_C is the damping coefficient.

2.1. PMSG Faults and Diagnosis Means

The faults that appear most frequently in PMSG are:

(a) inter-turn short circuit faults (ISC);
(b) static eccentricity (SE);
(c) dynamic eccentricity (DE);
(d) mixed eccentricity (ME);
(e) partial or complete demagnetization of the rotor (DM).

Amongst them, inter-turn short circuit fault is a fast-evolving situation, while the other four fault situations occur either due to manufacturing deficiencies or excessive strain conditions and are generally progressing more slowly.

All the mentioned fault types affect the operation of the generator, deteriorating its operation, so they can be detected using signal-processing techniques for analyzing their influence in the corresponding mechanical or electrical quantities. One of the most common ways to achieve this is to exploit the mechanical vibration signals, which means that a mechanical vibration sensor should be installed at the generator. This solution has been proven to be quite reliable, however it implies relatively high installation costs.

A well-proven alternative is the Machine Current Signature Analysis (MCSA), where the machine terminal electrical quantities are exploited to detect the fault indicative signatures. Most commonly, these signatures are characteristic frequencies that occur in the case of the corresponding fault.

Indicative signatures for the ISC fault lay in the frequencies given by the general formula $f_{isc} = (2k+1)f_s$ ($k = 1, 2, 3, \dots$) [9]. The main assumption to detect eccentricity faults (ME) is that, in practice, mixed faults occur; therefore, sideband components at frequencies of $f_{me} = \left(1 \pm \frac{k}{p}\right) f_s$, ($k = 1, 2, 3, \dots$) [27] can be utilized to detect eccentricity

faults. Moreover, the fault-indicative frequencies for the DM fault are $f_{dm} = \left(1 \pm \frac{k}{p}\right) f_s$ ($k = 1, 2, 3, \dots$) [3,7,11]. Table 1 shows the harmonics used for the detection of each fault:

Table 1. Fault types and the frequencies proposed for their detection.

Fault Type	Indicative Frequency
Inter-turn short circuit faults (ISC)	$f_{isc} = (2k+1) f_s$, ($k = 1, 2, 3, \dots$)
Mixed eccentricity (ME)	$f_{me} = \left(1 \pm \frac{k}{p}\right) f_s$, ($k = 1, 2, 3, \dots$)
Demagnetization of the rotor (DM)	$f_{dm} = \left(1 \pm \frac{k}{p}\right) f_s$, ($k = 1, 2, 3, \dots$)

From the previous table, it is obvious that the ME and DM fault signatures are the same, so to discriminate an eccentricity fault from a demagnetization condition, additional criteria should be considered.

2.2. Detection of Demagnetization Faults Using the Instataneous Power

According to the analysis in the literature (e.g., [8]), in the presence of a demagnetization fault, harmonic frequencies $\left(1 \pm \frac{k}{p}\right)\omega_s t$, where $k = 1, 2, 3, \dots$ appear in the motor terminal quantities. So, the voltage in the terminals of the generator can be written in the presence of this fault as in Equation (7). The same frequencies are expected to appear in the terminal currents, expressed as in Equation (8):

$$V_{abc} = \begin{bmatrix} V_a \\ V_b \\ V_c \end{bmatrix} = \begin{bmatrix} V\left\{\cos(\omega_s t + \varphi) + \sum a_{vk} \cos\left[\left(1 \pm \frac{k}{p}\right)\omega_s t + \varphi_{vk}\right]\right\} \\ V\left\{\cos\left(\omega_s t - \frac{2\pi}{3} + \varphi\right) + \sum a_{vk} \cos\left[\left(1 \pm \frac{k}{p}\right)\omega_s t + \varphi_{vk} - \frac{2\pi}{3}\right]\right\} \\ V\left\{\cos\left(\omega_s t + \frac{2\pi}{3} + \varphi\right) + \sum a_{vk} \cos\left[\left(1 \pm \frac{k}{p}\right)\omega_s t + \varphi_{vk} + \frac{2\pi}{3}\right]\right\} \end{bmatrix} \quad (7)$$

$$I_{abc} = \begin{bmatrix} I_a \\ I_b \\ I_c \end{bmatrix} = \begin{bmatrix} I\left\{\cos \omega_s t + \sum a_{ik} \cos\left[\left(1 \pm \frac{k}{p}\right)\omega_s t + \varphi_{ik}\right]\right\} \\ I\left\{\cos\left(\omega_s t - \frac{2\pi}{3}\right) + \sum a_{ik} \cos\left[\left(1 \pm \frac{k}{p}\right)\omega_s t + \varphi_{ik} - \frac{2\pi}{3}\right]\right\} \\ I\left\{\cos\left(\omega_s t + \frac{2\pi}{3}\right) + \sum a_{ik} \cos\left[\left(1 \pm \frac{k}{p}\right)\omega_s t + \varphi_{ik} + \frac{2\pi}{3}\right]\right\} \end{bmatrix}, \quad (8)$$

where ω_s is the fundamental electrical frequency and a_{vi}, a_{ii} are the relative amplitudes of the voltage and current harmonics corresponding to the fault, respectively.

Multiplying with the Clarke transformation matrix, we have the voltage coordinates in a stationary reference frame, denoted with indexes α and β, as calculated from Equation (9):

$$V_{\alpha\beta} = \frac{2}{3} \cdot \begin{bmatrix} 1 & -\frac{1}{2} & -\frac{1}{2} \\ 0 & \frac{\sqrt{3}}{2} & -\frac{\sqrt{3}}{2} \end{bmatrix} \cdot \begin{bmatrix} V_a \\ V_b \\ V_c \end{bmatrix} \quad (9)$$

which results to Equation (10):

$$V_{\alpha\beta} = \begin{bmatrix} u_\alpha \\ u_\beta \end{bmatrix} = \begin{bmatrix} V\left\{\cos(\omega_s t + \varphi) + \sum a_{vk} \cos\left[\left(1 \pm \frac{k}{p}\right)\omega_s t + \varphi_{vk}\right]\right\} \\ V\left\{\sin(\omega_s t + \varphi) + \sum a_{vk} \sin\left[\left(1 \pm \frac{k}{p}\right)\omega_s t + \varphi_{vk}\right]\right\} \end{bmatrix}, \quad (10)$$

The current coordinates are extracted from (8) in a similar way:

$$I_{\alpha\beta} = \begin{bmatrix} i_\alpha \\ i_\beta \end{bmatrix} = \begin{bmatrix} I\left\{\cos \omega_s t + \sum a_{ik} \cos\left[\left(1 \pm \frac{k}{p}\right)\omega_s t + \varphi_{ik}\right]\right\} \\ I\left\{\sin \omega_s t + \sum a_{ik} \sin\left[\left(1 \pm \frac{k}{p}\right)\omega_s t + \varphi_{ik}\right]\right\} \end{bmatrix}, \quad (11)$$

The instantaneous power, as measured in the generator terminals is given by Equation (12):

$$P_i = V_a I_a + V_b I_b + V_c I_c = u_\alpha i_\alpha + u_\beta i_\beta \quad (12)$$

Substituting values from (10), (11) to (12), results to Equation (10):

$$\begin{aligned} P_i \;=\; VI\Big\{\cos(\omega_s t+\varphi)+\sum\;\alpha_{vk}\cos\Big[\Big(1\pm\tfrac{k}{p}\Big)\omega_s t+\varphi_{vk}\Big]\Big\}\cdot\Big\{\cos\omega_s t+\sum\;\alpha_{ik}\cos\Big[\Big(1\pm\tfrac{k}{p}\Big)\omega_s t+\varphi_{ik}\Big]\Big\} \\ +VI\Big\{\sin(\omega_s t+\varphi)+\sum\;\alpha_{vk}\sin\Big[\Big(1\pm\tfrac{k}{p}\Big)\omega_s t+\varphi_{vk}\Big]\Big\} \\ \cdot\Big\{\sin\omega_s t+\sum\;\alpha_{ik}\sin\Big[\Big(1\pm\tfrac{k}{p}\Big)\omega_s t+\varphi_{ik}\Big]\Big\} \end{aligned} \tag{13}$$

As the coefficients α_{vk}, α_{ik} represent the amplitudes of the fault-indicative frequencies, it is well-known that each of them will be much lower that unit. So, we can safely make the approximation that $\alpha_{vk}\cdot\alpha_{ik} \ll 1$ and omit the products that include the expression, as their influence in the equation is negligible. This way, we conclude to Equation (14):

$$P_i \;=\; VI\Big\{1+\sum A_k cos\Big[\Big(\pm\frac{k}{p}\Big)\omega_s t+\varphi_k\Big]\Big\}, \tag{14}$$

where:

$$A_k \;=\; \text{sign}[\alpha_{vk}\cos\varphi_{vk}+\alpha_{ik}\cos(\varphi_{ik}-\varphi)]\sqrt{\alpha_{vk}^2+\alpha_{ik}^2+2\alpha_{vk}\alpha_{ik}\cos(\varphi+\varphi_{vk-}\varphi_{ik})} \tag{15}$$

$$\varphi_k \;=\; \tan^{-1}\Big(-\frac{\alpha_{vk}\sin\varphi_{vk}+\alpha_{ik}\sin(\varphi_{ik}-\varphi)}{\alpha_{vk}\cos\varphi_{vk}+\alpha_{ik}\cos(\varphi_{ik}-\varphi)}\Big) \tag{16}$$

From (14), it is obvious that the fault-indicative frequencies are also present in the instant power signal, making it the ideal signal for the detection of the fault. The presence of these frequencies is indicative of the ME and DM faults, however they do not give sufficient information to discriminate between them. Therefore, a unique fault-indicative condition should be supplied.

In the case of a partial or total loss of a permanent magnet in the rotor, a decrease in the magnetic flux produced by the permanent magnets, as calculated using the machine equations, is expected. This decrease is not expected in the ME fault, as eccentricity causes the airgap to variate around a constant or rotating center, without affecting its average value.

To calculate the magnet-produced flux, a simplified algorithm is presented in this paper. Equations (1) and (2) can be written as:

$$\begin{aligned} \tfrac{d\lambda_\alpha(t)}{dt} \;&=\; u_\alpha(t)-R_S i_\alpha(t) \\ \tfrac{d\lambda_\beta(t)}{dt} \;&=\; u_\beta(t)-R_S i_\beta(t) \end{aligned} \tag{17}$$

Especially in the steady-state condition, electrical quantities in (17) are sinusoidal, so the components of $\vec{\lambda}$ can be given by Equations (18) and (19). Considering relatively slow transient conditions where the rotor speed, and therefore the electrical frequency, is subject to slow variations, deviations from the steady state are not expected to introduce critically high errors to the flux components estimation.

$$\lambda_\alpha(t) \;=\; \frac{u_\alpha(t)-R_S i_\alpha(t)}{p\omega_m} \tag{18}$$

$$\lambda_\beta(t) \;=\; \frac{u_\beta(t)-R_S i_\beta(t)}{p\omega_m} \tag{19}$$

From the α-β components of the flux vector, the magnets' flux magnitude can be calculated as:

$$\lambda_m(t) \;=\; \sqrt{(\lambda_\alpha(t)-L_s i_\alpha(t))^2+(\lambda_\beta(t)-L_s i_\beta(t))^2} \tag{20}$$

One of the main conditions that the Clarke transformation should comply with, is that the machine must be symmetrical. It is straightforward that this condition should also be valid in (20). As demagnetization faults often introduce asymmetries, deviations are expected at the flux magnitude, which could be expressed as ripple and a reduced flux average value. The concept behind this work is to compare this average value of the flux with the respective value of the healthy machine to deduce the fault condition. For example, if one of the 32 magnets is lost, it can be estimated that the calculated average flux will decrease by a ratio of 1/32, which means 3% of its initial (healthy) value. In addition, for Equations (18) and (19) to be valid, it is essential the generator to operate at steady-state or quasi-steady-state condition. This can be assumed in our case, as it is expected that the wind generator will be operating with variating speed over time, however:

- Speed variations are assumed to be slow compared to the electric quantities period;
- Small deviations of the estimated flux from its actual value do not affect the proposed method.

However, to ensure the proposed strategy performance, the estimated flux value is filtered using a moving average filter with exponential forgetting. In addition, the filter has a variable forgetting factor, starting from a maximum value which decreases over time with a predefined factor to a minimum. This way, the filter can be reset when required (e.g., in a detected steady-state condition). The flow chart of the proposed methodology for DM fault detection is illustrated in Figure 1.

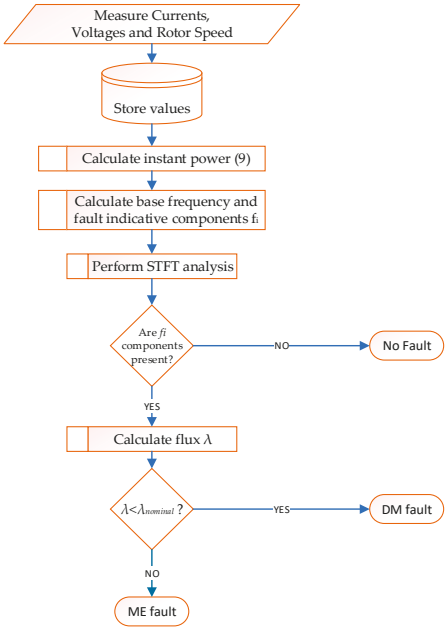

Figure 1. Flow chart of the proposed methodology for DM fault detection.

3. Experimental Setup

For the experimental investigation of the proposed technique, an Axial Flux Permanent Magnet Synchronous Generator (AFPMSG) is used. The machine has a double-sided rotor and one resin-embedded, coreless stator. Each rotor has 16 NdFeB magnets. Table 2 summarizes the most important of the generator parameters.

Table 2. Parameters of the double-rotor PMSG under study.

Parameter	Value
Nominal Power	350 W
Nominal Voltage	80 V
Nominal frequency (f_s)	50 Hz
Nominal speed (n_s)	375 rpm
Number of poles for each rotor	16
Stator Phase Resistance	5.89 Ohm
Stator Phase Inductance	17 mH

The AFPMSG is driven by a three-phase induction motor. Three current and three voltage hall-effect transducers were used to perform the stator voltages and currents measurement. Acquisition of the measurement values is performed using a LabView data acquisition card. The sampling frequency was set to 10 kHz. The measured data is collected in an ASCII file and the fault analysis is performed offline. To obtain the DM fault behavior without introducing eccentricity, one of the rotor magnets is removed and replaced by a part of equal weight.

In Figure 2. the laboratory test bench is shown, while in Figure 3. the block diagram of the whole test system structure is illustrated.

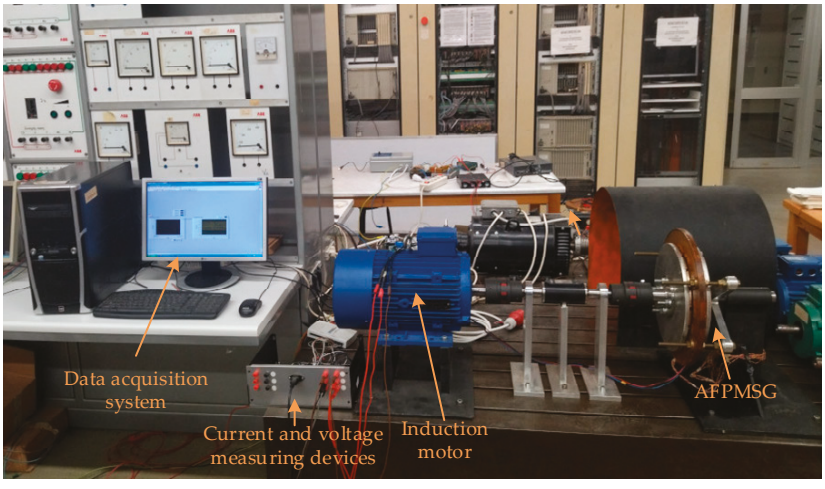

Figure 2. Laboratory setup used for the experimental tests.

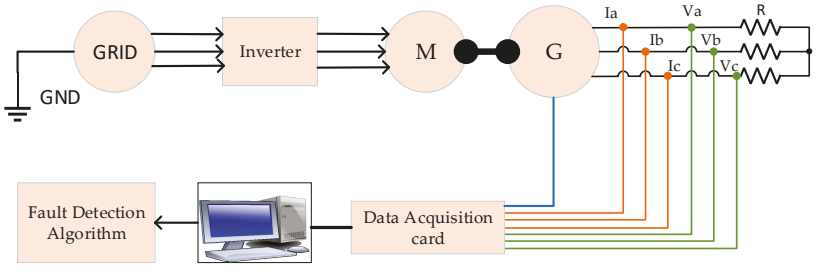

Figure 3. Block diagram of the system structure.

The synchronous generator was studied both in healthy situation and in demagnetization fault situation. The demagnetization fault was created by removing a magnet from

one of the two rotors. One of the two rotors with the magnets and the stator of the machine are illustrated in Figure 4a,b respectively.

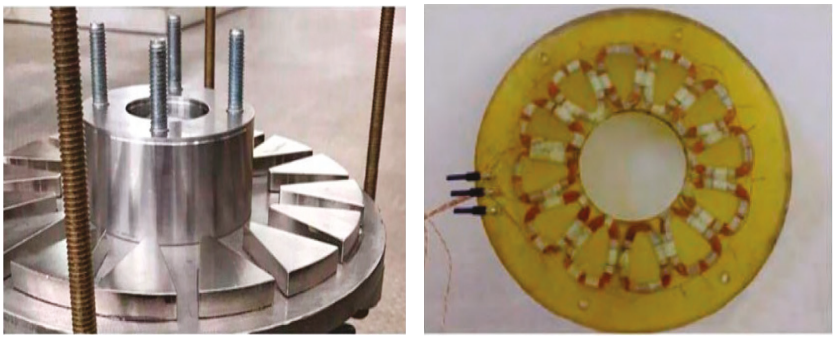

(**a**) (**b**)

Figure 4. (**a**) One of the two rotors with 16 permanent magnets, (**b**) the resin-immersed coils of the stator [2].

3.1. Operation under Steady-State Condition

To evaluate the operation of the proposed DM fault-detection methodology, various tests have been performed under different steady-state operating conditions, from which characteristic results are shown in Figures 5–10. In these figures, the output voltage, estimated flux and power FFT are depicted under healthy and operations under fault for nominal voltage and frequency with a load of 225 W and 290 W, respectively, connected at the generator output. Multiple frequency components ($\frac{11f_s}{p}$, $\frac{12f_s}{p}$, $\frac{13f_s}{p}$, $\frac{14f_s}{p}$) are chosen as fault-indicative to ensure reliability, considering the rule that if elevated magnitudes are detected at half or more of these frequencies, an error is signaled. The authors of this paper decided to choose these frequency components because it has been observed that their detection was easier under any operating condition at the laboratory experiments. The flux produced by the magnets in the healthy case is λ = 0.46T. If a level below 0.45 T is detected, a DM fault is signaled, otherwise the fault is considered as eccentricity. In this case, where a magnet is totally lost, it is also evident that the expected 3% decrease in the estimated flux value can be verified in both Figures 7 and 10. More specifically, in Figures 6 and 9, the instantaneous power frequency components (68.75 Hz, 75 Hz, 81.25 Hz, 87.5 Hz), produced for p = 8 and f_s = 50 Hz, can be detected at the demagnetization case both for the load of 225 W and for the load of 290 W. In both cases, a significant increase in the amplitude of these frequencies is observed in the faulty case, as shown from the measured values in Tables 3 and 4. More specifically, for a load of 225 W, it can be noticed that: at f_{DM1} = 68.75 Hz the power magnitude has changed from −81 dB (healthy machine) to −66.4 dB (demagnetized machine); at f_{DM2} = 75 Hz the magnitude has changed from −49.5 dB to −29.4 dB; at f_{DM3} = 81.25 Hz the magnitude has changed from −79.5 dB to −65 dB; and at f_{DM4} = 87.5 Hz the magnitude has changed from −81 dB to −67.3 dB. Respectively, for a load at 290 W, it can be noticed that: at f_{DM1} = 68.75 Hz the power magnitude has changed from −77 dB (healthy machine) to −59.5 dB(demagnetized machine); at f_{DM2} = 75 Hz the magnitude has changed from −47 dB to −29 dB; at f_{DM3} = 81.25 Hz the magnitude has changed from −73.5 dB to −65 dB; and at f_{DM4} = 87.5 Hz the magnitude has changed from −80 dB to −63.5 dB. In both cases, a detectable difference between the healthy and the faulty machine in the magnitude of these characteristic harmonics, combined with the estimated permanent magnet flux is providing a reliable means for the demagnetisation fault detection.

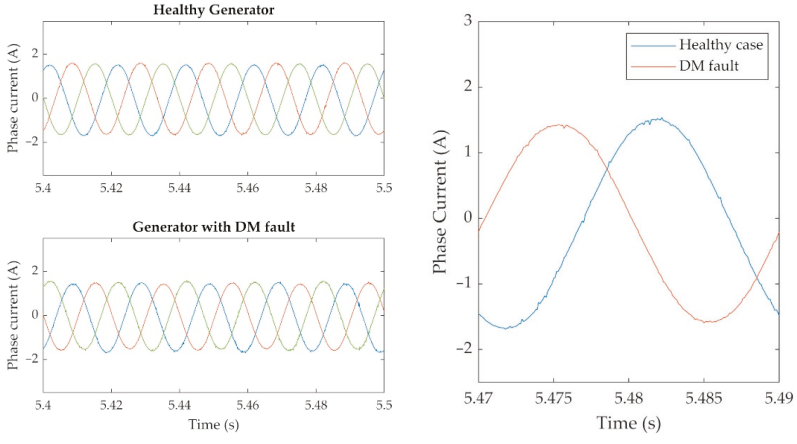

(**a**) (**b**)

Figure 5. Experimental results: (**a**) three phase stator currents waveform for healthy generator and for DM fault, (**b**) focused stator currents waveform at healthy case (blue) and demagnetized case (red). (Generator operating under nominal voltage and frequency, with a load of 225 W.)

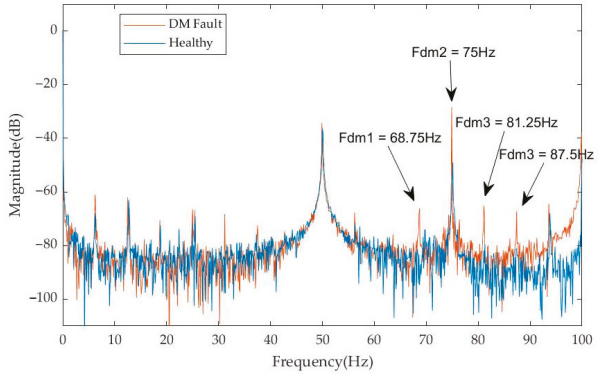

Figure 6. Experimental results: power spectrum for healthy generator and for DM fault (generator operating under nominal voltage and frequency, with a load of 225 W).

Table 3. Experimental results: instantaneous power frequency components at 225 W load.

Number of Harmonic	f(Hz)	Healthy Machine (dB)	Demagnetized Machine (dB)
$(11\,fs/p)$	68.75	−81.0	−66.4
$(12\,fs/p)$	75.00	−49.5	−28.4
$(13\,fs/p)$	81.25	−79.5	−65.0
$(14\,fs/p)$	87.50	−81.0	−67.3

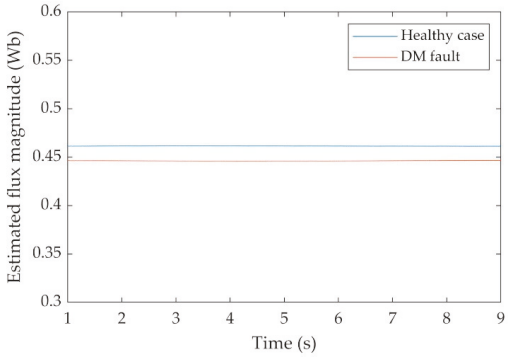

Figure 7. Experimental results: estimated flux magnitude for healthy generator and for DM fault (generator operating under nominal voltage and frequency, with a load of 225 W).

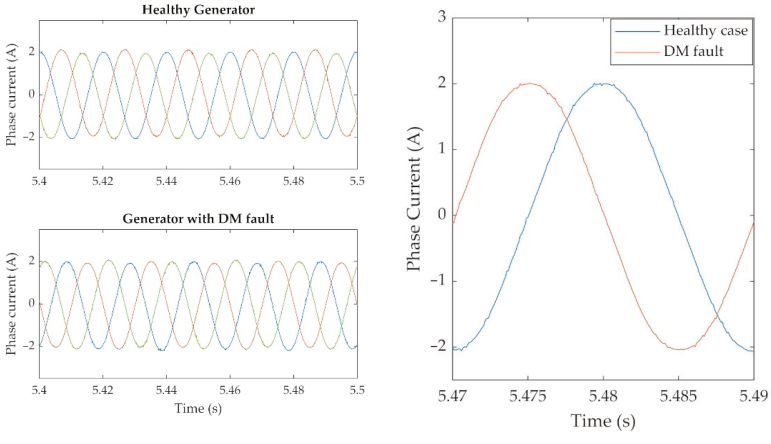

(**a**) (**b**)

Figure 8. Experimental results: (**a**) three phase stator currents waveform for healthy generator and for DM fault,;(**b**) focused stator currents waveform at healthy case (blue) and demagnetized case (red). (Generator operating under nominal voltage and frequency, with a load of 290 W.)

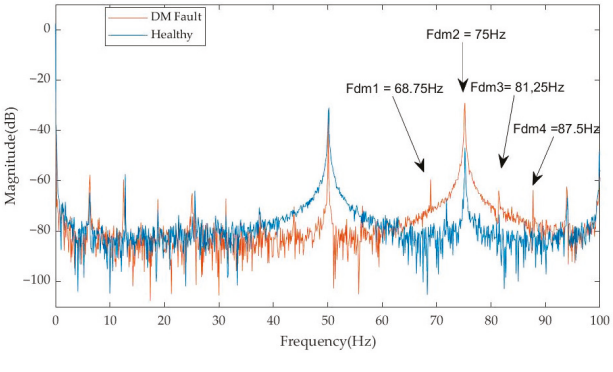

Figure 9. Experimental results: power spectrum for healthy generator and for DM fault (generator operating under nominal voltage and frequency, with a load of 290 W).

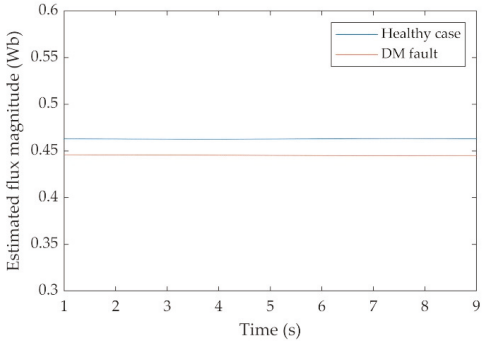

Figure 10. Experimental results: estimated flux magnitude for healthy generator and for DM fault (generator operating under nominal voltage and frequency, with a load of 290 W).

Table 4. Experimental results: instantaneous power frequency components at 290 W load.

Number of Harmonic	f(Hz)	Healthy Machine (dB)	Demagnetized Machine (dB)
(11 *fs*/*p*)	68.75	−77.0	−59.5
(12 *fs*/*p*)	75.00	−47.0	−29.0
(13 *fs*/*p*)	81.25	−73.5	−65.0
(14 *fs*/*p*)	87.50	−80.0	−63.8

From the experimental results, it is obvious that by using both harmonics and flux criteria the DM fault can be reliably detected and discriminated from eccentricity faults. To obtain the frequency spectrum, FFT is adequate. However, in general, wind generators are not expected to operate in steady state, so STFT analysis should be used to extract the power spectra.

3.2. Transient Operation

Finally, experimental tests have been performed to test the validity of the proposed fault-detection methodology during transient operation of the generator. These tests included operation of the machine considering variable load and rotating speed. Hereafter, characteristic results from a fast speed change of the generator, when the rotor speed doubles within a time interval of 0.4 s. As the FFT algorithm fails to perform due to the variable frequency, STFT analysis is used, as described. Results shown in Figures 11–14 prove that the fault can also be reliably detected at variable speed, combining the information obtained by the STFT and the flux estimation. More specifically, in Figure 11 the currents of the healthy and demagnetized machine are presented for a speed change. In Figures 12 and 13, the results of the STFT algorithm are presented for both the healthy machine and the demagnetized case, respectively. The instantaneous power frequency components (34.38 Hz, 37.5 Hz, 40.62 Hz, 43.75 Hz), produced for f_s = 25 Hz and k = 11, 12, 13, 14, can be detected at a time interval of 0–6 s at Figure 13 (demagnetized case), while they are not shown at Figure 12 (healthy). Additionally, when electrical frequency becomes 50 Hz at the time interval of about 6–10 s, it can be noticed that frequency components shift to the new values corresponding to f_s = 50 Hz (68.75 Hz, 75 Hz, 81.25 Hz, 87.5 Hz) at Figure 13, while these components do not show in Figure 12. It is worthy to refer that the frequency component of 75 Hz is present both in the healthy and demagnetized case for f_s = 50 Hz and the frequency component of 37.5 Hz for f_s = 25 Hz, but with a bigger amplitude in the demagnetized machine. The arrows depict the four frequency components for operation frequencies f_s = 25 Hz, 50 Hz both at healthy and demagnetization condition.

In Figure 14, the estimated flux amplitude is presented for speed change from 25 Hz to 50 Hz.

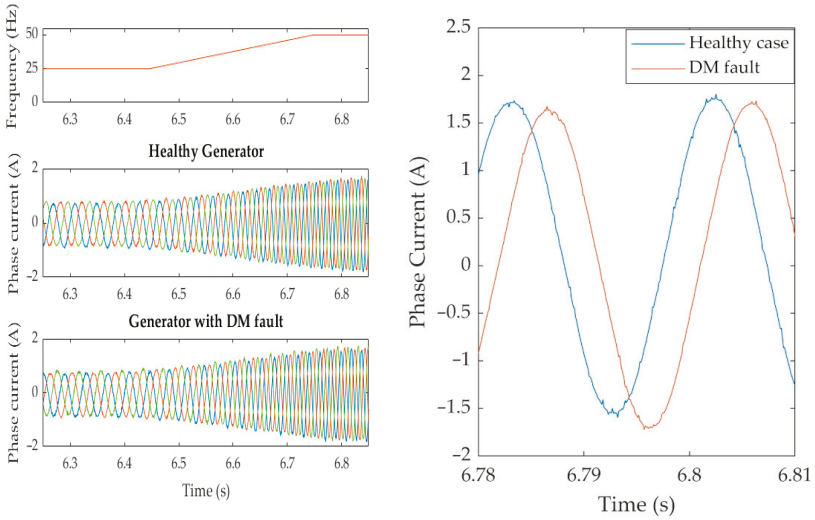

(**a**) (**b**)

Figure 11. (**a**) Experimental results: stator currents for healthy generator and for DM fault (frequency changes from 25 Hz to 50 Hz); (**b**) focused results for stator currents at healthy case (blue) and demagnetized case (red).

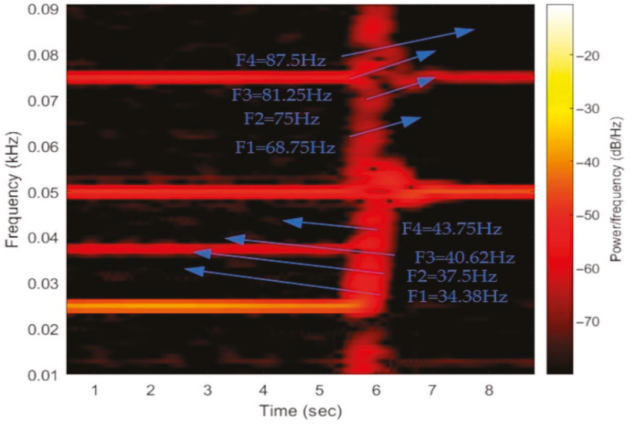

Figure 12. Power spectrum for healthy generator (frequency changes from 25 Hz to 50 Hz—examined fault indicative frequencies are shown with the blue arrows).

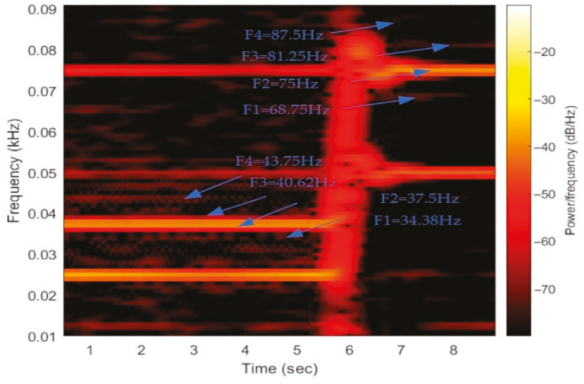

Figure 13. Power spectrum for DM fault (frequency changes from 25 Hz to 50 Hz—examined fault indicative frequencies are shown with the blue arrows).

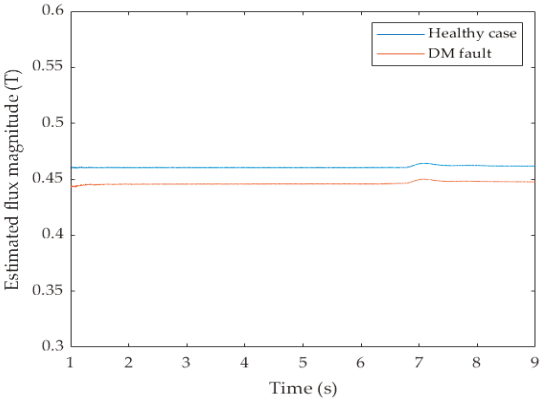

Figure 14. Experimental results: Estimated flux magnitude for healthy generator and for DM fault (frequency changes from 25 Hz to 50 Hz).

4. Conclusions

A new methodology for detecting demagnetization faults in axial flux permanent magnet synchronous wind generators is presented in this study. Demagnetization faults occur when a partial or total loss of the magnetic properties of the permanent magnet material appears and could concern only one of the machine magnets or all of them. In particular, when it comes to signature analysis and the demagnetization fault affecting only part of the magnets, DM fault signatures are almost identical to the ones of ME faults, making discrimination between the two fault types very difficult.

The proposed methodology consists of the analysis of the instant power spectrum of the generator, combined with an estimator to derive the permanent magnet flux based on the machine equations. To this purpose, the fault indicative signatures contained in the power spectrum are analyzed. STFT is proposed as a method to derive the power spectrum, so that the method can perform during variations of the generator shaft speed. A permanent magnet flux estimator based on the machine model has been developed, to detect whether the fault indicative signatures reveal a DM or an eccentricity fault.

Experimental laboratory tests have been performed under a wide range of operating conditions and characteristic results are presented. Experimental results show that the proposed methodology is capable of detecting demagnetization faults and distinguish them from eccentricity ones under a wide variety of operating conditions.

Author Contributions: All authors contributed to this paper: investigation, methodology, software, validation, writing, E.M. and A.L.; project administration E.M.; writing—validation, review and editing, A.B. All authors have read and agreed to the published version of the manuscript.

Funding: This research received no external funding.

Institutional Review Board Statement: Not applicable.

Informed Consent Statement: Not applicable.

Data Availability Statement: Data sharing is not applicable to this article.

Acknowledgments: The authors would like to acknowledge the contributions of Joya Kappatou, G. Zalokostas and D. Spiratos for their work in designing and constructing the AFPMSG which has been used as the test machine in the experimental part.

Conflicts of Interest: The authors declare no conflict of interest.

References

1. Chen, Y.; Liang, S.; Li, W.; Liang, H.; Wang, C. Faults and Diagnosis Methods of Permanent Magnet Synchronous Motors: A Review. *Appl. Sci.* **2019**, *9*, 2116. [CrossRef]
2. Moosavi, S.S.; Djerdir, A.; Amirat, Y.A.; Khaburi, D.A. Demagnetization fault diagnosis in permanent magnet synchronous motors: A review of the state-of-the-art. *J. Magn. Magn. Mater.* **2015**, *391*, 203–212. [CrossRef]
3. Urresty, J.C.; Riba, J.R.; Delgado, M.; Romeral, L. Detection of Demagnetization Faults in Surface-Mounted Permanent Magnet Synchronous Motors by Means of the Zero-Sequence Voltage Component. *IEEE Trans. Energy Convers.* **2012**, *27*, 42–51. [CrossRef]
4. Gao, C.; Nie, Y.; Si, J.; Fu, Z.; Feng, H. Mode Recognition and Fault Positioning of Permanent Magnet Demagnetization for PMSM. *Energies* **2019**, *12*, 1644. [CrossRef]
5. Haddad, R.Z.; Strangas, E.G. Fault Detection and Classification in Permanent Magnet Synchronous Machines using Fast Fourier Transform and Linear Discriminant Analysis. In Proceedings of the 2013 9th IEEE International Symposium on Diagnostics for Electric Machines, Power Electronics and Drives (SDEMPED), Valencia, Spain, 27–30 August 2013; pp. 99–104.
6. Haddad, R.Z.; Strangas, E.G. On the Accuracy of Fault Detection and Separation in Permanent Magnet Synchronous Machines using MCSA/MVSA and LDA. *IEEE Trans. Energy Convers.* **2016**, *31*, 924–934. [CrossRef]
7. Ruiz, J.R.; Rosero, J.A.; Espinosa, A.G.; Romeral, L. Detection of Demagnetization Faults in Permanent-Magnet Synchronous Motors Under Nonstationary Conditions. *IEEE Trans. Magn.* **2009**, *45*, 2961–2969. [CrossRef]
8. Ebrahimi, B.M.; Roshtkhari, M.J.; Faiz, J.; Khatami, S.V. Advanced Eccentricity Fault Recognition in Permanent Magnet Synchronous Motors using Stator Current Signature Analysis. *IEEE Trans. Ind. Electron.* **2013**, *61*, 2041–2052. [CrossRef]
9. Gliga, L.I.; Chafouk, H.; Popescu, D.; Lupu, C. Diagnosis of a Permanent Magnet Synchronous Generator using the Extended Kalman Filter and the Fast Fourier Transform. In Proceedings of the 2018 7th International Conference on Systems and Control (ICSC), Valencia, Spain, 24–26 October 2018; pp. 65–70.
10. El Sayed, W.; Abd El Geliel, M.; Lotfy, A. Fault Diagnosis of PMSG Stator Inter-Turn Fault Using Extended Kalman Filter and Unscented Kalman Filter. *Energies* **2020**, *13*, 2972. [CrossRef]
11. Rosero, J.; Romeral, L.; Ortega, J.A.; Urresty, J.C. Demagnetization Fault Detection by means of Hilbert Huang Transform of the stator current Decomposition in PMSM. In Proceedings of the 2008 IEEE International Symposium on Industrial Electronics, Cambridge, UK, 30 June–2 July 2008; Volume 68, pp. 310–324.
12. Kao, I.H.; Wang, W.J.; Lai, Y.H.; Perng, J.W. Analysis of Permanent Magnet Synchronous Motor Fault Diagnosis Based on Learning. *IEEE Trans. Instrum. Meas.* **2019**, *68*, 310–324. [CrossRef]
13. Moon, S.; Lee, J.; Jeong, H.; Kim, S.W. Demagnetization Fault Diagnosis of a PMSM Based on Structure Analysis of Motor Inductance. *IEEE Trans. Ind. Electron.* **2016**, *63*, 3795–3803. [CrossRef]
14. Hong, J.; Park, S.; Hyun, D.; Kang, T.J.; Lee, S.B.; Kral, C.; Haumer, A. Detection and Classification of Rotor Demagnetization and Eccentricity Faults for PM Synchronous Motors. *IEEE Trans. Ind. Appl.* **2012**, *48*, 923–932. [CrossRef]
15. Le Roux, W.; Harley, R.G.; Habetler, T.G. Detecting Rotor Faults in Low Power Permanent Magnet Synchronous Machines. *IEEE Trans. Power Electron.* **2007**, *22*, 322–328. [CrossRef]
16. De Bisschop, J.; Vansompel, H.; Sergeant, P.; Dupre, L. Demagnetization Fault Detection in Axial Flux PM Machines by Using Sensing Coils and an Analytical Model. *IEEE Trans. Magn.* **2017**, *53*, 8203404. [CrossRef]
17. De Bisschop, J.; Sergeant, P.; Hemeida, A.; Vansompel, H.; Dupré, L. Analytical Model for Combined Study of Magnet Demagnetization and Eccentricity Defects in Axial Flux Permanent Magnet Synchronous Machines. *IEEE Trans. Mag.* **2017**, *53*, 8107712. [CrossRef]
18. Ajily, E.; Ardebili, M.; Abbaszadeh, K. Magnet defect and rotor eccentricity modeling in axial-flux permanent-magnet machines via 3-D Field Reconstruction Method. *IEEE Trans. Ener. Conv.* **2016**, *31*, 486–495. [CrossRef]
19. Saavedra, H.; Riba, J.R.; Romeral, L. Magnet shape influence on the performance of AFPMM with demagnetization. In Proceedings of the IECON 2013-39th Annual Conference of the IEEE Industrial Electronics Society, Vienna, Austria, 10–13 November 2013; pp. 973–977.

20. Bahador, N.; Darabi, A.; Hasanabadi, H. Demagnetization analysis of axial flux permanent magnet motor under three phase short circuit fault. In Proceedings of the 4th Annual International Power Electronics, Drive Systems and Technologies Conference, Tehran, Iran, 13–14 February 2013; pp. 333–337.
21. Barmpatza, A.C.; Kappatou, J.C. Investigation of the combined eccentricity and demagnetization fault in an AFPMSG. In Proceedings of the 2020 International Conference on Electrical Machines (ICEM), Gothenburg, Sweden, 23–26 August 2020.
22. Barmpatza, A.C.; Kappatou, J.C. Study of the demagnetization fault in an AFPM machine in relation with the magnet location. In Proceedings of the 2018 XIII International Conference on Electrical Machines (ICEM), Alexandroupoli, Greece, 3–6 September 2018.
23. Barmpatza, A.C.; Kappatou, J.C. Study of a Combined Demagnetization and Eccentricity Fault in an AFPM Synchronous Generator. *Energies* **2020**, *13*, 5609. [CrossRef]
24. Verkroost, L.; De Bisschop, J.; Vansompel, H.; De Belie, F.; Sergeant, P. Active Demagnetization Fault Compensation for Axial Flux Permanent-Magnet Synchronous Machines Using an Analytical Inverse Model. *IEEE Trans. Ener. Conv.* **2020**, *35*, 591–599. [CrossRef]
25. Skarmoutsos, G.; Gyftakis, K.; Mueller, M. Detecting Partial Demagnetization in AFPM Generators by Monitoring Speed and EMF Induced in a Supplemental Winding. *IEEE Trans. Ind. Infor.* **2022**, *18*, 3295–3305. [CrossRef]
26. Mínaz, M.R.; Akcan, E. An Effective Method for Detection of Demagnetization Fault in Axial Flux Coreless PMSG with Texture-Based Analysis. *IEEE Access* **2021**, *9*, 17438–17449. [CrossRef]
27. Ioannis, P.T. Dynamic Analysis and Development of Diagnostic Methods for Controlled Motor System Consisting of a Slip Ring Asynchronous Machine and Power Electronic Converters. Doctoral Thesis, University of Patras, Patras, Greece, November 2007.

energies

MDPI

Article

Markov Chain Simulation of Coal Ash Melting Point and Stochastic Optimization of Operation Temperature for Entrained Flow Coal Gasification

Jinchun Zhang [1], Shiheng Guan [1] Jinxiu Hou [2,*], Zichuan Zhang [1], Zhaoqian Li [2], Xiangzhong Meng [3] and Chao Wang [3]

[1] School of Energy Science and Engineering, Henan Polytechnic University, Jiaozuo 454000, China; zjc@hpu.edu.cn (J.Z.); gsh18703952650@163.com (S.G.); zichuan5008@163.com (Z.Z.)
[2] State Key Laboratory Cultivation Base for Gas Geology and Gas Control, School of Safety Science and Engineering, Henan Polytechnic University, Jiaozuo 454000, China; hpulzq@163.com
[3] Henan Pingyuan Optics Electronics Co. Ltd., Jiaozuo 454000, China; mengxz1978@126.com (X.M.); alamwa@126.com (C.W.)
* Correspondence: houjx@hpu.edu.cn

Received: 18 October 2019; Accepted: 6 November 2019; Published: 7 November 2019

Abstract: In the entrained flow coal gasification process, the gas production is critically affected by the operating temperature (OT) and coal ash melting point (AMP), and the AMP is one of key factors for the determinations of OT. Considering the fact that coal is a typical nonhomogeneous substance and the coal ash composition varies from batch to batch, this paper proposes the application of the Markov Chain (MC) method in simulation of the random AMP series and the stochastic optimization of OT based on MC simulation for entrained flow coal gasification. The purpose of this paper is to provide a more accurate optimal OT decision method for entrained flow coal gasification practice. In this paper, the AMP was regarded as a random variable, and the random process method, Markov Chain, was used to describe the random AMP series of feed coal. Firstly, the MC simulation model about AMP was founded according to an actual sample data, 200 sets of AMP data from an industrial gasification plant under three simulation schemes (the sample data were individually divided into 16, eight and four state groups,). The comparisons between the simulation results and the actual values show that the founded MC simulation model descries the AMP series very well. Then, a stochastic programming model based on MC simulation for OT optimization was developed. Finally, this stochastic programming optimization model was optimized by genetic algorithm (GA). Comparing with the conventional OT optimization method, the proposed stochastic OT optimization model integrated MC simulation can ascertain a more accurate OT for guiding the coal gasification practice.

Keywords: entrained flow coal gasification; ash melting point; operation temperature; Markov process; stochastic optimization model; genetic algorithm

1. Introduction

Coal is the most wildly used natural energy resource with the largest reserves. Compared with other energy sources, the utilization of coal has attracted wider attention in view of the advantages of wide distribution and easy exploitation of coal. In recent years, the increasing environmental and health concerns in utilization of coal promote the emergence of clean coal technologies [1–4]. Among the clean coal technologies, coal gasification is regard as a promising utilization of coal because of its low technology cost and high conversion rate [5]. In the coal gasification practice, the basic equipment can be grouped into three main categories: fixed bed gasifiers, fluidized bed gasifiers and entrained flow gasifiers [6,7]. Differ from fixed bed and fluidized bed gasification, entrained flow gasification

operates at a higher temperature (above the melting temperature of ash) with smaller particles and produces high quality syngas with low methane and free tar content. In addition, this type of coal gasification has some advantages such as high carbon conversion, large production capacity, high thermal efficiency and a low environmental pollution [8,9]. On the contrary, there are also some disadvantages to be improved in entrained flow gasification such as slagging and fouling.

Because the ash discharging mode for entrained-flow bed gasifiers is liquid slagging, the melting characteristics of coal ash is a key factor influencing the gasifier operation [10]. Thus, the ash melting point (AMP) of the feed coal is an important reference index for the determination of operational temperature (OT), which is a critical parameter for the stable and efficient operation of the gasifier. When the temperature in a gasifier is lower than the AMP of the feed coal, the gasification reaction as well as coal conversion rate will be greatly reduced [11]. On the contrary, when the gasification temperature is far higher than the AMP, the ash in the coal may agglomerate, resulting in a reduction of the reaction contact between the gasifying agent and coal and an uneven air flow in the gasifier, which is not conducive to good gasification reactions [12]. Thus, the OT of the gasifier should usually be moderately higher than the AMP of the feed coal so as to facilitate the melting and flow of coal ash and maintain the gasification reaction [13]. Therefore, the AMP of feed coal is always paid special attention to in practice due to the important role it plays in the determination of the optimum OT for the gasification process.

Over the past years, in order to study the melting behavior of coal ash in gasifiers, many studies about the AMP of coal have been reported. Current studies on AMP of coal can be roughly divided into two categories: (i) the mechanism models that are based on the mechanism of chemical reactions; (ii) the empirical models that are based on data statistics. A large number of researchers have developed mechanism models in their studies on AMP of coal, for example, Chakravarty et al. [14], Dai et al. [15], Weber et al. [16], Kim et al. [17]. However, the mechanism models are very theoretical, with many assumptions, so the reaction process expressed by these formulas may deviate from the actual reaction process due to these assumptions. As for the empirical models for coal AMP, studies on this subject have developed rapidly and a great deal of literature on this subject has been published in recent years. Some statistic method such as linear and non-linear regression methods, as well as some advanced intelligent algorithms [18] such as artificial neural network(ANN), support vector machine (SVM), etc. were employed in these models. For instance, Ozbayoglu et al. [19] applied linear regression and non-linear regression, respectively, to the chemical composition of coal ash and the temperature of AMP for Turkish lignite. In [10,20–22], the authors took a large number of parameters of coal ash as training samples and used ANN to predict the AMP of different coals. In [23–25], the authors all took ash composition as input and AMP as output to build prediction models of AMP using SVM. Compared with the mechanism model, the advantage of the empirical models is that they avoid complex mechanism process analysis, and they can just extract information from historical data to predict the AMP of coal. Both the mechanism models and the empirical models have contributed to the study of ash problems (such as slagging and fouling), however, these models are static models, that is, the foundations for modelling are based on a point in time rather than a time series perspective. More importantly, these studies focus on the prediction of AMP based on the characteristics of coal rather than OT optimization based on dynamic AMP.

As one of the critical factors influencing the stable and efficient operation of a gasifier as well as the quality of gasification product, OT has always been one of the key parameters discussed in many entrained flow coal gasification studies, and its optimization is usually an important topic in a large number of published studies. For instance, Chen et al. [26] carried out some orthogonal designs to optimize some operating parameters of an entrained flow gasifier for coal-biomass co-gasification. As an important operating parameter, OT was optimized according to Taguchi's philosophy. Vejahati et al. [27] optimized three operating variables, including OT, for a coal-coke gasification in an entrained flow gasifier using response surface methodology (RSM). In addition to the experiment-based studies, many researchers also discussed the temperature optimization in their simulation-based researches.

Emun et al. [28] used Aspen Plus to study the effect of different operating variables on thermal efficiency. As a result, the optimal OT was 1550 °C with the highest thermal efficiency. Biagini et al. [29] developed an entrained-flow gasifier model in Aspen Plus, and obtained the optimal operating conditions including temperature through parametric analysis. Chen et al. [30] applied a computational fluid dynamics (CFD) simulation method to develop an optimization analysis procedure of the gasification process in an entrained-flow gasifier, and obtained a best temperature of 1227 °C. Shastri et al. [31] developed a CFD model for a single-stage coal gasifier. Eleven parameters including OT were stochastically optimized by using the parameter space investigation method. Wei et al. [32] used the iterative adaptive dynamic programming (IADP) method to establish a nonlinear optimization control scheme for the coal gasification system. They concluded that the optimal OT should be controlled at around 1320 °C. Actually, the composition of pulverized feed coal varies from batch to batch, and even in the same batch of pulverized coal, there may be fluctuations in composition depending on the feeding time. In turn, the AMP of feed coal usually manifests as a dynamic series over a period of time. Thus the target of OT optimization is actually to seek an optimal OT that is best adapted to the dynamic changes in coal composition from batch to batch and extending to the dynamic changes in AMP. However, in reviewing the current studies on OT optimization, a lot of the reported studies involve static optimization because they are mainly based on static small-scale experiments or simulation experiments and the dynamic changes in coal composition as well as in AMP series of feeding coal are not taken into account.

In this paper, the AMP of feed coal over a period of time is treated as a group of random data series based on random perspective. A stochastic process theory, Markov Chain (MC), is used to simulate and describe the AMP series. A Markov process is a stochastic process model describing a sequence of possible events that satisfies the Markov property. In the philosophy of MC, the probability of each event depends solely on the state attained in the previous event, and this dependence obeys a certain probability distribution [33]. MC models can express the dynamic changes of a random series and predict the future changes of the system through the transition probability of state change among different variables. Because of the clear mathematical meaning of the MC model, it is widely used in modelling or simulation for different applications. For example, Afzal et al. [34] established a hidden Markov model that solves the problem of information prediction in industrial process control. Reference [35] provided a general approximation framework for (path-dependent) option evaluation under time-varying Markov processes. Reference [36] applied the Markov decision process to the control of the hybrid energy storage system, increasing the self-consumption of photovoltaics by 5%. In [37], a semi-Markov process was used to describe the machine degradation process, and a fault detection scheme based on Bayesian estimation was proposed to achieve more effective early fault detection. Others similar reports can be found in [38–41]. Recently, there have been a few reports about the application of MC in coal gasification. References [42,43] introduced a residence time distribution model of the granular phase in a gasifier based on MC. The results showed that the simulation results are basically in agreement with the measured data, which can be used to predict the residence time distribution of granular phase in the gasifier. However, to our best knowledge, there no studies on the utilization of MC in the simulation of AMP of coal, especially studies on OT optimization based on MC simulation for entrained flow coal gasification process have been reported so far.

The purpose of this paper is to describe our study on: (i) using MC to simulate the AMP series of feed coal for an entrained flow gasification process, (ii) stochastic program modelling based on MC simulation of AMP for OT optimization, and (iii) solving OT optimization with a genetic algorithm (GA). In this study, the AMP series of a feed coal was regarded as a random series, and the simulation for the AMP series with MC was carried out based on 200 sets of actual AMP data collected from an industrial gasification plant. Then a stochastic programming model with the target of optimizing OT based on MC simulation was proposed. Finally, the optimal OT was ascertained by solving the stochastic programing model using GA.

2. Simulation Approach for AMP Series

2.1. Marckov Chain

The Markov chain is a modeling and prediction method that works based on a stochastic process in order to describe a series of uncertain events [33]. In this type of stochastic process, the Markov property that the future prediction of a process variable could be made independent of the process history should be satisfied. For a stochastic process $\{X_t, t = 0, 1, 2, \ldots\}$ with a finite number of possible values, the statement that X_t being equal to i expresses that the process is in state i when the time is at t. Figure 1 shows the state transition of a MC process. For a given past state $X_0, X_1, \ldots, X_{t-1}$ and the present state X_t, the condition distribution of the future state X_{t+1} is independent of the past state and depends only on the present state. As shown in Figure 1, state set $S = \{1, 2, \ldots, i, j, \ldots n\}$, and the state transition with non-aftereffect property can be achieved by a fixed possibility of P_{ij} [44]:

$$\begin{aligned} &P\{X_{t+1} = j \big| X_t = i_t, \ldots, X_1 = i_1, X_0 = i_0\} \\ &= P\{X_{t+1} = j \big| X_t = i_t\} \\ &= P_{ij} \end{aligned} \tag{1}$$

where P_{ij} indicates the probability of a process being transferred to state X_{t+1} at the time of state X_t.

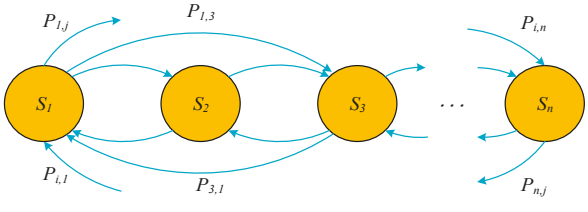

Figure 1. Markov probability transition diagrammatic sketch.

P_{ij} should satisfy the following conditions:

$$\begin{aligned} &\textstyle\sum_{j=1}^{n} P_{ij} = 1 \\ &P_{ij} \geq 0, \\ &i, j = 1, 2, \ldots, n \end{aligned} \tag{2}$$

where n is the total number of states. Then the Markov characteristic of a data series could be expressed by a matrix of transition probability $\boldsymbol{P}$:

$$\boldsymbol{P} = \begin{bmatrix} P_{11} & P_{12} & \cdots & P_{1n} \\ P_{21} & P_{22} & \cdots & P_{2n} \\ \vdots & \vdots & \ddots & \vdots \\ P_{n1} & P_{n2} & \cdots & P_{nn} \end{bmatrix} \tag{3}$$

Matrix $\boldsymbol{P}$ (Equation (3)) is the first order one-step transition matrix. In matrix $\boldsymbol{P}$, the ith row, vector $\boldsymbol{V}$, represents the one-step transition probability of state i. Then the n-step transition probability vector of state i could be expressed by the following formula:

$$\boldsymbol{V}_i^n = \boldsymbol{V}_i \boldsymbol{P}^{n-1} \tag{4}$$

As the embedded Markov chain is assumed ergodic, the stationary distribution, described by an k-element vector $\boldsymbol{\pi}$ [45], can be obtained solving the following system of linear equations:

$$\begin{cases} \boldsymbol{\pi P} = 0 \\ \sum_{i=1}^{n} \boldsymbol{\pi}_i = 1 \end{cases} \tag{5}$$

where the last equation specifies the normalization of the probability distribution.

2.2. MC Simulation Procedure for AMP

The state transition probability matrix $\boldsymbol{P}$ is the core of Markov theory. The n-dimensional state transition probability matrix can be used to describe the change rule of any state in the stochastic system, which greatly simplifies the complexity of the stochastic model. Thus, Markov theory has been widely used in stochastic modelling.

In this paper, a MC simulation for 200 sets of AMP data (see Appendix A Table A1) collected from a fertilizer plant in Xinxiang, Henan Province, China was carried out. Among them, 160 sets of data were used as training samples, and the remaining 40 sets were used as test samples. The dynamic changes in the AMP series of feeding coal were regarded as state changes, and then the MC process was used to stochastically simulate the AMP series. The specific steps [44] are as shown in Figure 2.

Step 1

Input *Samdata* = [] % Get sample data

Input *StateNum* = *n* % Set the number of states

MinData = min(*Samdata*) % Minimum value of sample data

MaxData = max(*Samdata*) % Maximum value of sample data

IntSize = (*Maxdata* - *Mindata*) \ *n* % Calculate interval size

State(i) = [*MinData* + (*i*-1)**IntSize*, *MinData* + *i***IntSize*] % Range of state *i*

Step 2

Fre(i,j) = *Count(i,j)* / (*n*-1) % Calculate the frequency of state *i* to *j*

$$\boldsymbol{P} = \begin{bmatrix} Fre(1,1) & Fre(1,2) & \cdots & Fre(1,n) \\ Fre(2,1) & Fre(2,2) & \cdots & Fre(2,n) \\ \cdots & \cdots & \cdots & \cdots \\ Fre(n,1) & Fre(n,1) & \cdots & Fre(n,n) \end{bmatrix}$$

State transition probability matrix

Step 3

Input *S(t)* = *i* % *S* indicates that the state at time *t* is *i*

Input *r* = rand(1) % *r* is a random number of 0~1

If $\sum_{j=1}^{m} P_{i,(j-1)} \le r \le \sum_{j=1}^{m} P_{i,j}$ % Get the state at time *t*+1 according to *P*

S(t+1) = m

End

Figure 2. Steps of Markov simulation for the AMP series of feeding coal.

Step 1: Partitioning the state. In order to convert the AMP data into state variables for the Markov process, the data should be divided into several regions and each region could be regarded as states S_1, $S_2, S_3, \ldots, S_n$. The number of states depends on the capacity of the original AMP data. The interval length of each state depends on the upper and lower bounds of the original AMP data and the error range of the final simulation data.
Step 2: Constructing the probability matrix of state transition. The AMP sample data is regarded as time series, and the change of data in time series is regarded as state transition. By counting the frequency of each state transition, the probability matrix of state transition could be constructed.
Step 3: Simulating the Markov sequences. It is assumed that the state transition probability vector of the initial state is $\boldsymbol{V}_1 = \left[P_{i_1 1}, P_{i_1 2}, \ldots, P_{i_1 m}, \ldots, P_{i_1 n}\right]$ and r is a random number of $[0, 1]$. If m is satisfied with:

$$\sum_{j=1}^{m} P_{i_1,(j-1)} \leq r \leq \sum_{j=1}^{m} P_{i_1,j} \tag{6}$$

The state S_m would be the second state of the sequence. By analogy, the remaining part of the state sequence could be simulated. Then, according to the rules of state partition, the state sequence is transformed into the sequence of AMP. That is, the simulation data are obtained. In this study, we carried out the MC simulation programming (see Appendix B) in the Matlab2015 platform.

3. Markov Chain Simulation for AMP Series

3.1. MC Simulation for AMP

In a MC simulation, the partition of the state intervals determines the simulation result. The common state partition methods include empirical-based partition, sample mean-variance-based partition and ordered clustering. Among these three methods, the empirical-based partition method is the simplest one and thus is mostly used. For instance, in [44], a wind speed series was divided into 28 states with the length of each state being 0.5 m/s using the empirical-based division method when it was simulated by MC method. References [44,46,47] also present the application of this method in dividing some data series for MC simulation in some practical problems. Similarly, in this paper, the empirical method was adopted to divide the states of the collected AMP series. In addition, in order to evaluate the simulation results, we proposed three portioning schemes and compared the simulation accurate in these three schemes so as to achieve a more precise simulation model for further OT optimization. The three portioning schemes are as follows:

Case I: dividing the original AMP data into 16 states.
Case II: dividing the original AMP data into 8 states.
Case III: dividing the original AMP data into 4 states.

For Case I, the original AMP data were divided into 16 intervals: [1310, 1315], [1315, 1320], ... , [1385, 1390], and each interval corresponds to one state of $\{S_1, S_2, \ldots, S_{16}\}$. Then the state transition probability matrix $\boldsymbol{P}_{CaseI}$ could be obtained by counting the frequency of various states transition:

$$
\boldsymbol{P}_{caseI} = \begin{bmatrix}
0 & 0 & 1 & 0 & 0 & 0 & 0 & 0 & 0 & 0 & 0 & 0 & 0 & 0 & 0 & 0 \\
0 & 0 & 0 & 0 & 1 & 0 & 0 & 0 & 0 & 0 & 0 & 0 & 0 & 0 & 0 & 0 \\
0 & 0 & 0 & 0 & 0 & 0.143 & 0.143 & 0.286 & 0 & 0 & 0.286 & 0.143 & 0 & 0 & 0 & 0 \\
0 & 0 & 0 & 0 & 0.286 & 0.143 & 0 & 0 & 0.286 & 0 & 0 & 0 & 0.286 & 0 & 0 & 0 \\
0 & 0 & 0 & 0 & 0.067 & 0.267 & 0.133 & 0.200 & 0.200 & 0.067 & 0.067 & 0 & 0 & 0 & 0 & 0 \\
0 & 0 & 0 & 0.053 & 0.105 & 0.211 & 0.053 & 0.263 & 0.105 & 0 & 0.105 & 0 & 0 & 0.105 & 0 & 0 \\
0 & 0.036 & 0.107 & 0.107 & 0.036 & 0.143 & 0.179 & 0.143 & 0 & 0.071 & 0.107 & 0.036 & 0.036 & 0 & 0 & 0 \\
0.003 & 0.01 & 0.036 & 0.066 & 0.171 & 0 & 0.086 & 0.143 & 0.257 & 0.057 & 0.057 & 0.029 & 0.076 & 0.025 & 0.01 & 0.013 \\
0 & 0 & 0 & 0 & 0.031 & 0.063 & 0.156 & 0.250 & 0.219 & 0.094 & 0.063 & 0.031 & 0.031 & 0.031 & 0.031 & 0 \\
0 & 0 & 0 & 0 & 0 & 0.067 & 0.133 & 0.133 & 0.133 & 0.267 & 0.067 & 0.067 & 0.133 & 0 & 0 & 0 \\
0.077 & 0 & 0 & 0 & 0 & 0 & 0.385 & 0.077 & 0.154 & 0.077 & 0.077 & 0.077 & 0 & 0.077 & 0 & 0 \\
0 & 0 & 0 & 0.1 & 0 & 0 & 0.2 & 0.2 & 0.2 & 0.1 & 0 & 0.2 & 0 & 0 & 0 & 0 \\
0 & 0 & 0 & 0.111 & 0 & 0.222 & 0 & 0.111 & 0.222 & 0 & 0 & 0.222 & 0.111 & 0 & 0 & 0 \\
0 & 0 & 0 & 0 & 0.25 & 0 & 0.5 & 0.25 & 0 & 0 & 0 & 0 & 0 & 0 & 0 & 0 \\
0 & 0 & 0 & 0 & 0 & 0 & 0 & 0 & 0.5 & 0.5 & 0 & 0 & 0 & 0 & 0 & 0 \\
0 & 0 & 0 & 0 & 0 & 0 & 0 & 0 & 0 & 0 & 0 & 0 & 0 & 0 & 0 & 0
\end{bmatrix} \tag{7}
$$

$$
\boldsymbol{\pi}_{caseI} = \begin{bmatrix} 0.005 & 0.005 & 0.035 & 0.035 & 0.07 & 0.095 & 0.14 & 0.175 & 0.15 & 0.075 & 0.07 & 0.06 & 0.05 & 0.02 & 0.01 & 0.005 \end{bmatrix}
$$

Figure 3 shows a graphical representation of the state transition probability matrix $\boldsymbol{P}_{CaseI}$, which highlights the peculiarities of its structure. As can be seen from Figure 3, the greater probabilities are almost all distributed near the diagonal, and their values identify the probabilities that the AMP data from one moment to the next remains in the initial state. Furthermore, the non-zero transition probabilities are concentrated around the diagonal, making transitions from an initial state to another far away much less probable.

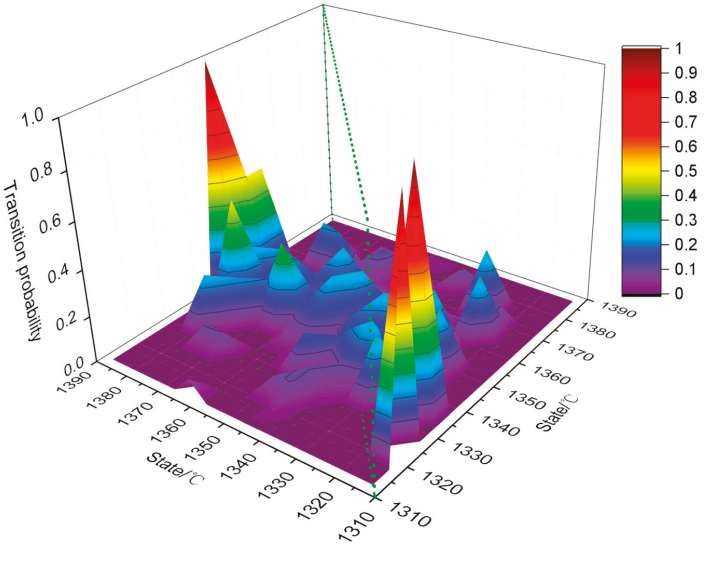

Figure 3. Graphical representation of the Markov transition matrix.

Then the simulation of AMP series was carried out. In simulation, S_8 was set as the initial state, which was the same as the initial state in the sample data, and let r be a random number with uniform distribution $X \sim [0,1]$. For a state to simulated S_m, if m satisfies:

$$
\begin{aligned}
&\textstyle\sum_{j=1}^{m} P_{8,(j-1)} \le r \le \sum_{j=1}^{m} P_{8,j} \\
&P_{ij} = 0 \qquad\qquad\qquad\qquad if\ i \times j = 0 \\
&1 \le m \le n
\end{aligned} \tag{8}
$$

S_m could be simulated according to random transformation principle. Similar to Equation (8), Figure 4 shows the schematic principle of the state transition chain in the simulation. As shown in Figure 4, the random number r is 0.04 and it falls into the third interval, so the second state is S_3. Then, taking S_3 as the starting state, the next state could be predicted according to the corresponding state transition probability vector. By analogy, a random state sequence with Markov property can be obtained.

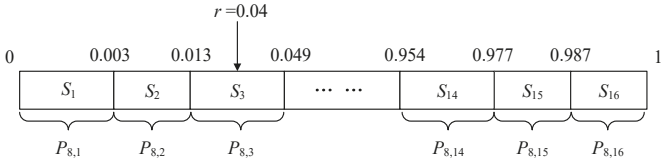

Figure 4. The schematic principle of the state transition chain in the simulation.

Furthermore, data reconstruction was carried out so as to get the simulated AMP series. In this step, the obtained random state sequence were transformed into the concrete simulation data of AMP according to the following equation:

$$X(t) = 1310 + j(t) \times 5 - r \times 5 \tag{9}$$

where, $X(t)$ is the final simulation data of AMP, r is a random number with uniform distribution $X \sim \mathrm{U}[0,1]$, $j(t)$ is the state at t.

After completing the steps described above, the simulated AMP series could been obtained by using Equation (9) (as shown in Figure 5 and provided in Appendix A Table A1).

Similar to Case I, the state transition probability matrices of the original AMP series in Case II and Case III, $\boldsymbol{P}_{CaseII}$ and $\boldsymbol{P}_{CaseIII}$, can be ascertained, individually:

$$\boldsymbol{P}_{caseII} = \begin{bmatrix} 0 & 0.5 & 0.5 & 0 & 0 & 0 & 0 & 0 \\ 0 & 0 & 0.286 & 0.214 & 0.143 & 0.214 & 0.143 & 0 \\ 0 & 0.026 & 0.325 & 0.325 & 0.186 & 0.086 & 0.053 & 0 \\ 0.018 & 0.164 & 0.175 & 0.275 & 0.193 & 0.114 & 0.046 & 0.014 \\ 0 & 0 & 0.08 & 0.336 & 0.356 & 0.114 & 0.098 & 0.016 \\ 0.038 & 0.05 & 0 & 0.431 & 0.265 & 0.177 & 0.038 & 0 \\ 0 & 0.056 & 0.236 & 0.431 & 0.111 & 0.111 & 0.056 & 0 \\ 0 & 0 & 0 & 0.5 & 0.5 & 0 & 0 & 0 \end{bmatrix} \tag{10}$$

$$\boldsymbol{\pi}_{caseII} = \begin{bmatrix} 0.01 & 0.07 & 0.165 & 0.315 & 0.225 & 0.13 & 0.07 & 0.015 \end{bmatrix}$$

$$\boldsymbol{P}_{caseIII} = \begin{bmatrix} 0.25 & 0.5 & 0.179 & 0.071 \\ 0.104 & 0.55 & 0.29 & 0.057 \\ 0.044 & 0.424 & 0.456 & 0.076 \\ 0.028 & 0.583 & 0.361 & 0.028 \end{bmatrix} \tag{11}$$

$$\boldsymbol{\pi}_{caseIII} = \begin{bmatrix} 0.08 & 0.48 & 0.355 & 0.085 \end{bmatrix}$$

The simulated AMP series in Case II and Case III are also shown in Figure 5 and provided in Appendix A Table A1.

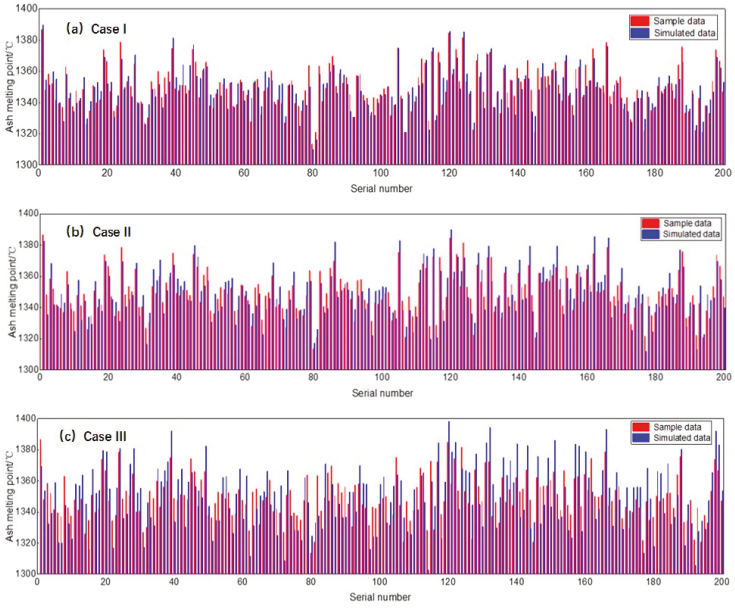

Figure 5. Original and simulated series of AMP in (**a**) Case I, (**b**) Case II and (**c**) Case III.

3.2. Accuracy Test

In order to evaluate the simulation accuracy by the MC approach, the goodness of fit between the simulated and the original AMP series was measured. Figure 6 shows the probability distribution of the original and simulated data in three cases, which correspond to the stationary distribution probability vector $\boldsymbol{\pi}$. It is obvious that the probability distribution of Case I is the most similar to that of the sample data. Its main characteristics are being high in the middle and low on both sides, which indicates that the AMP data are concentrated at about 1350 °C. In the other two cases, the probability distribution curves are relatively flat and the data are scattered.

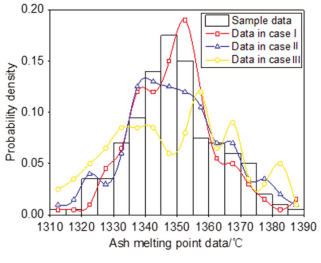

Figure 6. Comparison of probability density of the simulated and original AMP series in three cases.

Figure 7 shows the comparisons of the simulated and the original AMP series in three cases. As can be seen from this figure, the data points in Case I are closest to the diagonal. In addition, the error between simulation data and original data in Case I is within 13 °C, while the error in Case II and Case III are 18 °C and 26 °C, respectively. It can also be seen that there no simulated data locates on the diagonal line for Case III. This means that the simulated data is always inaccurate in this case. The reason may lie in the fact that the state range of Case III is too large. Although each state is simulated accurately, the simulation data of AMP that is randomly generated in a large state range will deviate

the sample data greatly. Therefore, the range of the state interval determines the accuracy of the data simulation. Some further statistical indexes i.e., Mean Absolute Deviation (MAD), Root Mean Square Error (RMSE) and Absolute Average Relative Error (AARE) were employed to measure the deviation between the simulated and the actual AMP values:

$$MAD = \frac{1}{n}\sum_{i=1}^{n}\left|\hat{y}_i - y_i\right| \tag{12}$$

$$RMSE = \sqrt{\frac{1}{n}\sum_{1}^{n}(\hat{y}_i - y_i)^2} \tag{13}$$

$$AARE = \frac{\sum_{i=1}^{n}\left|\frac{\hat{y}_i - y_i}{y_i}\right|}{n} \times 100 \tag{14}$$

where, y_i is the actual value of AMP and $\hat{y}_i$ is the simulated value of AMP by the MC simulation approach.

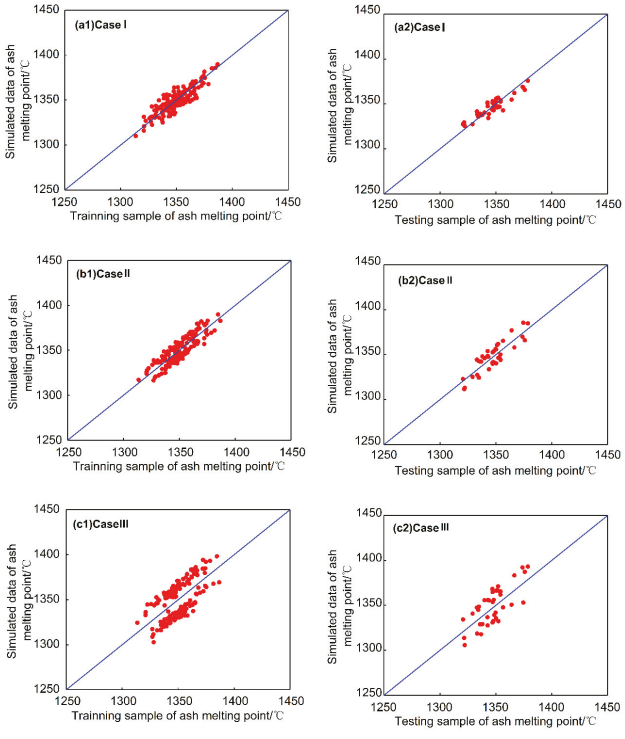

Figure 7. Comparisons of the simulated data and the sample data of AMP in three cases.

Table 1 presents the deviation statistics between the simulated and the original AMP series in three cases. As shown in Table 1, AARE in Case I and Case II are 0.42% and 0.52%, respectively, which are smaller than 1%; while the AARE in Case III is 1.04%, which is also a small deviation although it is larger than 1%. This indicates the simulation accuracy of the three cases are all acceptable. However, in comparing the three cases, the deviation indexes of MAD, RMSE and AARE in Case I are obviously smaller than those in Case II and Case III. This indicates that the simulation scheme of Case I that dividing the original AMP data into 16 states can provide better prediction accuracy.

Table 1. Deviation statistics in three cases.

Statistical Indexes	Case I	Case II	Case III
MAD	5.67	7.01	14.06
RMSE	6.98	7.63	15.21
AARE	0.42%	0.52%	1.04%

3.3. Further Discussion on the Selection of State Number

Based on the above discussion, it seems to be that the more states there are, the more accurate the simulation will be. However, there are still problems. According to [48], if the number of states is small, the probability the state changing will be significantly reduced, and searching for this other state is, after all, a goal of prediction. If on the other hand the AMP data is divided into a large number of states, the number of events per state will be smaller. This may be insufficient to estimate the actual distribution of the probability of state changes. By comparing Equations (7), (10) and (11), it could be found that the probability of transition between states is decreasing with the increase of the number of states. If the number of states is too large, a large number of state transition probability will be small, and the simulated data will be irregular. Such a Markov model with a large number of states obviously cannot reflect the characteristics of AMP data. Therefore, it is necessary to discuss the selection of a suitable state number.

In order to determine the optimal states number of Markov model, the MC models with state number from 4 to 16 were compared. The simulation results are shown in Table 2. As shown in Table 2, the simulation model with 16 states is not the best one, although the state number of this model is the largest. However, the most accuracy model with lower evaluation indexes among these simulation models is the one with 13 states. Then the simulation accuracy gradually decreases with the increase of the number of states when the state number is larger than 13. This is because too many states lead the probability of state transition to be very small, and further lead the simulation data to lose the distribution characteristics of the original data. Thus, the simulation scheme with 13 states would be employed in the latter optimization modelling for gasifier OT.

Table 2. Simulation results of MC model with four states to 16 states.

State Number	Evaluation Index of Simulation Results		
	MAD	RMSE	AARE
4	14.06	15.21	1.04%
5	11.53	12.49	0.86%
6	9.78	10.31	0.72%
7	8.23	8.58	0.59%
8	7.01	7.63	0.52%
9	6.24	6.42	0.45%
10	5.68	6.13	0.41%
11	5.10	5.89	0.38%
12	4.69	4.77	0.36%
13	4.38	4.52	0.35%
14	4.79	5.01	0.36%
15	5.46	5.98	0.38%
16	5.67	6.98	0.42%

4. Stochastic Optimization of OT

4.1. Stochastic Programing Modelling Based on MC Simulation

In coal gasification practice, the gas production will generally reach a maximum when the OT is 50~100 °C higher than the AMP of the feed coal [49,50]. Traditional determination of OT is just done according to a fixed AMP value and simply adding a temperature increment to this fixed AMP

value. This fixed AMP value is usually the AMP mean of the feed coal over a period of time or several successive batches. This traditional method is simple, but often results in inaccuracy in OT determination because the possible great changes in AMP of feed coal from batch to batch are not taken into account. This may greatly affect the gasification reaction and the stability of gasification production. In order to ascertain a more feasible OT for gasifier operation, it is necessary to take the fluctuations in the AMP of the pulverized feed coal into account when determining the OT. For these reasons, we proposed a stochastic programing model based on MC simulation for OT optimization in this paper.

Considering the random fluctuation in the AMP series of feed coal and treating the AMP series as a dynamic random series, the principle of this stochastic model is to gain an optimal OT that compromises the ideal OT series according to each data of the AMP series. In this model, a random increment (denotes as $\Delta(t)$) within the interval [50, 100] was added to each data of the simulated AMP series (denotes as $X(t)$) to represent the ideal value of OT (denotes as $Y(t)$), then the optimization target is to minimize the gap between the optimal OT (denotes as T) and each ideal OT $Y(t)$. The stochastic programing model based on MC simulation for OT optimization was proposed as follows:

$$\begin{aligned} &\min Z = \sum_{t=1}^{n} (T - Y(t))^2 \\ &s.t. \begin{cases} Y(t) = X(t) + \Delta(t) \\ \Delta(t) = 50(rand_1(t) + 1) \\ X(t) = 1300 + 5S(t) - 5rand_2(t) \\ \sum_{j=1}^{S(t)-1} \boldsymbol{P}_{CaseI}(S(t-1), j) \le rand_3(t) \le \sum_{j=1}^{S(t)} \boldsymbol{P}_{CaseI}(S(t-1), j) \\ S(1) = 8 \\ 1350 \le T \le 1450 \end{cases} \end{aligned} \tag{15}$$

where T is the decision variable; Z is the objective function, represented by the sum of squares of the difference between T and $Y(t)$; $\Delta(t)$ is obeyed the uniform distribution $\Delta(t) \sim U(50, 100)$; $rand(t)$ is a random number of $[0, 1]$; $S(t)$ is the state of AMP at t, and its initial value is set as $S(1) = 8$.

The most prominent feature of this stochastic programing optimization model is the integration of the MC simulation in it. In order to gain a more accurate optimal OT to provide more valuable guidance for gasifier operation practice, the simulated AMP data series were expanded to 10,000 data sets according to the change law of the original AMP data series using the found simulation program. Then the stochastic programing would be optimized based on the newly acquired large data sets.

The found mathematical model for OT optimization is a stochastic programming model due to the hybridization of MC random simulation in the constraints. These random, non-linear and non-quadratic constraints present multiple challenges in regard to solution methodology using traditional mathematical programming methods. However, these shortcomings can be easily handled using some artificial intelligence algorithms such as genetic algorithm (GA), simulated annealing algorithm (SAA), particle swarm optimization (PSO) and so on. Different from the traditional mathematical optimization methods, these artificial intelligence algorithms are evolutionary heuristics that are population-based search methods [50–52]. In an optimization procedure with these algorithms, the iterations move from a set of points (population) to another set of points with likely improvement using a combination of deterministic and probabilistic rules. Among these evolutionary algorithms, the GA employs the principal of "survival of the fittest" in its search process, and achieves evolution through crossover and mutation operations to explore new areas of solution space using best characteristics of previous population generations. Thus, it is well suited to and has been extensively applied to solve complex optimization problems such as nonlinear objectives and constrained functions without requiring gradient information. Therefore, we used GA to optimize the found stochastic optimization model of OT in this study.

4.2. Parameter Optimization Using GA

GA is an intelligent algorithm based on artificial population evolution [51]. The main idea is to screen individuals according to a series of genetic operations such as fitness function and cross-mutation, so that individuals with high fitness can be retained to form a new population. In this way, the fitness of each individual in the population continues to improve until certain limit conditions are met. At this time, the individual with the highest fitness in the population is the optimal solution of the parameters to be optimized.

In order to realize the programming of GA, the Sheffield GA optimizer coded in MATLAB is preferable due the operational convenience of this platform. Many optimization problems in various fields have been solved with it [53–55]. Similar to ordinary genetic algorithm programs, the Sheffield GA optimizer also contains standard crossover and mutation operators. Crossover is achieved by cloning pairs of parent solutions drawn randomly from the population and performing gene-swap between two gene positions selected at random. Similarly, mutation is achieved by cloning a parent solution drawn randomly from the population and then switching select genes in the cloned solution to new states randomly. Gene selection for mutation is done randomly with a 1% probability [56]. Figure 8 illustrates examples for crossover and mutation operators on solution candidates.

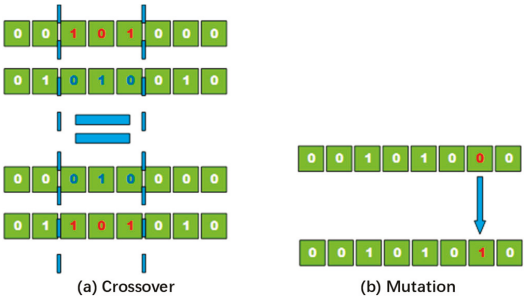

Figure 8. GA operators. (**a**) Crossover; (**b**) Mutation.

In this paper, the value of OT is regarded as different individuals. After substituting it into the objective function, the individual is evaluated according to the size of the objective value, and the individuals with good quality are selected for cross and variation to produce better individuals. Finally, after a certain number of iteration, we can get the best individual, that is, the best operation temperature. The GA procedure is shown in Figure 9.

In solving our stochastic optimization model (Equation (15)) by GA, the population size is set as $N = 30$ [57,58]. Besides, the roulette method [50] is used for selection, which is obey the rule that the higher the fitness, the greater the probability of being selected. Moreover, the crossover probability and the variation probability are usually set as $P_c = 0.8$ and $P_m = 0.01$ [58]. The iteration process of optimal solution is presented in Figure 10. It could be seen from Figure 10 that the convergence speed of the optimal solution is very fast, and the optimal solution has gradually stabilized at $T = 1424.80$ °C.

In order to verify this optimization result, we also optimized the found stochastic optimization model using SAA and PSO. Figure 11 shows the iterations of the optimal solution by SAA and PSO, and the optimal solutions by the these two algorithms are 1424.77 °C and 1424.75 °C, respectively. These two optimal results are almost consistent with that by GA algorithm. This indicates that the optimization result using GA is valid. However, the convergence speed of GA is the fastest comparing with SAA and PSO, which can be confirmed by their iterations.

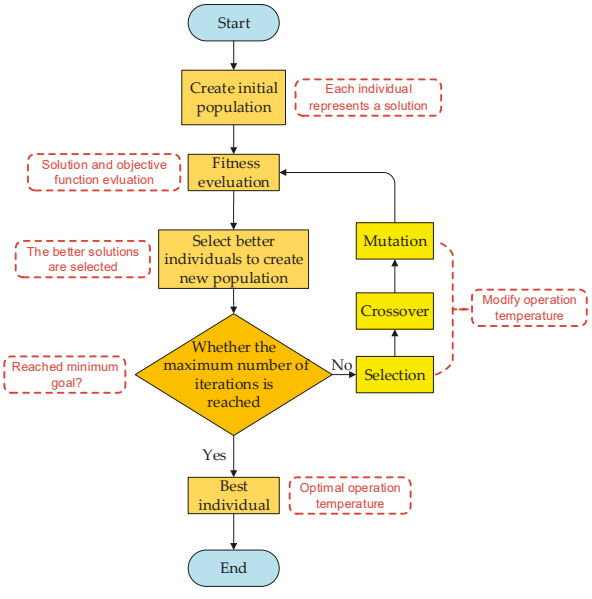

Figure 9. Flow chart of the genetic algorithm.

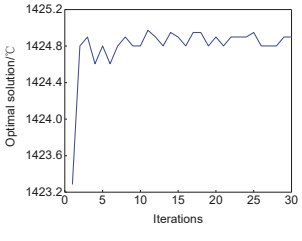

Figure 10. Iteration of optimization by GA.

4.3. Optimization Results Comparison between Stochastic Model and Conventional Model

As stated in Section 4.1, the traditional determination of OT is just according to the AMP mean of feed coal over a period of time or several successive batches. The determined OT with this method is usually inaccurate because the dynamic changes in AMP series are neglected. To verify whether our proposed stochastic programing model based on MC simulation can obtain a more accurate optimal OT or not for gasification practice, we compared the optimization results obtained from our model and those of the conventional method.

According to the conventional method, a random temperature increment with uniform distribution $\Delta(t) \sim U(50, 100)$ was added to the mean of the 200 AMP series ($\overline{X} = 1348$ °C), then the optimal OT obtained is 1398 $\sim$ 1448 °C. Figure 12 shows the range of optimal solutions obtained by the conventional method and by our stochastic optimization model. Compared the optimal result ascertained by the conventional model as shown in Figure 12, the optimal solution obtained by our proposed stochastic optimization model based on MC simulation converges to a narrower interval, which indicates that our proposed model can provide a more accurate optimal OT than that obtained from the conventional method.

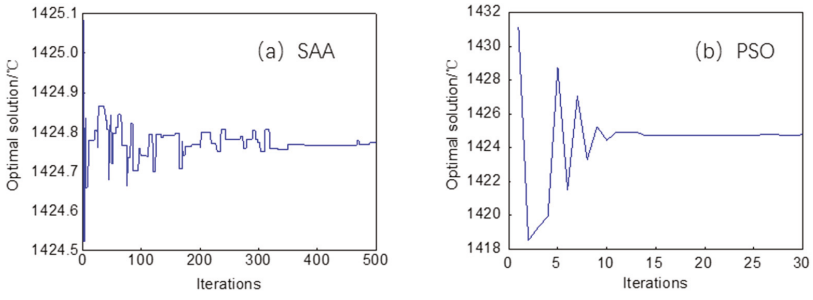

Figure 11. Iterations of optimization by (**a**) SAA and (**b**) PSO.

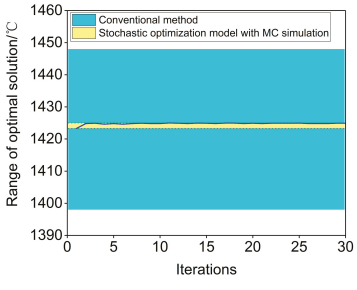

Figure 12. Comparison of the range of optimal solutions obtained by the conventional method and our stochastic optimization model.

5. Conclusions

Based on a stochastic process perspective, this paper focuses on the random simulation of AMP of feed coal for an entrained flow coal gasification process and the stochastic optimization of OT so as to provide more precise operational guidance for gasification operations. In this study, the AMP of coal was regarded as a random variable, and the MC method was used to simulate the dynamic changes in AMP. Then based on the MC simulation, a stochastic programing model for OT optimization was proposed. After a series of simulation with MC and optimization with GA, the optimal OT was gained. Some conclusions are as follows:

(1) MC is an effective simulation method to describe the dynamic changes in the AMP series when considering the characteristic variations of the feed coal from batch to batch. The MC simulation method can be further used in OT optimization.

(2) In the application of MC to simulate the collected original AMP data, the simulation result is best when the original AMP series is divided into 13 states. Under this partition scheme, the average relative deviation between the simulated and the original AMP is only 0.35%, which is very small. This indicates that founded MC simulation model under this scheme can accurately describe the dynamic change of AMP.

(3) Compared to the conventional OT determination method that just according to the AMP mean of the feed coal over a period of time or several successive batches, the proposed stochastic programing model that integrating MC simulation for OT optimization has obvious advantages, because the dynamic changes in AMP series are taken into account. Moreover, the final optimal OT value is $T = 1424.80$ °C, which is more accurate than the result $T \in [1398, 1448]$ obtained with the conventional method.

(4) The proposed stochastic programing model for OT optimization is a co-integration dynamic optimization problem, which can be optimized by some intelligent algorithms. The final optimal

OT ascertained from the proposed stochastic programing model is more accurate than that obtained using the conventional method, which has been verified by comparing the results. Thesr show that the proposed OT optimization model based on MC simulation can provide more accurate and reliable references for actual production.

Author Contributions: Conceptualization, J.Z. and J.H.; methodology, S.G.; software, S.G.; validation, Z.Z. and Z.L.; formal analysis, S.G.; investigation, J.H.; resources, X.M. and C.W.; data curation, X.M. and C.W.; writing—original draft preparation, J.Z. and S.G.; writing—review and editing, J.H.; visualization, S.G.; supervision, J.H.; project administration, J.Z.; funding acquisition, J.Z.

Funding: This research was funded by the National Nature Science Foundation of China (Grant no.51774113, 51674102), Science and Technology Project of Henan Province (Grant no.172102210288) and Priority Academic Program Development of Henan Higher Education Institutions (Grant no. 15B410001).

Acknowledgments: The authors also wish to thank the reviewers for the kindly advice.

Conflicts of Interest: The authors declare no conflicts of interest.

Nomenclature

The following nomenclature is used in this manuscript:

Abbreviation	**Meaning**
AMP	Ash melting point
OT	Operating temperature
MC	Markov chain
GA	Genetic algorithm
ANN	Artificial neural network
SVM	Support vector machine
RSM	Response surface methodology
CFD	Computational fluid dynamics
IADP	Iterative adaptive dynamic programming
MAD	Mean absolute deviation
RMSE	Root mean square error
AARE	Absolute average relative error
SAA	Simulated annealing algorithm
PSO	Particle swarm optimization
Symbols	
X_t	State at time t
S	State set
P_{ij}	Transition probability from state i to state j
$\boldsymbol{P}$	State transition probability matrix
n	Number of States
$\boldsymbol{V}_i^n$	n-step transition probability of state i
$\boldsymbol{\pi}$	Stationary distribution vector
r	A random number of [0, 1]
$\hat{y}_i$	The i-th simulated data
y_i	The i-th sample data
T	Actual operating temperature
$Y(t)$	Ideal operating temperature at time t
$X(t)$	Ash melting point at time t
$\Delta(t)$	The uniform distribution $\Delta(\mathrm{t}) \sim \mathrm{U}(50, 100)$
$rand(t)$	A random number of [0, 1] at time t
$S(t)$	State of ash melting point at time t
N	Population size
P_c	Crossover probability
P_m	Variation probability

Appendix A

Table A1. Simulation data and sample data deviation in three cases (the sample data of coal is from Hebi lean coal).

SerialNumber	Sample Data/°C	Simulated Data/°C			Absolute Deviation/°C			Relative Deviation		
		Case I	Case II	Case III	Case I	Case II	Case III	Case I	Case II	Case III
Training set										
1	1386.73	1389.71	1382.70	1369.38	2.98	4.03	17.35	0.21%	0.29%	1.25%
2	1348.07	1354.56	1335.43	1353.52	6.49	12.64	5.45	0.48%	0.94%	0.40%
3	1358.40	1351.29	1368.33	1332.41	7.11	9.93	25.99	0.52%	0.73%	1.91%
4	1351.90	1359.78	1341.63	1339.37	7.88	10.27	12.53	0.58%	0.76%	0.93%
5	1341.64	1355.24	1340.72	1358.78	13.60	0.92	17.14	1.01%	0.07%	1.28%
6	1339.47	1339.87	1348.71	1320.35	0.40	9.24	19.12	0.03%	0.69%	1.43%
7	1337.02	1327.97	1343.08	1319.99	9.05	6.06	17.03	0.68%	0.45%	1.26%
8	1363.06	1358.19	1354.76	1344.43	4.87	8.30	18.63	0.36%	0.61%	1.38%
9	1342.80	1345.99	1338.90	1332.40	3.19	3.90	10.40	0.24%	0.29%	0.77%
10	1337.50	1334.19	1324.86	1322.72	3.31	12.64	14.78	0.25%	0.94%	1.09%
11	1347.74	1339.69	1357.57	1357.87	8.05	9.83	10.13	0.60%	0.73%	0.75%
12	1341.27	1342.88	1331.90	1356.87	1.61	9.37	15.60	0.12%	0.69%	1.16%
13	1348.54	1356.14	1344.16	1363.90	7.60	4.38	15.36	0.56%	0.32%	1.14%
14	1325.90	1329.68	1333.87	1345.15	3.78	7.97	19.25	0.29%	0.59%	1.43%
15	1334.57	1340.74	1329.23	1316.11	6.17	5.34	18.46	0.46%	0.40%	1.37%
16	1350.79	1350.08	1356.87	1367.46	0.71	6.08	16.67	0.05%	0.45%	1.24%
17	1340.03	1352.85	1345.33	1352.07	12.82	5.30	12.04	0.96%	0.39%	0.89%
18	1341.68	1347.05	1337.75	1353.84	5.37	3.93	12.16	0.40%	0.29%	0.90%
19	1373.85	1369.05	1369.57	1379.70	4.80	4.28	5.85	0.35%	0.32%	0.43%
20	1366.54	1352.19	1360.16	1378.81	14.35	6.38	12.27	1.05%	0.47%	0.91%
21	1347.12	1353.11	1345.21	1354.98	5.99	1.91	7.86	0.44%	0.14%	0.58%
22	1334.47	1330.38	1343.30	1316.69	4.09	8.83	17.78	0.31%	0.65%	1.32%
23	1337.85	1344.44	1331.19	1355.52	6.59	6.66	17.67	0.49%	0.49%	1.31%
24	1378.56	1367.74	1369.45	1393.17	10.82	9.11	14.61	0.78%	0.67%	1.08%
25	1348.31	1349.75	1340.49	1335.76	1.44	7.82	12.55	0.11%	0.58%	0.93%
26	1353.46	1356.85	1344.97	1338.83	3.39	8.49	14.63	0.25%	0.63%	1.08%
27	1350.38	1343.74	1347.82	1370.86	6.64	2.56	20.48	0.49%	0.19%	1.52%
28	1364.58	1370.52	1368.53	1384.04	5.94	3.95	19.46	0.44%	0.29%	1.44%
29	1340.07	1339.51	1334.40	1352.34	0.56	5.67	12.27	0.04%	0.42%	0.91%
30	1340.46	1339.14	1347.80	1355.19	1.32	7.34	14.73	0.10%	0.54%	1.09%
31	1326.93	1325.98	1316.53	1317.35	0.95	10.40	9.58	0.07%	0.77%	0.71%
32	1330.30	1338.52	1336.44	1345.96	8.22	6.14	15.66	0.62%	0.45%	1.16%
33	1353.48	1348.41	1364.27	1336.46	5.07	10.79	17.02	0.37%	0.80%	1.26%
34	1348.87	1343.86	1357.31	1331.21	5.01	8.44	17.66	0.37%	0.62%	1.31%
35	1359.93	1351.68	1370.46	1367.87	8.25	10.53	7.94	0.61%	0.78%	0.59%
36	1343.38	1336.63	1335.99	1359.46	6.75	7.39	16.08	0.50%	0.55%	1.19%
37	1355.89	1345.46	1350.85	1366.49	10.43	5.04	10.60	0.77%	0.37%	0.79%
38	1359.67	1353.25	1362.24	1372.22	6.41	2.57	12.55	0.47%	0.19%	0.93%
39	1374.85	1381.48	1367.37	1392.06	6.63	7.48	17.21	0.48%	0.55%	1.27%
40	1348.89	1356.08	1358.36	1333.64	7.19	9.47	15.25	0.53%	0.70%	1.13%
41	1347.63	1351.04	1353.76	1361.04	3.41	6.13	13.41	0.25%	0.45%	0.99%
42	1351.14	1364.14	1356.53	1367.63	13.00	5.39	16.49	0.96%	0.40%	1.22%
43	1350.96	1345.71	1344.88	1330.36	5.25	6.08	20.60	0.39%	0.45%	1.53%
44	1347.80	1363.86	1344.08	1359.37	16.06	3.72	11.57	1.19%	0.28%	0.86%
45	1374.19	1377.24	1379.72	1365.53	3.05	5.53	8.66	0.22%	0.41%	0.64%
46	1365.98	1356.92	1372.45	1356.57	9.06	6.47	9.41	0.66%	0.48%	0.70%
47	1343.31	1355.47	1350.46	1353.59	12.16	7.15	10.28	0.91%	0.53%	0.76%
48	1360.68	1361.70	1353.86	1349.30	1.03	6.82	11.38	0.08%	0.51%	0.84%
49	1366.05	1362.88	1357.21	1382.42	3.17	8.84	16.37	0.23%	0.66%	1.21%
50	1337.96	1344.97	1330.62	1343.68	7.01	7.34	5.72	0.52%	0.54%	0.42%
51	1336.16	1342.94	1348.61	1321.16	6.77	12.45	15.00	0.51%	0.92%	1.11%
52	1345.54	1348.27	1337.59	1334.59	2.72	7.95	10.95	0.20%	0.59%	0.81%
53	1352.97	1344.34	1340.55	1334.51	8.63	12.42	18.46	0.64%	0.92%	1.37%
54	1351.54	1355.40	1356.38	1362.18	3.86	4.84	10.64	0.29%	0.36%	0.79%
55	1348.66	1335.77	1357.25	1362.75	12.89	8.59	14.09	0.96%	0.64%	1.04%
56	1352.53	1352.86	1358.76	1342.22	0.32	6.23	10.31	0.02%	0.46%	0.76%
57	1337.70	1336.94	1328.89	1326.37	0.76	8.81	11.33	0.06%	0.65%	0.84%
58	1338.66	1351.89	1347.45	1351.68	13.23	8.79	13.02	0.99%	0.65%	0.96%
59	1354.47	1352.95	1354.02	1367.61	1.52	0.45	13.14	0.11%	0.03%	0.97%
60	1347.44	1341.09	1350.47	1335.48	6.35	3.03	11.96	0.47%	0.22%	0.89%
61	1344.64	1347.91	1341.95	1363.21	3.27	2.69	18.57	0.24%	0.20%	1.38%
62	1327.90	1342.77	1336.12	1311.64	14.87	8.22	16.26	1.12%	0.61%	1.20%
63	1352.71	1353.57	1341.29	1331.23	0.87	11.42	21.48	0.06%	0.85%	1.59%
64	1354.91	1349.64	1348.88	1341.96	5.27	6.03	12.95	0.39%	0.45%	0.96%
65	1332.03	1337.47	1322.58	1350.36	5.44	9.45	18.33	0.41%	0.70%	1.36%
66	1347.41	1359.71	1338.76	1353.07	12.31	8.65	5.66	0.91%	0.64%	0.42%
67	1349.66	1355.90	1345.80	1366.27	6.24	3.86	16.61	0.46%	0.29%	1.23%
68	1360.46	1354.14	1368.66	1344.91	6.32	8.20	15.55	0.46%	0.61%	1.15%
69	1340.45	1338.66	1345.20	1353.01	1.78	4.75	12.56	0.13%	0.35%	0.93%
70	1341.74	1351.11	1353.30	1324.90	9.37	11.56	16.84	0.70%	0.86%	1.25%

Table A1. *Cont.*

SerialNumber	Sample Data/°C	Simulated Data/°C			Absolute Deviation/°C			Relative Deviation		
		Case I	Case II	Case III	Case I	Case II	Case III	Case I	Case II	Case III
71	1339.48	1352.09	1332.57	1357.05	12.61	6.91	17.57	0.94%	0.51%	1.30%
72	1327.03	1331.12	1338.95	1308.84	4.09	11.92	18.19	0.31%	0.88%	1.35%
73	1350.83	1351.57	1345.10	1366.57	0.73	5.73	15.74	0.05%	0.42%	1.17%
74	1354.03	1351.31	1362.81	1337.57	2.72	8.78	16.46	0.20%	0.65%	1.22%
75	1339.63	1345.42	1332.81	1328.27	5.79	6.82	11.36	0.43%	0.51%	0.84%
76	1337.69	1325.01	1338.63	1328.01	12.68	0.94	9.68	0.95%	0.07%	0.72%
77	1334.78	1341.37	1338.84	1321.79	6.60	4.06	12.99	0.49%	0.30%	0.96%
78	1347.45	1338.16	1356.30	1362.26	9.29	8.85	14.81	0.69%	0.66%	1.10%
79	1363.75	1350.05	1356.90	1345.89	13.70	6.85	17.86	1.00%	0.51%	1.32%
80	1313.52	1310.03	1317.17	1324.42	3.49	3.65	10.90	0.27%	0.27%	0.81%
81	1320.76	1315.98	1325.89	1332.86	4.77	5.13	12.10	0.36%	0.38%	0.90%
82	1363.40	1358.01	1355.64	1337.44	5.39	7.76	25.96	0.40%	0.57%	1.92%
83	1340.73	1351.84	1336.70	1329.16	11.10	4.03	11.57	0.83%	0.30%	0.86%
84	1349.17	1352.50	1339.24	1370.91	3.33	9.93	21.74	0.25%	0.74%	1.61%
85	1365.20	1359.60	1360.11	1347.30	5.60	5.09	17.90	0.41%	0.38%	1.33%
86	1369.65	1363.96	1382.09	1357.82	5.69	12.44	11.83	0.42%	0.92%	0.88%
87	1350.39	1346.00	1346.62	1336.76	4.39	3.77	13.63	0.32%	0.28%	1.01%
88	1358.48	1361.27	1350.87	1345.28	2.79	7.61	13.20	0.21%	0.56%	0.98%
89	1352.43	1357.78	1354.88	1336.48	5.34	2.45	15.95	0.40%	0.18%	1.18%
90	1356.11	1351.59	1351.27	1336.59	4.52	4.84	19.52	0.33%	0.36%	1.45%
91	1345.23	1334.22	1350.46	1352.74	11.01	5.23	7.51	0.82%	0.39%	0.56%
92	1330.57	1330.46	1338.78	1352.72	0.11	8.21	22.15	0.01%	0.61%	1.64%
93	1357.34	1357.05	1347.50	1340.17	0.28	9.84	17.17	0.02%	0.73%	1.27%
94	1358.07	1347.44	1350.16	1369.93	10.63	7.91	11.86	0.78%	0.59%	0.88%
95	1344.80	1341.04	1338.91	1358.36	3.76	5.89	13.56	0.28%	0.44%	1.00%
96	1342.66	1338.62	1352.12	1357.92	4.05	9.46	15.26	0.30%	0.70%	1.13%
97	1331.24	1333.67	1321.83	1316.00	2.43	9.41	15.24	0.18%	0.70%	1.13%
98	1343.07	1331.82	1350.44	1324.21	11.26	7.37	18.86	0.84%	0.55%	1.40%
99	1342.28	1339.84	1351.00	1323.86	2.44	8.72	18.42	0.18%	0.65%	1.36%
100	1345.14	1344.47	1353.39	1357.77	0.67	8.25	12.63	0.05%	0.61%	0.94%
101	1348.86	1345.30	1352.91	1362.40	3.55	4.05	13.54	0.26%	0.30%	1.00%
102	1349.97	1350.20	1340.68	1332.98	0.23	9.29	16.99	0.02%	0.69%	1.26%
103	1331.63	1343.49	1336.67	1346.17	11.86	5.04	14.54	0.89%	0.37%	1.08%
104	1338.13	1338.67	1332.93	1356.74	0.54	5.20	18.61	0.04%	0.39%	1.38%
105	1375.26	1374.54	1382.80	1363.95	0.72	7.54	11.31	0.05%	0.56%	0.84%
106	1344.16	1342.38	1338.07	1360.11	1.78	6.09	15.95	0.13%	0.45%	1.18%
107	1321.02	1320.90	1327.63	1336.23	0.12	6.61	15.21	0.01%	0.49%	1.13%
108	1346.84	1344.96	1338.04	1327.21	1.88	8.80	19.63	0.14%	0.65%	1.45%
109	1334.22	1349.67	1324.07	1325.54	15.45	10.15	8.68	1.16%	0.75%	0.64%
110	1340.50	1343.81	1334.08	1354.56	3.31	6.42	14.06	0.25%	0.48%	1.04%
111	1355.88	1350.83	1363.87	1341.61	5.05	7.99	14.27	0.37%	0.59%	1.06%
112	1368.10	1352.21	1374.40	1363.41	15.89	6.30	4.69	1.16%	0.47%	0.35%
113	1365.28	1367.24	1372.98	1346.23	1.96	7.70	19.05	0.14%	0.57%	1.41%
114	1328.10	1322.52	1319.77	1302.80	5.58	8.33	25.30	0.42%	0.62%	1.87%
115	1372.65	1375.14	1377.81	1359.52	2.49	5.16	13.13	0.18%	0.38%	0.97%
116	1328.56	1331.64	1320.73	1343.77	3.08	7.83	15.21	0.23%	0.58%	1.13%
117	1372.20	1365.77	1363.39	1384.40	6.42	8.81	12.20	0.47%	0.65%	0.90%
118	1338.50	1355.56	1331.21	1322.90	17.06	7.29	15.60	1.27%	0.54%	1.16%
119	1346.74	1354.33	1358.94	1359.28	7.59	12.20	12.54	0.56%	0.90%	0.93%
120	1384.66	1385.74	1389.84	1398.31	1.08	5.18	13.65	0.08%	0.38%	1.01%
121	1358.05	1361.48	1362.85	1378.58	3.44	4.80	20.53	0.25%	0.36%	1.52%
122	1374.22	1368.69	1372.46	1384.89	5.53	1.76	10.67	0.40%	0.13%	0.79%
123	1353.48	1348.76	1363.22	1341.72	4.72	9.74	11.76	0.35%	0.72%	0.87%
124	1381.55	1385.28	1371.94	1367.79	3.73	9.61	13.76	0.27%	0.71%	1.02%
125	1353.16	1358.33	1346.39	1366.69	5.17	6.77	13.53	0.38%	0.50%	1.00%
126	1345.60	1347.33	1335.89	1365.42	1.74	9.71	19.82	0.13%	0.72%	1.47%
127	1322.46	1326.85	1330.02	1344.65	4.38	7.56	22.19	0.33%	0.56%	1.64%
128	1367.18	1370.83	1375.06	1377.33	3.65	7.88	10.15	0.27%	0.58%	0.75%
129	1356.45	1359.37	1363.80	1344.95	2.91	7.35	11.50	0.21%	0.54%	0.85%
130	1346.80	1336.37	1338.47	1330.66	10.43	8.33	16.14	0.77%	0.62%	1.20%
131	1371.95	1370.92	1379.26	1384.49	1.03	7.31	12.54	0.07%	0.54%	0.93%
132	1372.25	1374.51	1356.88	1394.28	2.26	15.37	22.03	0.16%	1.14%	1.63%
133	1337.22	1336.79	1340.73	1357.82	0.44	3.51	20.60	0.03%	0.26%	1.53%
134	1346.18	1347.23	1347.63	1329.88	1.05	1.45	16.30	0.08%	0.11%	1.21%
135	1333.10	1341.81	1336.69	1349.41	8.70	3.59	16.31	0.65%	0.27%	1.21%
136	1362.21	1363.98	1365.94	1374.92	1.76	3.73	12.71	0.13%	0.28%	0.94%
137	1346.47	1336.83	1340.76	1363.58	9.64	5.71	17.11	0.72%	0.42%	1.27%
138	1354.52	1354.09	1348.02	1373.09	0.42	6.50	18.57	0.03%	0.48%	1.38%
139	1344.18	1332.21	1337.83	1358.81	11.97	6.35	14.63	0.89%	0.47%	1.08%
140	1362.00	1355.51	1370.63	1383.77	6.49	8.63	21.77	0.48%	0.64%	1.61%
141	1353.16	1348.27	1344.98	1336.42	4.88	8.18	16.74	0.36%	0.61%	1.24%
142	1354.90	1357.30	1345.64	1341.28	2.40	9.26	13.62	0.18%	0.69%	1.01%
143	1367.08	1355.35	1379.42	1382.62	11.74	12.34	15.54	0.86%	0.91%	1.15%
144	1347.93	1333.99	1337.25	1329.48	13.94	10.68	18.45	1.03%	0.79%	1.37%
145	1320.76	1331.25	1323.92	1333.23	10.49	3.16	12.47	0.79%	0.23%	0.92%
146	1362.00	1348.15	1362.02	1375.72	13.86	0.02	13.72	1.02%	0.00%	1.02%

Table A1. *Cont.*

SerialNumber	Sample Data/°C	Simulated Data/°C			Absolute Deviation/°C			Relative Deviation		
		Case I	Case II	Case III	Case I	Case II	Case III	Case I	Case II	Case III
147	1356.05	1365.03	1365.77	1332.50	8.98	9.72	23.55	0.66%	0.72%	1.74%
148	1356.70	1349.51	1358.20	1344.54	7.18	1.50	12.16	0.53%	0.11%	0.90%
149	1356.92	1351.13	1364.13	1374.77	5.79	7.21	17.85	0.43%	0.53%	1.32%
150	1360.67	1361.51	1367.79	1343.34	0.83	7.12	17.33	0.06%	0.53%	1.28%
151	1365.73	1360.14	1379.42	1386.15	5.60	13.69	20.42	0.41%	1.01%	1.51%
152	1351.39	1345.53	1358.19	1335.23	5.86	6.80	16.16	0.43%	0.50%	1.20%
153	1341.11	1356.04	1335.62	1336.91	14.93	5.49	4.20	1.11%	0.41%	0.31%
154	1366.60	1370.32	1358.88	1355.95	3.72	7.72	10.65	0.27%	0.57%	0.79%
155	1344.35	1345.94	1352.10	1328.24	1.59	7.75	16.11	0.12%	0.57%	1.19%
156	1338.34	1331.92	1345.56	1323.25	6.42	7.22	15.09	0.48%	0.53%	1.12%
157	1361.52	1349.03	1366.70	1383.43	12.50	5.18	21.91	0.92%	0.38%	1.62%
158	1362.76	1367.41	1359.42	1382.45	4.65	3.34	19.69	0.34%	0.25%	1.46%
159	1343.63	1344.88	1351.59	1327.58	1.25	7.96	16.05	0.09%	0.59%	1.19%
160	1364.30	1350.40	1367.28	1378.69	13.90	2.98	14.39	1.02%	0.22%	1.07%
Average	—	—	—	—	5.93	7.00	14.94	0.44%	0.52%	1.11%
Testing set										
161	1354.05	1354.20	1350.14	1361.92	0.15	3.91	7.87	0.01%	0.29%	0.58%
162	1374.49	1368.33	1385.49	1352.98	6.16	11.00	21.51	0.45%	0.82%	1.59%
163	1350.13	1352.84	1355.88	1335.53	2.71	5.75	14.60	0.20%	0.43%	1.08%
164	1349.69	1348.67	1356.28	1341.81	1.02	6.59	7.88	0.08%	0.49%	0.58%
165	1350.97	1345.98	1360.68	1366.76	4.98	9.71	15.79	0.37%	0.72%	1.17%
166	1378.59	1375.78	1384.70	1393.06	2.81	6.11	14.47	0.20%	0.45%	1.07%
167	1343.81	1338.89	1333.71	1355.59	4.92	10.10	11.78	0.37%	0.75%	0.87%
168	1346.99	1351.28	1341.02	1330.96	4.28	5.97	16.03	0.32%	0.44%	1.19%
169	1354.18	1352.49	1344.13	1365.41	1.69	10.05	11.23	0.12%	0.74%	0.83%
170	1356.40	1342.92	1365.30	1347.73	13.49	8.90	8.67	0.99%	0.66%	0.64%
171	1335.90	1339.09	1342.27	1328.86	3.19	6.37	7.04	0.24%	0.47%	0.52%
172	1343.18	1334.27	1347.59	1355.78	8.91	4.41	12.60	0.66%	0.33%	0.93%
173	1329.18	1327.50	1325.30	1340.73	1.69	3.88	11.55	0.13%	0.29%	0.86%
174	1339.83	1340.50	1346.03	1355.65	0.67	6.20	15.82	0.05%	0.46%	1.17%
175	1348.02	1342.93	1353.72	1356.07	5.09	5.70	8.05	0.38%	0.42%	0.60%
176	1342.70	1347.59	1348.48	1355.93	4.89	5.78	13.23	0.36%	0.43%	0.98%
177	1321.68	1329.50	1311.72	1313.64	7.81	9.96	8.04	0.59%	0.74%	0.60%
178	1346.92	1343.46	1340.80	1368.22	3.46	6.12	21.30	0.26%	0.45%	1.58%
179	1334.86	1339.25	1324.42	1348.45	4.39	10.44	13.59	0.33%	0.77%	1.01%
180	1336.79	1337.33	1342.21	1317.83	0.55	5.42	18.96	0.04%	0.40%	1.40%
181	1350.31	1356.17	1340.38	1366.35	5.86	9.93	16.04	0.43%	0.74%	1.19%
182	1347.10	1345.93	1352.54	1364.79	1.17	5.44	17.69	0.09%	0.40%	1.31%
183	1348.67	1350.40	1341.13	1339.23	1.73	7.54	9.44	0.13%	0.56%	0.70%
184	1352.02	1357.13	1361.94	1371.11	5.11	9.92	19.09	0.38%	0.73%	1.41%
185	1352.23	1347.39	1346.46	1332.36	4.84	5.77	19.87	0.36%	0.43%	1.47%
186	1342.50	1351.54	1348.20	1336.75	9.04	5.70	5.75	0.67%	0.42%	0.43%
187	1364.00	1354.88	1377.02	1350.65	9.12	13.02	13.35	0.67%	0.96%	0.99%
188	1375.80	1365.70	1365.94	1387.25	10.09	9.86	11.45	0.73%	0.73%	0.85%
189	1333.28	1338.41	1327.57	1318.59	5.13	5.71	14.69	0.38%	0.42%	1.09%
190	1334.23	1335.92	1343.19	1344.89	1.70	8.96	10.66	0.13%	0.66%	0.79%
191	1347.61	1345.71	1341.68	1332.43	1.90	5.93	15.18	0.14%	0.44%	1.12%
192	1322.17	1325.41	1313.04	1305.72	3.24	9.13	16.45	0.24%	0.68%	1.22%
193	1342.65	1350.87	1353.91	1327.61	8.21	11.26	15.04	0.61%	0.83%	1.11%
194	1320.65	1327.58	1322.85	1334.24	6.92	2.20	13.59	0.52%	0.16%	1.01%
195	1337.95	1337.95	1348.05	1329.05	0.00	10.10	8.90	0.00%	0.75%	0.66%
196	1333.07	1341.68	1344.45	1347.36	8.61	11.38	14.29	0.65%	0.84%	1.06%
197	1353.43	1346.88	1346.28	1365.41	6.55	7.15	11.98	0.48%	0.53%	0.89%
198	1373.85	1369.05	1369.84	1392.12	4.80	4.01	18.27	0.35%	0.29%	1.33%
199	1366.54	1362.19	1358.02	1383.25	4.35	8.52	16.71	0.32%	0.62%	1.22%
200	1347.12	1353.11	1339.85	1353.64	5.99	7.27	6.52	0.44%	0.54%	0.48%
Average	—	—	—	—	4.68	7.53	13.37	0.35%	0.56%	0.99%

Appendix B

```
# Constructing State Transition Probability Matrix
clear
A = xlsread('200sample', 'A1:A200');
t = length(A);
B = unique(A);
tt = length(B);
E = sort(B,'ascend');
T = zeros(16,16);
TR = zeros(16,16);
a = 0;
b = 0;
c = 0;
d = 0;
e = 0;
```

```
f = 0;
g = 0;
h = 0;
k = 0;
l = 0;
m = 0;
n = 0;
o = 0;
p = 0;
q = 0;
r = 0;
for j=1:1:tt
Localization=find(A==E(j));
for i=1:1:length(Localization)
if Localization(i)+1>t
break;
elseif A(Localization(i)+1)==E(1)
a = a+1;
elseif A(Localization(i)+1)==E(2)
b = b+1;
elseif A(Localization(i)+1)==E(3)
c = c+1;
elseif A(Localization(i)+1)==E(4)
d = d+1;
elseif A(Localization(i)+1)==E(5)
e = e+1;
elseif A(Localization(i)+1)==E(6)
f = f+1;
elseif A(Localization(i)+1)==E(7)
g = g+1;
elseif A(Localization(i)+1)==E(8)
h = h+1;
elseif A(Localization(i)+1)==E(9)
k = k+1;
elseif A(Localization(i)+1)==E(10)
l = l+1;
elseif A(Localization(i)+1)==E(11)
m = m+1;
elseif A(Localization(i)+1)==E(12)
n = n+1;
elseif A(Localization(i)+1)==E(13)
o = o+1;
elseif A(Localization(i)+1)==E(14)
p = p+1;
elseif A(Localization(i)+1)==E(15)
q = q+1;
elseif A(Localization(i)+1)==E(16)
r = r+1;
end
end
T(j,1:tt) = [a,b,c,d,e,f,g,h,k,l,m,n,o,p,q,r];
end
TT = T;
for u=2:1:tt
TT(u,:)=T(u,:)-T(u-1,:);
end
TT;
Y = sum(TT,2);
for uu = 1:1:tt
TR(uu,:) = TT(uu,:)./Y(uu,1);
end
```

```
TR
# Simulating 100000 AMP data
clear
A = xlsread('200sample', 'W1:AL16');#A is the state transition probability matrix TR
B = zeros(1,100000);
B(1) = 16;
i = 16;
s = zeros(1,16);
n = 2;
for n = 2:100000
r = rand(1);
i = B(n-1);
s(1) = A(i,1);
for j = 2:16
s(j) = s(j-1)+A(i,j);
if r >= 0&&r <= s(1)
B(n) = 1;
elseif r >= s(j-1)&&r <= s(j)
B(n) = j;
end
end
end
B
for i = 1:100000
r = rand(1);
B(i) = 1310+B(i)*5-5*r;
end
B'
```

References

1. Bezdek, R.H.; Wendling, R.M. The return on investment of the clean coal technology program in the USA. *Energy Policy* **2013**, *54*, 104–112. [CrossRef]
2. Chang, S.; Zhuo, J.; Meng, S.; Qin, S.; Yao, Q. Clean coal technologies in China: Current status and future perspectives. *Engineering* **2016**, *2*, 447–459. [CrossRef]
3. Cui, L.; Li, Y.; Tang, Y.; Shi, Y.; Wang, Q.; Yuan, X.; Kellett, J. Integrated assessment of the environmental and economic effects of an ultra-clean flue gas treatment process in coal-fired power plant. *J. Clean. Prod.* **2018**, *199*, 359–368. [CrossRef]
4. Tang, X.; Snowden, S.; McLellan, B.C.; Höök, M. Clean coal use in China: Challenges and policy implications. *Energy Policy* **2015**, *87*, 517–523. [CrossRef]
5. Christopher, H.; Samuel, T. Advances in coal gasification, hydrogenation, and gas treating for the production of chemicals and fuels. *Chem. Rev.* **2014**, *114*, 1673–1708.
6. di Carlo, A.; Borello, D.; Bocci, E. Process simulation of a hybrid SOFC/mGT and enriched air/steam fluidized bed gasifier power plant. *Int. J. Hydrogen Energy* **2013**, *38*, 5857–5874. [CrossRef]
7. Zhang, J.; Hou, J.; Yang, Y.; Qiang, Z.; Wu, L.; Li, F.; Ma, J. Numerical and statistical analyzing the effect of operating parameters on syngas yield fluctuation in entrained flow coal gasification using Split-plot design. *Energy Fuels* **2017**, *31*, 5870–5881. [CrossRef]
8. Hou, J.; Zhang, J. Robust optimization of the efficient syngas fractions in entrained flow coal gasification using Taguchi method and response surface methodology. *Int. J. Hydrogen Energy* **2017**, *42*, 4908–4921. [CrossRef]
9. Nguyen, T.D.B.; Lim, Y.; Song, B.; Kim, S.; Joo, Y.; Ahn, D. Two-stage equilibrium model applicable to the wide range of operating conditions in entrained-flow coal gasifiers. *Fuel* **2010**, *89*, 3901–3910. [CrossRef]
10. Sasi, T.; Mighani, M.; Örs, E.; Tawani, R.; Gräbner, M. Prediction of ash fusion behavior from coal ash composition for entrained-flow gasification. *Fuel Process. Technol.* **2018**, *176*, 64–75. [CrossRef]
11. Patterson, J.H.; Hurst, H.J. Ash and slag qualities of Australian bituminous coals for use in slagging gasifiers. *Fuel* **2000**, *79*, 1671–1678. [CrossRef]

12. Kong, L.; Bai, J.; Bai, Z.; Guo, Z.; Li, W. Improvement of ash flow properties of low-rank coal for entrained flow gasifier. *Fuel* **2014**, *120*, 122–129. [CrossRef]
13. Hsieh, P.Y.; Kwong, K.; Bennett, J. Correlation between the critical viscosity and ash fusion temperatures of coal gasifier ashes. *Fuel Process. Technol.* **2016**, *142*, 13–26. [CrossRef]
14. Chakravarty, S.; Mohanty, A.; Banerjee, A.; Tripathy, R.; Mandal, G.K.; Basariya, M.R.; Sharma, M. Composition, mineral matter characteristics and ash fusion behavior of some Indian coals. *Fuel* **2015**, *150*, 96–101. [CrossRef]
15. Dai, X.; He, J.; Bai, J.; Huang, Q.; Du, S. Ash fusion properties from molecular dynamics simulation: Role of the ratio of silicon and aluminum. *Energy Fuels* **2016**, *30*, 2407–2413. [CrossRef]
16. Weber, R.; Mancini, M.; Schaffel-Mancini, N.; Kupka, T. On predicting the ash behaviour using Computational Fluid Dynamics. *Fuel Process. Technol.* **2013**, *105*, 113–128. [CrossRef]
17. Kim, J.; Kim, G.; Jeon, C. Prediction of correlation between ash fusion temperature of ASTM and Thermo-Mechanical Analysis. *Appl. Therm. Eng.* **2017**, *125*, 1291–1299. [CrossRef]
18. Tambe, S.S.; Naniwadekar, M.; Tiwary, S.; Mukherjee, A.; Das, T.B. Prediction of coal ash fusion temperatures using computational intelligence based models. *Int. J. Coal Sci. Technol.* **2018**, *5*, 486–507. [CrossRef]
19. Özbayoğlu, G.; Özbayoğlu, M.E. A new approach for the prediction of ash fusion temperatures: A case study using Turkish lignites. *Fuel* **2006**, *85*, 545–552. [CrossRef]
20. Ding, W.; Wu, X.; Wei, H. Coal ash fusion temperature forecast based on Gaussian regularization RBF neural network. In Proceedings of the 2011 International Conference on Remote Sensing, Environment and Transportation Engineering, Nanjing, China, 24–26 June 2011; pp. 3006–3009.
21. Yin, C.; Luo, Z.; Ni, M.; Cen, K. Predicting coal ash fusion temperature with a back-propagation neural network model. *Fuel* **1998**, *77*, 1777–1782. [CrossRef]
22. Liu, Y.P.; Wu, M.G.; Qian, J.X. Predicting coal ash fusion temperature based on its chemical composition using ACO-BP neural network. *Thermochim. Acta* **2007**, *454*, 64–68. [CrossRef]
23. Wang, C.L. The study of building model to predict ash fusion temperature. In Proceedings of the 30th Chinese Control Conference, Yantai, China, 22–24 July 2011; pp. 5217–5221.
24. Gao, F.; Han, P.; Zhai, Y.J.; Chen, L.X. Application of support vector machine and ant colony algorithm in optimization of coal ash fusion temperature. In Proceedings of the 2011 International Conference on Machine Learning and Cybernetics, Guilin, China, 10–13 July 2011; Volume 2, pp. 666–672.
25. Zhao, B.; Zhang, Z.; Wu, X. Prediction of coal ash fusion temperature by least-squares support vector machine model. *Energy Fuels* **2010**, *24*, 3066–3071. [CrossRef]
26. Chen, W.H.; Chen, C.J.; Hung, C.I. Taguchi approach for co-gasification optimization of torrefied biomass and coal. *Bioresour. Technol.* **2013**, *144*, 615–622. [CrossRef] [PubMed]
27. Vejahati, F.; Katalambula, H.; Gupta, R. Entrained-flow gasification of oil sand coke with coal: Assessment of operating variables and blending ratio via response surface methodology. *Energy Fuels* **2012**, *26*, 219–232. [CrossRef]
28. Emun, F.; Gadalla, M.; Majozi, T.; Boer, D. Integrated gasification combined cycle (IGCC) process simulation and optimization. *Comput. Chem. Eng.* **2010**, *34*, 331–338. [CrossRef]
29. Biagini, E.; Bardi, A.; Pannocchia, G.; Tognotti, L. Development of an entrained flow gasifier model for process optimization study. *Ind. Eng. Chem. Res.* **2009**, *48*, 9028–9033. [CrossRef]
30. Chen, C.; Hung, C. Optimization of co-gasification Process in an entrained-flow gasifier using the Taguchi Method. *J. Therm. Sci. Technol.* **2013**, *8*, 190–208. [CrossRef]
31. Shastri, Y.; Diwekar, U. Stochastic modeling for uncertainty analysis and multiobjective optimization of IGCC system with single-stage coal gasification. *Ind. Eng. Chem. Res.* **2011**, *50*, 4879–4892. [CrossRef]
32. Wei, Q.; Liu, D. Adaptive dynamic programming for optimal tracking control of unknown nonlinear systems with application to coal gasification. *IEEE Trans. Autom. Sci. Eng.* **2013**, *11*, 1020–1036. [CrossRef]
33. Milios, D.; Gilmore, S. Markov chain simulation with fewer random samples. *Electron. Notes Theor. Comput. Sci.* **2013**, *296*, 183–197. [CrossRef]
34. Afzal, M.S.; Al-Dabbagh, A.W. Forecasting in industrial process control: A hidden Markov model approach. *IFAC PapersOnLine* **2017**, *50*, 14770–14775. [CrossRef]
35. Cui, Z.; Kirkby, J.L.; Nguyen, D. A general framework for time-changed Markov processes and applications. *Eur. J. Oper. Res.* **2019**, *273*, 785–800. [CrossRef]

36. Dimopoulou, S.; Oppermann, A.; Boggasch, E.; Rausch, A. A Markov Decision Process for managing a Hybrid Energy Storage System. *J. Energy Storage* **2018**, *19*, 160–169. [CrossRef]
37. Duan, C.; Makis, V.; Deng, C. Optimal Bayesian early fault detection for CNC equipment using hidden semi-Markov process. *Mech. Syst. Signal Process.* **2019**, *122*, 290–306. [CrossRef]
38. Fadıloğlu, M.M.; Bulut, Ö. An embedded Markov chain approach to stock rationing under batch orders. *Oper. Res. Lett.* **2019**, *47*, 92–98. [CrossRef]
39. Munkhammar, J.; Widén, J. A Markov-chain probability distribution mixture approach to the clear-sky index. *Sol. Energy* **2018**, *170*, 174–183. [CrossRef]
40. Yang, Y.; Zhang, Q.; Wang, Z.; Chen, Z.; Cai, X. Markov chain-based approach of the driving cycle development for electric vehicle application. *Energy Procedia* **2018**, *152*, 502–507. [CrossRef]
41. Yu, X.; Gao, S.; Hu, X.; Park, H. A Markov decision process approach to vacant taxi routing with e-hailing. *Transp. Res. Part B Methodol.* **2019**, *121*, 114–134. [CrossRef]
42. Yu, G.; Zhou, Z.; Qiang, Q.; Yu, Z. Experimental studying and stochastic modeling of residence time distribution in jet-entrained gasifier. *Chem. Eng. Process. Process Intensif.* **2002**, *41*, 595–600.
43. Guo, Q.; Liang, Q.; Ni, J.; Xu, S.; Yu, G.; Yu, Z. Markov chain model of residence time distribution in a new type entrained-flow gasifier. *Chem. Eng. Process. Process Intensif.* **2008**, *47*, 2061–2065. [CrossRef]
44. Bonakdari, H.; Zaji, A.H.; Binns, A.D.; Gharabaghi, B. Integrated Markov chains and uncertainty analysis techniques to more accurately forecast floods using satellite signals. *J. Hydrol.* **2019**, *572*, 75–95. [CrossRef]
45. Carapellucci, R.; Giordano, L. A new approach for synthetically generating wind speeds: A comparison with the Markov chains method. *Energy* **2013**, *49*, 298–305. [CrossRef]
46. Alinovi, D.; Ferrari, G.; Pisani, F.; Raheli, R. Markov chain modeling and simulation of breathing patterns. *Biomed. Signal Process. Control* **2017**, *33*, 245–254. [CrossRef]
47. Masseran, N. Markov chain model for the stochastic behaviors of wind-direction data. *Energy Convers. Manag.* **2015**, *92*, 266–274. [CrossRef]
48. Wilinski, A. Time series modeling and forecasting based on a Markov chain with changing transition matrices. *Expert Syst. Appl.* **2019**, *133*, 163–172. [CrossRef]
49. Li, F.; Ma, X.; Xu, M.; Fang, Y. Regulation of ash-fusion behaviors for high ash-fusion-temperature coal by coal blending. *Fuel Process. Technol.* **2017**, *166*, 131–139. [CrossRef]
50. Eberhart, R.C.; Shi, Y. Comparison between genetic algorithms and particle swarm optimization: Evolutionary programming VII. In Proceedings of the International Conference on Evolutionary Programming, San Diego, CA, USA, 25–27 March 1998; pp. 611–616.
51. Lee, C.K.H. A review of applications of genetic algorithms in operations management. *Eng. Appl. Artif. Intell.* **2018**, *76*, 1–12. [CrossRef]
52. Shieh, H.; Kuo, C.; Chiang, C. Modified particle swarm optimization algorithm with simulated annealing behavior and its numerical verification. *Appl. Math. Comput.* **2011**, *218*, 4365–4383. [CrossRef]
53. Qin, H.; Guo, Y.; Liu, Z.; Liu, Y.; Zhong, H. Shape optimization of automotive body frame using an improved genetic algorithm optimizer. *Adv. Eng. Softw.* **2018**, *121*, 235–249. [CrossRef]
54. Bottura, F.B.; Bernardes, W.M.; Oleskovicz, M.; Asada, E.N. Setting directional overcurrent protection parameters using hybrid GA optimizer. *Electr. Power Syst. Res.* **2017**, *143*, 400–408. [CrossRef]
55. Tao, Y.; Zhang, Y.; Wang, Q. Fuzzy c-mean clustering-based decomposition with GA optimizer for FSM synthesis targeting to low power. *Eng. Appl. Artif. Intell.* **2018**, *68*, 40–52. [CrossRef]
56. Salman, S.; Alaswad, S. Alleviating road network congestion: Traffic pattern optimization using Markov chain traffic assignment. *Comput. Oper. Res.* **2018**, *99*, 191–205. [CrossRef]
57. Mandol, S.; Bhattacharjee, D.; Dan, P.K. Structural optimisation of wind turbine gearbox deployed in non-conventional energy generation. In Proceedings of the International Conference on Research into Design, Guwahati, India, 9–11 January 2017; pp. 835–848.
58. Sreenivasan, K.S.; Kumar, S.S.; Katiravan, J. Genetic algorithm based optimization of friction welding process parameters on AA7075-SiC composite. *Eng. Sci. Technol. Int. J.* **2019**, *41*, 269–273. [CrossRef]

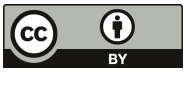

© 2019 by the authors. Licensee MDPI, Basel, Switzerland. This article is an open access article distributed under the terms and conditions of the Creative Commons Attribution (CC BY) license (http://creativecommons.org/licenses/by/4.0/).

MDPI
St. Alban-Anlage 66
4052 Basel
Switzerland
Tel. +41 61 683 77 34
Fax +41 61 302 89 18
www.mdpi.com

Energies Editorial Office
E-mail: energies@mdpi.com
www.mdpi.com/journal/energies

MDPI
St. Alban-Anlage 66
4052 Basel
Switzerland

Tel: +41 61 683 77 34

www.mdpi.com

ISBN 978-3-0365-5712-0